Εθνικό Μετσόβιο Πολυτεχνείο

Σχολή Εφαρμοσμένων Μαθηματικών & Φυσικών Επιστημών

Τομέας Φυσικής

Διδακτορική Διατριβή

Μελέτη αντιδράσεων νετρονίων σε ισότοπα της περιοχής των ακτινίδων

ΜΑΡΙΑ ΔΙΑΚΑΚΗ

Επιβλέπουσα Καθηγήτρια: Ρόζα Βλαστού-Ζάννη, Καθηγήτρια Ε.Μ.Π.

Αθήνα, Μάιος 2014

Η παρούσα έρευνα έχει συγχρηματοδοτηθεί από την Ευρωπαϊκή Ένωση (Ευρωπαϊκό Κοινωνικό Ταμείο - ΕΚΤ) και από εθνικούς πόρους μέσω του Επιχειρησιακού Προγράμματος "Εκπαίδευση και Δια Βίου Μάθηση" του Εθνικού Στρατηγικού Πλαισίου Αναφοράς (ΕΣΠΑ) – Ερευνητικό Χρηματοδοτούμενο Έργο: Ηράκλειτος ΙΙ . Επένδυση στην κοινωνία της γνώσης μέσω του Ευρωπαϊκού Κοινωνικού Ταμείου.

Εθνικό Μετσόβιο Πολυτεχνείο

Σχολή Εφαρμοσμένων Μαθηματικών & Φυσικών Επιστημών

Τομέας Φυσικής

Διδακτορική Διατριβή

Μελέτη αντιδράσεων νετρονίων σε ισότοπα της περιοχής των ακτινίδων

ΜΑΡΙΑ ΔΙΑΚΑΚΗ

Επταμελής εξεταστική επιτροπή

1. Ρόζα Βλαστού-Ζάννη, Καθηγήτρια Ε.Μ.Π. (συμβ. επιτροπή)
2. Μιχαήλ Κόκκορης, Επικ. Καθηγητής Ε.Μ.Π. (συμβ. επιτροπή)
3. Αναστάσιος Λαγογιάννης, Ερευνητής Β', Ε.Κ.Ε.Φ.Ε. "Δημόκριτος"(συμβ. επιτροπή)

4. Κωνσταντίνος Παπαδόπουλος, Αναπλ. Καθηγητής Ε.Μ.Π.
5. Σωτήριος Χαρισόπουλος, Ερευνητής Α', Ε.Κ.Ε.Φ.Ε. "Δημόκριτος "
6. Ηλίας Σαββίδης, Αναπλ. Καθηγητής Α.Π.Θ.
7. Νικόλαος Πατρώνης, Επικ. Καθηγητής Παν. Ιωαννίνων

Ευρωπαϊκή Ένωση
Ευρωπαϊκό Κοινωνικό Ταμείο

ΕΠΙΧΕΙΡΗΣΙΑΚΟ ΠΡΟΓΡΑΜΜΑ
ΕΚΠΑΙΔΕΥΣΗ ΚΑΙ ΔΙΑ ΒΙΟΥ ΜΑΘΗΣΗ
επένδυση στην κοινωνία της γνώσης
ΥΠΟΥΡΓΕΙΟ ΠΑΙΔΕΙΑΣ ΚΑΙ ΘΡΗΣΚΕΥΜΑΤΩΝ
ΕΙΔΙΚΗ ΥΠΗΡΕΣΙΑ ΔΙΑΧΕΙΡΙΣΗΣ

ΕΣΠΑ 2007-2013
πρόγραμμα για την ανάπτυξη
ΕΥΡΩΠΑΪΚΟ ΚΟΙΝΩΝΙΚΟ ΤΑΜΕΙΟ

Με τη συγχρηματοδότηση της Ελλάδας και της Ευρωπαϊκής Ένωσης

National Technical University of Athens

School of Applied Mathematical and Physical Science

Department of Physics

PhD thesis

Study of neutron induced reactions on actinide isotopes

MARIA DIAKAKI

Athens, May 2014

Σα βγεις στον πηγαιμό για την Ιθάκη, να εύχεσαι νάναι μακρύς ο δρόμος, γεμάτος περιπέτειες, γεμάτος γνώσεις. Τους Λαιστρυγόνας και τους Κύκλωπας, τον θυμωμένο Ποσειδώνα μη φοβάσαι, τέτοια στον δρόμο σου ποτέ σου δεν θα βρεις, αν μέν' η σκέψις σου υψηλή, αν εκλεκτή συγκίνησις το πνεύμα και το σώμα σου αγγίζει. Τους Λαιστρυγόνας και τους Κύκλωπας, τον άγριο Ποσειδώνα δεν θα συναντήσεις, αν δεν τους κουβανείς μες στην ψυχή σου, αν η ψυχή σου δεν τους στήνει εμπρός σου

Κ.Π. Καβάφης

...Στους γονείς μου...

Acknowledgements

As this journey comes to an end, I would like to express my thankfulness towards the people who helped for the realization of the present thesis, but also towards the people who were besides me all the way through.

I had the chance to work in the group of nuclear physics of the National Technical University of Athens (N.T.U.A.) since 2007, for my training, undergraduate thesis and then MSc thesis and finally PhD. After such a long time it feels like some people in this group are like a second family to me. We shared many hours of work, scientific interests and ideas, success and failure, joy and sorrow, which I will never forget.

More specifically, I would like to express my gratefulness to my teacher, professor of the N.T.U.A. Rosa Vlastou-Zanni, who is the supervisor of the present thesis, for the constant support and trust since the beginning, for always being there to help on whatever the issue, and for being at the same time a source of physics ideas and inspiration as a group leader, but also a kind and encouraging person. Michael Kokkoris, associate professor of the N.T.U.A., is the person who introduced me to the group for my undergraduate thesis, and the world of nuclear physics, and since then he has been strongly involved in my work, either as a supervisor or co-supervisor, putting in a lot of clever ideas, enthusiasm and pieces of advice I will never forget. I consider both of them as my mentors.

I would also like to thank Anastasios Lagoyannis, researcher at the I.N.P.P. of the N.C.S.R. “Demokritos”, for introducing me to the lab of the accelerator and to experimental physics, for providing precious explanations, help and advice at moments when really needed.

Special thanks to Costas Papadopoulos (N.T.U.A.), for the very careful correction of the whole manuscript, the help on understanding difficult meanings of nuclear physics and opening new ways of thinking. I would also like to thank Costas A. Kalfas, (I.N.P.P., “Demokritos”), who is a great teacher for all the younger students of the group and helped me personally a lot since my undergraduate thesis, in many aspects of the research work.

I would like to thank Dimitris Karadimos for providing me with his nice routines for the analysis of the FIC data, and for being a very good teacher in C++, ROOT and data analysis.

I thank Sotirios Harissopulos, (I.N.P.P., “Demokritos”), for his constant suport since my undergraduate years, Nicolaos Patronis (University of Ioannina) for the fruitful and educative discussions and nice time during the experiments, and Vivian Demetriou (I.A.E.A.) for accurate explanations and help on the theory of fission. I thank Ilias Savvidis (Aristotle University of Thessaloniki) for accepting to be a member of my examining committee.

Special thanks to my friend Andrea Tsinganis for sharing many hours of experimental and theoretical work, ideas and fun at CERN and other places around the world. Also to my friends and office-mates George Eleftheriou, Valentina Paneta, Froso Androulakaki, Antigonh Kalamara for the nice discussions, moments and friendship. Furthermore, the work of Alex Kyrtsos and Eleftherios Skordis for their undergraduate and MSc thesis, respectively, was valuable to the present thesis and I would like to thank them for the nice cooperation.

I spent a lot of time at the Tandem laboratory of the I.N.P.P. of “Demokritos”and I will never forget the help of Dr. Mike Axiotis, Dr. George Provatas and Dr. Varvara Foteinou, and the nice moments we shared. Many

thanks to the technical staff of the lab for doing their best during our experiments, especially Miltos Andrianis, Nick Papakostopoulos, Nick Divis, and Manos Tsopanakis.

During the thesis I spent long periods at the n_TOF facility at CERN, which I enjoyed a lot, both scientifically and personally, thanks to the n_TOF members at CERN, to whom I would like to express my thankfulness, not only for the nice environment they created, but for the help they gave me, each one in their own way: Eric Berthoumieux, Carlos Guerrero, Enrico Chiaveri, Christina Weiss. I have a long list of n_TOF members from whom I learned a lot, either by working with them at the facility, or by fruitful discussions during the meetings, some of them are Samuel Andriamonje, Thomas Papaevangelou, Nicola Colonna, Frank Gunsing, Laurent Tassan-Got, Vasilis Vlachoudis, Peter Schillebeeckx, Franz Käppeler, Vlad Avrigeanu, Christian Massimi, Raul Sarmento, Christos Lampoudis, Javier Praena.... Special thanks to Eric and Frank for the opportunity they gave me and also to Pierfrancesco Mastinu.

This research has been co-financed by the European Union (European Social Fund – ESF) and Greek national funds through the Operational Program "Education and Lifelong Learning" of the National Strategic Reference Framework (NSRF) - Research Funding Program: Heracleitus II. Investing in knowledge society through the European Social Fund.

Last but not least, my gratefulness to my family and beloved, who are always there for me and with their love and support make everything better.

Εκτεταμένη περίληψη

Σκοπός της παρούσας διατριβής είναι η μέτρηση της ενεργού διατομής της αντίδρασης ^{237}Np(n,f) στα πλαίσια της συνεργασίας n_TOF (neutron Time-of-Flight) ως προς τις αντιδράσεις αναφοράς ^{235}U(n,f) και ^{238}U(n,f), στο ενεργειακό εύρος keV-MeV και η θεωρητική μελέτη της ενεργού διατομής της αντίδρασης αυτής με στατιστικά πρότυπα. Τέτοιες μετρήσεις είναι απαραίτητες για τις ανάγκες της μελλοντικής Πυρηνικής Τεχνολογίας αλλά και της κατανόησης του φαινομένου της πυρηνικής σχάσης που είναι ένα από τα πιο ενδιαφέροντα και ακόμη όχι πλήρως κατανοητά φαινόμενα της πυρηνικής φυσικής. Με σκοπό τη μείωση των συστηματικών αβεβαιοτήτων, η ενεργός διατομή της αντίδρασης ^{237}Np(n,f) μετρήθηκε σε δύο εγκαταστάσεις με τελείως διαφορετικά χαρακτηριστικά, την εγκατάσταση n_TOF στο CERN με λευκή δέσμη νετρονίων και την εγκατάσταση παραγωγής νετρονίων στο Ινστιτούτο Πυρηνικής και Σωματιδιακής Φυσικής του Ε.Κ.Ε.Φ.Ε. ``Δημόκριτος'' με μονοενεργειακές δέσμες νετρονίων. Ακολουθεί μία σύντομη εισαγωγή στη θεώρηση του φαινομένου της σχάσης όπως εξελίχθηκε από την ανακάλυψή της μέχρι σήμερα, παρουσίαση της κατάστασης των πειραματικών δεδομένων της ενεργού διατομής της ^{237}Np(n,f) που αποτέλεσε και το κίνητρο της παρούσας εργασίας, περιγραφή των πειραμάτων που έγιναν και της ανάλυσης που ακολουθήθηκε, παρουσίαση των τελικών αποτελεσμάτων και της θεωρητικής μελέτης που έγινε με τον κώδικα EMPIRE 3.2.

Η πυρηνική σχάση προτάθηκε το 1939, από τους Meitner και Frisch [90] ως η διαίρεση βαρέος πυρήνα σε δύο περίπου ίσα μέρη συνοδευόμενο από την έκλυση μεγάλου ποσού ενέργειας. Εξηγήθηκε από τους Bohr και Wheeler [91] στα πλαίσια του Προτύπου της Υγρής Σταγόνας (Liquid Drop Model -LDM), σύμφωνα με το οποίο ο πυρήνας αναπαρίσταται από μία ομοιόμορφα ηλεκτρικά φορτισμένη υγρή σφαιρική σταγόνα η οποία παραμορφώνεται και ταλαντώνεται. Σε αυτή τη διαδικασία η σταγόνα σχηματίζει ένα ελλειψοειδές εκ περιστροφής (παράμετρος παραμόρφωσης ε) διατηρώντας σταθερό τον όγκο της, οπότε η διαφορά ενέργειας μεταξύ αυτού του σχήματος και της σφαιρικής σταγόνας δίνεται από τον τύπο 1.1, στον οποίο υπεισέρχονται μόνο οι όροι ενέργειας Coulomb (μειώνεται όσο επιμηκύνεται ο πυρήνας) και ο όρος ενέργειας λόγω επιφανειακής τάσης (αυξάνεται όσο επιμηκύνεται ο πυρήνας).

$$\Delta E = E(\epsilon) - E(\epsilon = 0) \tag{1.1}$$

$$= c_2 \cdot A^{2/3}(1 + \frac{2}{5}\epsilon^2 + ...) + c_3 \cdot Z^2/A^{1/3}(1 - \frac{1}{5}\epsilon^2 + ...) - c_2 \cdot A^{2/3} - c_3 \cdot Z^2/A^{1/3} \tag{1.2}$$

$$\approx -\frac{2}{5}E_{surf}(\epsilon = 0) + \frac{1}{5}E_{coul}(\epsilon = 0) \tag{1.3}$$

Εάν το ΔΕ είναι μεγαλύτερο από το 0, τότε ο πυρήνας κερδίζει ενέργεια με αυτή τη διαδικασία και θα συνεχίσει να επιμκύνεται μέχρι που θα φτάσει σε ένα σημείο που οι δυναμεις Coulomb είναι τόσο ισχυρές (της τάξεως των 180 MeV) που υπερνικούν την επιφανειακή τάση και ο πυρήνας σχάζεται σε δύο μικρότερους πυρήνες που ονομάζονται ``θραύσματα σχάσης''. Στα πλαίσια του προτύπου αυτού ορίζεται η παράμετρος σχάσης x από τον τύπο $x = \frac{E_{coul}}{2E_{surf}}$, όπου E_{coul} και E_{surf} αναφέρονται στις αντίστοιχες ενέργειες στην αρχική κατασταση της υγρής σταγόνας. Αν x>1 (για πυρήνες με Z>114) προκύπτει αυθόρμητη σχάση του πυρηνικού συστήματος χωρίς προσθήκη ενέργειας. Για την περιοχή των ακτινίδων το x κυμαίνεται από 0.7 έως 0.8, και συνεπώς η αυθόρμητη σχάση παρεμποδίζεται από ένα φράγμα δυναμικού.

Αυτή η δραστική αλλαγή σχήματος του πυρήνα από το αρχικα σφαιρικό σχήμα μέχρι τα τελικά θράυσματα σχάσης αναπαρίσταται με μία επιφάνεια δυναμικής ενέργειας ως προς διάφορες παραμέτρους παραμόρφωσης.

Αυτή η επιφάνεια δυναμικής ενέργειας συναρτήσει των δύο κυριότερων παραμέτρων παραμόρφωσης (τετραπολική παραμόρφωση, δεκαεξαπολική παραμόρφωση) φαίνεται στο σχήμα 7.1.

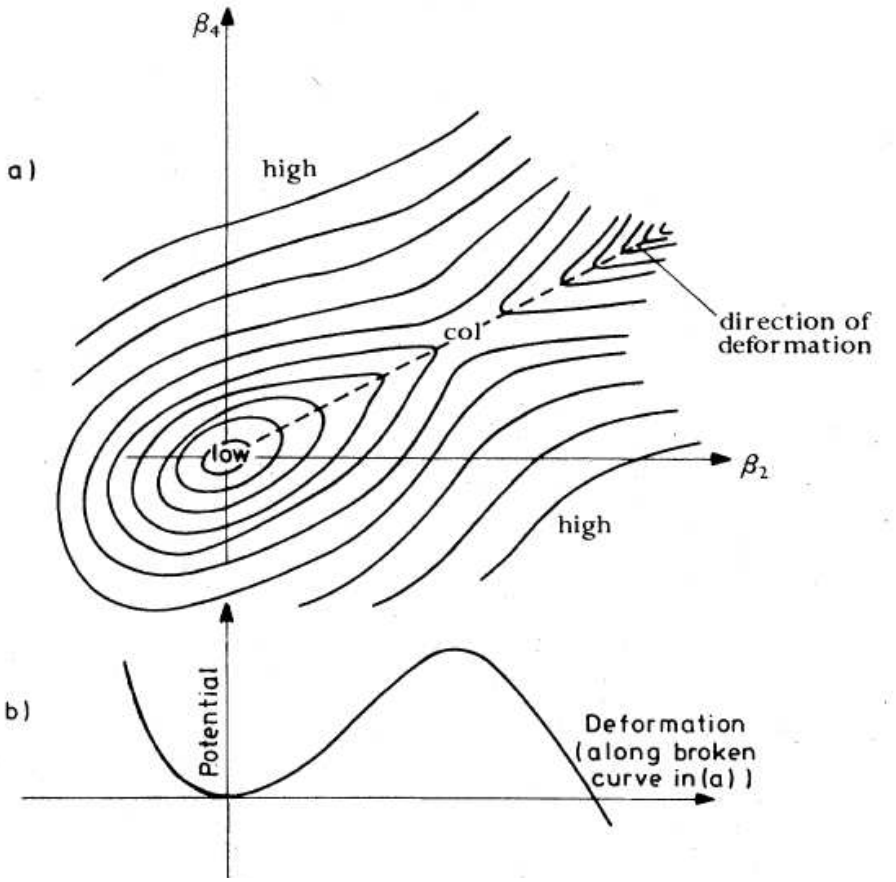

Σχήμα 1.1: α) Σχηματικό διάγραμμα της επιφάνειας δυναμικής ενέργειας σχάσιμου πυρήνα ως συνάρτηση της τετραπολικής και δεκαεξαπολικής παραμόρφωσης. Η ενεργειακά προτιμητέα διαδρομή προς τη σχάση σημειώνεται με διακεκομμένη γραμμή (``διαδρομή σχάσης-fission path'') και το φράγμα δυναμικού με ``col''. β) Η δυναμική ενέργεια κατά μήκος της διαδρομής σχάσης συναρτήσει της παραμέτρου παραμόρφωσης β [93].

Η θεώρηση του μονού φράγματος δυναμικού που προβλέπει το LDM παρουσίαζε αδυναμίες στην εξήγηση πειραματικών δεδομένων όπως το περίπου σταθερό ύψος φράγματος που παρατηρείται στις ακτινίδες Μετά την προσθήκη μικροσκοπικών διορθώσεων λόγω των φαινομένων φλοιών στον υπολογισμό της ενέργειας της βασικής κατάστασης των πυρήνων [95, 96] προέκυψε το λεγόμενο διπλό φράγμα δυναμικού (εικ. 1.2).

Σχηματίζονται έτσι δύο ``σαγματικά σημεία'' (Α και Β στην εικ. 7.2), δύο πηγάδια σταθερότητας, παραμόρφωσης β_1 που αντιστοιχεί στο πηγάδι της βασικής στάθμης και β_2 που αντιστοιχεί σε μερική σταθερότητα του πυρήνα σε σχήμα ελλειψοειδές εκ περιστροφής με λόγο αξόνων 2:1 περίπου. Με χρήση του διπλού φράγματος δυναμικού επετεύχθη η εξήγηση φαινομένων συντονισμών σε ενέργειες κάτω από το κατώφλι της σχάσης, ισομερών σταθμών σχάσης και ικανοποιητική αναπαραγωγή δεδομένων ενεργών διατομών σχάσης. Εντούτοις, αποτελει μία απλουστευμένη προσέγγιση και η θεωρητική μελέτη της σχάσης βρίσκεται ακόμη σε εξέλιξη, βασισμένη στο LDM με πιο λεπτομερή παραμετροποίηση του σχήματος της σταγόνας, ενώ έχουν προταθεί τριπλό φράγμα δυναμικού, η σχάση μέσω περισσότερων της μίας δυνατών διαδρομών σχάσης (multimodal fission) κλπ. Μέχρι σήμερα δεν υπάρχει θεωρία βασικών αρχών με ισχύ πρόβλεψης ενεργών διατομών σχάση και όλων των χαρακτηριστικών της, και βασιζόμαστε σε φαινομενολογική ανάλυση με με παραμέτρους που ρυθμίζονται για αναπαραγωγή των πειραματικών δεδομένων. Συνεπώς, υπάρχει μεγάλη ανάγκη για ακριβή δεδομένα ενεργών διατομών σχάσης ώστε να ελχιστοποιηθούν οι αβεβαιότητες στις παραμέτρους των μοντέλων και να αποκτήσουν οι θεωρητικοί υπολογισμοί ισχύ πρόβλεψης.

Όσον αφορά στις ανάγκες της Πυρηνικής Τεχνολογίας, σκοπός για τα μελλοντικά συστήματα είναι η μείωση

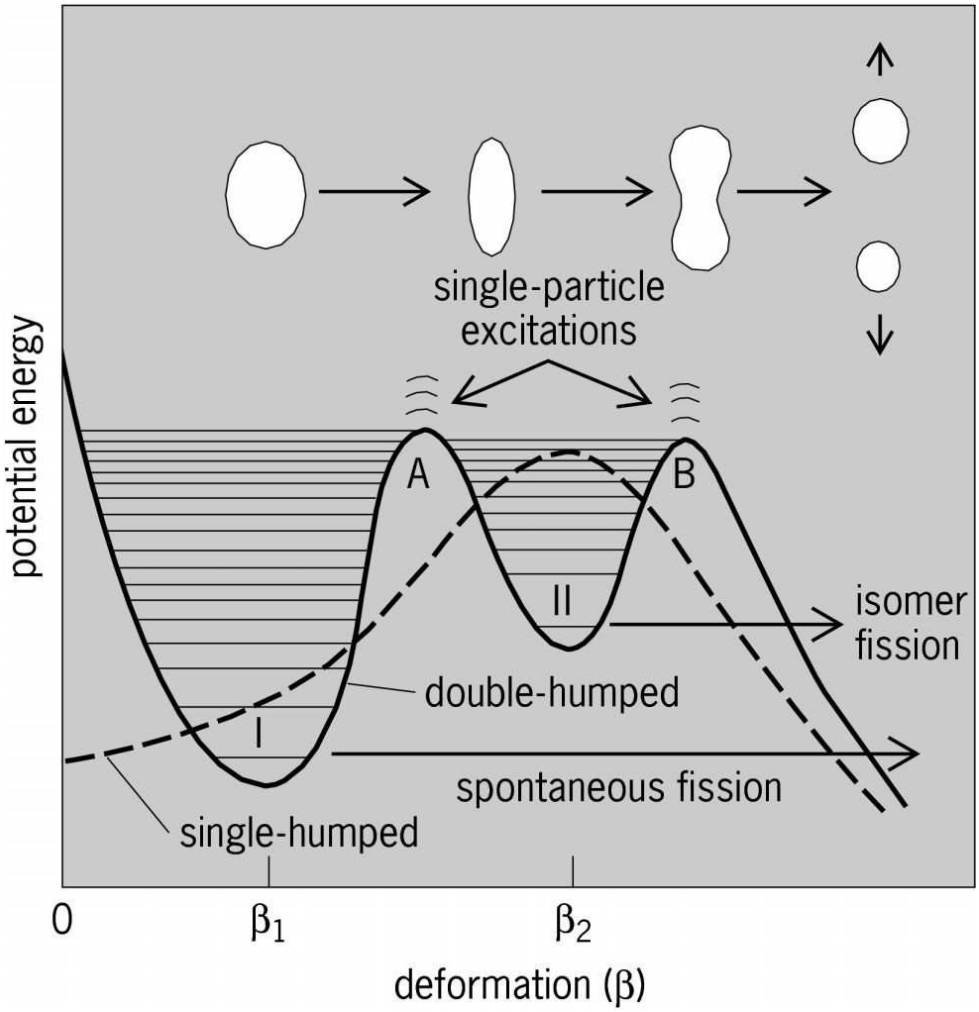

Σχήμα 1.2: Η δυναμική ενέργεια κατά μήκος της διαδρομής σχάσης συναρτήσει της παραμέτρου παραμόρφωσης β μετά την εισαγωγή του ταλαντούμενου διορθωτικού όρου ενέργειας λόγω φαινομένων φλοιών.

της πιθανότητας ατυχήματος και η ανακύκλωση των πυρηνικών αποβλήτων. Για τον σκοπό αυτό σχεδιάζεται η νέα γενιά πυρηνικών αντιδραστήρων (Generation IV, fast reactors, Accelerator Driven Systems) και συστήματα διαχωρισμού και αποτέφρωσης των πυρηνικών αποβλήτων (τεχνικές Partitioning and Transmutation). Για τον σχεδιασμό των νέων αυτών συστημάτων με όσο το δυνατόν μικρότερες αβεβαιότητες είναι προφανής η ανάγκη πειραματικών δεδομένων υψηλής ακριβείας όλων των ενεργών διατομών αντιδράσεων νετρονίων με ισότοπα της περιοχής των ακτινίδων σε μεγάλο ενεργειακό εύρος και κυρίως στην περιοχή keV-MeV.

Το ^{237}Np συγκεκριμένα είναι το πρώτο υπερουράνιο στοιχείο που ανακαλύφθηκε και αποτελεί το βασικό στοιχείο πυρηνικών καταλοίπων με μεγάλο χρόνο ημιζωής ($\sim 10^6$ χρόνια), συνεπώς η δυνατότητα μεταστοιχείωσής του αποτελεί προτεραιότητα. Εντούτοις,τα υπάρχοντα δεδομένα ενεργού διατομής της ^{237}Np(n,f) παρουσιάζουν αποκλίσεις που φτάνουν μέχρι και το 8% στο πλατώ της αντίδρασης, όπως φαίνεται στην εικ. 1.17.

Αυτή η διαφορά είναι μη αποδεκτή για θεωρητική μελέτη της αντίδρασης αυτής αλλά και για τις ανάγκες της πυρηνικής τεχνολογίας. Τέτοιες διαφορές έγκεινται κυρίως στη δυσκολία των μετρήσεων με δέσμες νετρονίων οι οποιες γίνονται πάντα σχετικά με πρότυπες αντιδράσεις αναφοράς.

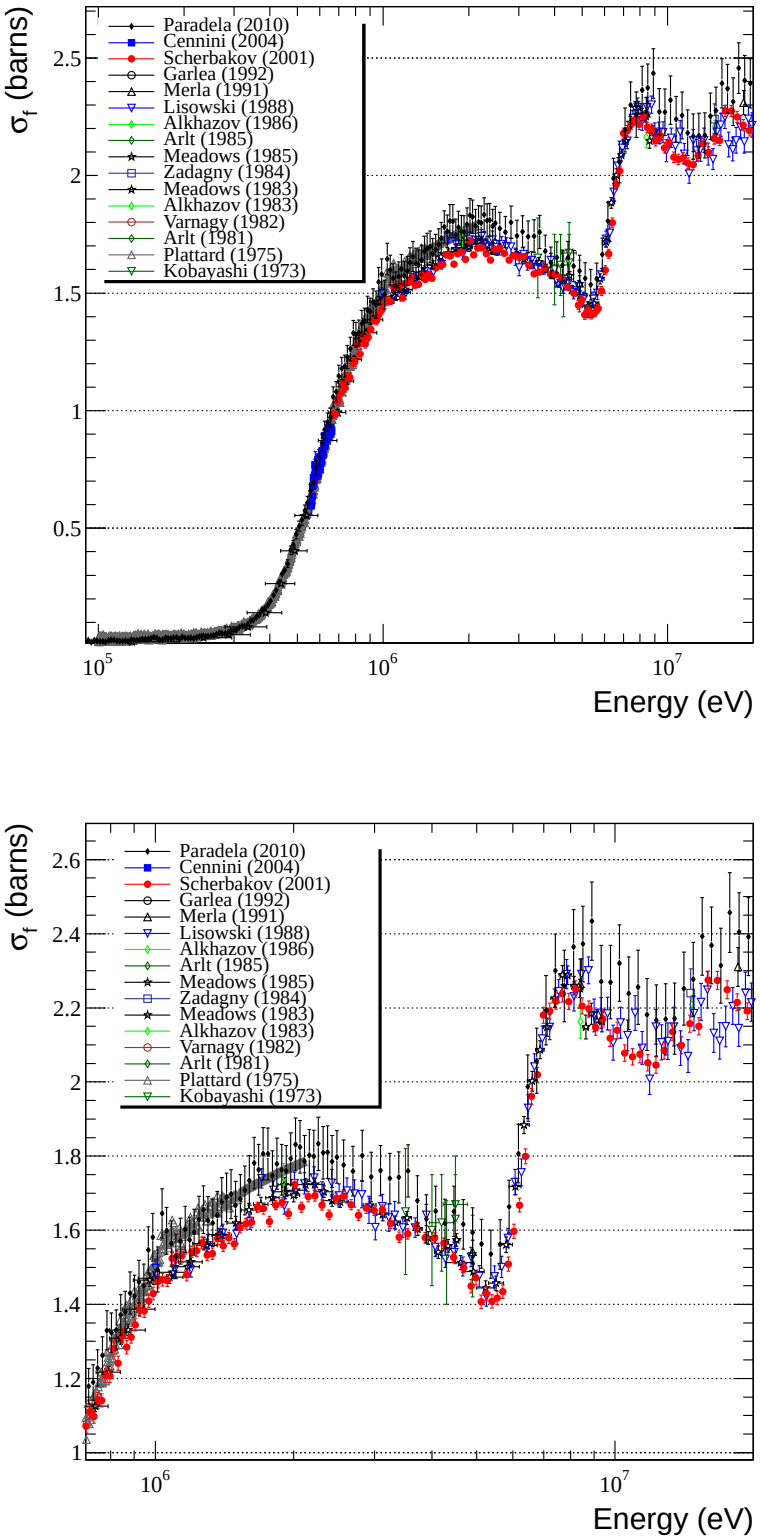

Σχήμα 1.3: Πάνω: Δεδομένα ενεργού διατομής της αντίδρασης ^{237}Np(n,f) [7] στο ενεργειακό εύρος 100 keV-20 MeV (μετά το 1973). Κάτω: Η ίδια εικόνα εστιασμένη στην ενεργειακή περιοχή πάνω από το κατώφλι.

Με βάση τα παραπάνω, η μέτρηση της ενεργού διατομής της ^{237}Np(n,f) πρέπει να ξαναγίνει και ήταν ο σκοπός της παρούσας διδακτορικής διατριβής, που έγινε στα πλαίσια της συνεργασίας n_TOF . Για τη μείωση των συστηματικών αβεβαιοτήτων μετρήθηκε η ίδια αντίδραση σε δύο εγκαταστάσεις: στην εγκατάσταση n_TOF (neutron Time-of-Flight) στο CERN και στο Ινστιτούτο Πυρηνικής και Σωματιδιακής Φυσικής (Ι.Σ.Π.Φ.) στο ΕΚΕΦΕ ``Δημόκριτος''. Ακολουθεί σύντομη παρουσίαση των μετρήσεων στις δύο εγκαταστάσεις, της ανάλυσης και των αποτελεσμάτων που προέκυψαν.

1.1 Η μέτρηση της ενεργού διατομής της ^{237}Np(n,f) στην εγκατάσταση n_TOF στο CERN

Η εγκατάσταση n_TOF στο CERN παρέχει δέσμη νετρονίων που παράγονται μέσω αντιδράσεων κατακερματισμού από τον βομβαρδισμό παχέος στόχου μολύβδου με υψηλοενεργειακά πρωτόνια ($\sim$ 20 GeV) που παρέχονται από τον επιταχυντή Proton Synchrotron (PS) του CERN σε παλμούς εύρους 7ns ανά χρονικά διαστήματα >1s. Η παραγόμενη δέσμη νετρονίων περιέχει μεγάλο εύρος ενεργειών, από θερμικά μέχρι GeV (λευκή δέσμη) και η ενέργεια του κάθε νετρονίου προσδιορίζεται από τον χρόνο πτήσης, από τη στιγμή δημιουργίας μέχρι τη στιγμή που απορροφάται στον στόχο προς ανάλυση και προκαλεί πυρηνική αντίδραση. Χάρη στο μεγάλο μήκος της γραμμής μεταφοράς των νετρονίων ($\sim$200m) η διακριτική ικανότητα στον προσδιορισμό της ενέργειας των νετρονίων είναι μικρότερη του 10^{-2} στις ενέργειες των GeV. Επιπροσθέτως, χάρη στην υψηλή ροή νετρονίων που παρέχεται σε μικρό χρονικό παράθυρο (Δt$\sim$80ms) στο οποίο καταγράφεται το σήμα, και στη σχετικά μικρή συχνότητα άφιξης παλμών πρωτονίων, μεγιστοποιείται ο λόγος σήματος προς υπόβαθρο, ενώ ελαχιστοποιείται η πιθανότητα επικάλυψης διαδοχικών παλμών νετρονίων. Τέλος, από τις αντιδράσεις κατακερματισμού μεταξύ άλλων παράγονται ακτίνες γ και σχετικιστικά σωματίδια που ταξιδεύουν με την ταχύτητα του φωτός, φτάνουν πριν από τα νετρόνια στον πειραματικό χώρο και δημιουργούν τον λεγόμενο παλμό-γ (γ-flash) που εναποθέτει μεγάλο ποσό ενέργειας στους ανιχνευτές και χρησιμοποιείται για τον ακριβή προσδιορισμό του χρόνου πτήσης των νετρονίων. Συγκεκριμένα, ο χρόνος πτήσης για ενα νετρόνιο n από τη στιγμή δημιουργίας του μέσα στον στόχο του Pb μέχρι τη στιγμή που προκαλεί μία πυρηνική αντίδραση (tof$_n$) υπολογίζεται μέσω της σχέσης: $tof_n = t_n - (t_{\gamma-flash} - L/c)$, όπου t_n η χρονική στιγμή καταγραφής του σήματος που προκάλεσε το νετρόνιο n στον εκάστοτε ανιχνευτή, $t_{\gamma-flash}$ η χρονική στιγμή καταγραφής του σήματος του παλμού-γ, L το μήκος πτήσης και c η ταχύτητα του φωτός (άρα L/c ο χρόνος πτήσης των ακτίνων γ που αποτελούν τον παλμό-γ).

Η μέτρηση του αριθμού των πυρηνικών αντιδράσεων σχάσης έγινε με την καταμέτρηση ενός εκ των δύο θραυσμάτων σχάσης που δημιουργούνται μέσα στον στόχο, εξέρχονται αυτού και εναποθέτουν μέρος ή ολόκληρο το ποσό της ενέργειάς τους μέσα στο αέριο του ανιχνευτή. Στη συγκεκριμένη μέτρηση χρησιμοποιήθηκε ο λεγόμενος Fast Ionization Chamber (FIC0), ανιχνευτής κλειστού τύπου με αέριο Ar (90%)-CF_4 (10%) σε 720mbar. Ο κάθε στόχος υπό μέτρηση τοποθετείται μέσα σε μία κυψελίδα με ενεργό πάχος αερίου 2cm. Όπως φαίνεται και στην εικ. 1.4 στο εσωτερικό του θαλάμου τοποθετούνται οι κυψελίδες η μία μετά την άλλη κεντραρισμένες.

Η αλληλουχία των στόχων που χρησιμοποιήθηκαν φαίνεται στον πίνακα 1.1. Για τις ανάγκες της παρούσας μέτρησης χρησιμοποιήθηκαν ένας στόχος ^{237}Np, τρεις στόχοι ^{238}U και τρεις στόχοι ^{235}U.

Το σήμα κάθε κυψελίδας καταγραφόταν σε ψηφιοποιητές Flash Analog-to-Digital Converter (FADC) με ρυθμό ψηφιοποίησης 40MHz σε 4096 κανάλια που το καθένα αντιστοιχεί σε χρονικό διάστημα $\times 25$ ns. Ένα τυπικό σήμα FADC από μία κυψελίδα φαίνεται στην εικ. 3.7.

Με αυτό τον ρυθμό ψηφιοποίησης καταγράφηκαν δεδομένα για ενέργειες νετρονίων μέχρι $\sim$100keV. Όπως προαναφέρθηκε, το πρώτο σήμα που καταγράφεται είναι ο παλμός-γ και ακολουθούν σε τυχαία κανάλια οι παλμοί από θραύσματα σχάσης που προκαλούν τα εισερχόμενα στον εκάστοτε στόχο νετρόνια (πχ. στα κανάλια 2725 και 2825 της εικ. 3.7). Η επεξεργασία αυτών των σημάτων συνίσταται στην αναγνώριση και καταμέτρηση των παλμών των θραυσμάτων σχάσης. Για κάθε στόχο αναλύθηκαν $\sim$300000 τέτοια σήματα, οπότε ήταν

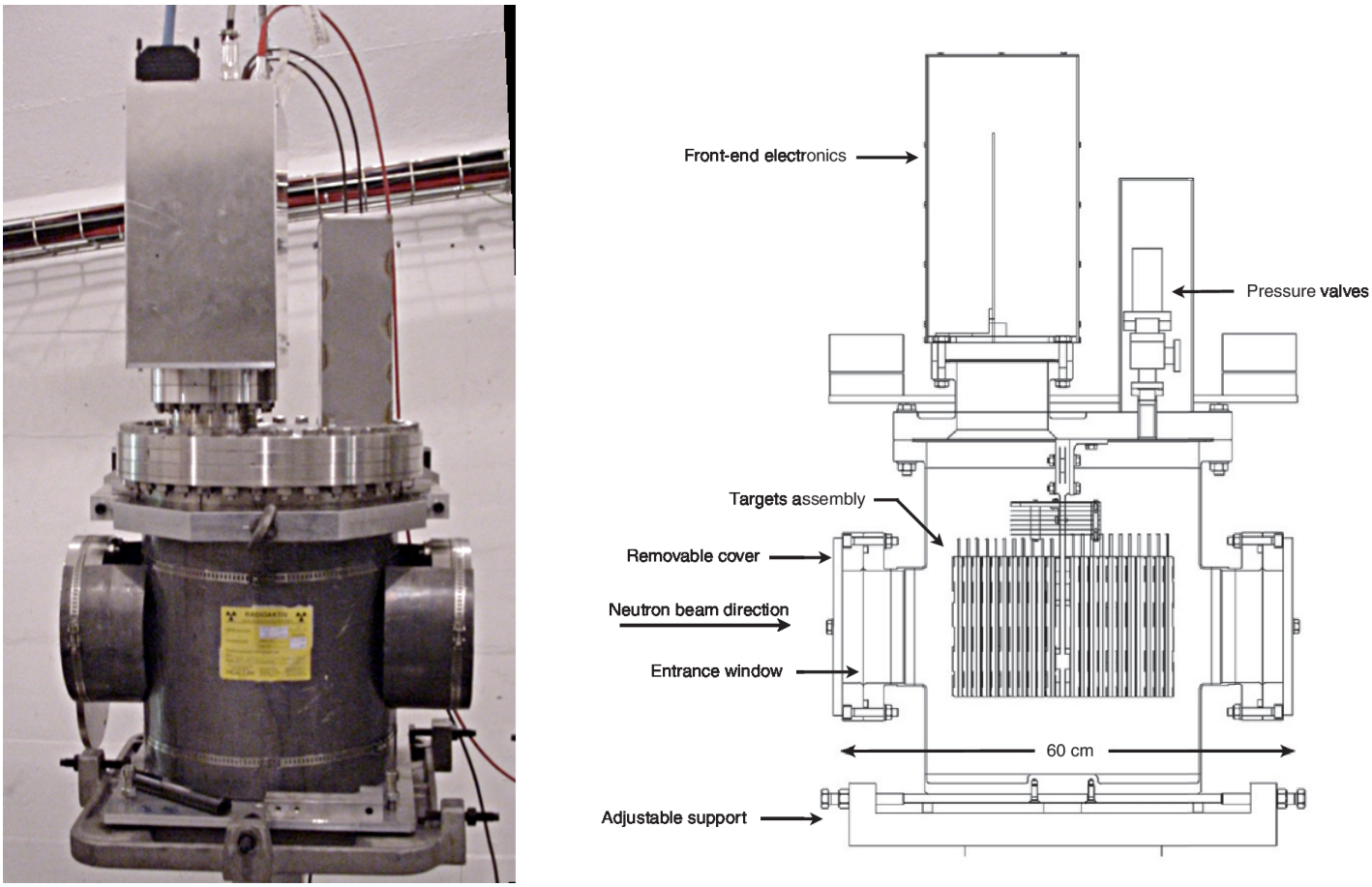

Σχήμα 1.4: Φωτογραφία (αριστερά) και σχηματικό διάγραμμα (δεξιά) του ανιχνευτή FIC0.

απαραίτητη η αυτοματοποίηση της διαδικασίας της ανάλυσης. Επιπροσθέτως, αμέσως μετά την άφιξη του παλμού-γ και λόγω της μεγάλης εναπόθεσης ενέργειας στους ανιχνευτές παρουσιάζεται έντονος ηλεκτρονικός θόρυβος που προκαλεί ταλαντώσεις του σήματος του ανιχνευτή (μέχρι το κανάλι 500 στην εικ. 1.5), συνεπώς δυσκολία αφαίρεσης του υποβάθρου πάνω στο οποίο επικάθονται οι παλμοί των θραυσμάτων σχάσης. Για την ανάλυση χρησιμοποιήθηκε κατάλληλο λογισμικό [58, 51] που αφαιρεί το ταλαντούμενο υπόβαθρο με την τεχνική των ``μέσων σημάτων'' και ακολούθως προσαρμόζει τους παλμούς θραυσμάτων σχάσης με κατάλληλη συνάρτηση. Στα συγκεκριμένα δεδομένα οι ταλαντώσεις του υποβάθρου ήταν τόσο μεγάλες που για κανάλια πριν από το 200 (δηλαδή για ενέργειες νετρονίων >10MeV) παρουσιάστηκε κορεσμός σε αρκετές περιοχές, συνεπώς απώλεια των δεδομένων του ψηφιοποιητή και έτσι δεν εξήχθησαν τιμές ενεργών διατομών για ενέργειες μεγαλύτερες από 10 MeV.

Η λειτουργία ``μέσου σήματος'' για την αφαίρεση του υποβάθρου βασίζεται στην παρατήρηση ότι η μορφή των ταλαντώσεων είναι σχεδόν όμοια για διαφορετικά σήματα (ακόμη και σε διαφορετικούς στόχους) ενώ οι παλμοί θραυσμάτων σχάσης έρχονται σε τυχαίους χρόνους. Συνεπώς ένα μέσο σήμα ($Y_{average}$(t)) που εξάγεται από πολλά τέτοια σήματα (διαπιστώθηκε ότι 20 είναι επαρκής αριθμός σημάτων για στόχο μέτριας ενεργότητας σε θραύσματα σχάσης) είναι απαλλαγμένο από παλμούς θραυσμάτων σχάσης και έχει τη μορφή των ταλαντώσεων, συνεπώς με μία μικρή προσαρμογή στο εκάστοτε σήμα αναπαράγει το υπόβαθρό του. Χωρίστηκαν τα σήματα σε κατηγορίες με βάση το ολοκλήρωμα του παλμού-γ και από κάθε κατηγορία εξήχθη το αντιστοιχο μέσο σήμα ($Y_{average}$(t)). Κατά την ανάλυση κάθε σήματος ο κώδικας αναγνωρίζει τον παλμό-γ, τον προσαρμόζει με τη συνάρτηση 4.2, υπολογίζει το ολοκλήρωμά του, επιλέγει το αντίστοιχο μέσο σήμα $Y_{average}$(t) και το προσαρμόζει με μία γραμμική συνάρτηση πάνω στο σήμα προς ανάλυση ($Y_{fittedaverage}(t) = Y_0 + A \cdot Y_{average}(t)$- δύο ελεύθερες παράμετροι), και τελικά αφαιρεί το $Y_{fittedaverage}(t)$ από το σήμα προς ανάλυση, οπότε προκύπτει από το αρχικό σήμα αφαιρούνται οι ταλαντώσεις του υποβάθρου χωρίς να επηρεάζονται οι παλμοί θραυσμάτων σχάσης (γκρι γραμμή στο σχήμα 1.6).

Θέση	Μήκος πτήσης n (m)	Ισότοπο	Label	Όνομα	Μάζα (mg)	Διάμετρος (cm)
4	185.390	U-235	9,10	U5	36.6	8
7	185.421	U-238	20,21	U8b	26.3	8
8	185.432	U-238	22,23	U8a	25.4	8
9	185.442	Np-237	28,29	Np7	12.64 ± 0.22	8
16	185.530	U-235	13,14	U5b	12.79	5
17	185.540	U-235	78	U5c	4.96 ± 0.06	5
18	185.551	U-238	209, 210	U8c	18.93 ± 0.18	5

Πίνακας 1.1: Οι στόχοι που χρησιμοποιήθηκαν για τις ανάγκες του υπολογισμού της ενεργού διατομής της ^{237}Np(n,f) με τη σειρά που τους συναντά η εισερχόμενη δέσμη νετρονίων. Οι μάζες που συνοδεύονται από αβεβαιότητες (Np7, U5c and U8c) προσδιορίστηκαν πειραματικά με φασματοσκοπία α στα πλαίσια της παρούσας εργασίας (κεφ.2), ενώ για τους υπόλοιπους στόχους χρησιμοποιήθηκαν οι αναγραφόμενες τιμές από τον κατασκευαστή.

Ακολούθως ο κώδικας προχωρά στην αναζήτηση τοπικών μεγίστων και προσαρμόζει τις κορυφές με τη συνάρτηση 1.4. Η συνάρτηση αυτή βρέθηκε ότι προσαρμόζει καλύτερα το σχήμα των παλμών του ανιχνευτή ιονισμού, έχει 6 παραμέτρους, 3 εκ των οποίων διατηρήθηκαν σταθερές.

$$Y_{peak} = Y_0 + A \cdot \left(1 - e^{-\frac{t-t_0}{t_1}}\right)^p \cdot e^{-\frac{t-t_0}{t_2}} \tag{1.4}$$

Οι παράμετροι και τα σφάλματα από τις προσαρμογές των παλμών-γ, των μέσων σημάτων και των παλμών θραυσμάτων σχάσης αποθηκεύονται σε ιστογράμματα για περαιτέρω διαλογή. Υπάρχει η δυνατότητα απόρριψης ολόκληρου σήματος αποκλείοντας παραμέτρους ή αντίστοιχα σφάλματα από προσαρμογή του παλμού-γ ή του μέσου σήματος, καθώς και παλμών θραυσμάτων σχάσης αποκλείοντας τις αντίστοιχες παραμέτρους/σφάλματα. Έγινε ξεχωριστή ανάλυση για κάθε στόχο ώστε να βρεθούν τα αποδεκτά όρια των παραμέτρων και των σφαλμάτων τους. Από αυτή την ανάλυση προέκυψαν ιστογράμματα με την κατανομή του ύψους των επιλεγμένων παλμών θραυσμάτων σχάσης για κάθε στόχο όπως αυτό που φαίνεται στο σχήμα 1.7. Ολοκληρώνοντας τέτοια ιστογράμματα προέκυψε ο αριθμός των θραυσμάτων σχάσης για κάθε στόχο.

Έγιναν διάφορα τεστ για την εύρεση της ευαισθησίας της μεθόδου ανάλυσης παλμών αλλάζοντας εντός ρεαλιστικών ορίων διάφορες παραμέτρους (όπως την κατηγοριοποίηση των σημάτων για την εύρεση του μέσου σήματος, την επιλογή του επιπέδου κατωφλίου πάνω από το οποίο ο κώδικας ψάχνει για τοπικά μέγιστα ή του επιπέδου υποβάθρου κάτω από το οποίο σταματά να ψάχνει για επόμενο τοπικό μέγιστο κλπ), με βασικότερο συμπέρασμα ότι για την ενεργειακή περιοχή ενδιαφέροντος ο μεγάλος όγκος παλμών άλλαζε ελάχιστα ενω επηρεαζόταν πολύ ο αριθμός των χαμηλού ύψους παλμών. Συνεπώς, αποφασίστηκε να τεθεί επιπλέον κατώφλι ανάλυσης ώστε να διώξει αυτούς τους παλμούς διότι δεν προέρχονταν μόνο από θραύσματα σχάσης αλλά και πιθανώς και από σωματίδια α ή/και θόρυβο (τυπικά ήταν γύρω στο κανάλι 70 για όλους τους στόχους).

Ο υπολογισμός της ενεργού διατομής έγινε με χρήση της εξίσωσης 1.5.

$$\sigma_{tar} = \frac{C_{tar} \cdot S_{tar} \cdot Nt_{ref} \cdot nEvents_{ref} \cdot eff_{ref}}{C_{ref} \cdot S_{ref} \cdot Nt_{tar} \cdot nEvents_{tar} \cdot eff_{tar}} \sigma_{ref} \tag{1.5}$$

όπου

1. C_{tar} και C_{ref} είναι ο αριθμός των παλμών θραυσμάτων σχάσης που έγιναν αποδεκτοί για τον κάθε στόχο και τον στόχο αναφοράς.

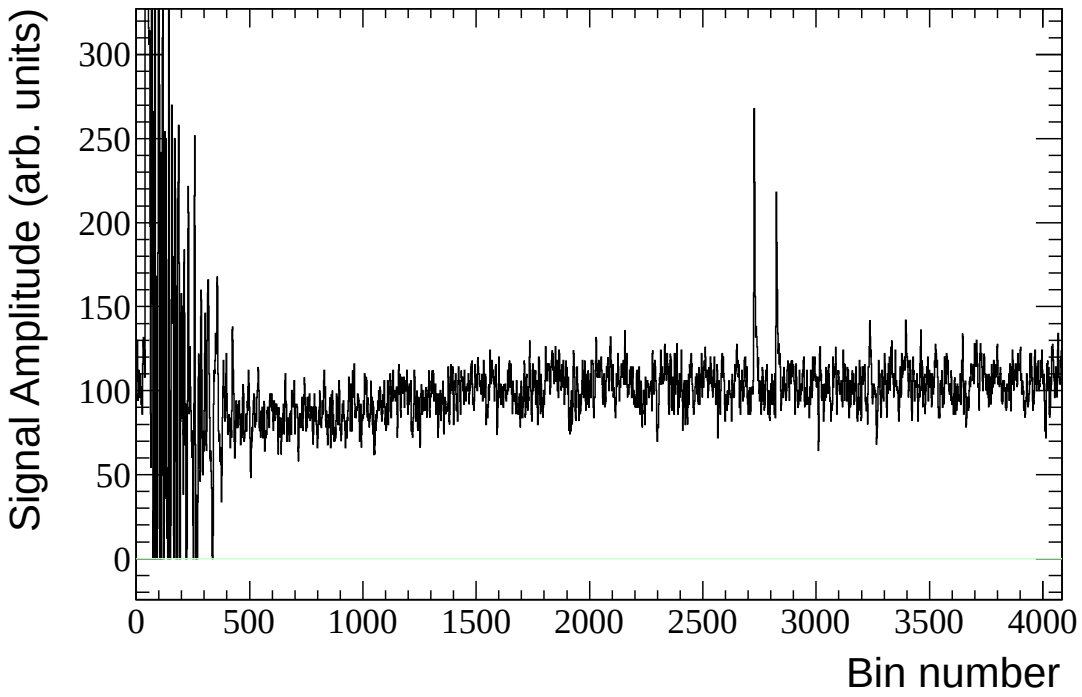

Σχήμα 1.5: Τυπικό σήμα FADC. Το σήμα του ανιχνευτή καταγραφόταν σε 4096 κανάλια που το καθένα αντιστοιχεί σε χρονικό διάστημα $\times 25$ ns.

2. S_{tar} και S_{ref} είναι οι διορθωτικοί πολλαπλασιαστικοί παράγοντες για τα θραύσματα σχάσης με ύψος μικρότερο από το κατώφλι ανάλυσης που υπολογίζεται με προσομοιώσεις FLUKA.

3. Nt_{tar} και Nt_{ref} είναι ο αριθμός των πυρήνων του κάθε στόχου που προσδιορίστηκαν είτε με φασματοσκοπία α ή χρησιμοποιήθηκαν οι τιμές του κατασκευαστή (πίνακας 3.3).

4. $nEvents_{tar}$ και $nEvents_{ref}$ είναι παράγοντες κανονικοποίησης του αριθμού των παλμών θραυσμάτων σχάσης για τον αριθμό των αποδεκτών σημάτων από την ανάλυση του κάθε στόχου..

5. eff_{tar} και eff_{ref} είναι η απόδοση του ανιχνευτή λόγω της γεωμετρίας ανίχνευσης και της ενδοαπορρόφησης του κάθε στόχου και προσδιορίστηκαν με προσομοιώσεις FLUKA.

6. σ_{ref} είναι η ενεργός διατομή της αντίδρασης αναφοράς. Χρησιμοποιήθηκε η αντίδραση ^{235}U(n,f) μέχρι τα 2 MeV, και η αντίδραση ^{238}U(n,f) μέχρι τα 10 MeV.

Οι διορθωτικοί παράγοντες S_{tar} και eff_{tar} για κάθε στόχο εκτιμήθηκαν με Monte Carlo προσομοιώσεις με τον κώδικα FLUKA, όπως περιγράφονται αναλυτικά στο κεφάλαιο 4. Για να γίνουν αυτές οι προσομοιώσεις αναπτύχθηκε εξωτερική ρουτίνα γενέσεως θραυσμάτων σχάσης με μαζικό και ατομικό αριθμό και ενέργεια που προβλέπονται με βάση τη συστηματική στην περιοχή των ακτινίδων [64]. Ένα τυπικό ιστόγραμμα εναπόθεσης ενέργειας μέσα στο αέριο του ανιχνευτή που προέκυψε από την προσομοίωση FLUKA φαίνεται στο σχήμα 1.8.

Με βάση την εξίσωση 1.5 πρώτα έγινε ο υπολογισμός της ενεργού διατομής της ^{238}U(n,f) που θεωρείται πρότυπη αντίδραση αναφοράς ως προς την ^{235}U(n,f) με διάφορους συνδυασμούς στόχων αναφοράς (U8a, U8b, U8c, U5, U5b, U5c) και σύγκριση των τιμών που προέκυψαν με την ENDF/B-VII.1 [28]. Από τέτοιες συγκρίσεις προέκυψε ότι ενώ με συνδυασμούς στόχων μικρής διαμέτρου η αναπαραγωγή της ENDF/B-VII.1 είναι πολύ ικανοποιητική (U8c με αναφορά τους U5c,U5b), στους συνδυασμούς στόχων μεγάλης διαμέτρου (με U5 στόχο αναφοράς) η απόκλιση από τις προτεινόμενες τιμές φτάνει και το 10%, μεταβαλλόμενη με την ενέργεια, κυρίως στην ενεργειακή περιοχή (600 keV-4 MeV). Αυτό βρέθηκε ότι οφείλεται σε αδυναμία προσαρμογής όλων των παλμών θραυσμάτων σχάσης κατά την ανάλυση των δεδομένων του στόχου αυτού

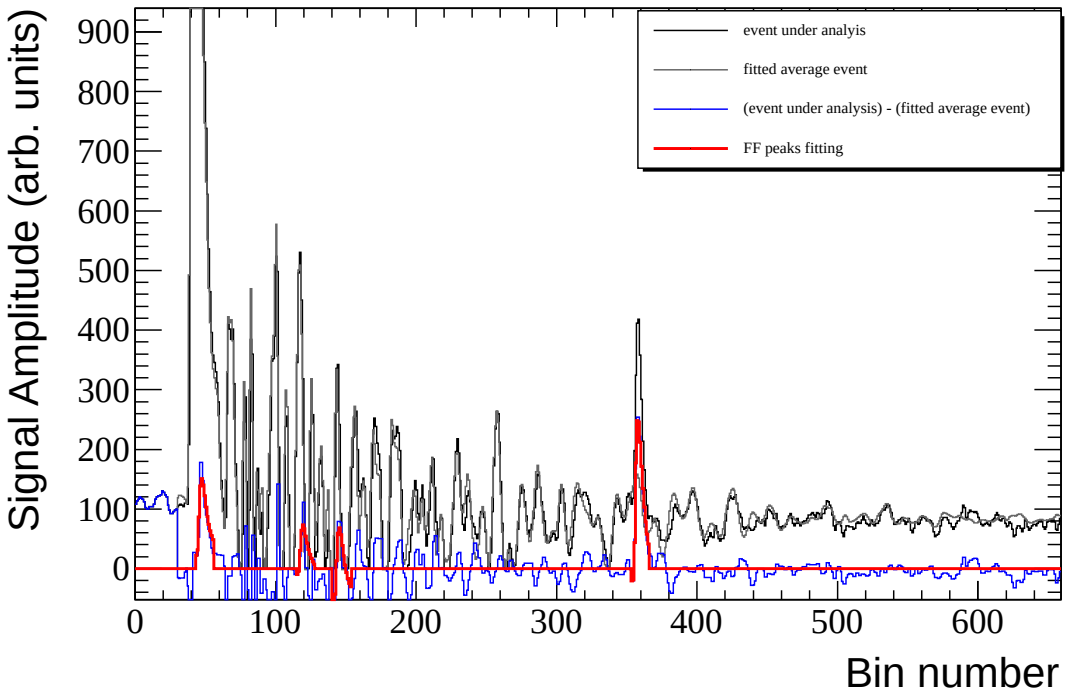

Σχήμα 1.6: Παράδειγμα ανάλυσης ενός σήματος με το λογισμικό που χρησιμοποιήθηκε στην παρούσα εργασία, όπου φαίνεται το αντίστοιχο προσαρμοσμένο ``μέσο σήμα", απαλλαγμένο από παλμούς θραυσμάτων σχάσης (γκρι γραμμή), που αφαιρείται από το σήμα προς ανάλυση (προκύπτει η μπλε γραμμή) και η εύρεση και προσαρμογή κορυφών θραυσμάτων σχάσης (κόκκινη γραμμή) από τον κώδικα.

στη συγκεκριμένη ενεργειακή περιοχή γιατί το μέσο σήμα υπερεκτιμούσε συχνά το υπόβαθρο του εκάστοτε σήματος. Αυτό οφείλεται στον υψηλό ρυθμό εμφάνισης παλμών στα σήματα του συγκεκριμένου στόχου λόγω της πολύ μεγάλης του μάζας σε συνδυασμό με τη μεγάλη ενεργό διατομή της ^{235}U(n,f) και τη μεγιστοποίηση της ροής των νετρονίων σε αυτή την ενεργειακή περιοχή. Συνεπώς αποφασίστηκε να χρησιμοποιηθεί το U5b ως στόχος αναφοράς μέχρι τα 2 MeV επειδή παρουσιάζει παρόμοια ενεργότητα με το Np7 σε αυτή την ενεργειακή περιοχή. Εντούτοις, οι δύο στόχοι έχουν διαφορετική επιφάνεια και από προσομοιώσεις του προφίλ της δέσμης των νετρονίων (εικ. 4.37, κεφάλαιο 4), φαίνεται ότι η ροή των νετρονίων μειώνεται στα άκρα στόχου ακτίνας 4 cm (όπως το Np7), ενώ παραμένει σταθερή στην επιφάνεια του στόχου ακτίνας 2.5 cm (όπως το U5b). Επομένως πρέπει να εισαχθεί επιπλέον πολλαπλασιαστικός παραγοντας $S_{effectiveneutronfluence}$ στον υπολογισμό της ενεργού διατομής με τον τύπο 4.5 όταν ο στόχος υπό μελέτη και ο στόχος αναφοράς είναι ακτίνας 4 και 2.5 cm αντίστοιχα. Αυτός ο παράγοντας προσδιορίστηκε πειραματικά με βάση λόγους ρυθμών ενεργοποίησης στόχων αναφοράς διαφορετικής διαμέτρου από το ίδιο ισότοπο καθώς και λόγους ενεργών διατομών της ^{238}U(n,f) υπολογισμένων με συνδυασμούς στόχων αναφοράς διαφορετικής διαμέτρου προς τις προτεινόμενες τιμές της ENDF [28], και βρέθηκε ίσος με 1.10 ± 0.02. Χρησιμοποιήθηκε ως επιπλέον πολλαπλασιαστικός παράγοντας στον υπολογισμό της ενεργού διατομής της αντίδρασης ^{237}Np(n,f) στην ενεργειακή περιοχή 400 keV- 2 MeV.

Τα τελικά αποτελέσματα μαζί με τα πιο πρόσφατα δεδομένα [8] και τις τελευταίες βιβλιοθήκες προτεινόμενων τιμών [28, 30, 29] παρουσιάζονται στο γράφημα 1.9.

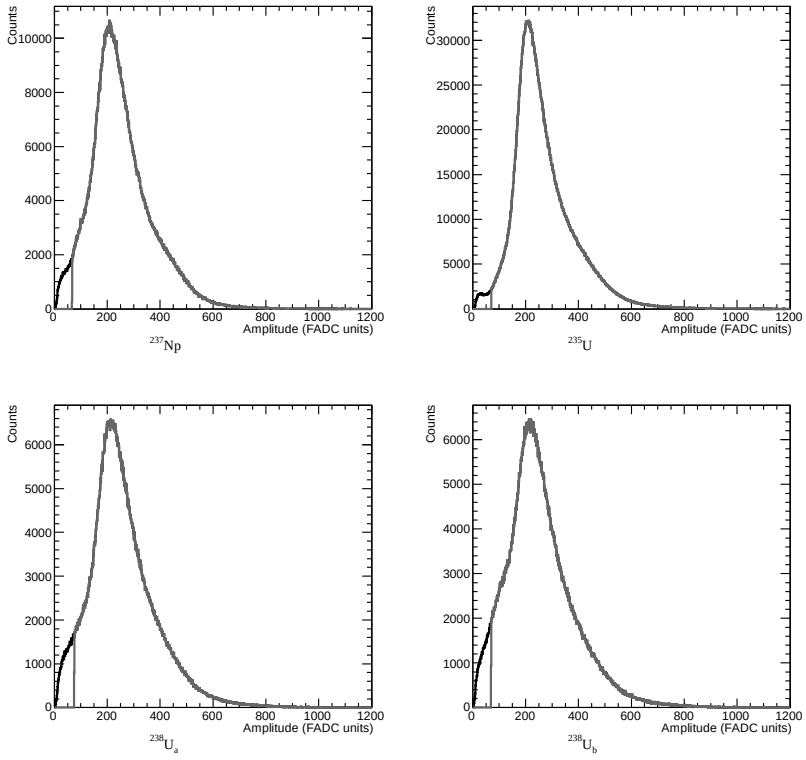

Σχήμα 1.7: Κατανομή παλμών θραυσμάτων σχάσης που προέκυψαν από την παρούσα ανάλυση για τους στόχους Np7, U5, U8a and U8b, όπου φαίνεται και το κατώφλι ανάλυσης που χρησιμοποιήθηκε.

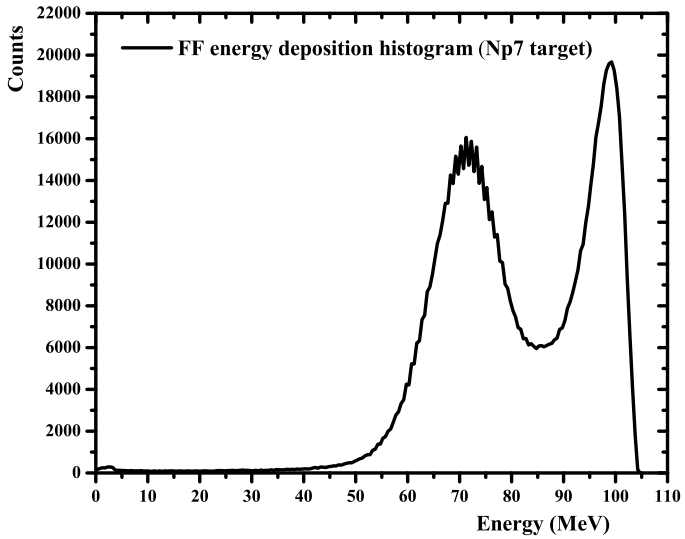

Σχήμα 1.8: Τυπικό ιστόγραμμα εναπόθεσης ενέργειας των θραυσμάτων σχάσης μέσα στο αέριο του ανιχνευτή, που προέκυψε από την προσομοίωση FLUKA για την κυψελίδα του στόχου Np7.

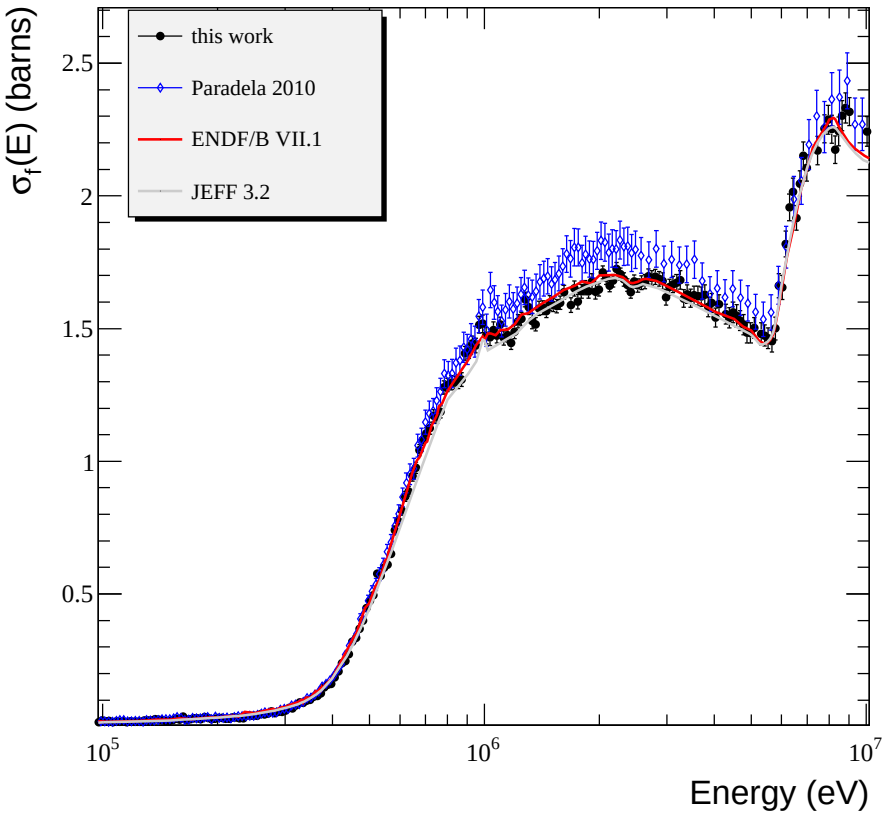

Σχήμα 1.9: Οι τελικές τιμές της ενεργού διατομής της ^{237}Np(n,f) από το n_TOF σε όλο το ενεργειακό εύρος, με τις στατιστικές αβεβαιότητες. Τα δεδομένα της παρούσας εργασίας συγκρίνονται με τις βιβλιοθήκες προτεινόμενων τιμών (ENDF/B-VII.1 [28], JEFF 3.2 [30]), και τα τελευταία πειραματικά δεδομένα [8].

Οι συστηματικές αβεβαιότητες παρατίθενται στον πίνακα 1.2.

Συνεισφορά	Αβεβαιότητα (%)	Ενεργειακό εύρος (MeV)
Μάζα στόχων	1.3-1.7	-
Διορθωτικός παράγοντας θραυσμάτων σχάσης κάτω από κατώφλι ανάλυσης	<0.5	-
Απόδοση ανιχνευτή	2	-
$S_{effectiveneutronfluence}$	1.8	0.4-2
$\sigma_{^{235}U(n,f)}$	< 1	0.01-2
$\sigma_{^{238}U(n,f)}$	< 1	2-10

Πίνακας 1.2: Οι συστηματικές αβεβαιότητες των υπολογισμένων τιμών ενεργού διατομής της ^{237}Np(n,f) από το n_TOF.

Από τη σύγκριση προκύπτει ότι μέχρι 1 MeV η συμφωνία είναι καλή με τα τελευταία δεδομένα και τις προτεινόμενες τιμές. Εντούτοις, πάνω από 1 MeV είναι σαφές ότι τα δεδομένα της παρούσας εργασίας συμφωνούν εντός σφάλματος με τις βιβλιοθήκες προτεινόμενων τιμών και είναι συστηματικά χαμηλότερα από τα τελευταία πειραματικά δεδομένα [8] με αποκλίσεις που σε κάποιες περιοχές είναι μεγαλύτερες από το στατιστκό σφάλμα (θεωρώντας 1σ). Ένα άλλο ενδιαφέρον αποτέλεσμα είναι η εμφάνιση μικρών πλατώ στο κατώφλι της σχάσης ($\sim$700 keV-1 MeV) που χρίζουν περαιτέρω διερεύνησης καθώς μπορεί να οφείλονται σε κάποια δομή, στη διαδικασία της σχάσης.

1.2 Η μέτρηση της ενεργού διατομής της ^{237}Np(n,f) στο Ι.Π.Σ.Φ. του Ε.Κ.Ε.Φ.Ε. "Δημόκριτος"

Όπως προαναφέρθηκε, για να μειωθούν οι συστηματικές αβεβαιότητες της μέτρησης, αποφασίστηκε να ξαναμετρηθεί η ίδια αντίδραση χρησιμοποιώντας τον ίδιο στόχο σε άλλη εγκατάσταση με διαφορεικά χαρακτηριστικά: την εγκατάσταση παραγωγής νετρονίων του Ι.Π.Σ.Φ. του Ε.Κ.Ε.Φ.Ε. ``Δημόκριτος''. Ο επιταχυντής του ινστιτούτου είναι ένας 5.5 MV Van de Graaff Tandem. Η παραγωγή των μονοενεργειακών δεσμών νετρονίων έγινε με την αντίδραση ^{2}H(d,n). Η δέσμη των δευτερίων επιταχύνθηκε σε ενέργειες 2-2.6 MeV με βήμα 200 keV, και βομβάρδιζε μία κυψελίδα γεμάτη αέριο δευτέριο σε πίεση 1300 mbar. Η κυψελίδα έχει ένα λεπτό παράθυρο εισόδου (5 μm Mo) και 1 mm Pt παράθυρο εξόδου για να σταματά τη δέσμη των δευτερίων χωρίς να επηρεάζει τα παραγόμενα νετρόνια. Οι αντίστοιχες ενέργειες των παραγόμενων νετρονίων κυμαίνονται από 4.58-5.32, ενώ η αβεβαιότητα στην ενέργεια οφείλεται κυρίως στην απώλεια ενέργειας των δευτερίων μέσα στο παράθυρο εισόδου, και δεν ξεπέρασε τα 150 keV. Η ροή των παραγόμενων νετρονίων ήταν της τάξης του 5×10^{4} n/(cm^{2}·s).

Για την ανίχνευση των θραυσμάτων σχάσης χρησιμοποιήθηκε ο ανιχνευτής ιονισμού MicroMegas, βασισμένος στην πρωτοποριακή τεχνολογία Micro-bulk [72, 76]. Σε αυτή την περίπτωση ο ανιχνευτής χωρίζεται σε δύο ενεργές περιοχές, την περιοχή ολίσθησης όπου τα ιόντα προς ανίχνευση ιονίζουν το αέριο του ανιχνευτή και τα παραγόμενα ηλεκτρόνια ωθούνται με ένα χαμηλό ηλεκτρικό πεδίο προς την περιοχή ενίσχυσης περνώντας μέσα από ένα ηλεκρόδιο με τρύπες, το λεγόμενο micromesh. Στην περιοχή ενίσχυσης εφαρμόζεται πολύ υψηλό ηλεκρικό πεδίο (της τάξης των 50 kV/cm) και λόγω φαινομένου Townsend ο αριθμός των ηλεκρονίων πολλαπλασιάζεται και συνεπώς ενισχύεται το παραγόμενο σήμα (ενίσχυση της τάξης του 10^{3}-10^{4}). Στους ανιχνευτές Micro-bulk η περιοχή ενίσχυσης αποτελείται από 5μm Cu (micromesh)- 50 ή 25 μm Kapton - 5μm Cu (άνοδος). Με την τεχνολογία αυτή ελαχιστοποιείται το υλικό του ανιχνευτή, γεγονός που τον καθιστά ιδανικό για μετρήσεις μέσα σε δέσμη νετρονίων. Για κάθε στόχο που μετρήθηκε σχηματίστηκε μία κυψελίδα που φαίνεται σχηματικά στην εικ. 5.7.

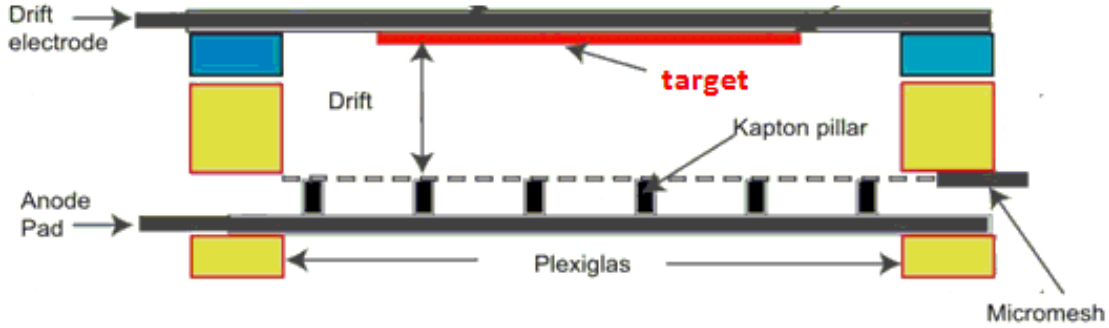

Σχήμα 1.10: Σχηματικό διάγραμμα του ανιχνευτή MicroMegas, βασισμένου στην τεχνολογία Micro-bulk. Το υπόστρωμα που στηρίζει τον κάθε στόχο χρησιμοποιήθηκε ως ηλεκρόδιο εφαρμογής δυναμικού για την περιοχή ολίσθησης (drift).

Το αέριο που χρησιμοποιήθηκε ήταν 80% Argon και 20% CO_2. Τοποθετήθηκαν οι στόχοι με την ακόλουθη σειρά: ^{238}U-front - ^{237}Np - ^{235}U - ^{238}U-back. Η διάταξη φαίνεται στην εικόνα 5.8.

Λόγω της υψηλής ενεργότητας του στόχου ^{237}Np, παρατηρήθηκε επισσυσώρευση παλμών σωματιδίων α (pile-up). Για τη μείωση του φαινομένου αυτού βρέθηκε κατά τη διάρκεια των δοκιμών ότι ο πιο αποτελεσματικός τρόπος ώστε να μη χειροτερεύσει η διακριτική ικανότητα ήταν η τοποθέτηση μασκών Al διαμέτρου 4 cm μπροστά από τον εν λόγω στόχο, και για λόγους ομοιομορφίας το ίδιο έγινε και στους στόχους αναφοράς. Χρησιμοποιήθηκαν προενισχυτές χαμηλής ενίσχυσης και ενισχυτές με shaping time 500 ns, επιλογή που κατέστη δυνατή λόγω της χαμηλής ροής νετρονίων. Ένα τυπικό φάσμα με τις παραπάνω ρυθμίσεις από τον στόχο του ^{237}Np φαίνεται στην εικόνα 5.9.

Όπως φαίνεται στην εικ. 5.9, τα σωματίδια α που εκπέμπει ο στόχος είναι τάξεις μεγέθους περισσότερα από

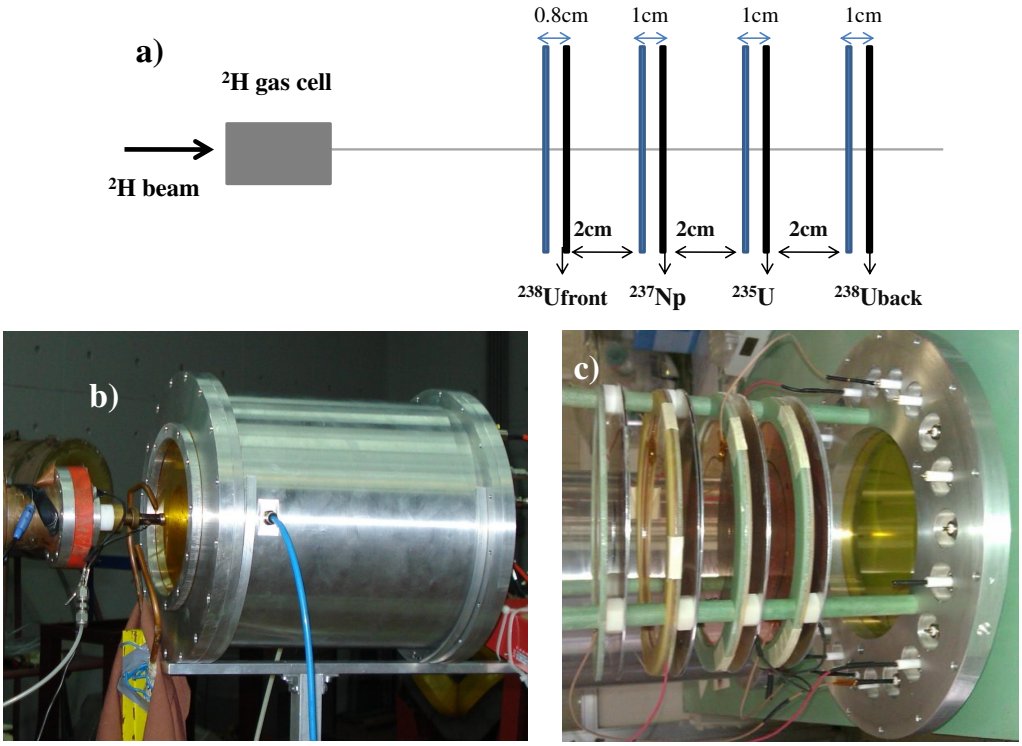

Σχήμα 1.11: α) Σχηματική αναπαράσταση της κυψελίδας δευτερίων και της διάταξης των κυψελίδων με τους στόχους. β) Φωτογραφία του θαλάμου του ανιχνευτή μπροστά από την κυψελίδα του δευτερίου. γ) Φωτογραφία του εσωτερικού του θαλάμου με τη διάταξη στόχων - Micro-bulks. Η δέσμη έρχεται από αριστερά.

τα παραγόμενα θραύσματα σχάσης, εντούτοις είναι σαφώς διαχωρισμένα, συνεπώς με την εφαρμογή ενός κατωφλίου ανάλυσης που επιλέγεται από φάσματα χωρίς δέσμη αποκόπτουμε όλα τα σωματίδια α από την καταμέτρηση των παλμών για την εξαγωγή της ενεργού διατομής. Ο υπολογισμός αυτός έγινε με τον τύπο 6.1:

$$\sigma(E) = \frac{C_{tar} N t_{ref} \Phi_{ref} \epsilon_{ref}}{C_{ref} N t_{tar} \Phi_{tar} \epsilon_{tar}} \sigma_{^{238}U(n,f)}(E) \tag{1.6}$$

όπου:

1. C_{tar} και C_{ref} είναι ο αριθμός των παλμών θραυσμάτων σχάσης που έγιναν αποδεκτοί για τον στόχο του ^{237}Np (tar) και τον στόχο αναφοράς (ref). Και σε αυτή την περίπτωση έγινε διόρθωση για τα θραύσματα σχάσης με ύψος μικρότερο από το κατώφλι ανάλυσης και υπολογίστηκε με προσομοιώσεις Monte Carlo με τον κώδικα FLUKA.

2. Nt_{tar} και Nt_{ref} είναι ο αριθμός των πυρήνων του κάθε στόχου που προσδιορίστηκαν με φασματοσκοπία α.

3. Φ_{tar} και Φ_{ref} είναι οι τιμές της ροής των εισερχόμενων νετρονίων σε κάθε στόχο. Ο λόγος Φ_{ref}/Φ_{tar} προσδιορίστηκε με προσομοιώσεις Monte Carlo με τον κώδικα MCNP5 [82], περιγράφοντας αναλυτικά τη γεωμετρία όλων των κυψελίδων με τους στόχους, του θαλάμου, και της κυψελίδας δευτερίων και η ποιότητα των προσομοιώσεων ελέγχθηκε με τον λόγο των ροών μεταξύ του ^{238}U-front και ^{238}U-back.

4. ϵ_{tar} και ϵ_{ref} είναι η απόδοση του ανιχνευτή λόγω της γεωμετρίας ανίχνευσης και της ενδοαπορρόφησης του κάθε στόχου και προσδιορίστηκαν με προσομοιώσεις με τον κώδικα FLUKA (με χρήση εξωτερικής ρουτίνας γενέσεως θραυσμάτων σχάσης όπως και στη μέτρηση στο n_TOF). Η ποιότητα των προσομοιώσεων για κάθε στόχο ελέγχθηκε με σύγκριση των τελικών ιστογραμμάτων εναπόθεσης ενέργειας σωματιδίων

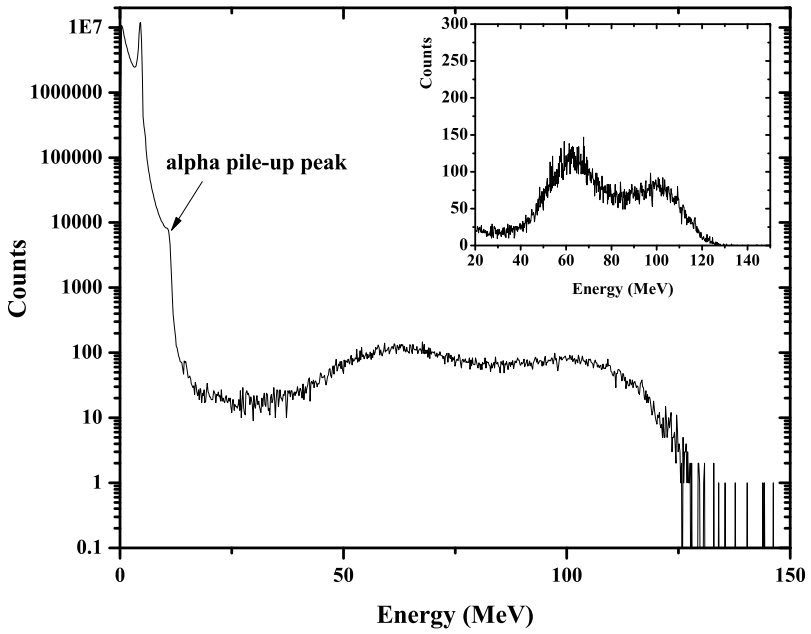

Σχήμα 1.12: Τυπικό φάσμα από τον στόχο ^{237}Np σε λογαριθμική κλίμακα. Τα σωματίδια α που εκπέμπει ο στόχος είναι τάξεις μεγέθους περισσότερα από τα παραγόμενα θραύσματα σχάσης. Η ένθετη εικόνα περιέχει το ίδιο φάσμα εστιασμένο στην περιοχή των θραυσμάτων σχάσης, η αριστερή κορυφή προέρχεται από βαρέα θραύσματα σχάσης που εναπόθεσαν όλη τους την ενέργεια μέσα στο αέριο και η δεξιά από τα αντίστοιχα ελαφριά θραύσματα σχάσης.

α στο αέριο με τα αντίστοιχα πειραματικά και η συμφωνία ήταν εντός 2-3%. Οι τιμές του πάχους των στόχων προσδιορίστηκαν από τα αποτελέσματα της ανάλυσής τους με την τεχνική RBS θεωρώντας στοιχειομετρία NpO_2 και U_3O_8.

5. $\sigma_{^{238}U(n,f)}$ είναι η ενεργός διατομή της αντίδρασης αναφοράς ^{238}U(n,f) που θεωρείται πρότυπη και στο συγκεκριμένο ενεργειακό εύρος έχει αβεβαιότητα <0.8% [69].

Για κάθε μέτρηση, δύο τιμές ενεργού διατομής υπολογίστηκαν, μία με στόχο αναφοράς το ^{238}U-front και μία με στόχο αναφοράς το ^{238}U-back και ο σταθμισμένος μέσος όρος ήταν το τελικό αποτέλεσμα.

Η μέτρηση της μάζας των στόχων έγινε με χρήση φασματοσκοπίας σωματιδίων α, αφού οι στόχοι των ακτινίδων είναι ραδιενεργοί και εκπέμπουν σωματιδια α. Χρησιμοποιήθηκαν δύο ανιχνευτές πυριτίου επιφανειακού φραγμού SSB με διαφορετική ενεργό επιφάνεια, ένας με 50 mm^2 ώστε να γίνουν οι μετρήσεις των σωματιδίων α με καλή ενεργειακή διακριτική ικανότητα και ένας με 3000 mm^2 ώστε να εξασφαλιστεί καλή στατιστική, και ο σταθμισμένος μέσος όρος ήταν το τελικό αποτέλεσμα. Με τις μετρησεις αυτές προέκυψαν τιμές για τις μάζες των στόχων με ακρίβεια καλύτερη του 2%, και βρέθηκε ότι οι στόχοι ήταν λεπτοί ($<$0.5 mg/cm^2) και με αμελητέες προσμείξεις ($<10^{-6}$mg/cm^2). Φωτογραφία της διάταξης με τον στόχο μεγάλης ενεργού επιφάνειας φαίνεται στην εικ. 1.13.

Η ομοιογένεια και το πάχος των στόχων προσδιορίστηκε με την τεχνική οπισθοσκέδασης Rutherford (Rutherford Backscattering Spectrometry Technique -RBS), με χρήση της διάταξης εξωτερικής δέσμης ιόντων του Ι.Π.Σ.Φ ``Δημόκριτος'' (εικ. 1.13), ώστε να αποφευχθεί πιθανή μόλυνση θαλάμων με αέρια ισότοπα που προκύπτουν από την αποδιέγερση των στόχων των ακτινίδων. Χρησιμοποιήθηκε δέσμη πρωτονίων με αρχική ενέργεια δέσμης 2MeV. Η δέσμη εξερχόταν της επιταχυντικής γραμμής μέσα από ένα λεπτό παράθυρο Si_3N_4 πάχους 100 nm, διένυε 3.8 mm αέρα και εισερχόταν στο σημείο προς ανάλυση της επιφάνειας του στόχου. Τα οπισθοσκεδασθέντα πρωτόνια σε γωνία 134° διέσχιζαν $\sim$2.9 cm αέρα και ανιχνεύονταν από ένα ανιχνευτή

επιφανειακού φραγμού (SSB). Εξετάστηκαν 5-10 σημεία σε κάθε στόχο και επετεύχθη πολύ καλός διαχωρισμός της κορυφής οπισθοσκεδασθέντων πρωτονίων από τους πυρήνες της ακτινίδας του εκάστοτε στόχου και του υποστρώματος Al. Τα φάσματα αναλύθηκαν με το λογισμικό SIMNRA v. 6.06 και βρέθηκε η επιφανειακή πυκνότητα (άτομα/cm^2) σε κάθε κάθε σημείο. Με την ανάλυση αυτή προσδιορίστηκε ένα μέσο πάχος για τον κάθε στόχο που χρησιμοποιήθηκε στις προσομοιώσεις FLUKA, διαπιστώθηκε ότι οι στόχοι ήταν ομοιογενείς και δεν παρατηρήθηκε συστηματική κατανομή υλικού πάνω στην επιφάνεια των στόχων (πχ. λιγότερο υλικό στις άκρες κλπ.). Περισσότερες λεπτομέρειες για τον χαρακτηρισμό των στόχων μπορούν να βρεθούν στο κεφ. 2.

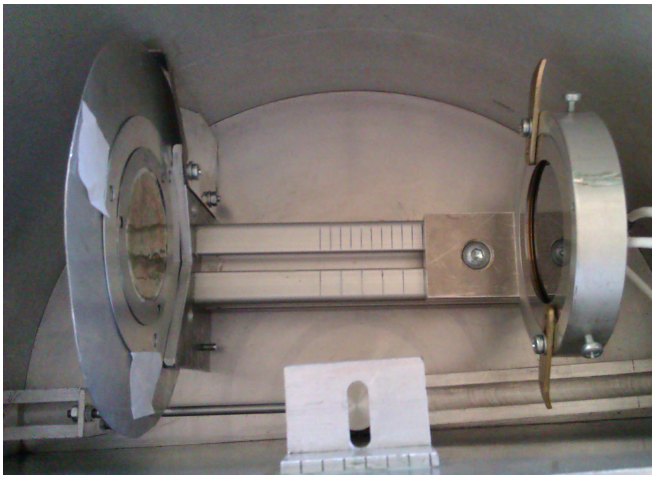

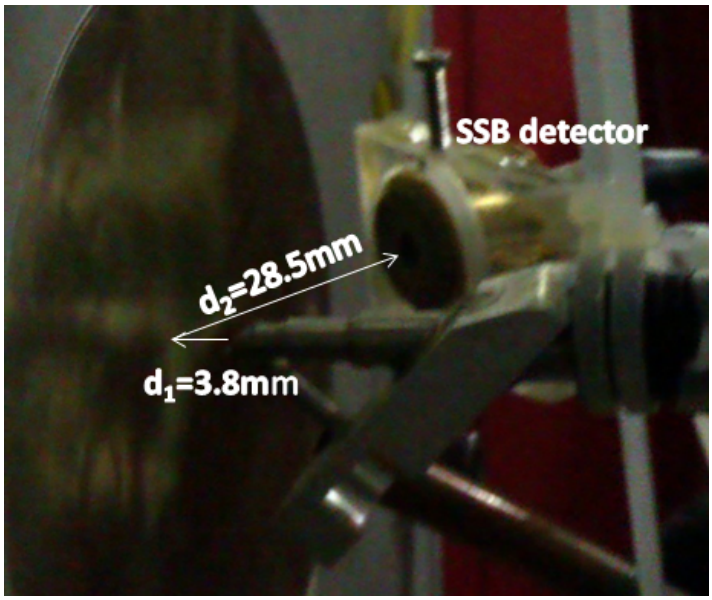

Σχήμα 1.13: Αριστερά: Η διάταξη της μέτρησης της μάζας του στόχου ^{235}U με τον ανιχνευτή SSB μεγάλης επιφάνειας (3000 mm^2). Δεξιά: Η διάταξη εξωτερικής δέσμης ιόντων του Ι.Π.Σ.Φ. του Ε.Κ.Ε.Φ.Ε. ``Δημόκριτος'' για τη μέτρηση του πάχους και της ομοιογένειας των στόχων με την τεχνική οπισθοσκέδασης Rutherford (RBS). Στη συγκεκριμένη φωτογραφία φαίνεται ο στόχος ^{237}Np.

Διαπιστώθηκε ότι η ενεργειακή βαθμονόμηση των φασμάτων με βάση τις ενέργειες των κορυφών (σωματιδίων α και θραυσμάτων σχάσης) που προβλέπονται από τις προσομοιώσεις FLUKA γίνεται με γραμμική συνάρτηση παρά τη μεγάλη διαφορά σε ενέργειες, ατομικούς και μαζικούς αριθμούς των σωματιδίων. Με αφορμή αυτό και την ικανοποιητική διακριτική ικανότητα που επετεύχθη έγινε μελέτη της απόκρισης του MicroMegas προσπαθώντας να αναπαραχθεί το πειραματικό φάσμα με συνέλιξη γκαουσιανής συνάρτησης απόκρισης με τα ιστογράμματα εναπόθεσης ενέργειας που προέκυψαν από τις προσομοιώσεις FLUKA. Όπως παρουσιάζεται αναλυτικά στην ενότητα 5.4, η συμφωνία του πειραματικού φάσματος με το τελικό προσομοιωμένο φάσμα ήταν ικανοποιητική και οι τιμές της διακριτικής ικανότητας του ανιχνευτή δεν ξεπέρασαν το 20% (για την περιοχή των βαρέων θραύσματων σχάσης).

Τα αποτελέσματα της ενεργού διατομής της ^{237}Np(n,f) που προέκυψαν από τις μετρήσεις με τον ανιχνευτή MicroMegas φαίνονται στην εικόνα 1.14, όπου φαίνεται η σύγκριση με προηγούμενα πειραματικά δεδομένα και βιβλιοθήκες προτεινόμενων τιμών αλλά και με τα αποτελέσματα των μετρήσεων με τον FIC στο n_TOF που αναλύθηκαν στα πλαίσια της παρούσας εργασίας. Διαπιστώνεται ότι η συμφωνία είναι πολή καλή και αυτό ενισχύει την αξιοπιστία των αποτελεσμάτων που προέκυψαν.

Τα συστηματικά σφάλματα των αποτελεσμάτων από τις μετρήσεις με τον MicroMegas παρουσιάζονται στον πίνακα 1.3

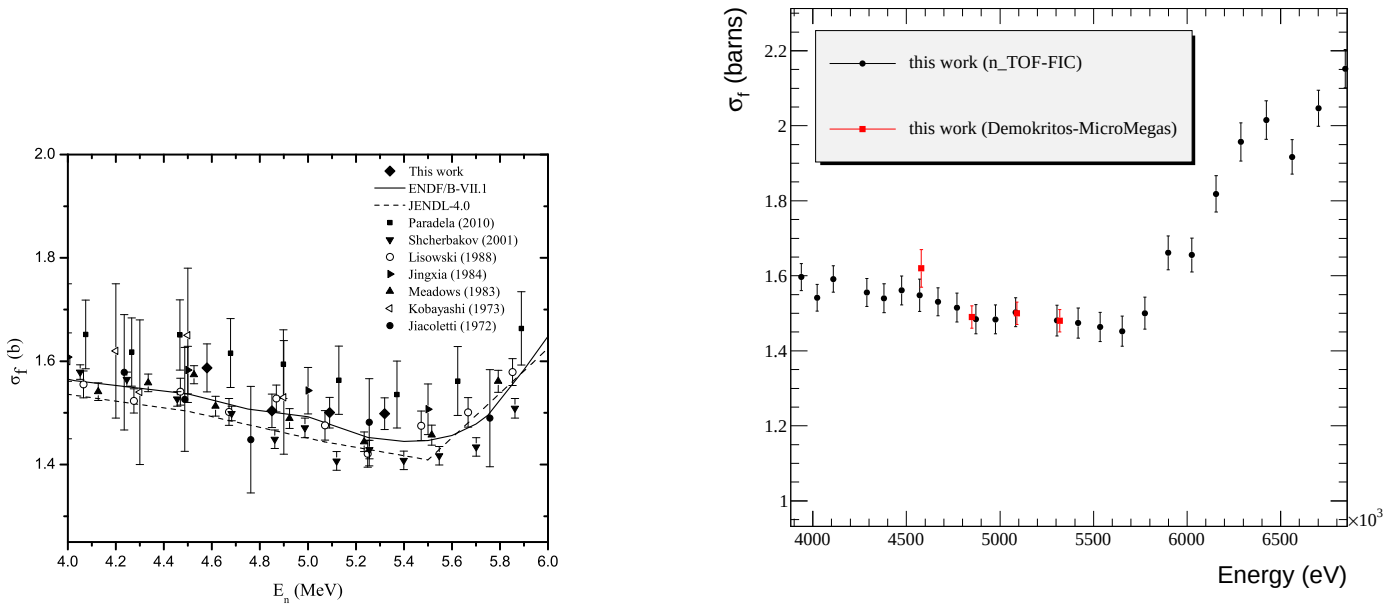

Σχήμα 1.14: Αριστερά: Η σύγκριση των αποτελεσμάτων από τις μετρήσεις με τον MicroMegas με προηγούμενα δεδομένα και προτεινόμενες τιμές βιβλιοθηκών. Δεξιά: σύγκριση των αποτελεσμάτων από τις μετρήσεις με τον MicroMegas με τα αποτελέσματα από τις μετρήσεις με τον ανιχνευτή FIC, στο n_TOF .

Συνεισφορά	Αβεβαιότητα (%)
Μάζα στόχων	1.3-1.7
Διορθωτικός παράγοντας θραυσμάτων σχάσης κάτω από κατώφλι ανάλυσης	$\prec$0.5
Απόδοση ανιχνευτή	2-3
Ροή νετρονίων	3-4
$\sigma^{238}U(n,f)$	$\prec$ 0.9

Πίνακας 1.3: Συνεισφορά των διαφορετικών παραγόντων συστηματικών αβεβαιοτήτων στην τελική ενεργό διατομή.

Τέλος, έγιναν θεωρητικοί υπολογισμοί της ενεργού διατομής της ^{237}Np(n,f) με τον κώδικα EMPIRE, έκδοση 3.2-MALTA. Οι θεωρητικοί υπολογισμοί βασίζονται στη θεωρία Hauser-Feshbach επειδή η διέγερση των πυρήνων υπό μελέτη γίνεται στο συνεχές τους, όπου πολλές στάθμες περιέχονται στο ενεργειακό εύρος της δέσμης και πολλά πιθανά ανταγωνιστικά κανάλια εξόδου ανοιχτά. Η πιθανότητα να ακολουθηθεί ένα κανάλι εξόδου υπολογίζεται από τους συντελεστές διέλευσης εισόδου-εξόδου (με βάση το κατάλληλο οπτικό δυναμικό) και την πυκνότητα καταστάσεων στην περιοχή διέγερσης του σύνθετου πυρήνα και του τελικού πυρήνα του καναλιού εξόδου. Στη θεώρηση αυτή η πυρηνική σχάση αντιμετωπίζεται ως ένα πιθανό κανάλι εξόδου όπου ο συντελεστής διέλευσης υπολογίζεται για διπλό φράγμα δυναμικού. Στο EMPIRE ο τελικός συντελεστής διέλευσης είναι το άθροισμα δύο όρων, του άμεσου, που αφορά στην άμεση διέλευση μέσα από το φράγμα (για χαμηλές ενέργειες) και του έμμεσου, που υποθέτει και ανταγωνισμό με την αποδιέγερση μέσα στο ενδιάμεσο πηγάδι και με την επαναφορά του συστήματος σε στάθμες του πρώτου πηγαδιού (εικ. 1.2). Επίσης, η πυκνότητα καταστάσεων που επηρεάζει την ενεργό διατομή της σχάσης είναι αυτή των σταθμών πάνω στα σαγματικά σημεία (``transition states''). Επειδή όπως αναφέρθηκε στην αρχή δεν υπάρχει θεωρία βασικών αρχών να υπολογίζει την ενεργό διατομή της σχάσης, γίνεται ρύθμιση παραμέτρων ώστε να αναπαράξουμε τα πειραματικά δεδομένα, προσπαθώντας οι αλλαγές να είναι εντός επιτρεπτών ορίων και κατά προτίμηση σε παραμέτρους που δεν είναι γνωστές πειραματικά. Οι υπολογισμοί της παρούσας εργασίας βασίστηκαν στα πειραματικά δεδομένα που προέκυψαν από τη μέτρηση με τον FIC για τη σχάση, και για τα ανταγωνιστικά κανάλια ελήφθησαν υπ' όψιν πειραματικά δεδομένα της βιβλιογραφίας ή/και προετοιμασμένες τιμές.

Η σχάση του ^{237}Np μελετήθηκε μέχρι τα 10MeV και τα άλλα ανταγωνιστικά κανάλια εξόδου που θεωρήθηκαν ανοιχτά είναι η αποδιέγερση γ και νετρονικά κανάλια εξόδου όπως η (n,el), (n,inl), (n,2n), καθώς τα κανάλια εξόδου με φορτισμένα σωματίδια εμποδίζονται από το φράγμα δυναμικού Coulomb. Χρησιμοποιήθηκε το οπτικό δυναμικό RIPL-2408 για τους συντελεστές διέλευσης του καναλιού εισόδου (σχηματισμός του σύνθετου πυρήνα ^{238}Np) αλλά και για τα νετρονικά κανάλια εξόδου. Οι διακριτές στάθμες των πυρήνων που εμπλέκονται στους υπολογισμούς προέρχονται από βιβλιοθήκες δεδομένων για τις στάθμες του πρώτου πηγαδιού και από προτεινόμενες τιμές για τις στάθμες των σαγματικών σημείων και του δεύτερου πηγαδιού. Το μοντέλο πυκνότητας καταστάσεων που χρησιμοποιήθηκε ήταν το Enhanced Generalized Superfluid Model (EGSM) καθώς έχει αποδειχθεί ότι συμπεριφέρεται καλά σε βαρείς πυρήνες. Το μοντέλο αυτό χρησιμοποιήθηκε για την πρόβλεψη των πυρηνικών καταστάσεων στο συνεχές τόσο του πρώτου πηγαδιού όσο και των σαγματικών σημείων. Το διπλό φράγμα δυναμικού είναι ομαλά συνδεδεμένες παραβολές με ύψος (V) και κυρτότητα ($\hbar\omega$) από τη βιβλιοθήκη προτεινόμενων τιμών Reference Input Library RIPL-3. Αρχικά η υπολογισμένη ενεργός διατομή της σχάσης υπερεκτιμούσε μέχρι και 500 keV το κατώφλι και ακολούθως υπερεκτιμούσε την τιμή της ενεργού διατομής στο πλατώ της σχάσης. Έγιναν αλλαγές στις παραμέτρους σχάσης στον πρώτο και δεύτερο σχάσιμο πυρήνα (^{238}Np, ^{237}Np) ως προς το ύψος, την κυρτότητα των φραγμάτων αλλά και την πυκνότητα καταστάσεων στα σαγματικά σημεία. Περισσότερες λεπτομέρειες μπορούν να βρεθούν στην ενότητα 7.3.2. Τελικά, όπως φαίνεται και στο σχήμα 1.15 οι θεωρητικοί υπολογισμοί αναπαράγουν ικανοποιητικά την ενεργό διατομή της σχάσης αλλά ταυτόχρονα και των υπόλοιπων ανταγωνιστικών καναλιών.

Συμπερασματικά, στα πλαίσια της παρούσας εργασίας έγινε ο πειραματικός προσδιορισμός της ενεργού διατομής της ^{237}Np(n,f) σε δύο ανεξάρτητες πειραματικές διατάξεις με διαφορετικά χαρακτηριστικά και μέθοδο ανάλυσης και τα δεδομένα συμφωνούν εντός στατιστικού σφάλματος, γεγονός που αποδεικνύει ότι πρόκειται για αξιόπιστα δεδομένα υψηλής ακριβείας που μπορούν να χρησιμοποιηθούν για περαιτέρω θεωρητική ανάλυση και για τις ανάγκες της Πυρηνικής Τεχνολογίας. Επίσης, μελετήθηκε η συμπεριφορά ενός καινότομου ανιχνευτή MicroMegas, βρέθηκαν οι βέλτιστες συνθήκες λειτουργίας του και η συνάρτηση απόκρισής του ως προς την ανίχνευση των θραυσμάτων σχάσης. Ακόμη, αναπτύχθηκε πειραματική διάταξη για τον ακριβή προσδιορισμό της μάζας στόχων ακτινίδων μέσω φασματοσκοπίας α. Τέλος, έγιναν θεωρητικοί υπολογισμοί της ενεργού διατομής της ^{237}Np(n,f) με τον κώδικα EMPIRE, για την αναπαραγωγή των πειραματικών δεδομένων της παρούσας εργασίας για τη σχάση αλλά και ταυτόχρονη αναπαραγωγή όλων των ανταγωνιστικών καναλιών εξόδου. Οι βασικότερες προοπτικές που προκύπτουν από την παρούσα εργασία είναι οι ακόλουθες: Προτείνεται η χρήση του συστήματος MicroMegas για μετρήσεις ενεργών διατομών σχάσης σε άλλες ακτινίδες και ενεργειακές περιοχές, με ακριβή προσδιορισμό της μάζας των στόχων των ακτινίδων με την πειραματική διάταξη φασματοσκοπίας-α που αναπτύχθηκε, στο Ι.Π.Σ.Φ. του Ε.Κ.Ε.Φ.Ε. ``Δημόκριτος''. Επίσης, προτείνεται πιο

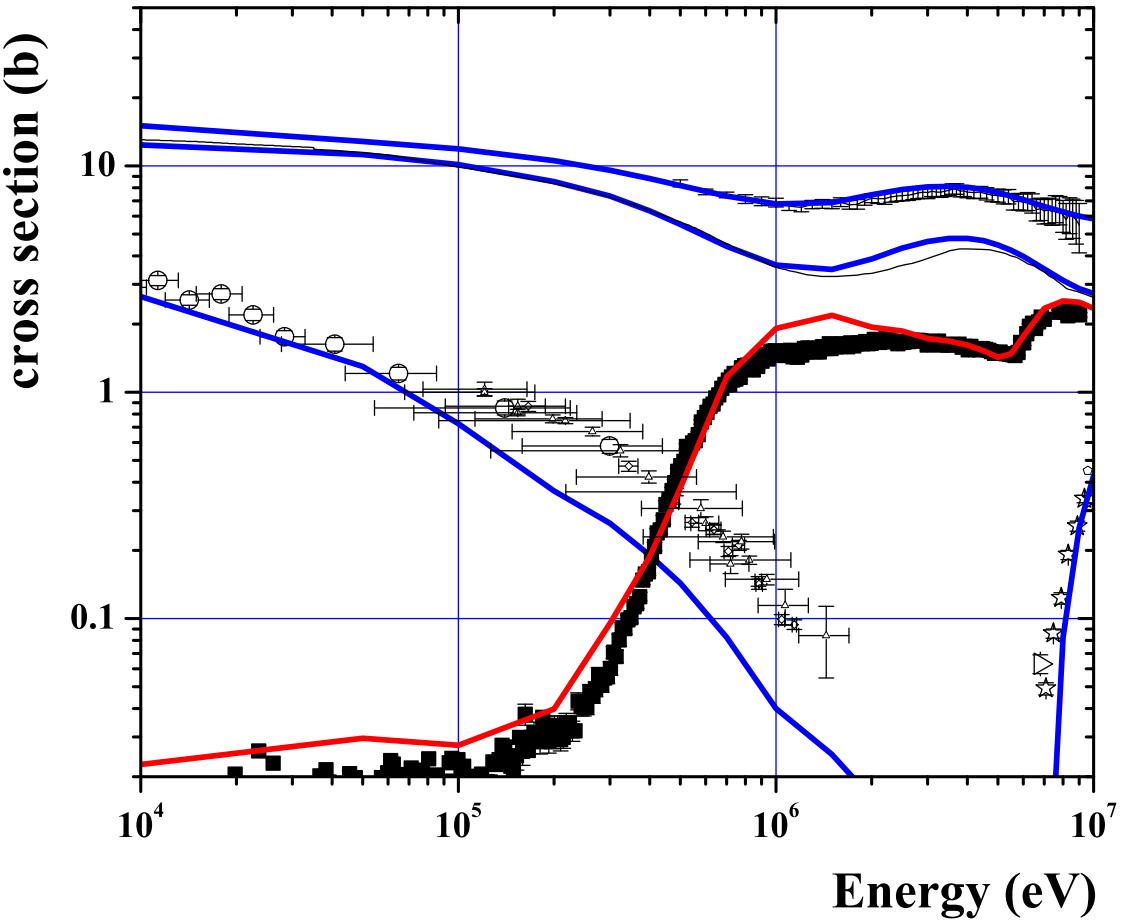

Σχήμα 1.15: Τα τελικά αποτελέσματα των θεωρητικών υπολογισμών με τον κώδικα EMPIRE, για το κανάλι της σχάσης (κόκκινη γραμμή) και τα ανταγωνιστικά κανάλια (μπλε γραμμές) μαζί με τα αντίστοιχα πειραματικά δεδομένα (n,el), (n,inl), (n,2n) στην ενεργειακή περιοχή 10^4-10^7 eV.

εκτενής μελέτη της συνάρτησης απόκρισης του ανιχνευτή MicroMegas με αύξηση της στατιστικής των πειραματικών φασμάτων και χρήση του κώδικα GEF για ρεαλιστικότερη παραγωγή των θραυσμάτων σχάσης που θα χρησιμοποιηθούν ως πηγές στις προσομοίωσεις εναπόθεσης ενέργειας μέσα στο αέριο του ανιχνευτή. Τέλος, προτείνεται η εκτενής πειραματική και θεωρητική μελέτη της ενεργειακής περιοχής 500 keV $< E_n <$ 1 MeV, για τη διερεύνηση μικρών πλατώ που βρέθηκαν. Για μία τέτοια διερεύνηση χρειάζεται πολύ καλή ενεργειακή διακριτική ικανότητα και καλή στατιστική σε αυτό το ενεργειακό εύρος και μία υποψήφια εγκατασταση που προβλέπεται να συνδυάζει τέτοια χαρακτηριστικά είναι η καινούργια εγκατάσταση EAR-2 , CERN.

Abstract

The main goal of the present thesis is to provide new high accuracy data for the ^{237}Np(n,f) cross section, relative to the standard ^{235}U(n,f) and ^{238}U(n,f) cross sections, within the context of the n_TOF collaboration. The existing data are numerous, however present discrepancies that reach 8% at the plateau, which limits the accuracy of the evaluations, and thus the subsequent theoretical analysis. Furthermore, accurate cross section data for this reaction are needed for the design of the future nuclear reactor technology. In order to reduce the systematic uncertainties, measurements were performed at two facilities with totally different characteristics of the neutron beam, data acquisition system and subsequent data analysis: 1) the n_TOF facility at CERN, which provides a white neutron beam with high instantaneous flux, and with use of a gaseous detector (Fast Ionization Chamber), and 2) the neutron production facility of the Institute of Nuclear and Particle Physics of the N.C.S.R. "Demokritos", which provides quasi-monoenergetic neutron beams, with use of a state-of the-art MicroMegas detector. The actinide targets used were characterized experimentally as far as their masses and homogeneity are concerned, with α-spectroscopy and the Rutherfod Backscattering Spectrometry technique, respectively. The cross section data from the independent measurements agree within errors, validating the obtained results. Finally, a theoretical investigation of the ^{237}Np(n,f) reaction cross section was performed, in an effort to reproduce the obtained cross section results, within the Hauser-Feshbach formalism and phenomenological models, as implemented in the EMPIRE code.

Contents

Introduction

The fission process is one of the most interesting subjects of nuclear physics, discovered back in the 1930s and yet still not well understood. The experimental and theoretical study of this phenomenon is very important for the improvement of our knowledge of the nucleus and the nuclear reactions but also for the technological applications in the current and future nuclear industry. A short review of the discovery of this phenomenon, a short description of the fission mechanism and our theoretical knowledge up to date are given in chapter 7. In the following paragraphs, a short introduction on the current and future nuclear technology and the increasing need of accurate cross section data is presented.

1.3 Nuclear data for nuclear energy production

The rapidly increasing demand for energy, mainly due to the increasing needs of the developing countries, but also due to the extended overconsumption in the developed countries has been faced with considerable concern, and has raised issues of improvement in the existing ways of energy production, but also to renewable sources, with two main goals: the availability and abundance of the fuel and the reduction of the pollution of the environment. Currently, the world needs in electricity are mainly covered by the combustion of fossil fuels (oil, coal, natural gas), renewable energies and nuclear fission (fig. 1.16).

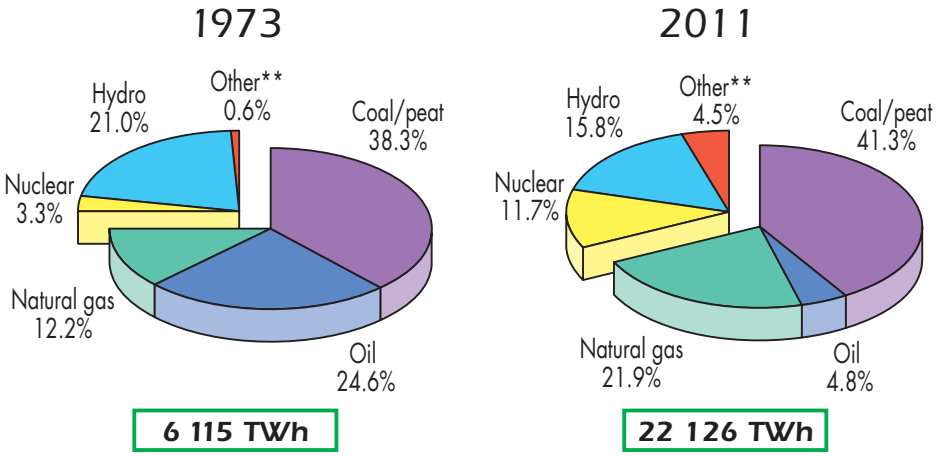

Figure 1.16: The fuel shares of electricity generation, as reported by the International Energy Agency (taken from [1]). ``Other'' includes geothermal, solar, wind, biofuels and waste, and heat.

The combustion of fossil fuels which is the main source of energy production has two main disadvantages: the greenhouse effect, as a result of the emission of CO_2 in the atmosphere, and the foreseen exhaustion of the fuel reserves. The renewable sources of energy are intermittent and cannot cover a very large fraction of the world energy needs, although with the present technological development their contribution is expected to increase (up to 20% by 2020).

Nuclear energy presently covers about 12% of the total world energy production but there are constraints to the large scale development of this energy source. In the following sections, a short description of the current nuclear reactor technology, the limitations against their wider use and the solutions proposed are given.

1.3.1 Present nuclear reactor technology and limitations

The standard nuclear reactors (``thermal reactors") use the fission of ^{235}U, induced by thermal neutrons (E$\sim$0.025 eV), based on a controlled fission *chain reaction* [2, 3]. As explained in chap. 7, each fission event of an actinide nucleus is accompanied by the release of $\sim$200MeV of energy, in the form of kinetic energy of the fission fragments (FFs) and radiation, and the emission of 2-3 neutrons. In order to sustain a chain reaction, at least one of these neutrons needs to induce another fission event. This is expressed by the so-called ``neutron reproduction factor" or ``effective multiplication factor", **k**, defined as the ratio of the number of neutrons in one generation divided by the number of fissions in the preceding generation. The neutrons emitted during the fission of a nucleus are fast, i.e. of high energy. The controlled moderation of the neutrons produced is preferred, in order to take advantage of the high cross section value of the ^{235}U(n,f) reaction at thermal energies ($\sim$580b, see fig. 7.6), which is approximately 200 times larger than the capture cross section. The nuclear reactors currently in use are working in a steady energy release state, the so-called ``critical condition", which means k=1. If k exceeds the value 1, then the reactor is entering the ``supercritical condition", where the amount of released energy and consequently the temperature severely increases and can lead to a nuclear accident. However, if k$<$1 (``subcritical condition") the reactor cannot maintain the chain reaction and eventually the operation is stopped. The moderator typically used is carbon in the form of graphite. The most widely used thermal reactors are the Light Water Reactor systems (LWR). The above briefly described function of the thermal reactor has three main drawbacks, which are the main arguments against the wider use of nuclear energy: 1) The normal working condition of a reactor is at the limit of a nuclear accident and despite the new technological developments minimizing the risk as well as the consequences, this is always a possibility, emerging safety issues. 2) The fuel, ^{235}U, is only $\sim$0.7% of natural uranium, thus only a very small part of natural uranium is actually converted into energy: thus even if at present consumption rates the uranium sources are expected to last for hundreds of years, it is considered as a non-renewable energy source (especially if the share of nuclear energy in the -increasing- energy consumption is wanted to increase). 3) The highly radioactive waste (plutonium isotopes, minor actinides and FFs) generated from the nuclear energy chain is the greatest challenge in the exploitation of this energy source. They have to be completely isolated from any biological systems for their active life, which can be millions of years (for example ^{237}Np has a half life of 2 millions of years). The waste are currently stored in deep geological sites (emerging issues on the stability of the material surrounding the radioactive waste for such a long time), but this cannot be a solution if the waste were to be severely increased. Some countries have adopted the recycling of the nuclear waste, reusing uranium and plutonium from the nuclear waste, although this solution is currently uneconomical and thus not widely used.

1.3.2 Proposed solutions for the development of nuclear industry

In the prospect of an extended use of nuclear energy the above mentioned drawbacks have to be overcome. Several interesting proposals have been made for this purpose, based on innovative nuclear technologies. The Generation VI nuclear energy systems [4] which are currently in the R&D phase are designed to have enhanced safety, economical construction and use, minimal radioactive waste and proliferation resistance. Such systems should be available for international deployment by 2030.

Another interesting proposal is the ``fast reactor strategy", producing energy with fast neutrons and having a closed fuel cycle for plutonium. This can be extended for all minor actinides (Integral Fast Reactor concept) [5], which is considered to lead to the future of nuclear energy production with the highest level of ``radiological cleanliness", combined with the highest usage of the uranium fuel (see fig. 1.1, of ref. [5]).

The partitioning and transmutation (P&T) is considered the most promising way to reduce the radiotoxicity of the nuclear waste and lead to a closed fuel cycle, by removing the plutonium and minor actinides (Np, Am, Cm) from the nulear waste (``partitioning'') and fissioning them (``transmutation''), with the remaining nuclear waste having lost a lot of the initial long term radiotoxicity, since the FFs have much shorter half lives. Additionally, energy is gained from fission. The transmutation of an actinide is completed when the transformation chain, which involves sequential nuclear reactions and radioactive decays, terminates with a fission. The closure of the fuel cycle for plutonium reduces the natural uranium requirement by 30%, and the additional transmutation of actinides by another 5%. The P&T of the actinides can be performed with all types of reactors (thermal, fast, critical and subcritical), but preferrably with fast reactor systems[6]. In this perspective, the Accelerator Driven System (ADS), a sub-critical reactor operating with thermal or fast neutrons supplied by an external source, such as a proton accelerator and a spallation target seems to be the most promising solution. The main advantages of an ADS are the sub-criticality, the proportionality of the reactor power to the accelerator current which simplifies the reactor control, the need of simpler transmutation infrastructure but also the development of the ^{232}Th-^{233}U cycle as an alternative fuel cycle (^{232}Th is a monoisotopic element, three times more abundant than uranium).

The above mentioned solutions, which are in the R&D phase, require the knowledge of the cross section of all the involved nuclear reactions with great accuracy, mainly of the neutron induced reactions on minor actinides. However, severe discrepancies exist in the evaluations and the cross section data in literature, thus, new accurate data are required in order to reduce the uncertainties in the design of the proposed systems.

1.3.3 The status of cross section data for the ^{237}Np(n,f) reaction

^{237}Np is a major component of the spent nuclear fuel in current reactors, mainly produced by neutron captures in ^{235}U and (n,2n) reactions in ^{238}U. Thus the repository or transmutation of this isotope requires the accurate determination of the cross section of all the neutron induced reactions in ^{237}Np. Furthermore, in the new type of reactors (“fast reactors”) the flux in the fast neutron region (in the unresolved resonance region and up to 20 MeV) will be orders of magnitude larger than in the existing thermal ones. The fission channel is the most intense channel in this region, so accurate data are required in order to reduce the uncertainties of the reactor design paremeters.

There is a number of cross-section data in literature (EXFOR database [7]) above the fission threshold for the ^{237}Np(n,f) reaction which in the MeV region present discrepancies up to 8% [8, 11, 10, 12, 13, 14, 15, 16, 17, 18, 20, 19, 21, 22, 23, 24, 25, 26] (fig. 1.17).

Furthermore, the new evaluations ENDF/B-VII.1 [28], JENDL-4.0 [29] JEFF-3.2[30], CENDL 3.1[31] and ROSFOND-2010[32] present differences of 3-4% (fig. 1.18).

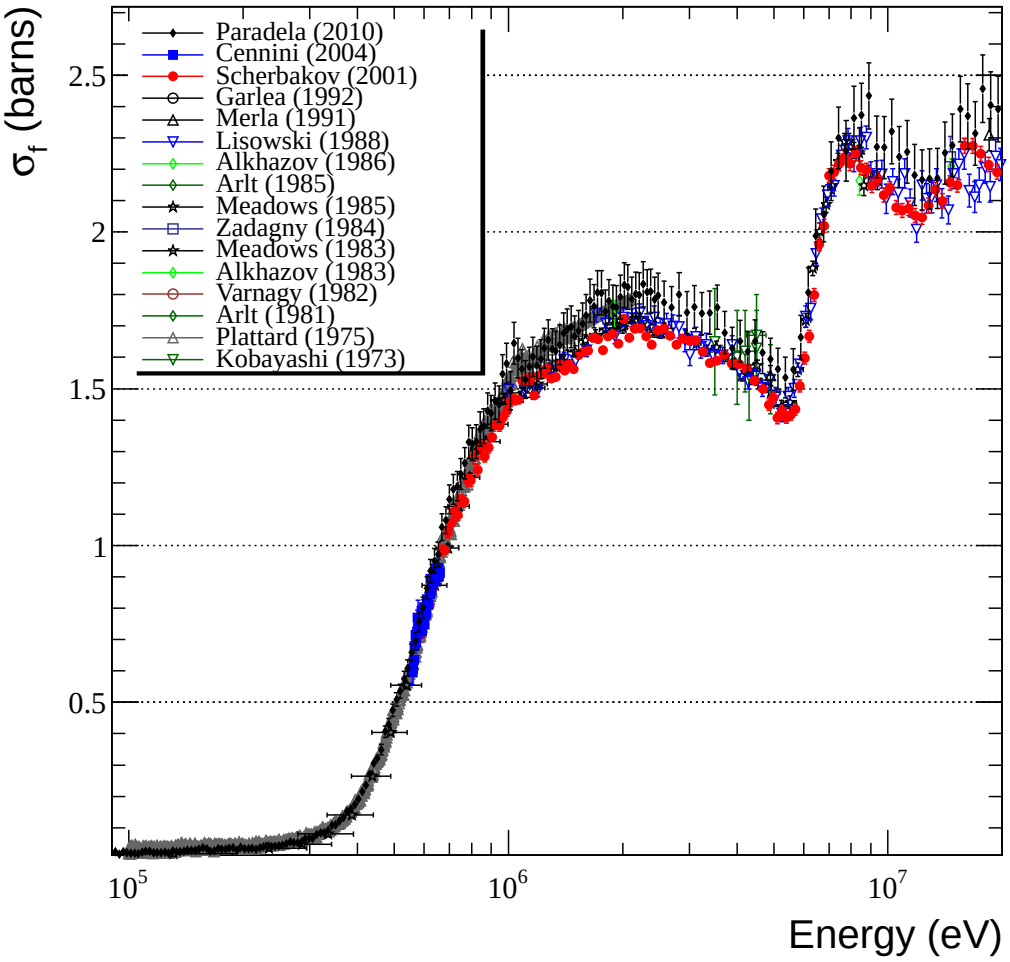
σf (barns)
Paradela (2010)
Cennini (2004)
Scherbakov (2001)
Garlea (1992)
Merla (1991)
Lisowski (1988)
Alkhazov (1986)
Arlt (1985)
Meadows (1985)
Zadagny (1984)
Meadows (1983)
Alkhazov (1983)
Varnagy (1982)
Arlt (1981)
Plattard (1975)
Kobayashi (1973)
2.5
2
1.5
1
0.5
10^5
10^6
10^7
Energy (eV)

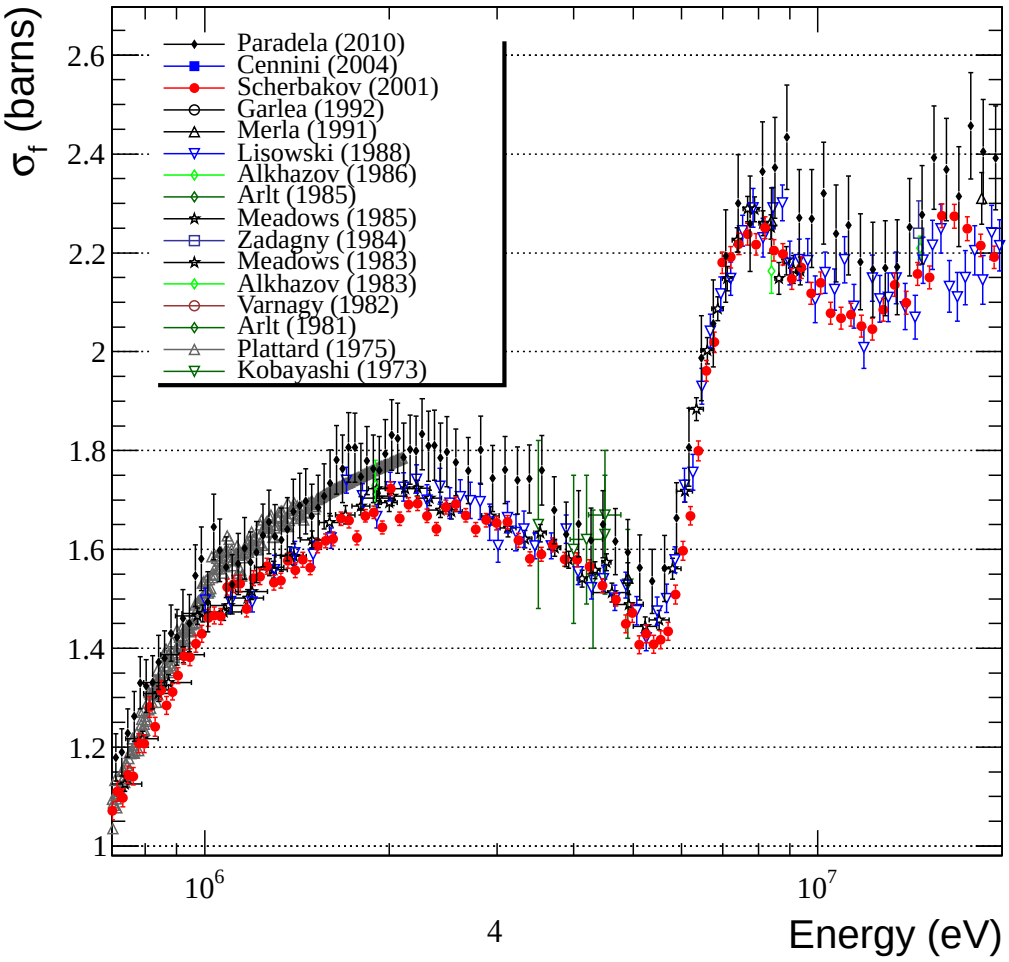
σf (barns)
Paradela (2010)
Cennini (2004)
Scherbakov (2001)
Garlea (1992)
Merla (1991)
Lisowski (1988)
Alkhazov (1986)
Arlt (1985)
Meadows (1985)
Zadagny (1984)
Meadows (1983)
Alkhazov (1983)
Varnagy (1982)
Arlt (1981)
Plattard (1975)
Kobayashi (1973)
2.6
2.4
2.2
2
1.8
1.6
1.4
1.2
1
10^6
10^7
Energy (eV)

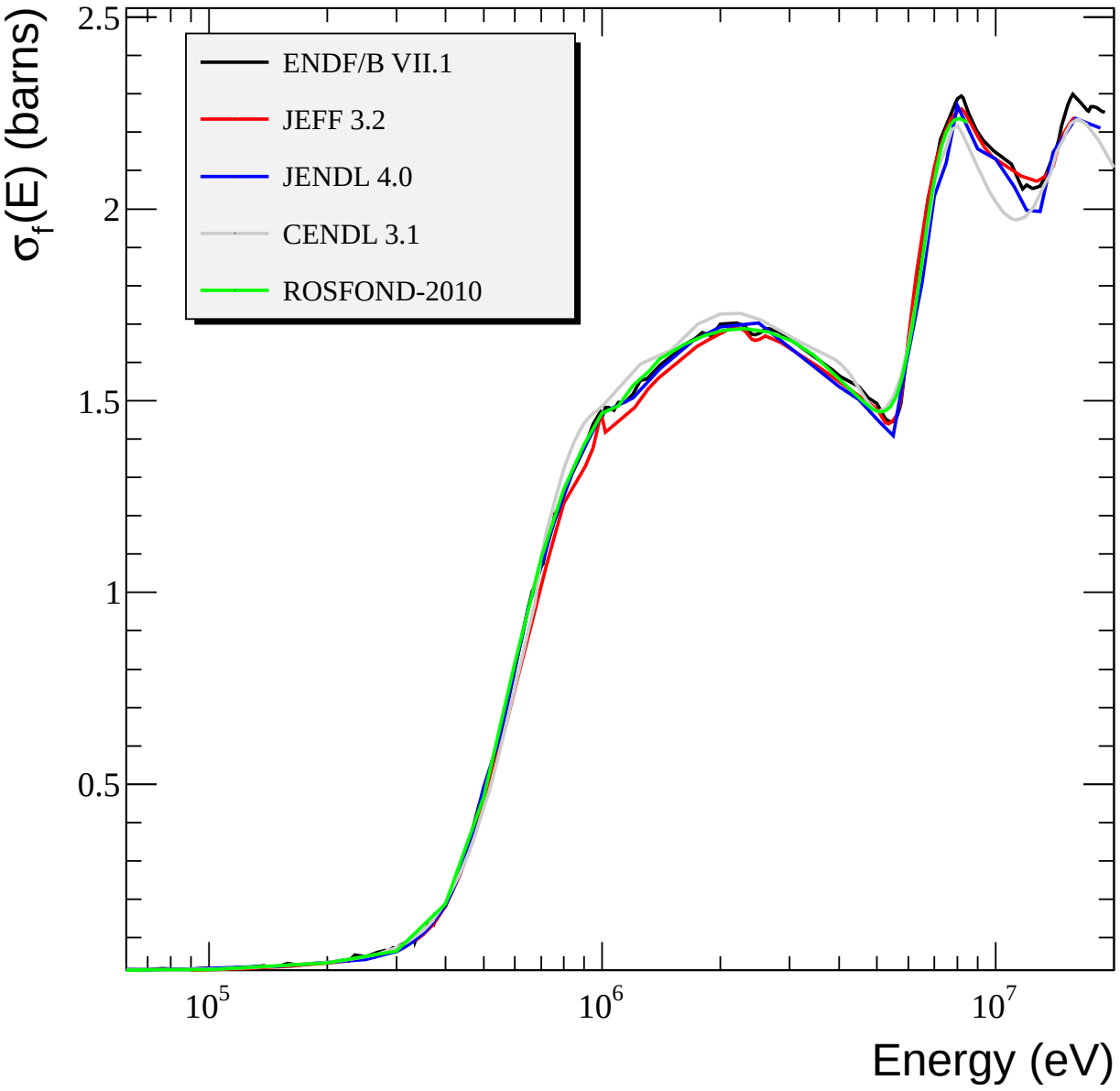

Figure 1.18: Evaluated cross section data from ENDF/B-VII.1 [28], JENDL-4.0 [29] and JEFF-3.2 [30] CENDL 3.1[31] and ROSFOND-2010[32] for the ^{237}Np(n,f) reaction.

1.3.4 The aim of this work

Due to the complication of neutron induced reaction cross section measurements and of the fission process, which is still not very well understood, new measurements with different techniques are necessary in order to improve the accuracy of the evaluations and thus facilitate the subsequent theoretical investigation. The n_TOF collaboration [42] has been created in order to improve the accuracy of nuclear data required for advanced nuclear technologies and nuclear astrophysics. In this context, the main goal of the present thesis is to provide new high accuracy data for the ^{237}Np(n,f) cross section, for which the current uncertainties reach unacceptable limits. In order to reduce the systematic uncertainties, two independent measurements were performed, at two facilities with totally different characteristics of the neutron beam, data acquisition system and subsequent data analysis. The first facility used was the n_TOF facility at CERN [45], with an intense spallation neutron source that covers a continuous energy range from thermal to 1 GeV, with great accuracy due to the long neutron flight path. The high-intensity neutron flux facilitates the measurement of cross sections of neutron-induced reactions for highly radioactive materials, like ^{237}Np. The data analyzed in the context of the present thesis were collected during n_TOF phase 1 (2003). The detector used was a Fast Ionization Chamber (FIC) consisting of a stack of cells filled with the ionization gas, especially designed for such experiments at the n_TOF facility, while the high instantaneous flux made the use of fast electronics and Flash ADCs necessary. The n_TOF facility and the experimental setup are described in chapter 3, while the pulse shape analysis procedure, the data analysis and results are given in chapter 4. The second one was the neutron production facility at the Institute of Nuclear and Particle Physics (I.N.P.P.) of the N.C.S.R. ``Demokritos", in Athens. The monoenergetic or quasi-monoenergetic neutron beams are produced via nuclear reactions of ions accelerated with use of a 5.5 MV Van de Graaff Tandem, impinging on gas or solid targets. A state-of-the-art MicroMegas detector based on the Micro-bulk technology was used for the detection of the fission fragments (FFs), for the first time in the measurement of fission cross sections, developed within the context of the n_TOF collaboration. The comparatively low FF counting rate allowed for the use of charge sensitive preamplifiers and amplifiers, in an effort to check the response function of the detector. The experimental setup and the MicroMegas detector tests, simulations and response function are presented in the chapter 5 while the data analysis and results in the chapter 6. A crucial parameter in the cross section measurement is the number of nuclei the targets used contain, and in the case of inhomogeneous neutron beams, the spatial distribution of the material on the surface of the targets. These two factors were carefully accounted for, with high accuracy alpha spectroscopy measurements using Silicon Surface Barrier (SSB) detectors and the Rutherford Backscattering Spectrometry (RBS) technique using an external ion-beam setup, respectively. Both measurements were perfomed at the I.N.P.P. of ``Demokritos" and the experimental setup, the analysis and the results are presented in chapter 2. Finally, an effort to reproduce the experimentally obtained cross section data with the Hauser-Feshbach formalism and phenomenological models as implemented in the code EMPIRE (version 3.2) was made (chapter 7). The conclusions and future perspectives drawn from this work are presented in 8.

Chapter 2

The characterization of actinide targets used at the fission cross section measurements

The experimental determination of accurate cross section data requires the knowledge of the number of nuclei that the target contains, both for the target of interest and the reference target, with high precision. It is also important to know the distribution of the nuclei on the surface of the target, especially when the incident beam is inhomogeneous as far as its energy and/or spatial distribution is concerned.

2.1 The characteristics of the actinide targets under study

The actinide targets used for fission cross section measurements at the n_TOF facility and at the I.N.P.P. of the N.C.S.R. ``Demokritos", ^{237}Np and the reference targets ^{238}U and ^{235}U are thin disks of actinide oxides (NpO_2 and U_3O_8), deposited on 100 μm Al backings as can be seen in the picture 2.1. A double sided ^{237}Np target (sides with labels 28 and 29), two single sided ^{238}U targets (labels 209 and 210) and one single sided ^{235}U target (label 78) were used. These are all the targets used for the measurement at "Demokritos", and part of the targets used at the measurement at the n_TOF facility. The diameter of all the Uranium oxide targets is 5.2 cm while the corresponding value for the Neptunium oxide target is 8 cm. They were manufactured via the painting technique and provided by the Institute of Physics and Power Engineering, Obninsk, and the Joint Institute of Nuclear Research, Dubna. Some general properties of the targets can be found in table 2.1. The specific activity $A_{/mg}$ reported in the table is a characteristic value for each isotope and is calculated as follows.

Supposing that a radioactive sample contains N_0 nuclei of a specific isotope at t=0, the number of the remaining nuclei at a later time t can be found from the simple exponential law of radioactive decay: $N(t) = N_0 e^{-\lambda t}$, where λ is the decay constant and inversely proportional to the half life ($T_{1/2}$) of the isotope according to the formula $\lambda = \frac{ln(2)}{T_{1/2}}$. The activity of the radioactive sample at a time t is the number of decays per second, given by eq. 2.1:

$$A(t) = -\frac{dN(t)}{dt} = \lambda N(t) = \lambda N_0 e^{-\lambda t}. \tag{2.1}$$

The number of nuclei N_0 is given by the formula $N_0 = N_A \frac{m}{A}$, where N_A is the Avogadro constant, m the total mass of the sample and A the atomic mass of the isotope. Taking this into account, eq. 2.1 gives $A(t) = \lambda N_A \frac{m}{A} e^{-\lambda t} = \frac{ln(2)}{T_{1/2}} N_A \frac{m}{A} e^{-\lambda t}$. Dividing both sides of the equation by the mass m and 1000, one can get the specific activity of the isotope $A_{/mg}$ via the formula $A_{/mg} = \frac{ln(2) N_A}{1000 T_{1/2} A} e^{-\lambda t}$. For long half lives, as in this case,

Target properties	^{237}Np	^{238}U	^{235}U
Oxide form	NpO_2	U_3O_8	U_3O_8
Target Diameter (cm)	8	5	5
Labels	28,29	209,210	78
Half life* (y)	$(2.144 \pm 0.007) \cdot 10^6$	$(4.468 \pm 0.003) \cdot 10^9$	$(7.038 \pm 0.007) \cdot 10^8$
Specific Activity $A_{/mg}$ (Bq/mg)	26031± 85	12.44± 0.01	79.98± 0.08

Table 2.1: Summary of the target properties

Figure 2.1: The picture of one of the ^{238}U reference targets (label 210).

$e^{-\lambda t} \sim 1$ so it turns out that the specific activity only depends on the half life and mass number of the isotope (eq. 2.2):

$$A_{/mg} = \frac{ln(2)N_A}{1000T_{1/2}A}. \tag{2.2}$$

2.2 Total mass measurements

The actinide targets under study are purely alpha emitters. The counting of the alpha particles emitted by the target of unknown mass at a well defined solid angle is amongst the most accurate methods for the determination of the corresponding number of target nuclei.

The mass m of the actinide content is the ratio of the alpha activity at 4π ($A_{4\pi}$) to the corresponding specific activity ($A_{/mg}$): $m = \frac{A_{4\pi}}{A_{/mg}}$. The activity at 4π can't be directly measured, but can be determined by measuring the activity in a solid angle Ω subtended by a detector (A_Ω). Since the alpha emission is isotropic, the activity at 4π ($A_{4\pi}$) is given by: $A_{4\pi} = \frac{4\pi A_\Omega}{\Omega}$. Thus, the mass value m for a given isotope is given by eq. 2.3.

*The values were taken from [33].

$$m = \frac{4\pi A_\Omega}{\Omega A_{/mg}}, \tag{2.3}$$

In the present work, the activity of each target was measured with two SSB detectors with different active surfaces. A small detector with 50 mm^2 was used in order to obtain good energy resolution, whereas a big detector with 3000 mm^2 was used in order to increase statistics. Both detectors were 100 μm thick. Thus two mass values were extracted using eq. 2.3 and the weighted average value was taken as the final result.

A special holder for the targets and the detectors has been made in order to ensure that a) the surface of both detectors would be at the same distance from the targets, b) the surface of the detectors would be coaxial to the targets and c) there would be a reproducibility of the geometrical conditions among all the targets measured. Tantalum masks were put in front of both detectors in order to avoid edge effects, the radius of which was carefully chosen in order to attain the highest possible acceptance while avoiding shadow effects (i.e. alphas that pass through the mask but don't enter the active surface of the detector). Thus, the active surface of each detector was determined from the mask hole, which could be more easily and accurately measured. According to the geometrical measurements, the distance target-detector surface was d_{meas}=(15.8±0.1) cm, the radius of the mask of the small and the big detector were r_{meas}=(0.350±0.015) cm and R_{meas}=(2.902±0.002) cm respectively. The setup was housed in an Al chamber under a vacuum of the order of 10^{-3} mbar). The setup with the big detector mounted can be found in fig. 2.2.

Concerning the electronics, a preamplifier (ORTEC, model 142), a standard fast energy amplifier (C.A.E.N., model N968) and an analog-to-digital-converter (ORTEC, model 919E) were used for the acquisition of the data, and MHV-4 by Mesytec was used for the high voltage supply of the detectors.

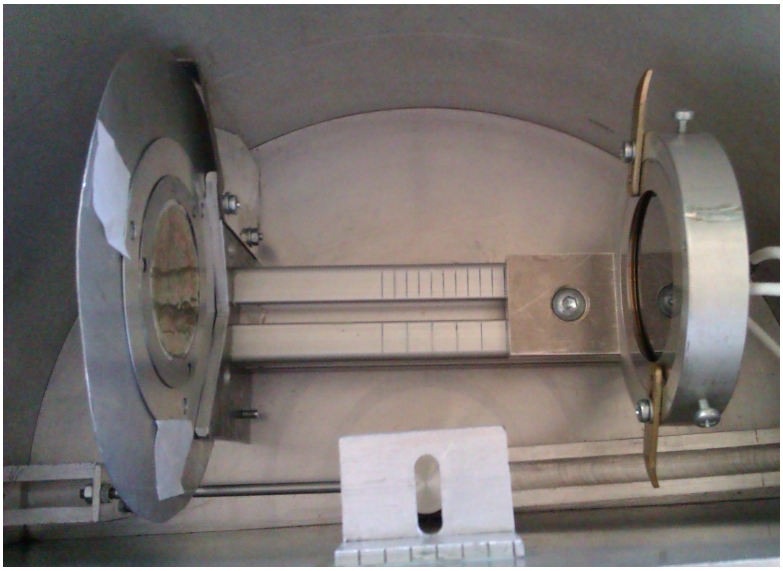

Figure 2.2: A picture of the setup during the measurement of the ^{235}U target with the big detector.

Determination of the activity A_Ω

The A_Ω of eq. 2.3 was estimated by integrating the total counts from the peak to the “noise threshold”because counts at lower energies than the ``nominal" peak are due to energy losses in the target and scattering at the edges of the mask. Background measurements were used in order to estimate the channel from which the noise begins as well as possible background counts in the region of integration. The dead time in all the spectra used did not exceed 0.3%. The calibration of the spectra was done with use of a triple ^{241}Am/^{239}Pu/^{244}Cm source. Spectra from a calibrated ^{241}Am source* as well as background spectra were taken frequently between two measurements in order to check possible variations at the measuring conditions (extra noise at the spectra,

possible contaminations etc.). The small detector offers good resolution and peaks with energy difference bigger than 50 keV could be distinguished (fig. 2.3,2.4, 2.4).

.

- ^{237}**Np:** The pile-up effect due to the high activity of the targets caused difficulties in the analysis. The mass values that occured from the analysis of the big detector spectra agreed within errors with the corresponding values from the small detector spectra but only the latter value was used for the final mass result. Typical spectra from both detectors can be seen in fig. 2.3. The big detector spectrum is presented with logarithmic scale in order to make the pile-up tail evident. The error of the A_Ω in the case of the small detector spectra was 0.7%.

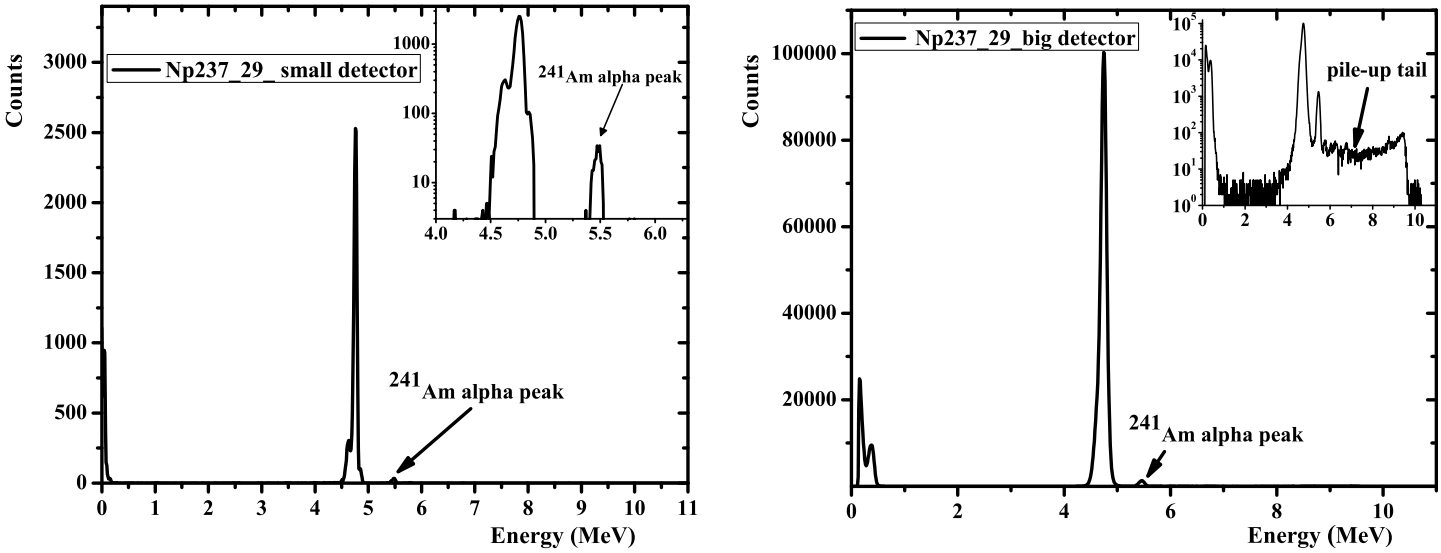

Figure 2.3: Typical alpha particle spectra from the ^{237}Np targets (label 29) with use of the SSB with the small surface (left figure) and the big surface (right figure). In the insets of both pictures (logarithmic scale) the small peak from the ^{241}Am can be seen, and the intense pile-up in the big detector spectra due to the high alpha activity of the ^{237}Np targets.

The expected alphas from the decay of the ^{237}Np isotope have energies of 4.788 MeV (47.64%), 4.771 MeV (23.2 %), 4.766 MeV (9.3 %) and others with intensities less than 5 % which do not exceed 4.9 MeV. All these contribute to the main peak and this can be more clearly seen in the small detector spectra. The target has a small contamination from ^{241}Am, as can be seen in the inset of fig. 2.3 (5.442 MeV with 13.1% and 5.486 MeV with 84.8%). ^{237}Np is made by sequential neutron captures in the reactors, starting from the isotope ^{235}U (^{235}U + 1n $\rightarrow$ ^{236}U + 1n $\rightarrow$ ^{237}U $\stackrel{\beta^-}{\rightarrow}$ ^{237}Np). The chemical separation for the production of the target is not exclusive and the ^{241}Am trace is commonly found in it. The ^{241}Am contamination in the targets of this work turned out to be very small ($\sim 10^{-5}$ mg) but visible in the spectra because of the small half life (432.6 years) compared to the half life of ^{237}Np ($2.144 \cdot 10^6$ years). For fission cross section measurements, as the ones reported in this work, this ^{241}Am contamination will not affect the number of fission fragment counts since the fission cross section of the two isotopes is similar and the ^{241}Am content in the ^{237}Np target is 5 orders of magnitude lower than the main isotope. As a final remark, it was found out that the first ``noise" peak in the ^{237}Np spectra which has a much higher rate than in the other target spectra corresponds to gamma and X-rays from the target. An SSB detector of 300 μm can detect photons of up to approximately 20-30 keV [87], and approximately 70% of the X- and gamma-ray radiation from the ^{237}Np decay is below 30 keV [33].

*The source was re-calibrated right after the measurements as discussed in section 2.2.

- **^{238}U:** Typical spectra obtained from the ^{238}U targets can be found in fig. 2.4. The expected energies from the ^{238}U decay are mainly 4.151 MeV (21 %) and 4.198 MeV (79%) and contribute to the same peak. The specific activity of this target is very low as can be seen from table 2.1 and the spectra from both the small and the big detector were clear. The statistical error from the analysis of the small detector spectra was $\sim$ 3.5%, while the corresponding value from the big detector spectra was less than 0.4%. These measurements were long ($\sim$ 20h), so in order to check the reproducibility of the measuring conditions the data acquisition system was set to save a spectrum every hour and the rate of the peak of interest and the "noise peak"was checked.

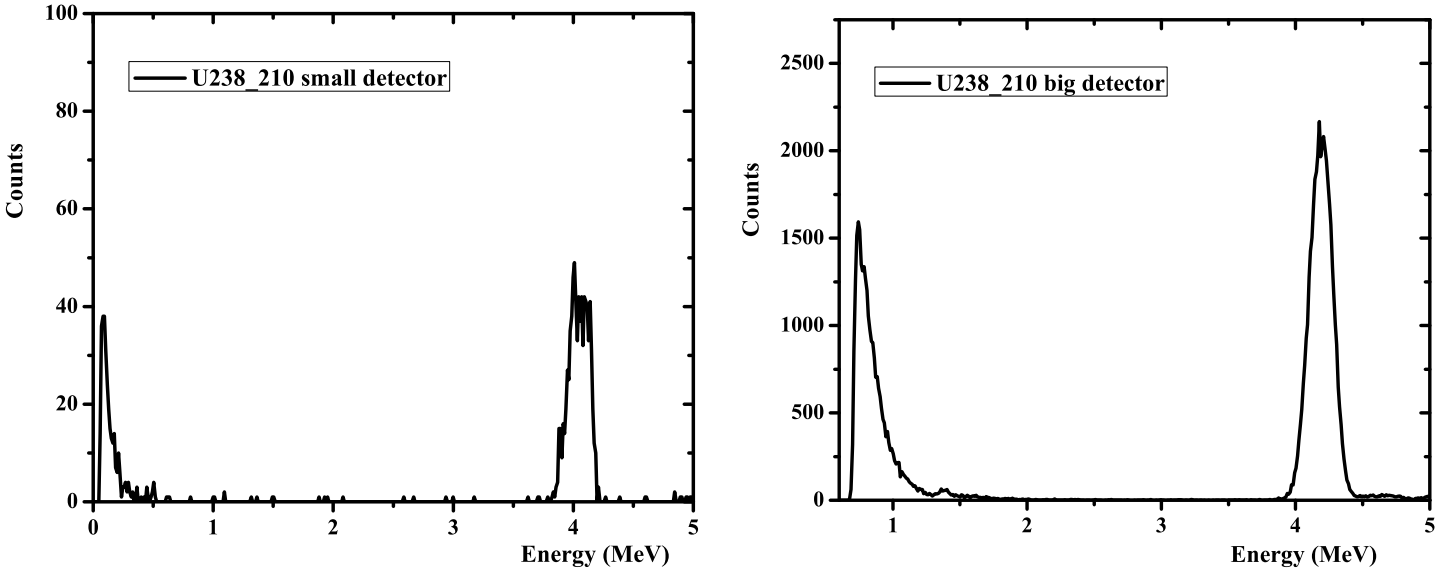

Figure 2.4: Typical spectra obtained from the ^{238}U target - label 210, with use of the SSB with the small surface (left figure) and the big surface (right figure)

- **^{235}U:** Typical spectra from the ^{235}U target (label 78) can be found in fig. 2.5.

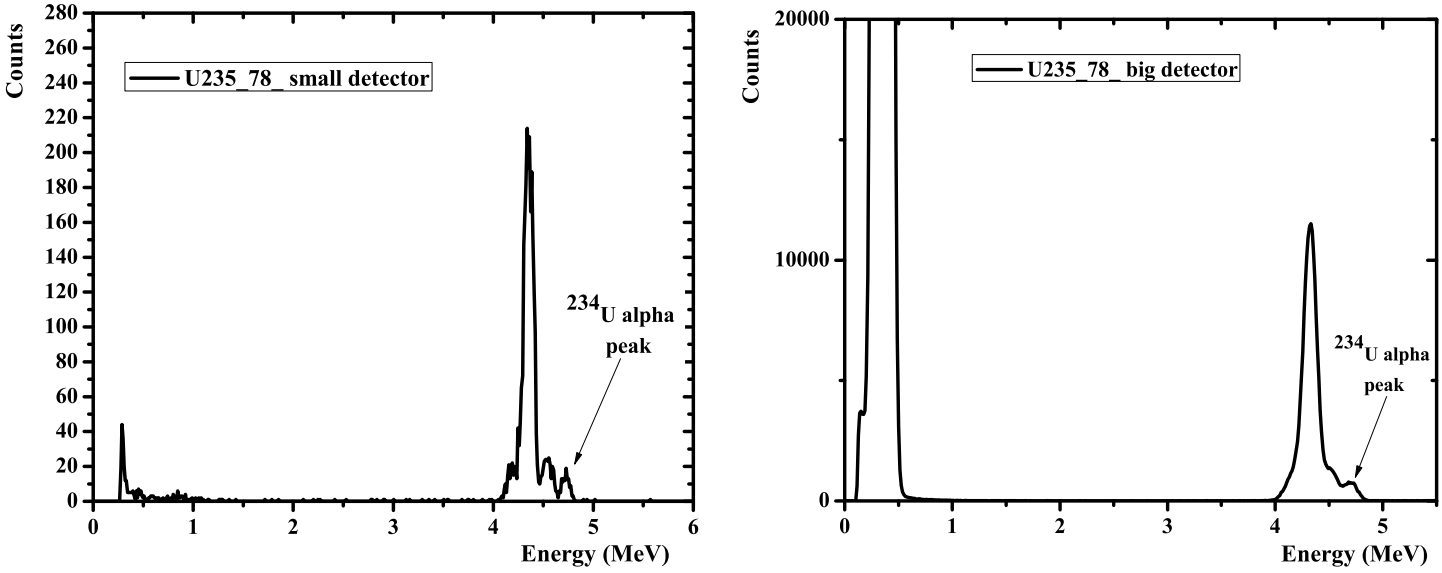

Figure 2.5: Typical alpha particle spectra from the ^{235}U target (label 78) with use of the SSB with the small surface (left figure) and the big surface (right figure).

At the small detector spectrum with the good resolution the most intense alpha decays of this isotope can be nearly distinguished: 4.215 MeV (5.7%), 4.366 MeV (17%) and 4.398 MeV (55%) - the highest peak, 4.556 MeV (4.2%) and 4.596 MeV (5%). The statistical error for the A_Ω was 1.7% for the small detector

spectra and $\prec$ 0.5% for the big detector spectra. The small peak at 4.77 MeV is attributed to a small ^{234}U contamination ($\sim 10^{-5} mg$). However, in fission cross section measurements it will result in a negligible amount of fission fragments since the cross section of ^{235}U is even higher than the one of ^{234}U and the amount is 5 orders of magnitude larger for ^{235}U than for the ^{234}U contamination.

Determination of the solid angle Ω

The solid angle subtended by both detectors needs to be accurately determined. As already mentioned, according to the geometrical measurements, the distance target-detector mask surface was d_{meas}=(15.8$\pm$0.1) cm, while the radius of the mask of the small and the big detector were r_{meas}=(0.350$\pm$0.015) cm and R_{meas}=(2.902$\pm$0.002) cm respectively. For big target-to-detector distance with respect to the radii of the target and the detector, as in this case, the target and the detector can be considered as flat disks and the solid angle was calculated considering a circular detector mask coaxial to a circular isotropic source. The average solid angle was obtained by the multiplication of the analytical relationship for the solid angle subtended by a circular detector from the center of the circular source with a correction factor F, as described in [34], and given by equation 2.4.

$$\Omega = \Omega_{source-center} F = 2\pi \, (1 - \frac{d}{\sqrt{r^2 + d^2}}) F \tag{2.4}$$

where $\Omega_{source-center}$ the solid angle subtended by a circular detector from the center of the source, d the distance target-detector mask surface, r the detector mask radius and F the corresponding correction factor. A schematic of the geometry of the calculations can be found in fig. 2.6. For the following, the solid angle subtended by each detector will be named Ω_{bs} (big source-small detector) and Ω_{bb} (big source-small detector), for the small and big detector respectively.

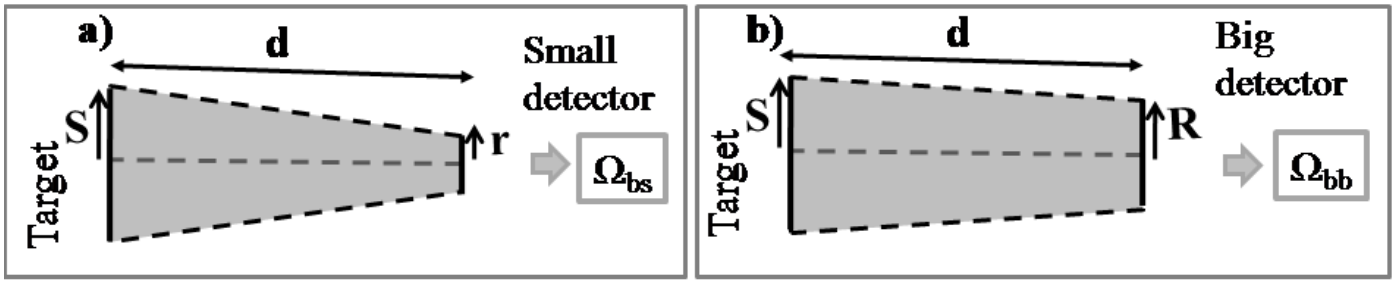

Figure 2.6: Schematics of the geometry of the alpha spectroscopy measurements with the a) small and the b) big detector. The solid angles subtended by the detectors from the target, namely Ω_{bs} for the small and Ω_{bb} for the big detector, need to be known with great accuracy. Thus, the radii r and R and the distance d need to be determined with small uncertainties.

As explained in [34], F is obtained by interpolation of tabulated values calculated by appropriate numerical integrations and depends on the ratios r/d and S/d, where S is the radius of the source. The interpolation was performed with linear least-squares fitting with the following polynomial expression 2.5:

$$F(S/d, r/d) = exp(\sum_{m=0}^{3} \sum_{n=1}^{4} A_{mn} (S/d)^n (r/d)^m) \tag{2.5}$$

The coefficients A_{mn} from the polynomial fit can be found in [34], so F can be calculated for every S/d and r/d combination. Thus, it is clear that d, S and r should be accurately determined in order to obtain high accuracy Ω values, and for this purpose a high accuracy calibrated ^{241}Am alpha source was used. The source was

re-calibrated at the Institute for Reference Materials and Measurements (JRC-IRMM), right after the measurements, both with alpha spectroscopy with a silicon surface barrier detector and gamma ray spectroscopy with a HPGe detector and the value of the activity was obtained with an uncertainty of 0.3%. A schematic of the source is shown in fig. 2.7.

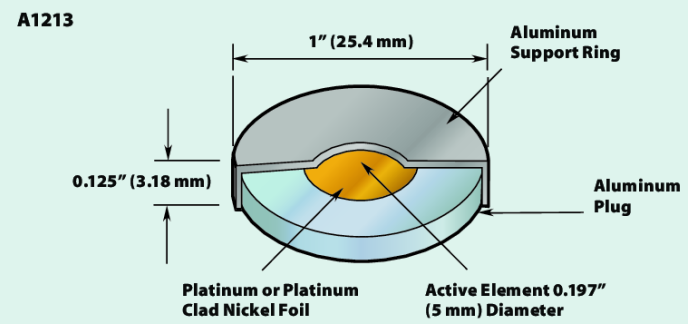

Figure 2.7: A schematic of the ^{241}Am source, taken from [35]. The active diameter of the source is 5 mm.

For each setup, spectra from the ^{241}Am source, well centered with respect to the detector axis, were taken in order to experimentally determine the Ω subtended by the detectors from the source, namely the $\Omega_{ss,exp}$ (small source-small detector) and $\Omega_{sb,exp}$ (small source-big detector) for the small and big detector respectively. The statistical uncertainty for these measurements were 1.4% for the small detector and less than 0.5% for the big detector and the dead time was negligible for both setups.

With use of the Gardner's formalism (eq. 2.4, 2.5) for disk-to-disk solid angle calculations an effective geometry was defined (d_{eff}, r_{eff}, R_{eff} - see fig. 2.8), in order to match the $\Omega_{ss,eff}$ and $\Omega_{sb,eff}$ values to the $\Omega_{ss,exp}$ and $\Omega_{sb,exp}$ ones. The source in these calculations was considered to be a 5 mm diameter disk as reported in the ^{241}Am source information sheet (fig. 2.7) and confirmed by geometrical measurements in the lab.

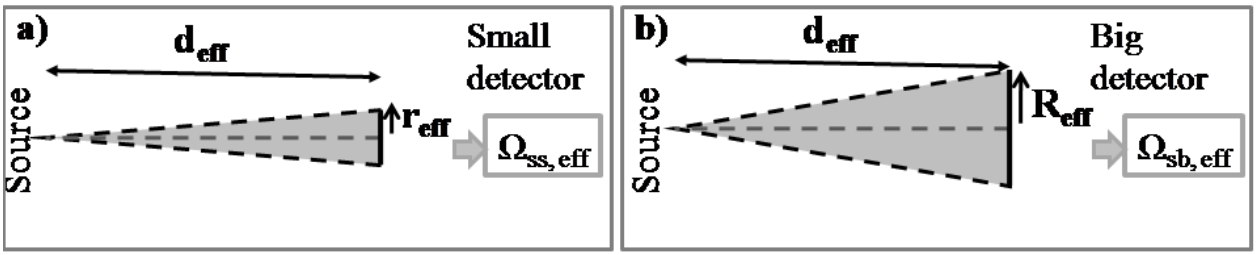

Figure 2.8: Schematics of the effective geometry of the measurements with the a) small and the b) big detector with use of a 5 mm diameter disk source. The radii r_{eff} and R_{eff} and the distance d_{eff} were defined in order to match the calculated $\Omega_{ss,eff}$ and $\Omega_{sb,eff}$ to the experimental $\Omega_{ss,exp}$ and $\Omega_{sb,exp}$ values obtained with use of a high accuracy calibrated ^{241}Am source.

It turned out that a small change was needed to the d_{meas}, r_{meas} and R_{meas} values (up to 1.1 %), showing that the geometrical conditions of the measurements were under good control. With the use of this effective geometry and the measured radius of the targets (see table 2.1) the Ω_{bs} and Ω_{bb} were defined with the Gardner's formalism. It has to be noted that small changes in d from the source to the target measurements, due to different thicknesses, were taken into account in the calculations. Due to the large target-to-detector distance the results are not very sensitive to small variations in the geometry, i.e. a small deviation from perpendicularity of the setup or slightly different radii of the target or the detector etc. For example, if d is changed by about 1 mm, this would cause a change of 1% at the calculated Ω. As another example, the difference between $\Omega_{ss,eff}$ (S=0.25 cm, d$\sim$15.7 cm, r$\sim$0.35 cm), and the resulting calculated Ω_{bs} (S=2.6 cm, d$\sim$15.9 cm, r$\sim$0.35 cm) is about 5%.

The uncertainties of the Ω_{bs} and Ω_{bb} are the quadratic sum of two factors: a) the uncertainty of the $\Omega_{ss,exp}$ ($\sim$ 1.4%) and $\Omega_{sb,exp}$ ($\sim$ 0.5%) values with which the effective distance and radius of the detectors were defined and b) the change in the calculated values when changing the geometrical parameters that were not fixed with

Target label	Small detector mass results value (mg)	error (mg)	Big detector mass results value (mg)	error (mg)	Final mass results value (mg)	error (mg)
^{237}Np (28)	6.28	0.11	*6.43*	*0.08*	**6.28**	**0.11**
^{237}Np (29)	6.36	0.11	*6.44*	*0.08*	**6.36**	**0.11**
^{235}U (78)	4.92	0.13	4.97	0.07	**4.96**	**0.06**
^{238}U (209)	9.70	0.38	9.93	0.14	**9.90**	**0.13**
^{238}U (210)	9.06	0.35	9.02	0.13	**9.03**	**0.12**

Table 2.2: The final mass results. As already mentioned, the big detector values for ^{237}Np were not used for the extraction of the final mass values, but are shown in the table for comparison.

Target label	Contamination	value (mg)	error (mg)
^{237}Np (28)	^{241}Am	$1.56 \cdot 10^{-5}$	$0.03 \cdot 10^{-5}$
^{237}Np (29)	^{241}Am	$1.54 \cdot 10^{-5}$	$0.04 \cdot 10^{-5}$
^{235}U (78)	^{234}U	$8.5 \cdot 10^{-5}$	$0.1 \cdot 10^{-5}$
^{238}U (209)	-	-	
^{238}U (210)	-	-	

Table 2.3: Target contaminations

the ``effective geometry" within their experimental errors, for example the radius of the target ($\pm$ 0.2 cm) and the difference in d between the source and target setups ($\pm$ 0.1 cm). The final error did not exceed 1.9%.

As an extra check, the ratio Ω_{bs}/Ω_{bb} calculated with this method was compared to $\Omega_{ss,exp}/\Omega_{sb,exp}$. These two values should be equal within their errors since the activities cancel out. Furthermore, MCNPX [36] simulations of the setup showed that at this target-to-detector distance the correction needed at the sub-threshold counts between the source and the target spectra, due to scattering at the chamber and the holder, is negligible (of the order of 1 ‰).

Final mass values

With the above method high accuracy mass values occured. For lower-activity targets, such as ^{238}U and ^{235}U, spectra from both detectors were used in order to extract two mass values and the final mass was the weighted average value. For ^{237}Np the intense pile-up effect precluded the use of the big detector spectra for the extraction of safe results, so the final mass value was derived only from the small detector. The results can be found in table 2.2. The final results agreed within 5% with the values given by the manufacturer, for which no error information was provided. The same calculation was performed for the contaminations found in the targets and the final results are presented in table 2.3. The mass content of the contaminations found is 5 orders of magnitude lower than the main actinide of the corresponding target, thus the targets can be considered as being of high purity.

2.3 Thickness and homogeneity measurements

The actinide targets were examined as far as their thickness and homogeneity are concerned via the Rutherford Backscattering Spectrometry technique (RBS) at the external ion-beam setup of the 5.5 MV HV TN-11 Tandem

accelerator of the Institute of Nuclear Physics at NCSR ``Demokritos" [37].

2.3.1 Introduction to the Rutherford Backscattering spectrometry (RBS) technique

The Rutherford Backscattering Spectrometry (RBS) technique is currenty the most widely used Ion Beam Analysis (IBA) technique for depth profiling of elements in thin targets from nm to μm. The technique is based on the elastic backscattering of an ion beam impinging on a sample (fig. 2.9).

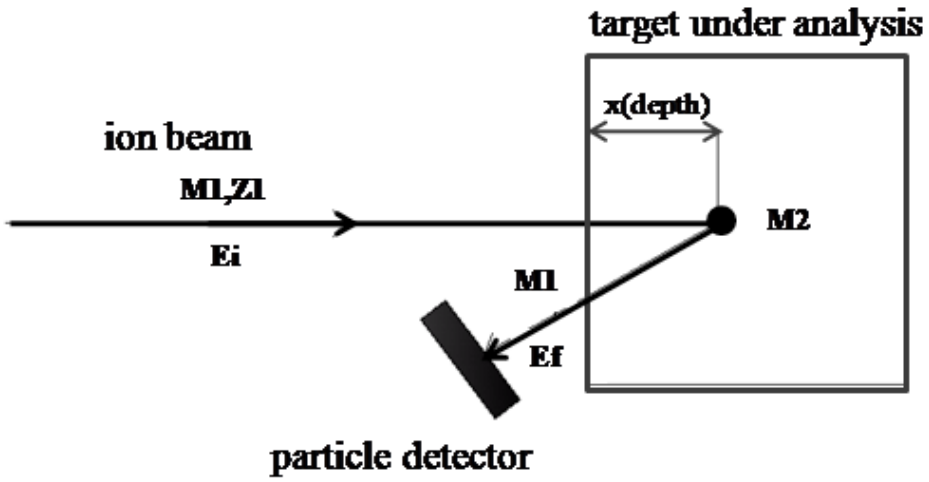

Figure 2.9: Schematic representation of the Rutherford Backscattering Spectrometry technique. An ion with atomic number Z_1, mass M_1 and initial energy E_i enters the target under analysis and is scattered by the Coulomb potential ("elastically scattered") of a nucleus with mass M_2 in a depth x. The scattered ion exits the sample and enters the detector put at a specific scattering angle θ with a solid angle Ω, where the corresponding energy is detected.

A beam of ions with mass M_1, charge Z_1, and energy E_i enters the sample under analysis and reacts with the atoms in it. If an ion from the beam interacts with the Coulomb potential of a nucleus with mass M_2, and charge Z_2, then it gets scattered in a scattering angle θ. When $\theta \geq 90^\circ$ then ``backscattering" takes place and the scattered ions are detected with particle detectors (usually silicon detectors in order to have good energy resolution). Most of the samples under analysis are thick for ion beams accelerated with small accelerators (i.e. Van de Graaff of 2-5 MV) so ions scattered at $\theta \leq 90^\circ$ get absorbed in the sample, this is why the detection of the backscattered particles is the only possibility for material analysis. The energy E_f of an ion scattered from a target nucleus located at the surface of the sample will be less than E_i by a factor k (eq. 2.6):

$$E_f = k\, E_1 \tag{2.6}$$

where k is the kinematic factor given by eq. 2.7:

$$k = \frac{(M_1 cos\theta + \sqrt{M_2^2 - M_1^2 \sin^2\theta})^2}{(M_1 + M_2)^2} \tag{2.7}$$

k depends on the masses of the impinging ion and the target nucleus and the scattering angle θ [38].
When the scattering takes place in a depth x from the surface of the sample then the impinging ion loses some energy before interacting with the target nucleus ($\Delta E_{inc}(x)$) and after the scattering it loses energy before exiting the sample due to the interaction ($\Delta E_{out}(x)$), depending on the stopping power dE/dx of the sample under analysis for the corresponding ion and the depth in which the interaction takes place.

As a result eq. 2.6 changes as follows (eq. 2.8):

$$E_f = k\,[E_1 - \Delta E_{inc}(x)] - \Delta E_{out}(x) \tag{2.8}$$

When the stopping power dE/dx is known for the target-ion combination, the depth x can be estimated from E_f and this is how the spatial distribution of the different isotopes in the sample is estimated.

The differential cross section $d\sigma/d\Omega$ for Rutherford scattering in a depth x in the center-of-mass frame is well known with analytical formulas (eq. 2.9):

$$\frac{d\sigma}{d\Omega} = (\frac{Z_1\,Z_2\,e^2}{2\,E_1^{'}\,\sin^2\theta})^2\,\Delta\omega \tag{2.9}$$

where

$$E_1^{'} = E_1 - \Delta E_{inc}(x) = E_1 - \int_0^x \frac{dE}{dx'}dx',\ \Delta\omega = \frac{[\sqrt{1-(\frac{M_1 sin\theta}{M_2})^2} + cos\theta]^2}{\sqrt{1-(\frac{M_1 sin\theta}{M_2})^2}} \tag{2.10}$$

Consequently, the yield ΔY_i of the elastic scattering of the impinging ions from an isotope i that is present in the sample under analysis with a surface concentration N_i, at a time interval Δt, is given by eq. 2.11:

$$\Delta Y_i = \frac{d\sigma}{d\Omega}\,N_i\,Q\,\Omega \tag{2.11}$$

where Q the total number of the impinging ions at the corresponding time interval Δt and Ω the solid angle subtended by the particle detector. From eq. 2.11 the concentration N_i of the isotope i can be determined. This is how the quantitative analysis of a sample is made with the RBS technique.

The Rutherford scattering cross section increases, as can be seen from eq. 2.9, as the atomic numbers of the projectile and target increase, this is why the method is proposed for the detection and analysis of heavy elements. Furthermore, as M_2 increases, the kinematic factor and as a result E_f are increased (eq. 2.7,2.8), pushing the signals from scattering on heavy elements to the upper part of the obtained spectrum, separating them from signals from light elements. Thus, the RBS technique is ideal for the analysis of heavy elements on light substrates. This is the case for the targets used in the context of the present thesis, which consist of a very thin layer of actinide (heavy element) on an Al substrate (light element), and this is why RBS was chosen for thickness and homogeneity measurements of these targets.

2.3.2 The experimental setup

It was decided to measure the actinide targets at the external ion-beam setup of the 5.5 MV HV TN-11 Tandem accelerator of the Institute of Nuclear Physics at NCSR ``Demokritos" in order to avoid possible contaminations of the chamber. Details on this setup can be found in [37]. The targets were mounted on a holder specially designed to provide the possibility to move perpendicularly with respect to the beam axis with an accuracy of 0.01 mm, with use of a computer-controlled motorized xy stage.

The incident proton beam was decided to have an energy as low as 2 MeV, in order to avoid opening of inelastic reaction channels. The proton beam provided by the accelerator was confined through appropriate collimation

at the exit ion-beam nozzle (see fig. 2.10), minimizing the beam dimensions at the measuring point. At the end of the nozzle, the protons traversed a 100 nm Si_3N_4 exit window (Silson, Northampton, UK), chosen in order to minimize the ion beam energy loss and the energy and angle straggling effect. According to SRIM calculations [40], 2 MeV protons lose $\sim$ 5 keV when passing through the exit window. In order to avoid radiation damage of the ultra thin exit window , the beam current was kept low at $\sim$ 10 nA.

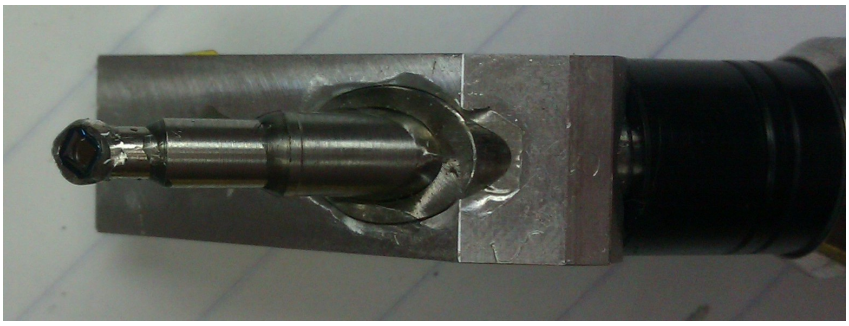

Figure 2.10: A photo of the nozzle that shaped the proton beam, along with the 100 nm Si_3N_4 exit window.

The proton beam then traversed 3.8 mm of air and reached the surface of the actinide layer at the measurement point. The beam radius at the measurement point was $\sim$1 mm. The elastically scattered protons traversed 28.5 mm of air and were detected by a silicon surface barrier detector of 300 μm at a scattering angle θ=134° (see fig. 2.11). A tantalum mask was put in front of the detector in order to avoid edge effects, with a radius of (0.17 $\pm$ 0.01) cm and a thickness of 1 mm. In order to have an estimate of the solid angle Ω subtended by the detector, spectra from a calibrated triple ^{241}Am/^{239}Pu/^{244}Cm source centered at the measuremet point were taken. The value of the Ω obtained was (0.0121 $\pm$ 0.0002) sr, and agreed within 10% with the Ω calculated with 2.4, assuming the geometrical measurements.

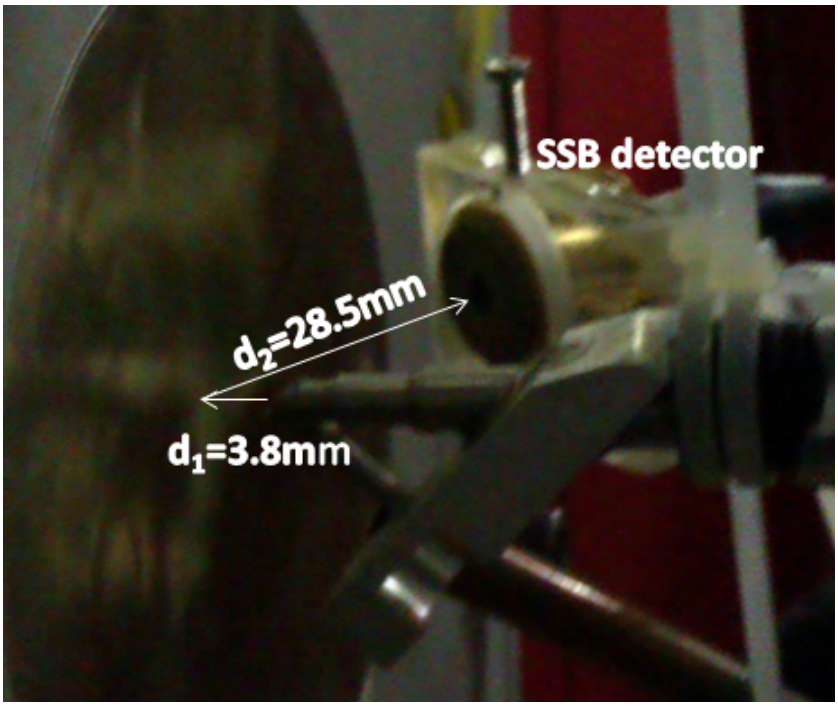

Figure 2.11: A photograph from the RBS measurements, with the ^{237}Np target mounted. The arrows show the direction of the impinging and backscattered protons.

For each target 5-10 points were measured in order to check the homogeneity.

A typical spectrum obtained is shown in fig. 2.12.

The acquisition time needed in order to obtain enough statistics ($\prec$ 0.5%) was short, not more than 500 s, due to the high cross section value for the elastic scattering of protons on actinides. Nevertheless, for high activity

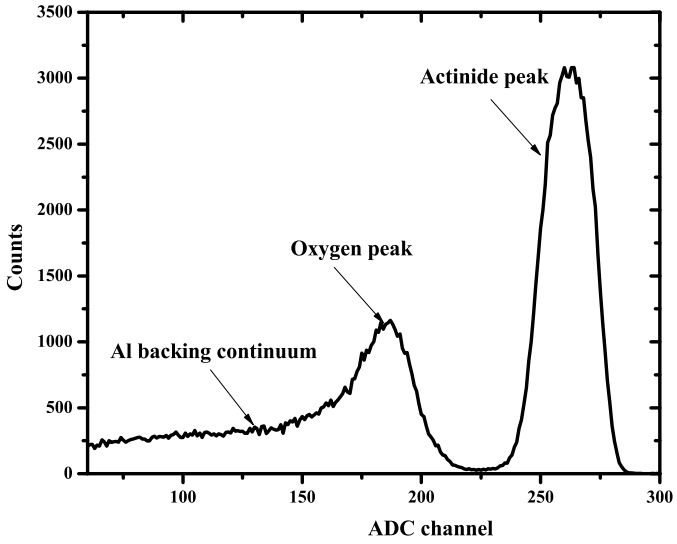

Figure 2.12: Typical RBS spectrum from the central point on the surface of a ^{238}U target. The protons scattered by the actinide content of the targets (``actinide peak'') are well distinguished from those scattered at the aluminum backing (``Al backing continuum'') and those scattered at the oxygen (``oxygen peak'') from the actinide layer, the air and the aluminum backing of the targets.

targets, as ^{237}Np (0.16 MBq at 4π) the alphas appear at the spectrum as a continuum from higher energies (around channel 600) and going down to the beginning of the spectrum, due to the straggling of the ion energy from the air layer. This alpha background under the proton spectrum causes difficulties in the analysis and was removed by using time normalized beam-off spectra for each point (fig. 2.13). For the uranium targets the alpha background was negligible.

Three ways were used in order to check the homogeneity of the targets. Firstly, a comparison of the ratio $\frac{ActinidePeakIntegralCounts}{AlBackingIntegral}$ among the different points was performed, keeping the same integration region among the points of the same target. This comparison is independent of the number of the impinging proton ions (namely Q) and the solid angle subtended by the detector (namely Ω). The statistical uncertainty for the determination of the actinide peak and the Al backing integral was lower than 0.6%. The final error was derived from the propagation of the statistical uncertainties and did not exceed 1%.

Secondly, the FWHM of the actinide peak gives an estimation of the energy loss of the proton beam in the actinide layer and thus the thickness of the layer, so a comparison of the FWHM among the different points was also performed.

Finally, the RBS spectrum occuring for each point was analyzed using SIMNRA v. 6.06 [39]. The actual experimental parameters (Ziegler-Biersack-Littmark stopping power data, Chu and Yang's straggling model, multiple scattering, choice of a small energy step for incoming and outgoing protons, beam divergence) were used as implemented in the code. This analysis includes a lot of free parameters in order to successfully reproduce the experimental spectrum, such as the energy of the impinging proton beam, the calibration of the RBS spectrum, the product QΩ, the detector resolution and the description of the absorber layer (which the scattered protons traverse until they reach the detector), the description of the target and the backing. The surface concentration of the actinide content for each point was obtained by this analysis, giving an estimate of the mean thickness of each target.

According to SRIM calculations [40], the 2 MeV proton beam, after passing through the Si_3N_4 window and 3.8 mm of air, reaches the layer surface at the measurement point with an energy of 1.931 MeV and energy spread of 6 keV. The calibration of the spectrum as well as the determination of the atomic concentration of the

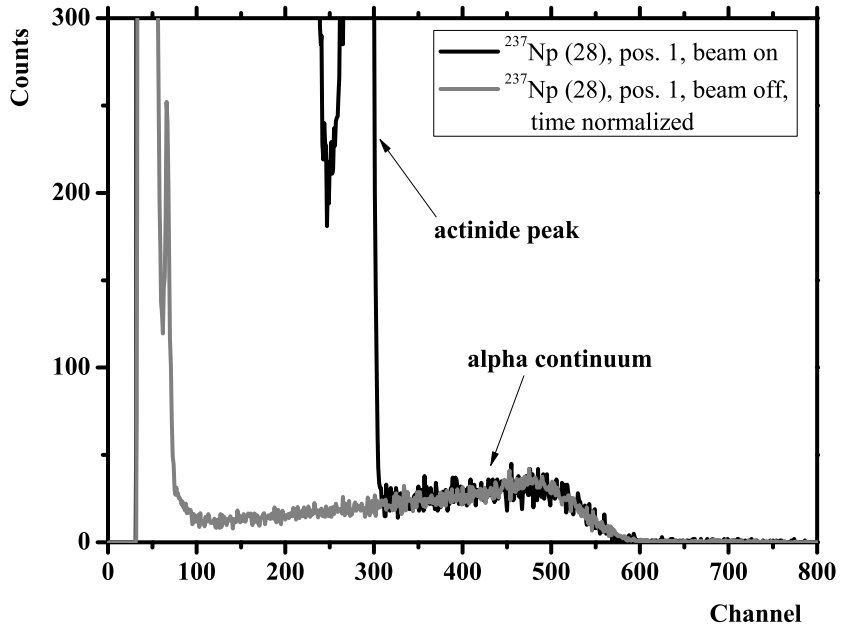

Figure 2.13: Example of the alpha background subtraction from the RBS spectra. The RBS spectrum from the target ^{237}Np , label 28, obtained from the bombardment of the central point of the disk of the target (black line) and the corresponding time normalized beam off spectrum (grey line), with the alpha particles alone. From the subtraction of the two spectra the RBS spectrum was cleared from the alpha particles.

absorber layer (28.5 mm of air) were defined by the simulation of additional RBS spectra of thick Au, Ta and Al foils (considered as of infinite thickness for protons of $\sim$ 2 MeV). The previously mentioned values were kept constant for all the measurement points. Examples from the analysis of these spectra can be found in fig. 2.14.

The oxygen peak was observed at all the RBS spectra, even at the ones taken from ^{197}Au which is not oxidized, comes from the scattering of the protons at the oxygen of the air layer(s) which the impinging and backcattered protons traverse. This scattering can not be simulated due to the big uncertainty of the exact point of the scattering (causing large uncertainties in the RBS angle, the exact energy of the impinging ion, the thickness of the absorber layer etc.). Furthermore, this oxygen peak can not be distinguished from protons scattered at the oxygen content of the actinide target under study, precluding the exact determination of the latter value. In order to obtain a correct oxygen content value, one needs to perform the experiment in a high vaccuum chamber, which, in our case was not possible due to radioprotection issues. However, the ``actinide peak'' is well separated from this ``oxygen peak'' of uncertain origin (see fig. 2.12) so the reproduction of the actinide peak is safe.

The actinide targets were initially assumed to be actinide oxides with the most commonly occuring stoichiometry (NpO_2, U_3O_8). The $Q\Omega$ product was defined by simulating the Al backing continuum at each spectrum separately with an uncertainty less than 3%. For each point various values for target stoichiometry, layer and substrate roughness, detector resolution were tried in order to reproduce the actinide peak. All gave similar values of actinide content, and the average value was taken as the final result.

In most of the cases the three methods were used and gave consistent results within 10%. As an example, in table 2.4 the results from the three methods for 5 points measured are reported. The points are schematically shown in fig. 2.15.

From table 2.4 it can be concluded that the homogeneity can be checked by all the three methods since they show the same trend. For example, point 3 presented the lowest actinide content, as shown by all the three methods: the value obtained from each method for this point was approximately 16% lower than the corresponding average value.

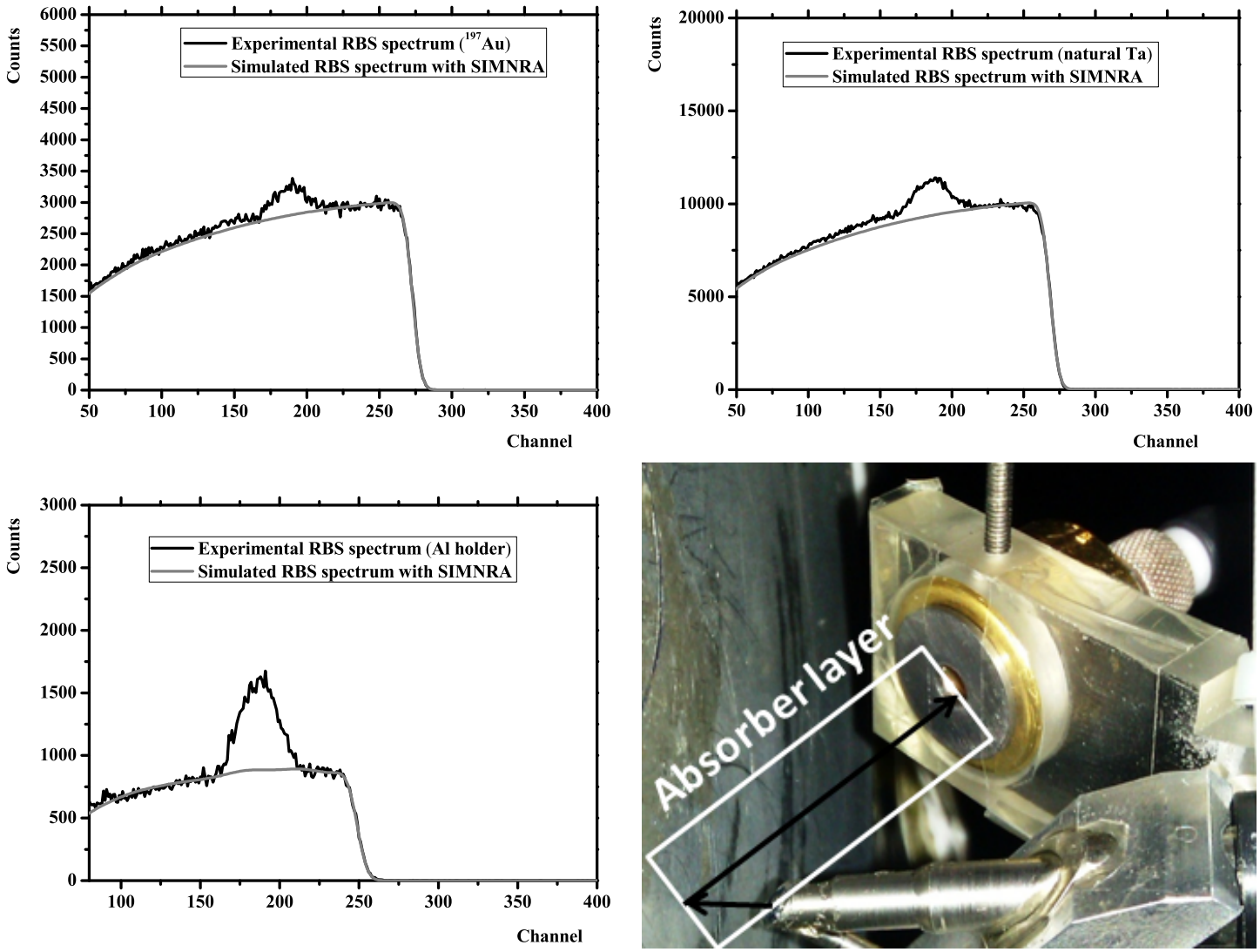

Figure 2.14: Examples of the simulation of the RBS spectra from ^{197}Au, natural Ta foils (upper pictures) and the Al holder of the ^{237}Np target (down-left picture). The ^{197}Au foil is not oxidized, nevertheless a small peak from protons backscattered on ^{16}O occured on top of the RBS spectrum of backscattered protons on Au. This peak is bigger at the RBS spectra on Ta and Al, because these materials are oxidized. The air absorber layer assumed is schematically shown in the down-right picture.

Another important remark is that points equidistant from the center of the target (such as 2 and 5, 3 and 4, see fig. 2.15) do not present the same trend. The situation was similar for all the targets under analysis and it was concluded that the actinide surface concentration did not present any systematic trend as for example less material at the edges or very similar values at points of equal distance from the center of the target.

The mean value of the actinide content of all the points measured at each target obtained from the SIMNRA analysis, which is an estimate of their thickness, is reported in the table 2.5. The error reported in the table is the standard deviation of the mean value, the large value of which can be attributed to the small number of points. As expected from the mass measurements, ^{237}Np is the thinnest since the mass of this target is slightly bigger than the mass of ^{235}U and smaller than the mass of both ^{238}U targets and is distributed over a larger surface. The targets characterized turned out to be homogeneous within satisfactory levels with respect to their use for fission cross section measurements (within 17% for the points examined).

	$\frac{ActinidePeakIntegralCounts}{AlbackingCounts}$	FWHM (keV)	Surface concentration (10^{15} at/cm^2)
point 1	2.90 ± 0.02	154	1178± 10
point 2	2.81 ± 0.02	143	1181± 10
point 3	2.28 ± 0.02	114	946± 5
point 4	2.87 ± 0.03	143	1179± 10
point 5	2.70 ± 0.02	131	1132± 7
average	2.71 ± 0.25	137 ± 15	1123 ± 100

Table 2.4: The results from the analysis of 5 points on the surface of the ^{238}U target (label 210), schematically shown in fig. 2.15. The values obtained from the three methods, namely the ratio $\frac{ActinidePeakIntegralCounts}{AlbackingCounts}$, the FWHM and the analysis of the spectra with the SIMNRA program.

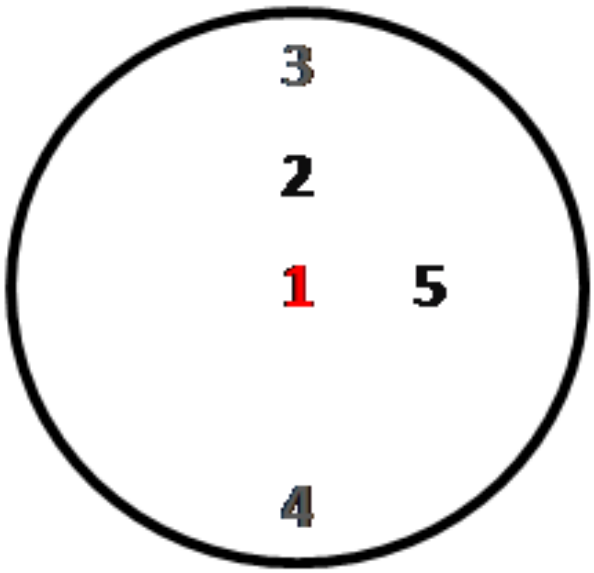

Figure 2.15: Schematic view of some points measured on the surface of the ^{238}U target (label 210). Points 3 and 4 are at the edges of the target and have equal distance from the central point 1. Points 2 and 5 also are of equal distance from point 1.

	^{237}Np	^{238}U	^{235}U
Target Diameter (cm)	8	5	5
Mass values (mg)	6.28 ± 0.11 (28)	9.90 ± 0.13 (209)	4.96 ± 0.06
	6.36 ± 0.11 (29)	9.03 ± 0.12 (210)	
Mean actinide surface concentration (10^{15} at/cm^2)	307 ± 53 (28)	1112 ± 95 (209)	626 ± 90
	249 ± 25 (29)	1120 ± 100 (210)	

Table 2.5: The mean actinide surface concentration for each target. The error is the standard deviation of all the points measured. The mass values obtained with the alpha spectroscopy and the diameters of the targets are also reported for completeness.

Chapter 3

The ^{237}Np(n,f) measurement at n_TOF with FIC: Experimental setup

The n_TOF facility (neutron Time-Of-Flight) is located at CERN (European Organization for Nuclear Research [41]) in Switzerland and has been designed and built from an international collaboration after a proposal from C. Rubbia et al. [42] in order to provide high accuracy neutron induced reaction cross section data for nuclear technology and nuclear astrophysics purposes. This innovative neutron beam facility combines unique features as high flux, neutron spectrum in a wide energy range, high resolution and low background. The first commissioning took place in 2002 and the measurements performed can be divided in two areas: neutron capture and fission. The data analyzed in the context of the present thesis were collected during the fission campaign of 2003.

This chapter contains a description of the facility and of the main characteristics of the n_TOF neutron beam [45, 49, 50, 51] . After a brief introduction on the production method, the neutron flux, the energy resolution and the beam profile are described because these parameters are necessary for the present analysis. Furthermore, a short description of the Data Acquisition System (DAQ) used is given and finally the fission detection setup used.

3.1 Description of the CERN n_TOF facility at CERN

The white neutron beam at the CERN n_TOF facility is produced via the spallation process occuring from the collision of protons with a momentum of 20GeV/c on a thick lead target. A short description of the different parts of the facility are given below. It has to be noted that the description below refers to the facility during n_TOF phase 1 (i.e. period 2001-2004) because the data analysed in the present thesis were collected during the fission campaign in 2003.

- **The Proton Beam:** The high energy and high flux pulsed proton beam is provided by the Proton Synchrotron (PS) accelerator complex (fig. 3.1). The PS normally operates in ``supercycles" (i.e. successions of machine states, in which several particle pulses can be accelerated and extracted for different users. The duration of the supercycle varies between 14.4 s and 19.2 s and the time interval between two sequential pulses (``bunches") could vary from 1.2s to 16.7s. Nevertheless, due to several limitations as the radioactivity in the lead target area and combinatorial use with other experiments at CERN the repetition rate of the proton pulses was limited to 0.25 Hz and the time interval between two sequential proton bunches is 4s, thus avoiding the overlapping of two sequential neutron pulses, since the thermal neutrons reach the experimental area approximately 80ms after the collision of the proton beam on the lead target.

Up to 7e12 ppp (protons per pulse) can be provided, in the form of short (7 ns width) pulses. The number of neutrons produced via the spallation process varies with the target material but above the projectile energy of 2 GeV it is nearly constant and about 25 neutrons/proton for lead. The total number of neutrons produced reaches 2e15 per proton pulse. The neutrons cover a long flight path of 182.5 m in vacuum before entering the experimental area. These features make the n_TOF facility a unique neutron source with very high instantaneous flux and excellent time resolution, up to 10^{-4}E for thermal neutrons and 6% for neutrons with energies close to GeV.

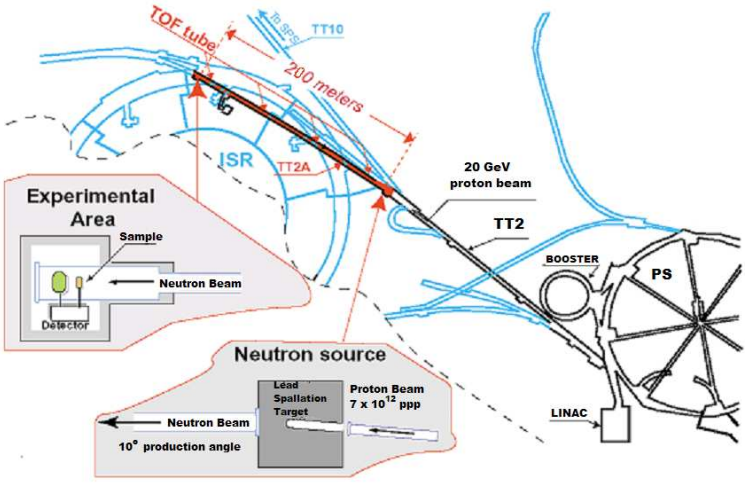

Figure 3.1: The Proton Synchrotron complex at CERN (picture taken from [43]). The proton beam passes through the TT2 line and collides on the lead target. The neutrons produced from spallation traverse approximately 182m in vacuum until they reach the experimental area.

There are two proton beam operation modes provided for the n_TOF facility: 1) The dedicated mode, in which bunches with 7e12 protons/bunch at a momentum of 20 GeV/c are delivered, and 2) the parasitic mode, in which 4e12 protons/bunch are delivered, with a momentum of 24 GeV/c (the number of neutrons per proton produced is not significantly affected by the higher momentum value because, as it is already mentioned, this value is nearly stable above 2GeV).

Information on the proton beam is provided by several devices installed near the end of the TT2 tunnel (fig. 3.1): The Beam Current Transformer (BCT) is placed about 6m before the spallation target for the monitoring of the proton intensity sent to the target, pulse by pulse, with an accuracy of 1%. The Wall Current Monitor (WCM) is placed right after the BCT and provides a pulse (pick-up signal) that is related to the instantaneous proton beam intensity and can also be used for timing purposes. The BCT proton intensity and the pick-up signal are included in the DAQ for further use in data analysis. The trigger signal for the n_TOF DAQ is the signal from the BCT. False trigger signals are sometimes provided without protons in the target, and in this case the pick-up signal must be used to confirm the presence of the beam. Finally the position of the proton beam is monitored with use of scintillating surfaces and cameras (Beam Position Monitors) during the preparation of the measurements.

- **The spallation target:** Lead was chosen as the spallation target, because it presents high radiation damage resistivity and transparency to neutrons below 1MeV. It was provided by the TARC experiment [52]. It consists of a high purity (99.99%) $80 \times 80 \times 60$ cm^3 lead block in contact with demineralized water that serves for cooling and moderation. The water flows in a closed loop for safety reasons and the thickness of the water layer is about 3cm at the entrance for avoiding possible parasitic reactions and 5 cm at the exit window in order to increase the moderation. It is separated from the TOF tube with an aluminum window. The spallation of protons in the lead target creates a large amount of high energy secondary particles, such as gammas, muons, protons and pions, preferentially emitted along the proton beam direction. In order to minimize the contamination of the neutron beam with primary protons, and

Material	Internal-External radius (cm)	Initial co-ordinate (m)	Length (m)
First Collimator			
Iron	5.5-25	135.54	1
Concrete	5.5-25	136.54	1
Second Collimator	**Fission mode**		
Borated polyethylene 5%	4.0-20.0	175.35	0.5
Concrete	4.0-20.0	175.85	1.25
Borated polyethylene 5%	4.0-20.0	178.10	0.75

Table 3.1: Summary of the collimator properties. Data taken from [45]. For the capture mode only the internal radius of the second collimator is different and has a value of 0.9cm.

other secondary particles, the proton beam line forms an angle of 10° relative to the TOF tube as can be seen in fig. 3.1. However, part of gamma rays and ultra-relativistic particles are reaching the experimental area, and their energy deposition in the targets and the detectors produces the so-called γ-flash, which serves for the accurate determination of the time-of-flight of neutrons, as explained in sec. 3.2 in this chapter.

- **The neutron beam line:** The neutrons produced from spallation are propagated in the TOF tube which is 199.607 m long, starts from the water tank, passes through the experimental area to the so-called "Neutron Escape Line"(NEL) and is ended at the beam dump. The vacuum tube is made of stainless steel and consists of different parts with progressively reduced diameter. The pressure in the beam line is kept constant at approximately 1mbar.Shielding walls made with concrete and iron are severely reducing the background. A sweeping magnet at a flight path of 145.4m removes remaining charged particles. Two collimators placed at 135.5 and 175.35m shape the neutron beam in the experimental area. The inner diameter of the second collimator is different according to the beam profile wanted in the experimental area: for fission reactions an inner diameter of 8cm is needed since the sample material is deposited on a large surface in order to be thin and have the smallest self absorption of FF possible. For capture reactions an inner diameter of approx. 2 cm is needed. Characteristics of the two collimators can be found in table 3.1.

  The neutron escape line (NEL) extends for 12 m after the experimental area to the beam dump, behind a shielding wall, in order to reduce backscattering. The beam dump consists of a $490 \times 490 \times 475$ mm^3 polyethylene box, separated in 19 slices, covered by a cadmium foil and an additional polyethylene layer.

3.2 Neutron beam characteristics

As it has already been mentioned, the features of the n_TOF faciliy at CERN that make it a unique neutron source facility worldwide is the high instantaneous flux maximizing the signal-to-background ratio, the excellent energy resolution due to the long flight path, low background and the large time interval between the proton bunches, minimizing the possibility of overlapping neutrons from successive bunches.

3.2.1 Neutron flux

The simulation of the neutron flux, one of the most important parameters of the facility, is a difficult task due to the large length of the neutron flight path in the n_TOF tunnel. Detailed Monte Carlo simulations were performed in order to estimate the neutron flux that reaches the experimental area [45, 46] with the combination of three codes, FLUKA, EA-MC and MCNPX and the simulations were divided in two steps: 1) the production of

the neutrons entering the TOF tube and 2) the geometrical transport of the neutrons generated into the experimental area. The uncollimated neutron flux in the experimental area obtained from the simulations is shown in fig. 3.2 (in units of dn/dlnE/cm^2/7·10^{12} protons). The two codes (FLUKA and MCNPX) give similar results, especially in the energy range between 1 eV and few MeV, with some discrepancies in the high energy part ($\geq$100 MeV) which could be due to differences in the physics models and nuclear data used by the two codes. With the collimation the neutron flux is scaled down by a constant factor [47], for the capture mode for example the scaling factor is $\sim$7.3.

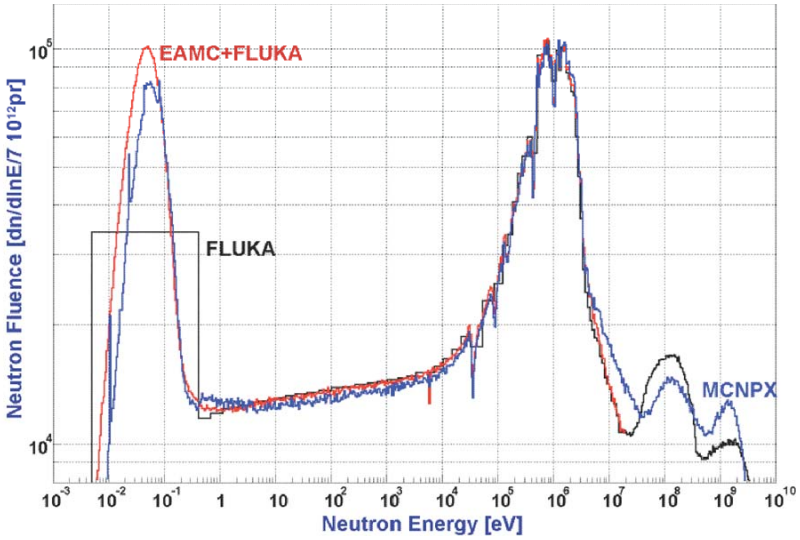

Figure 3.2: Monte Carlo simulation of the uncollimated neutron flux at 185 m using the combined codes, FLUKA and EA-MC, FLUKA and MCNPX (picture taken from [45]).

The isolethargic behavior between 1 eV and $\sim$100 keV is due to the water used for moderation after the Pb target. The flux presents some dips at 30 keV, 100 keV and 300 keV, which are attributed to neutron absorptions at the Al window that separates the moderator from the TOF tube. Furthermore, the dips at 500 keV and 1 MeV are attributed to absorptions at the oxygen content in the moderator. It was found out that the above shown simulation results were lower up to 20% than the experimental results of neutron flux measurements performed with various detectors and techniques during the commissioning [48] and this was due to an incorrect moderator thickness taken into account in the simulations (it was actually 5.8 cm instead of 5 cm), so these simulations were corrected. Nevertheless, the shape is the one shown in fig. 3.2 and more details are not of interest for the present thesis since the neutron flux for the cross section calculation is defined experimentally with the use of the standard cross sections ^{235}U(n,f) and ^{238}U(n,f).

The integrated neutron fluence at 182.5 m with the collimating system used in the commissioning of the beam line was $9.6 \cdot 10^5$ neutrons per proton bunch (with 7·10^{12} protons) [46]. The solid angle is so small that only one neutron out of 10^7 emerging from the lead target reaches the detector station at the end of the neutron tube. Nevertheless, the instantaneous flux is still high, compared to other facilities with shorter flight paths and thus worse energy resolution.

3.2.2 TOF technique and neutron energy resolution

The time-of-flight technique is based on the determination of the neutron kinetic energy by measuring the time difference between the production and the interaction. In the general relativistic case, the time-energy relation is given by eq. 3.1.

$$E_n = E_{tot} - m_n c^2 = m_n c^2 (\frac{1}{\sqrt{1-\beta^2}} - 1), \beta = \frac{v_n}{c} = \frac{L}{c \cdot tof} \quad (3.1)$$

where E_n is the kinetic energy of the corresponding neutron, v_n the velocity of the neutron given by the ratio of **L** (flight path) to **tof** (the time-of-flight) for the corresponding neutron, c the speed of light in vacuum [53].

So it is very important to accurately determine the tof and L of the neutron that undergoes the reaction of interest.

- **tof:** The time scheme of each recorded signal at n_TOF is schematically shown in fig. 3.3. The tof for each recorded event at a detector caused by neutrons is equal to the time of the recorded event subtracted by the time of the neutron creation.

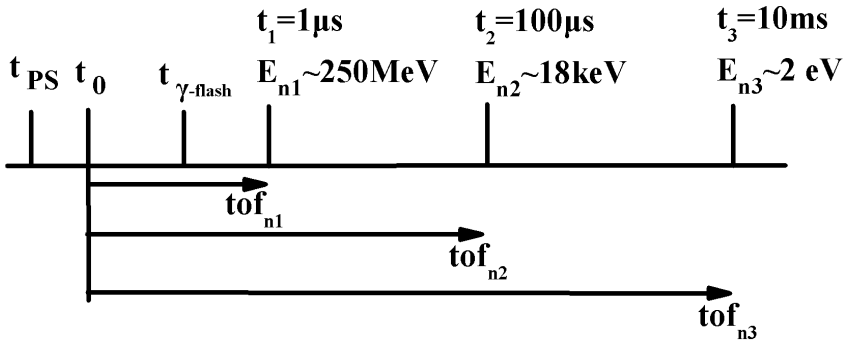

Figure 3.3: Time scheme of the recorded signals at the n_TOF facility.

The t_{PS} is the trigger signal for the n_TOF DAQ i.e. the signal from the BCT which corresponds to the time protons are arriving on the lead target. The t_0 is the time of the neutron creation from spallation, value unknown and related to the time the protons hit the target. The gamma rays and remaining ultra-relativistic particles produced in the spallation process reach the experimental area before the neutrons and produce the so-called "γ-flash", which is found at the first channels of the recorded signals namely $t_{\gamma-flash}$. The gamma rays travel in the TOF tube with the speed of light so the time interval from the neutron creation to the $t_{\gamma flash}$ can be estimated by the equation $\Delta t_{\gamma-flash} = L/c = 616ns$. So, $t_{\gamma-flash} = t_0 + \Delta t_{\gamma-flash} = t_0 + 616ns$. Neutrons start arriving at the experimental area at later times inversely proportional to their velocity. So, if an event caused by a neutron is recorded at some detector at a time t_n, then the tof is calculated by eq. 3.2.

$$tof = t_n - t_0 = t_n - t_{\gamma-flash} + \Delta t_{\gamma-flash} = t_n - t_{\gamma-flash} + L/c \quad (3.2)$$

For example, as schematically shown in fig. 3.3, a neutron (n1) detected at t_1=1 μs has a kinetic energy of $E_{n1} \sim 250$ MeV, a neutron n2 detected at t_2=100 μs has $E_{n2} \sim 18$ keV and a neutron n3 detected at t_3=10 ms has $E_{n3} \sim 2$ eV (calculated with eq. 3.1).

- **L:** Depending on the position of production of the neutrons in the Pb target the neutrons will have a different flight path L and time-of-flight, depending on the neutron energy. So, in order to accurately estimate L, another term λ has to be added to the geometrical flight path (namely L_{geom}, starting from the Pb target surface) which corresponds to a ``moderation"neutron path covered in the Pb target and the moderator before entering the TOF tube, and is correlated to the neutron velocity v_n right after the moderator and the time t elapsed since the neutron creation with the formula: $\lambda = v_n \cdot t$. So the total flight path L is given by $L = L_{geom} + \lambda$.

  In order to estimate the term λ, Monte Carlo simulations were performed [45, 46] and the results are presented in fig. 3.4.

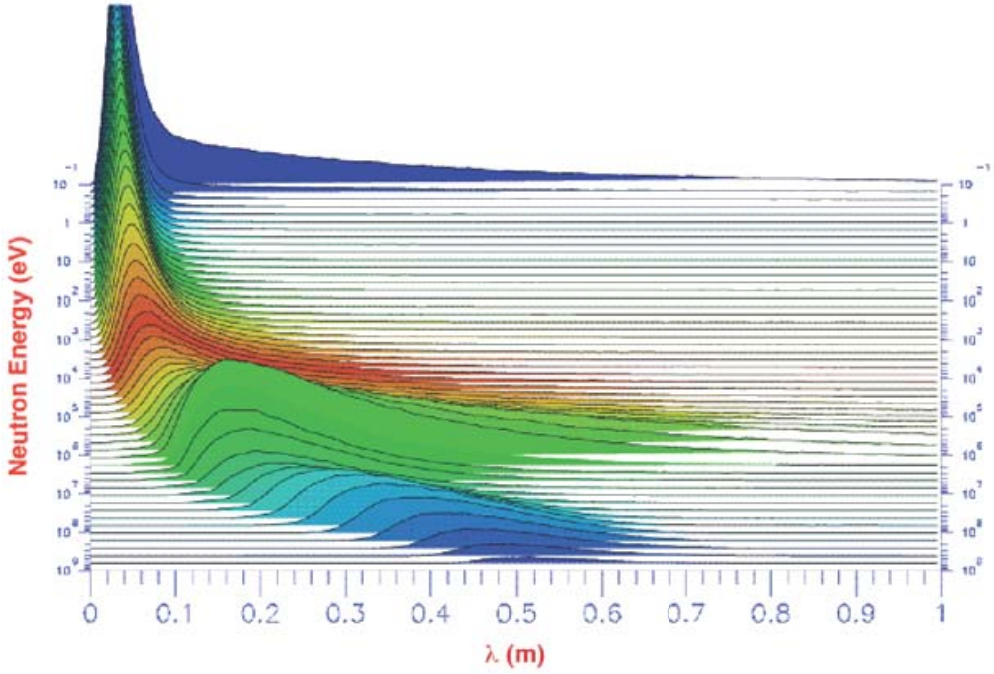

Figure 3.4: Distribution of λ with respect to the neutron energy, obtained with Monte Carlo simulations [45, 46].

- **Energy Resolution:** The energy resolution of the neutron beam is due to the uncertainty in L which is dominated by the uncertainty in the calculation of λ, and due to the uncertainty in the measured tof which is dominated by the spread of the proton beam distribution ($\sim$7 ns spread). The first component has been evaluated using the relation $\Delta E/E = (2\Delta\lambda)/(\lambda + L_{geom})$, where $\Delta\lambda$ is the variance estimated taking the r.m.s of the calculated λ distributions, or the standard deviation from a gaussian fit of the peaks [46]. The results are shown in fig. 3.5, along with the corresponding $\Delta E/E$. For low neutron energies this is the dominant component of the total energy resolution of the neutron beam. The 7 ns resolution due to the spreading of the proton beam becomes important at higher neutron energies (above a few MeV), as shown in the same figure. The final excellent energy resolution of $10^{-4} \prec \Delta E/E \prec 10^{-2}$ in combination with the high instantaneous flux makes the n_TOF facility ideal both for astrophysical and ADS related cross section measurements.

3.3 The fission detection setup

The fission detection setup used for the data analysed in the context of this thesis consisted of a Fast Ionisation Chamber (FIC) with fast timing properties, specially built at CERN for measuring neutron induced fission on minor actinides at the n_TOF facility [54]. This detector was developed by a collaboration between the Joint Institute of Nuclear Research (JINR), Dubna, the Institute of Physics and Power Engineering (IPPE), Obninsk (Russian Federation) and the EET group of CERN. At the time of the costruction this detector presented advantages as a) easy mounting in vacuum and simple installation of radioactive samples in it, b) minimum material at all the parts for in-beam applications and c) fast collection time for reliable operation at high counting rates expected at n_TOF. Two similar designs of the fission chamber were built to comply with the safety rules at CERN for the handling of radioactive sources. The first detector design, of which two copies were made, the so-called FIC0 and FIC1, was designed for the measurement of isotopes with very high alpha activity (as ^{237}Np , ^{234}U etc.), following the requirements of the ISO2919 standard as ISO/04/43323 (``sealed source for a general neutron source application"). The FIC of the second type, called FIC2, was used only as a neutron flux monitor. The data of the present thesis were taken from a run with FIC0 in 2003.

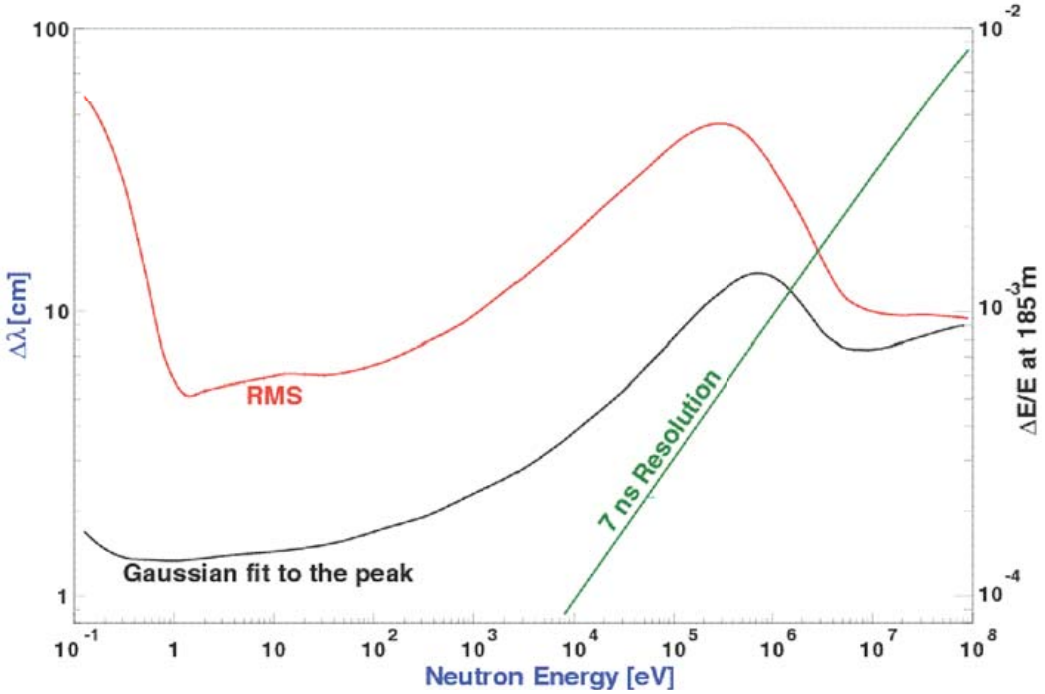

Figure 3.5: Uncertainty $\Delta\lambda$ in the determination of the neutron effective path at 185 m flight path, calculated with two ways: the r.m.s. of the calculated λ distributions (red line), and the standard deviation from a gaussian fit of the peaks (black line) and the resulting $\Delta E/E$. In the same figure the resulting $\Delta E/E$ due to the 7ns spread of the proton beam (green line) is included [46].

The detector consists of a stack of cells mounted one after the other with respect to the beam direction, filled with the gas used for the detection of the FFs. Each cell consists of three electrodes. The central Al electrode, of 100 μm thickness, was actually the backing of the actinide targets and in most of the cases it was plated on both sides with a disk of actinide target. The external electrodes, of 15 μm thickness, are used to define the electric field in the active gas-filled volume of the detector. In this way two separate active detection volumes are created but the corresponding signals are taken through the same DAQ channel, so at the end there is one signal coming out from each cell. The stack of cells was put in a sealed Al chamber. A photo and a drawing of the detector is shown in fig. 3.6.

The principle of operation of the FIC for fission cross section measurements is the measurement of the energy deposited in the detector gas by the fission fragments produced in very thin targets, which is considered as a standard technique for such measurements. The detector gas is in physical contact with the target in order to reduce the energy losses before entering the detection volume and obtain a solid angle coverage of very close to 2π. The FIC is working in the ionization mode, i.e. the ion pairs created by the incoming ionizing particle are detected without further multiplication. The higher the charge and the kinetic energy of the incoming particle the more ion pairs it produces and thus the higher the current created and consequently the amplitude of the pulse detected.

The main operation parameters of the detector FIC0 are summarized in table 3.2.

In order to avoid possible outgassing towards the atmosphere, all the welded parts were checked with X-ray imaging and the gas pressure in the chamber was kept below atmospheric pressure at 720 mbar. Since the detector was not working in proportional mode, gas circulation was not needed. The detector gas was chosen to be Ar (90%) / CF_4 (10%) which presents high electron drift velocity. At an electric field of 600 V/cm and a pressure of 720 mbar, the field strength per unit pressure is $\sim$0.83 VmN^{-1} and the corresponding electron drift velocity for this gas composition is $\sim$12 cm/μs (calculated tabulated values found at [55]). It has to be noted that the electron drift velocity at the same field strength per unit pressure for a pure Ar gas is $\sim$ 0.4 cm/μs while for a

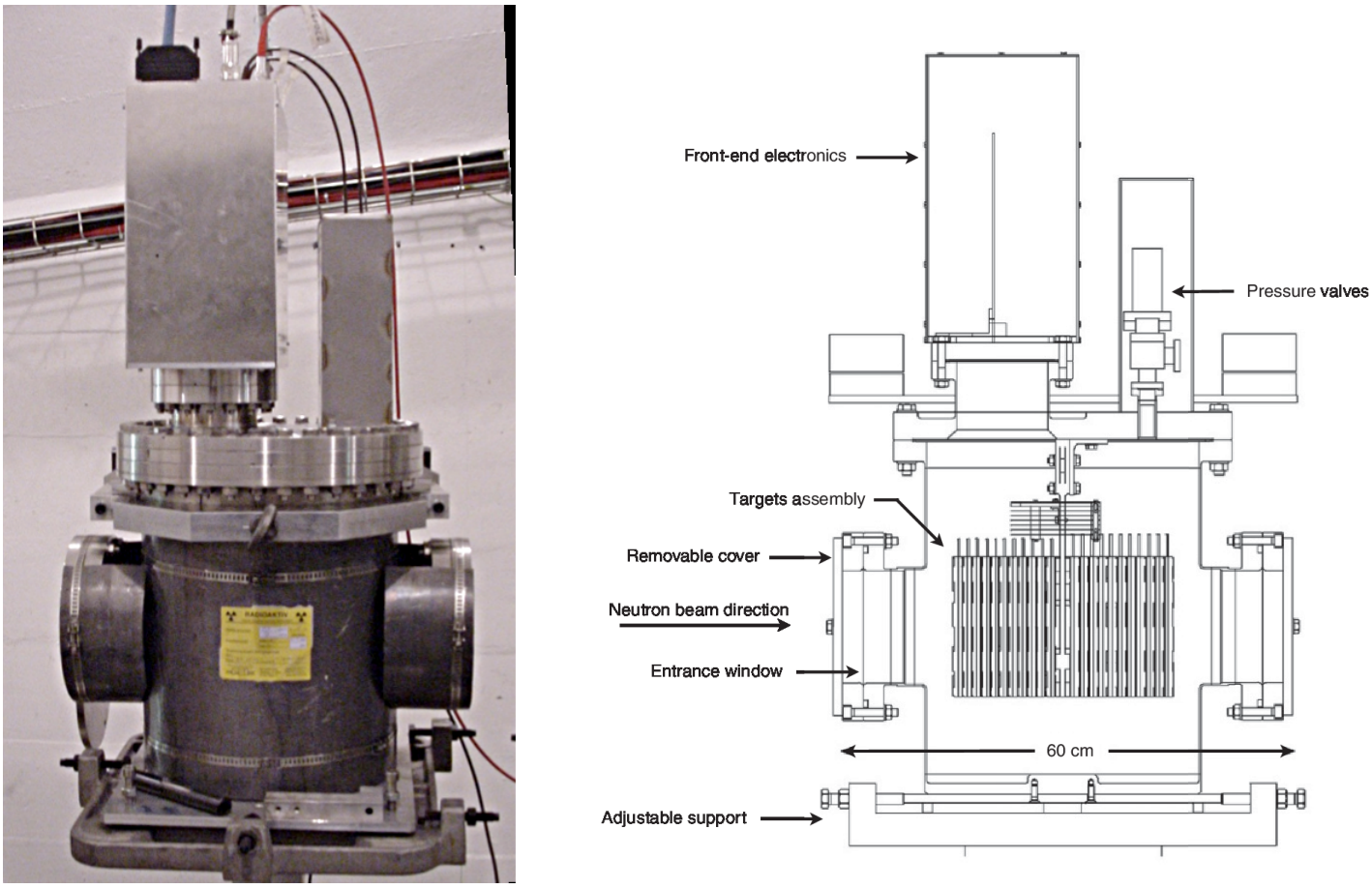

Figure 3.6: A photo (left) and a schematic (right) of the FIC0 detector used for highly radioactive isotopes.

pure CF_4 gas it is $\sim$ 10.5 cm/μs. With this drift velocity the charge collection time for electrons corresponds to (2cm)/(12cm/μs)$\sim$ 170ns, which is comparatively low and makes this counter very suitable for measurements of even the most α- active isotopes, minimizing pile-up effects.

Since the chamber was sealed before being transported into the experimental area, the alignment of the samples relative to the neutron beam was performed in two steps: during the mounting they have been aligned inside the detector body with their position determined relative to external reference points on the detector chamber. When the chamber was transported in the experimental area, the external reference points have been used for the alignment of the whole detector to the beam axis.

Since the detector is used in a neutron-rich environment the mass of the material in the parallel beam provided by the n_TOF facility needed to be significantly reduced. Indeed, as reported in [54], detailed Monte Carlo simulations with use of the MCNPX code [56] showed that the attenuation factor in each parallel plate, defined as the ratio of the transmitted neutron flux to the impinging neutron flux, is of the order of a few per thousand, with a total attenuation in the detector of less than 1%. Another important result is that the background induced by scattered neutrons in the materials of the detector is very low.

The chamber housed a stack of 18 actinide samples, connected to Fast Analog-to-Digital Converter (FADC) channels or oscilloscopes: one ^{237}Np , two ^{236}U, six ^{234}U and two ^{232}Th targets as well as three ^{235}U and three ^{238}U reference targets. The properties of the targets used in the present thesis are summarized in table 3.3. For the following, the names in this table will be used. The double sided Np7 target, consists of the two targets already mentioned in chap. 2 with labels 28 and 29, put back to back on the central electrode of the cell, so this target was characterized as far as the mass, thickness and homogeneity are concerned. The same stands for the double sided ^{238}U target (position 18, name: U8c) which consists of the targets with label 209 and 210, and for the single sided ^{235}U target (position 17, name U5c). For the rest, the nominal values of mass provided by the

Gas composition	Ar(90%) +CF_4(10%)
Gas pressure	720 mbar
Gap between electrodes	20 mm
Electric field	600 V/cm
Electrode diameter	12 cm
Target backing thickness	100 μm
Sample diameter	8 cm, 5 cm
Total length of chamber	60 cm

Table 3.2: Summary of the FIC0 detector used for the data analyzed in the present thesis. Data taken from [54].

manufacturer are reported in the table and used for the ^{237}Np(n,f) cross section calculation.

Position	Flight path (m)	Isotope	Label	Name	Mass (mg)	Diameter (cm)
4	185.390	U-235	9,10	U5	36.6	8
7	185.421	U-238	20,21	U8b	26.3	8
8	185.432	U-238	22,23	U8a	25.4	8
9	185.442	Np-237	28,29	Np7	12.64 ± 0.22	8
16	185.530	U-235	13,14	U5b	12.79	5
17	185.540	U-235	78	U5c	4.96 ± 0.06	5
18	185.551	U-238	209, 210	U8c	18.93 ± 0.18	5

Table 3.3: Summary of the FIC0 detector samples used for the cross section calculation in the present thesis. The rest of the targets in the chamber are not reported here. The mass values with errors (for Np7, U5c and U8c) are the ones experimentally determined with alpha spectroscopy in the context of the present thesis (see chap.2), while the rest are the nominal values provided by the manufacturer. The name of each target will be used for the following analysis of the FIC detector data.

3.4 The n_TOF Data Acquisition System at phase 1

The high instantaneous neutron flux at n_TOF represents a great advantage especially for the measurements of small mass and radioactive samples but poses relevant problems on signal processing and acquisition due to pile-up events and large dead times respectively. In order to overcome those problems, an innovative data acquisition (DAQ) system based on fast digitizers has been developped [57]. The main feature of this system is the possibility to sample and record the full analogue waveform of the detector signal in digitized form, for off-line analysis. The sampling is performed by means of fast Flash Analogue to Digital Converters (FADC), with sampling rates up to 2 GSamples/s, minimizing the acquisition dead time. The difficulties of such a system are the huge amount of accumulated data, thus requiring large storage capabilities, high data transfer rates, and sufficient computing power for the analysis of the FADC data. The FADC modules used at n_TOF are the DC240 and DC270 Acqiris Digitizers. Each detector in the experimental setup is coupled to a corresponding FADC channel. Groups of 4 or 8 FADCs are physically plugged to readout PCs for improving the transfer rate. The raw FADC data files are sent via GigaBit ethernet to a temporary Disk Server located close to the measuring station. Once the files are closed, they are transferred via GigaBit ethernet to a second disk pool from which they are finally migrated to the CERN tape pool CASTOR. During the data acquisition the control of these units and a quasi-online monitoring of events is performed with use of PCs in the control room, via TCP/IP protocols. The data stored by the digitizer in its memory buffer contain the full sequence of signals produced within a single neutron bunch. For this reason it is normally referred to as a FADC “movie”. As already mentioned the

trigger signal for the start of the data acquisition is given by the PS (BCT signal) and corresponds to the time the protons nearly hit the lead target (t_{PS} at fig. 3.3). For the data acquisition of the FIC detector, the DC270 modules are used, with a sampling rate of 40 MHz. At this rate detector signals were recorded in bins of 25 ns width in a time window of 100 μs which corresponds to neutron energies from GeV down to ∼20 keV. A typical movie obtained from the FIC0 2003 runs can be found in fig. 3.7. The same movie is zoomed in the high energy region (i.e. the first bins of the FADC) in fig.3.8.

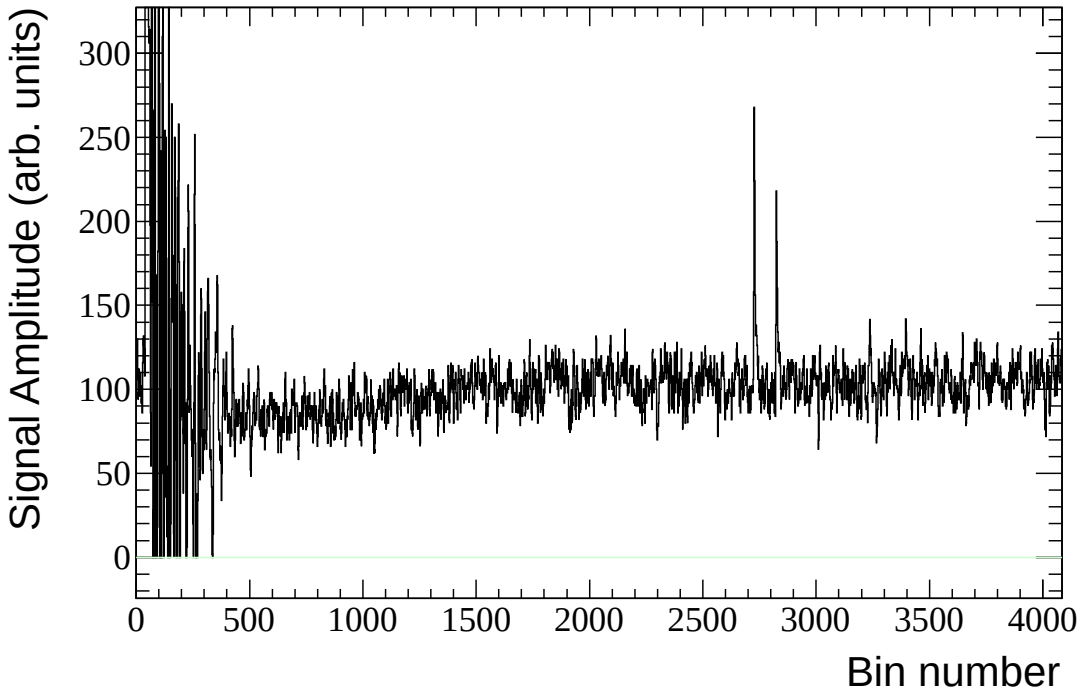

Figure 3.7: Typical FADC content. The full detector signal has been recorded for 4096 bins with a width of $\times 25$ ns.

The first large signal (at bin 62 in fig. 3.8) occurs from large energy deposition of gamma rays and relativistic particles produced from the spallation processes and arrive first at the experimental area and it is called "γ-flash". This signal, as already mentioned, is used for the estimation of the tof of the neutrons. However, this large signal causes malfunctions in the electronic chain of the detector, so the baseline of the signal at times after the "γ-flash"peak presents intense rippling (see fig. 3.8) until the bin ∼400 (corresponding to neutron energy of E_n ∼1.98 MeV) and even an undershooting until the bin ∼ 2000, corresponding to E_n ∼73.5 eV (see fig. 3.7). The signal distortion is so large that saturates at some bins, and there the data are lost, especially for bins before 200 (E_n <9 MeV). Two FF peaks are recorded at the event shown here at the bins 2725 (E_n ∼39 keV) and 2825 (E_n ∼37 keV). The typical FF pulses have a width of 250-300ns and are digitized with 10-12 points. The rising time of the peaks is ∼ 4 bins, i.e. ∼ 100ns wide in time.

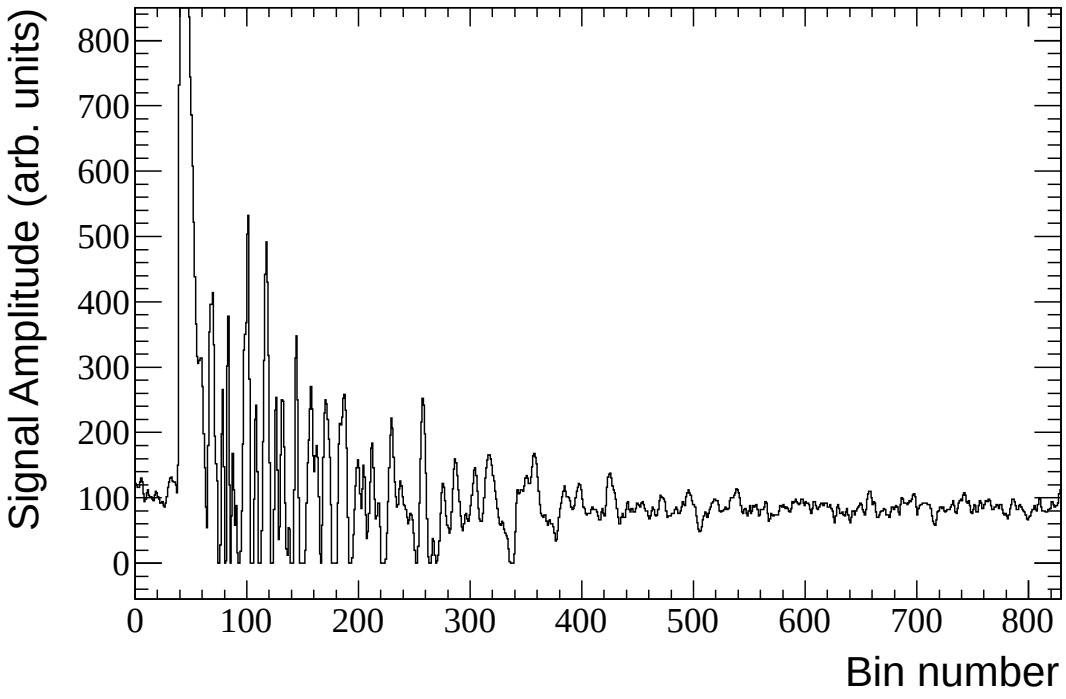

Figure 3.8: Typical FADC content, zoomed in the early phase of the movie.

Chapter 4

The ^{237}Np(n,f) measurement at n_TOF with FIC: Data analysis and results

4.1 The pulse shape analysis procedure

A method for analyzing the data taken with the Flash Analog to Digital Converters (FADC) in an automated way was developed, in order to provide a reliable background subtraction and identification of FF events even at high energies [58, 51], based on pulse shape analysis techniques.

As already mentioned in sec. 3.4, the main difficulty is the proper estimation and subtraction of the background under the FF peaks, because the large energy deposition of the γ-flash causes malfuctions in the detector eletronic chain, which results in an undershooting of the signal baseline and intense rippling, especially for bins in the early phase of the movie (bins $\sim$50-400) (see fig. 3.7 and 3.8). In order to properly fit the FF peaks, the background subtraction is a major issue.

In the context of the present work the background was subtracted from the raw data based on the observation that all the movies seem to follow the same baseline pattern in this region, thus allowing to produce an "average "FADC output ("average event"-$Y_{average}$(t)) for each detector channel by adding all the events starting from the time of the γ-flash. This average event is free of FF peaks because they appear in random times so they are smeared out. Due to the large number of bins available for the recording of the FIC signal, providing a time resolution of 25 ns, the possibility of having FF peaks that appear in the same bin of the movie (i.e. the same tof) for many events is very low. For the analysis of each event, the average event was fitted with a linear function in order to reproduce the baseline ($Y_{fittedaverage}$(t)). Then, the $Y_{fittedaverage}$(t) was subtracted from the raw event under analysis and in the resulting event the unwanted oscillations and the baseline undershooting were removed (see fig. 4.1). Then, the fitting of the FF peaks was easily and more accurately performed even if they were initially lying on an oscillating background (see fig. 4.2).

The above described procedure, is a very powerful technique, able to extract FF events even if they are very close to the γ-flash, where the oscillations are severe, so the fission cross section results can be extended to very high neutron energies. However, the raw data analysed in the context of the present thesis, obtained from FIC0 2003, presented saturations, especially in the neutron energy region above 10 MeV (i.e. for bins $\prec$ 200). At these regions of saturation the data is lost and cannot of course be recovered (see fig. 4.3). This problem limited the neutron energy range of the present work up to $E_n \sim 9$ MeV, as will be shown in the following.

The above briefly described data processing steps were included in a software, which was developed in the context of a previous work [59, 58].

The code has two operation modes, the "average signal"mode and the "pulse shape analysis"mode, and each

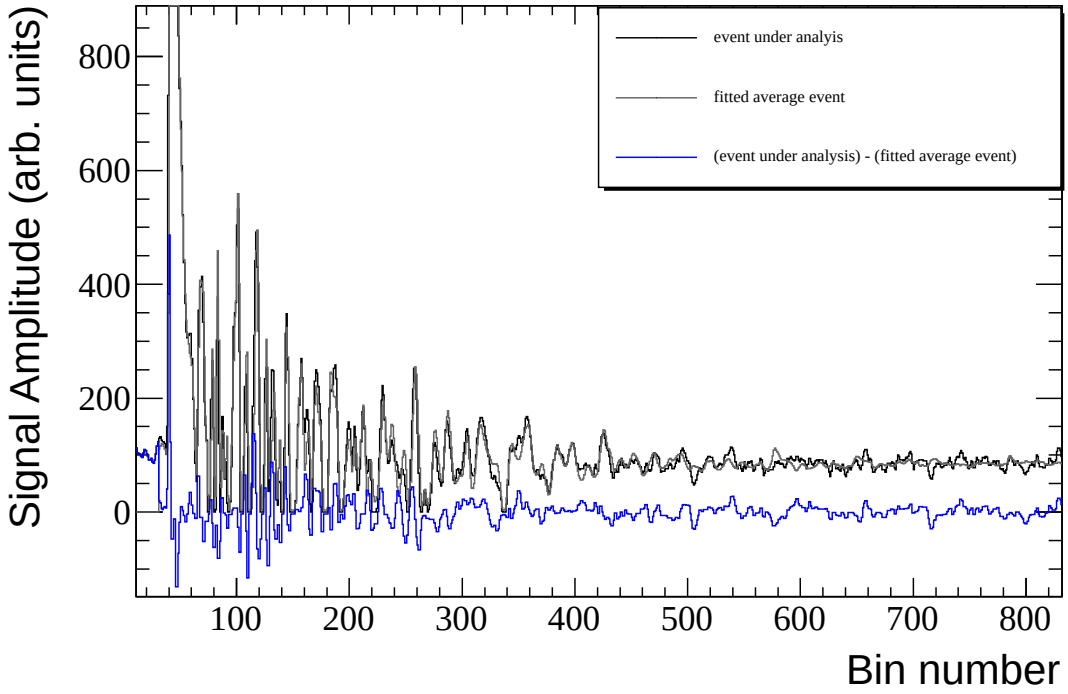

Figure 4.1: Example of the background subtraction. The event under analysis is shown with a black line (an event without FF signals was chosen, from the U5c target). The $Y_{fittedaverage}$(t) is shown with a grey line and is clearly free of FF signals, even if it has occured from the addition of events that contained FF signals at random bins. The resulting event after the subtraction is shown in blue.

FADC channel is processed with both modes on an event-by-event basis. The code reads one event, and tries to find the γ-flash, i.e the first peak in the movie that surpasses a given threshold and fits it with eq. 4.2. If the fitting is not successful it continues to the next event, otherwise the flash fitting parameters are stored, the integral of the flash peak is calculated and the code proceeds according to the selected mode of operation. In order to create "average"events as close as possible to the baseline of the events under analysis, the events are grouped into categories according to their flash integral values. A different categorization was performed for events created by dedicated TOF proton bunches and parasitic EASTC proton bunches, the second ones generally having lower flash integrals than the first ones. For each category a different average event is calculated.

- **The "average event"mode:** In this mode, the code copies the whole movie in the corresponding "average event"group, according to the flash integral value, and proceeds to the next event. The categorization of the events in groups according to their flash integral is chosen by the user, and it is a compromise between enough statistics in each group and similarity at the flash integral values for the events in each group (see 4.2.1).

- **The "pulse shape analysis"mode:** In this mode, the code finds out the average event group the event belongs to, and fits the corresponding "average event"($Y_{average}$(t)) to the event under analysis with equation 4.1, using the MINUIT code [60].

$$Y_{fittedaverage}(t) = Y_0 + A \cdot Y_{average}(t) \tag{4.1}$$

The Y_0 and A parameters from the fitting are stored and then $Y_{fittedaverage}(t)$ is subtracted from the event under analysis and the remaining signal is processed with a median filter with width 3 in order to remove any sharp spikes left from the subtraction (blue line in fig. 4.2).

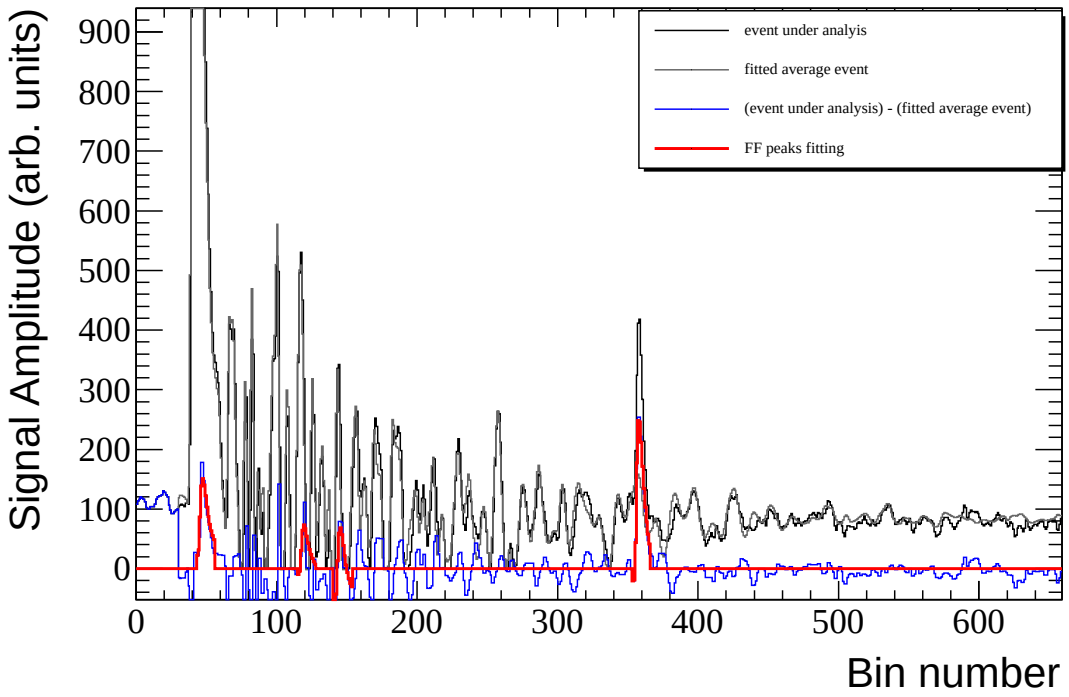

Figure 4.2: Example of the fitting of FF peaks after the background subtraction. The event under analysis is shown with a blue line. The $Y_{fittedaverage}$(t) is shown with a yellow line and the resulting event after the subtraction is shown in green. The fitted FF peaks are marked in red.

Then, the remaining event is checked, bin by bin, and if a certain threshold is surpassed, the code searches for local maximum-a, and local minmum-a until the background level chosen by the user is reached. Then the FF peak candidate-s are fitted with eq. 4.2. The shape of this peak can be found in fig. 4.4.

$$Y_{peak} = Y_0 + A \cdot \left(1 - e^{-\frac{t-t_0}{t_1}}\right)^p \cdot e^{-\frac{t-t_0}{t_2}} \tag{4.2}$$

This equation involves 6 parameters, 3 of them are kept constant: t_1=1.2, t_2=2.3 and p=9.9 (these values were found to reproduce well the shape of the peaks). The other three concern the starting point of the peak (t_0), the amplitude at this point (Y_0) and a multiplication factor for the amplitude of the peak (A).

If the fit converges, the time of flight is obtained from the point where the maximum of the peak is, i.e. from eq. 4.3.

$$tof = t_0 + t_1 \cdot (\ln(pt_2 + t_1) - \ln(t_1)) = t_0 + 4.316 \tag{4.3}$$

The amplitude of the peak at t=tof, namely the **Ampl**, is given by eq. 4.4:

$$Ampl = Y_0 + A \cdot \left(1 - e^{-\frac{tof}{t_1}}\right)^p \cdot e^{-\frac{tof}{t_2}} \tag{4.4}$$

The gamma flash peak is also fitted with eq. 4.2. Consequently, for each event 4 parameters and the corresponding errors occur from the fitting of the γ-flash peak (eq. 4.2 and 4.4), namely fA, fY0, ft0, fAmpl and 2 parameters and the corresponding errors from the fitting of the selected ``average event'' on the data of the event under analysis (eq. 4.1), namely aA and aY0. For each FF peak candidate 4 parameters and the corresponding errors occur from the fitting with eq. 4.2, namely pA, pY0, pt0 and pAmpl. All these parameters and the errors are stored in binary files. Another code creates the corresponding histograms in ROOT files [61] for further selection.

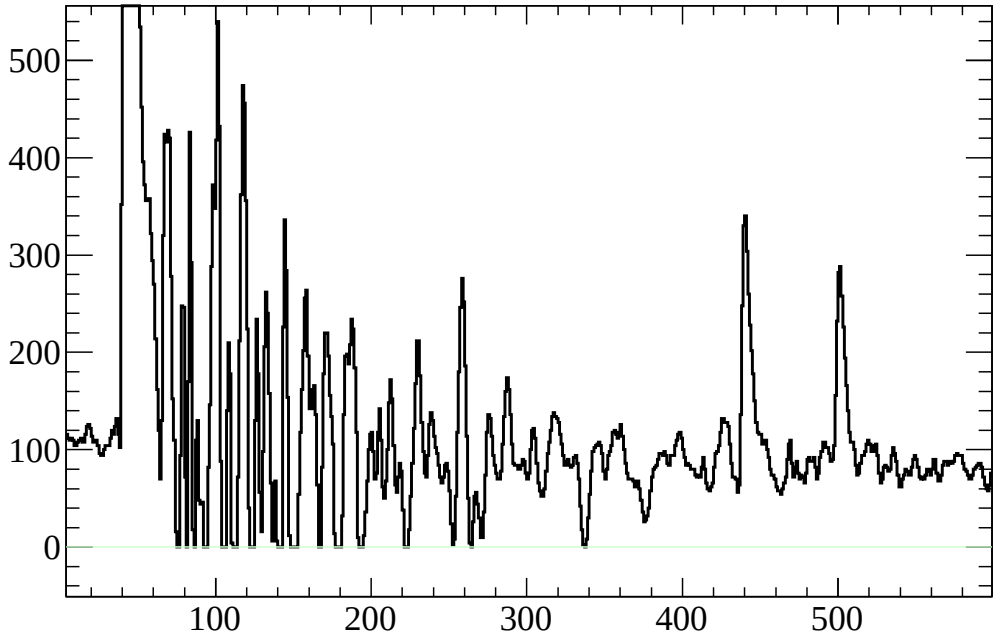

Figure 4.3: Example of an event with saturations. Saturations can be seen in the region up to bin 350, which corresponds to a neutron energy range down to 2.6 MeV (from the U5c target).

Rejection of whole events with exclusion of γ-flash fitting parameters and errors (fA, fY0, ft0, fAmpl) or "average event"fitting parameters and errors (aA and aY0), as well as FF pulses with exclusion of peak fitting parameters and errors (pA, pY0, pt0, pAmpl) is possible with *rootres*. For each target a separate analysis was performed in order to estimate the accepted limits of the fitting parameters and their errors, by checking the raw data. More than 300000 events were accepted for each target, the events from parasitic EASTC proton pulses being $\sim$40% more than the events from TOF proton pulses.

4.2 Sensitivity of the pulse shape analysis on various parameters

The sensitivity of the analysis results on the change of various factors was examined and shown in this section.

4.2.1 Sensitivity on the grouping of the events according to the γ-flash integral values

As mentioned above, the events were grouped into categories with similar γ-flash integral and an "average event"was extracted from each group. An effort has been made to have the finer binning possible in the categorization but also enough statistics in each group in order to smear out the FF peaks at the "average event". It was found out that a group with less than 20 events gives an average event with residual peaks, thus not suitable for the baseline subtraction. The binning of the events was based on the histograms of the flash integral values of the accepted events. As an example, the histogram of the integral values of the accepted events can be found in fig. 4.5. Various binnings were tried in order to find the best settings by checking the raw data and the reaction rate of each target.

For bins after $\sim$ 400 and until the end of the movie, the rippling of the baseline is not intense and the frequency of the FF peaks is low, so the reproduction with ``average'' events was very easy even with the coarsest binnings, for all the targets. For the early phase of the movie, however, where the frequency of the FFs is higher, and the

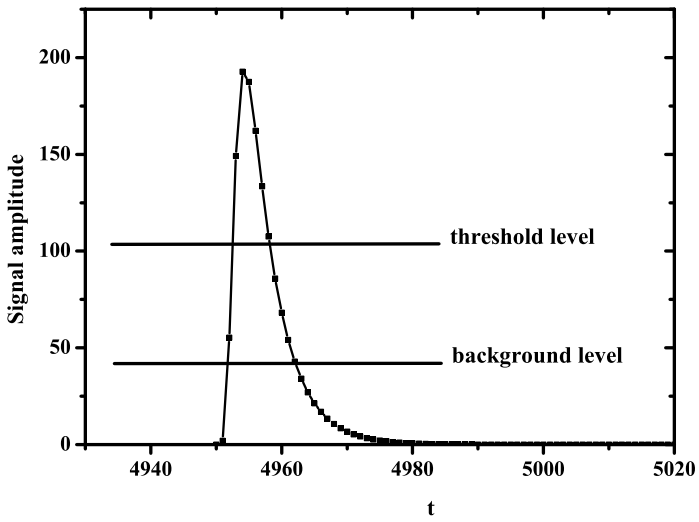

Figure 4.4: Indicative shape of the FF peaks, predicted by eq. 4.2.

rippling intense, the situation is a bit more complicated. It was found out that for targets with low FF activity the effect of the different binning in the reproduction of the baseline was negligible and the fitted ``average'' event in almost all the cases was very good. The low FF activity targets are U5c, U8c, U8a, U8b (with increasing FF activity order), because they have low mass and/or low fission cross section value at the "plateau"(bins before 400 correspond to neutrons with energy higher than $\sim$ 2 MeV). In fig. 4.6 the comparison of the pulse shape analysis with a very coarse grouping of events (14 groups for EASTC pulses - 17 groups for TOF pulses) and a fine binning of events (50 groups for EASTC pulses - 40 groups for TOF pulses) is shown, and it is evident that the differences are negligible.

This is reflected in the obtained reaction rate from the pulse shape analysis of all the events for this target with the two binnings examined. The differences are negligible as can be seen in fig. 4.7, within the statistical errors of the reaction rate values.

For higher FF activity (for the targets Np7 and U5b), especially in the early phase of the movie, the reproduction of the baseline was often not so successful, as can be seen in fig. 4.8. The fitted average event overestimated the data, especially in the region 300-700, and this was due to the high FF counting rate in this region, making the complete smearing out of the FF pulses more difficult. However, the code generally succeeds to fit the FF peaks, as can be seen in the same figure. The reproduction of the baseline with two different binnings, a coarse binning (15 groups for EASTC pulses - 17 groups for TOF pulses), and a fine binning (66 groups for EASTC pulses - 61 groups for TOF pulses) is shown in this figure.

However, the pulse shape analysis is not sensitive to the binning chosen in this case either. In fig. 4.9, the comparison of the pulse shape analysis results for the two binnings of events is shown for the Np7 target. The differences in this case do not exceed 0.6% in the energy region below 3MeV, smaller than the statistical error in the region (as an example, for 5e5 eV the statistical error is 1.1%, while at 2 MeV 0.7%). In the energy region 3-10 MeV, which is more difficult as far as the reproduction of the baseline is concerned, the differences are somewhat larger but still lower than the statistical errors (1.3-1.5%).

Even for the case of the U5 target which is of the highest FF activity, the differences in the obtained reaction rate for different binning of events were less than 2%. However, in this case, the reproduction of the baseline of the events with the fitted average events was not good and it resulted in losses of FF peaks, as it will be discussed in the following. As a final remark, the analysis procedure was not found sensitive to the selection of the binning of the events according to the flash integral values, and this is due to the large similarity of the pattern of the oscillations after the γ-flash.

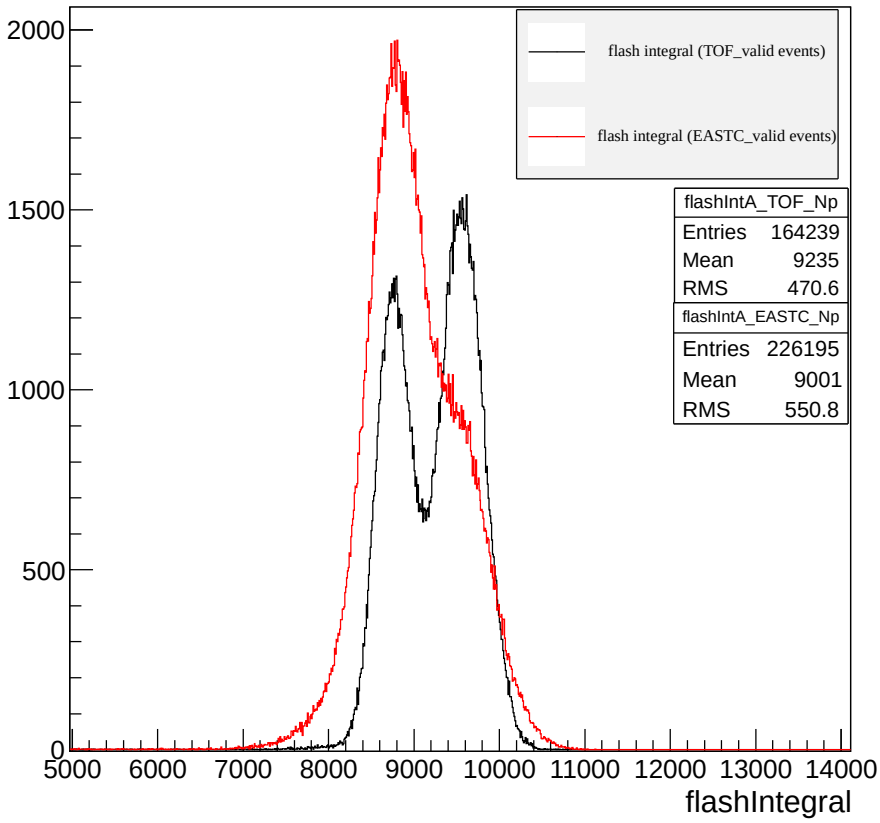

Figure 4.5: Histogram containing the integrals of the fitted γ-flash peaks of accepted TOF and EASTC events for the Np7 target.

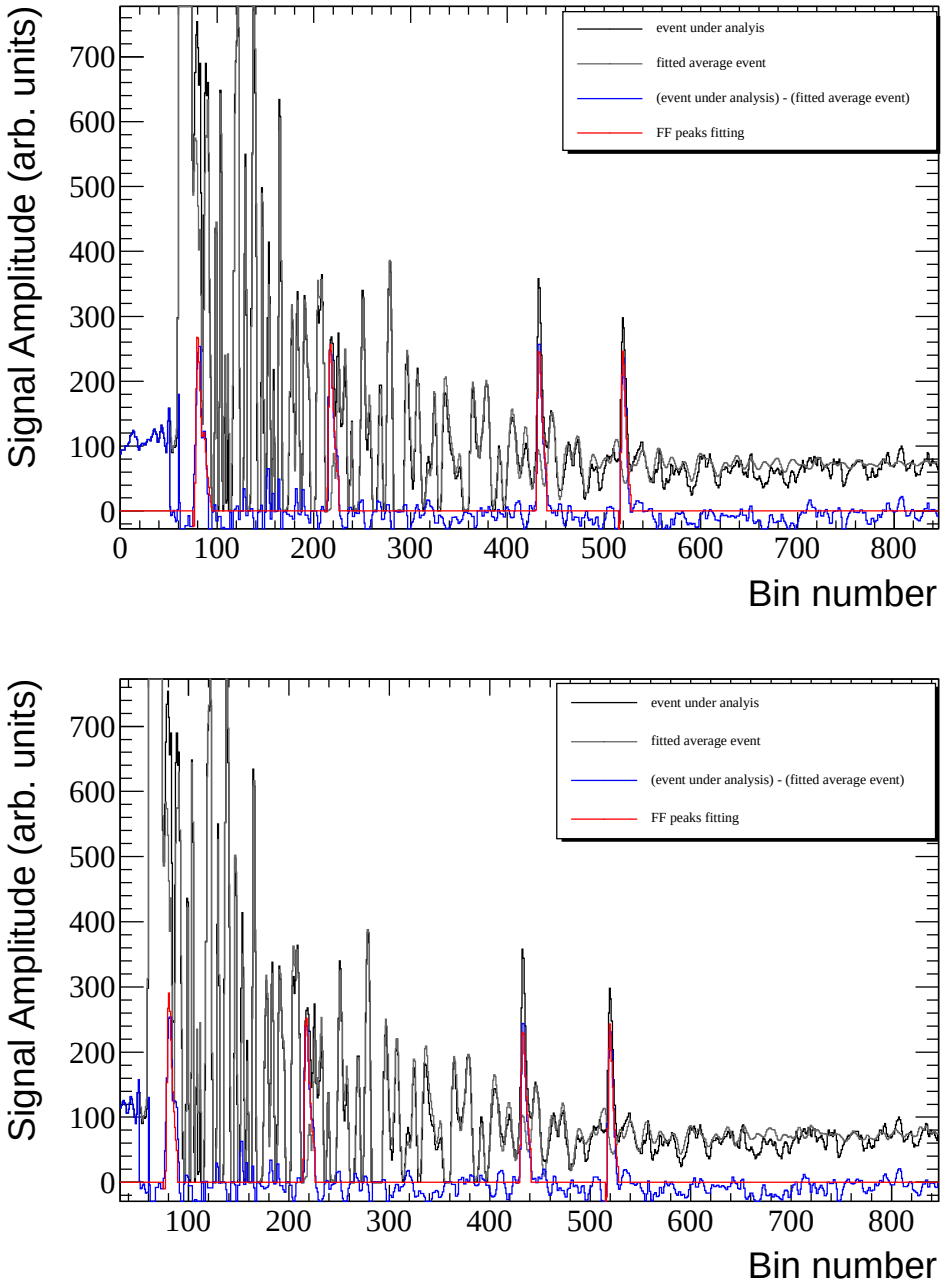

Figure 4.6: The pulse shape analysis for an event from the U5c target with coarse grouping of events (14 groups for EASTC pulses - 17 groups for TOF pulses)-upper figure, and fine binning of events (50 groups for EASTC pulses - 40 groups for TOF pulses)- lower figure. The differences in the reproduction of the baseline by the fitted average event are negligible.

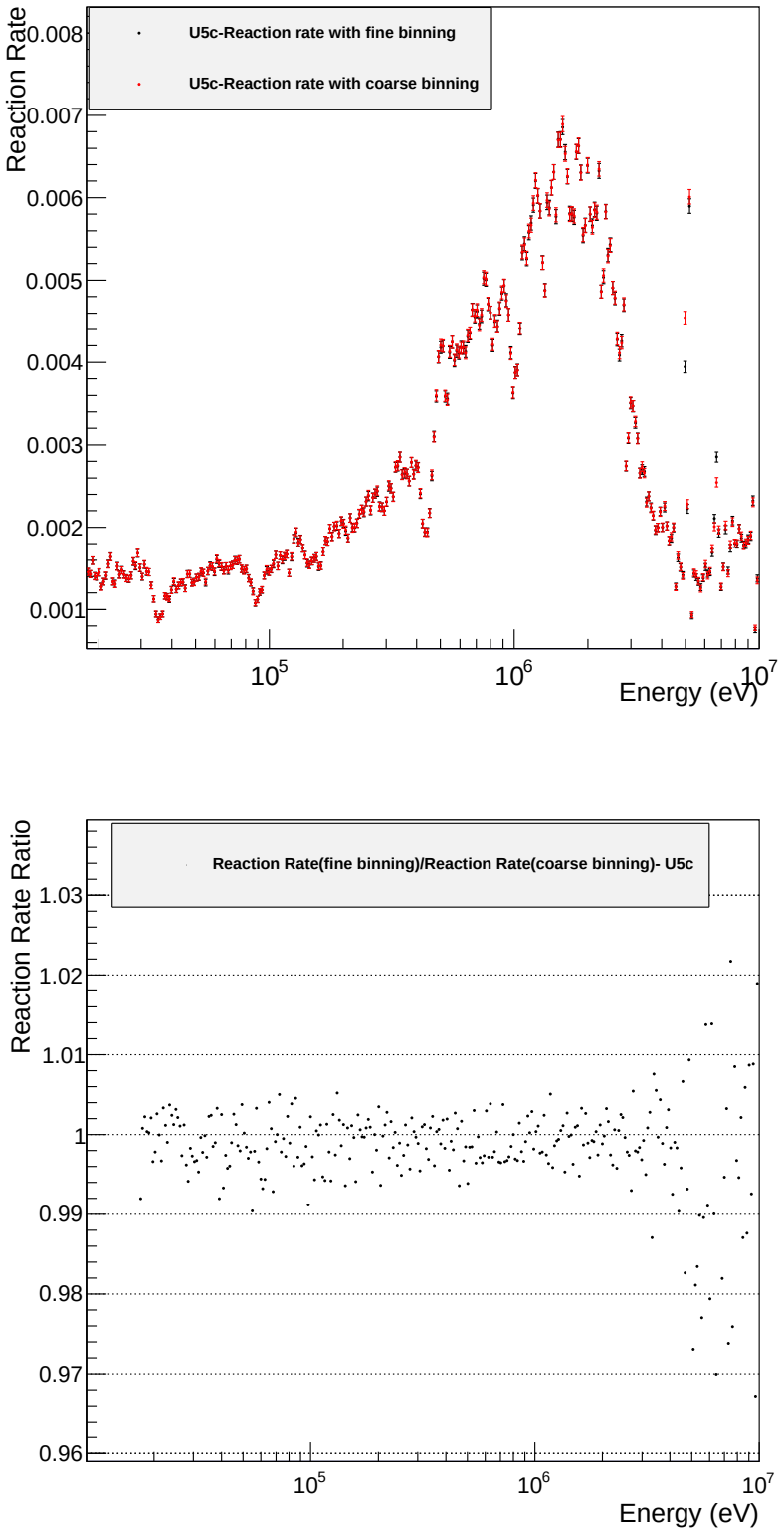

Figure 4.7: Upper figure: The comparison of the reaction rate obtained from the pulse shape analysis of the U5c target events, with coarse binning (14 groups for EASTC - 17 groups for TOF) - red points and fine binning (50 groups for EASTC - 40 groups for TOF) - black points. Lower figure: The ratio of the obtained reaction rates shown above: it is very close to 1, with deviations that do not exceed the statistical error of the reaction rates. Above 3 MeV the reaction rate at this target presents large oscillations due to saturations.

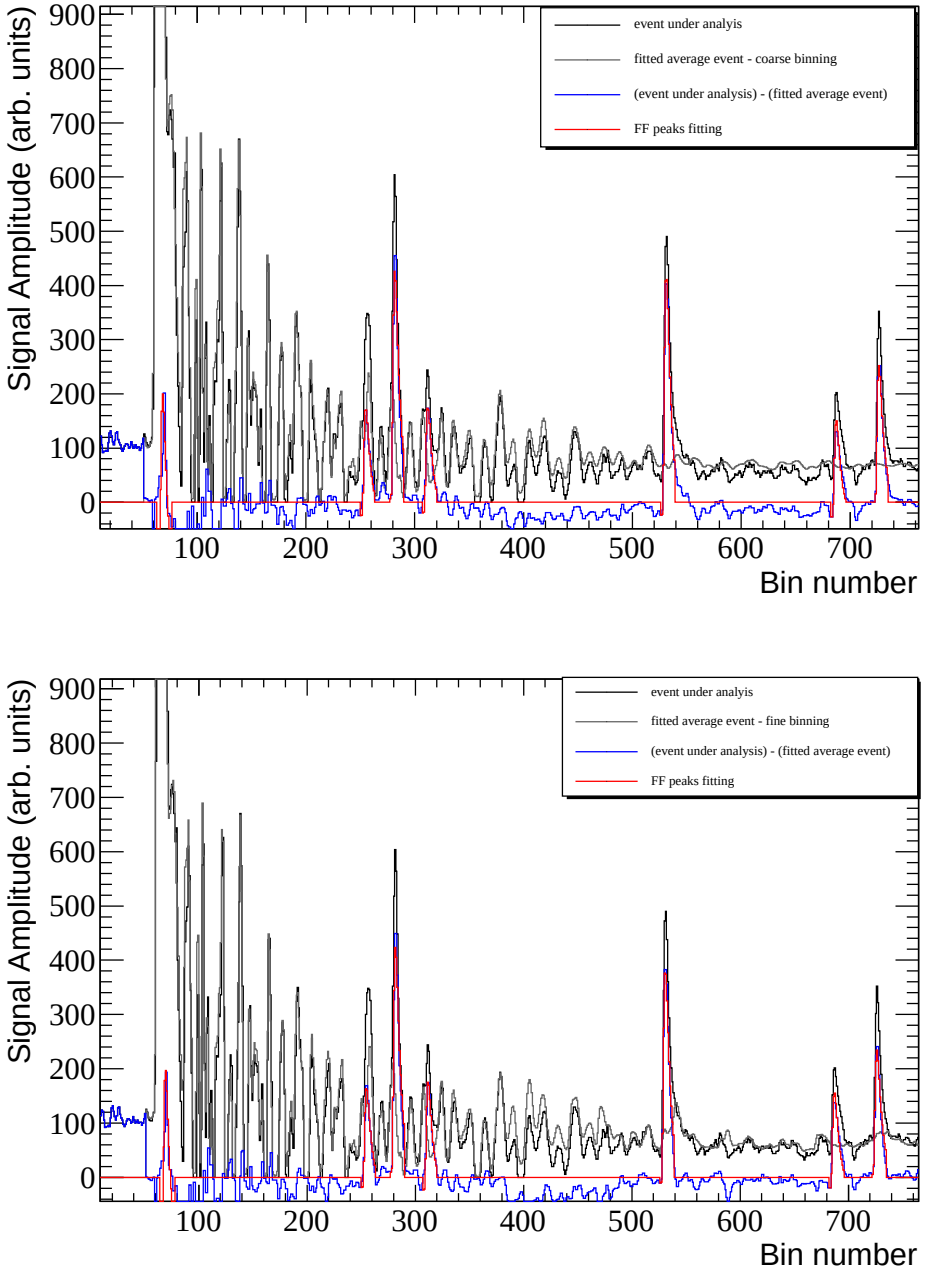

Figure 4.8: The reproduction of the baseline and FF fitting with a coarse binning of events (15 groups for EASTC pulses - 17 groups for TOF pulses) - upper figure, and a fine binning (66 groups for EASTC pulses - 61 groups for TOF pulses) - lower figure. The fitted "average event"from the fine binning overestimates more the baseline of the event under analysis.

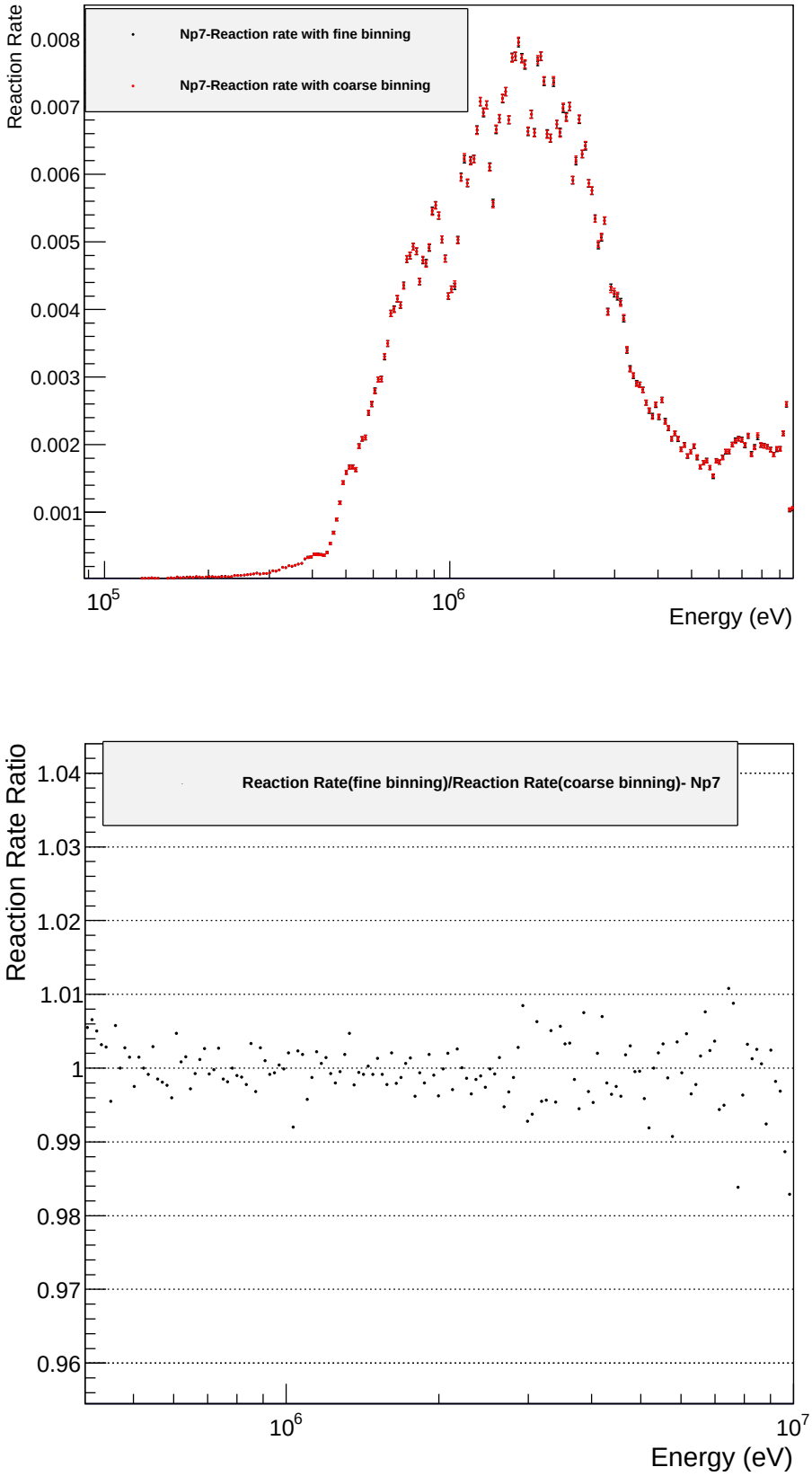

Figure 4.9: Upper figure: The comparison of the reaction rate obtained from the pulse shape analysis of the Np7 target events, with coarse binning (15 groups for EASTC pulses - 17 groups for TOF pulses) -red points, and fine binning (66 groups for EASTC pulses - 61 groups for TOF pulses)- black points. Lower figure: The ratio of the obtained reaction rates shown above: it is very close to 1, with deviations that do not exceed the statistical error of the reaction rates.

4.2.2 Sensitivity on the choice of threshold for the pulse shape analysis

As mentioned above, the code tries to find local maxima after a threshold is surpassed. The sensitivity of the results on the choice of this threshold was examined. For threshold levels below 50 the FF candidates with low amplitude severely increase as can be seen in fig. 4.10, where a comparison of the obtained amplitude distribution with threshold 20 and 50 from the analysis of the Np7 target data is shown. However, the majority of these low amplitude pulses cannot correspond neither to real FFs or alphas because the first peak is nearly the same for other targets tested with much lower alpha and FF activity (like U8a, U8b, U5c).

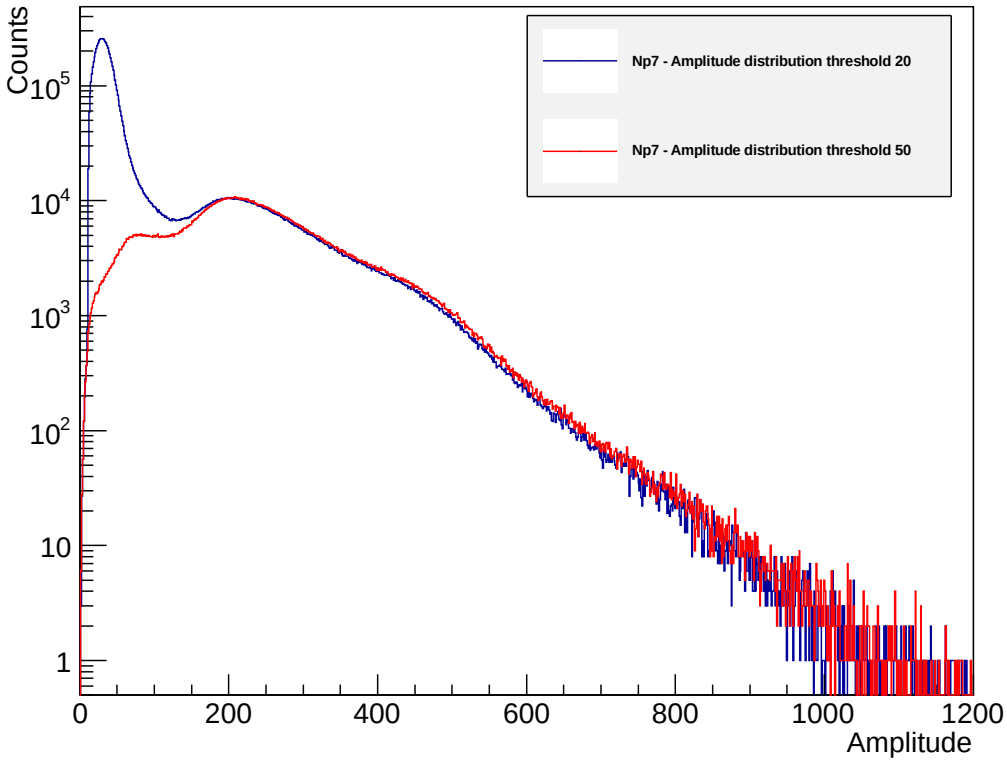

Figure 4.10: The amplitude distribution of FF candidates obtained for the Np7 target with threshold level 20 and 50 in the analysis, shown in logartithmic scale. It is clear that the low amplitude pulses are severely increased by decreasing the threshold level while the high amplitude pulses are even slightly decreased.

Furthermore, the resulting reaction rate does not correspond to the expected one, taking into account the neutron flux at n_TOF (fig. 3.2) and the cross section of the corresponding isotope as can be seen in fig. 4.11, for the Np7 target.

Consequently, threshold levels below 50 were not accepted for reliable analysis.

For threshold levels abobe 50 the pulse shape anaysis results do not severely change with the change of threshold level. The threshold levels of 50, 70 and 80 were tried for the targets U5c and U8b (low FF and alpha activity), Np7 (high FF and alpha activity) in order to find the most appropriate value. The resulting reaction rates can be found in fig. 4.12, 4.14 and 4.13. As a general remark the reaction rates obtained with threshold levels 70 and 80 are very similar, the second ones being slightly lower by no more than 1% in the neutron energy ranges of interest for each isotope. The analysis with threshold level 50 gives higher reaction rate values, with differences that become much larger at higher neutron energy regions where the oscillations of the raw data are severe (and even cause saturations as shown above) and it is more probable for a spike of low amplitude to remain from the subtraction of the fitted average event from the data. This effect is very pronounced in the U5c target analysis (fig. 4.12) where the statistics is low and small changes in the numbers are more easily revealed. If a threshold

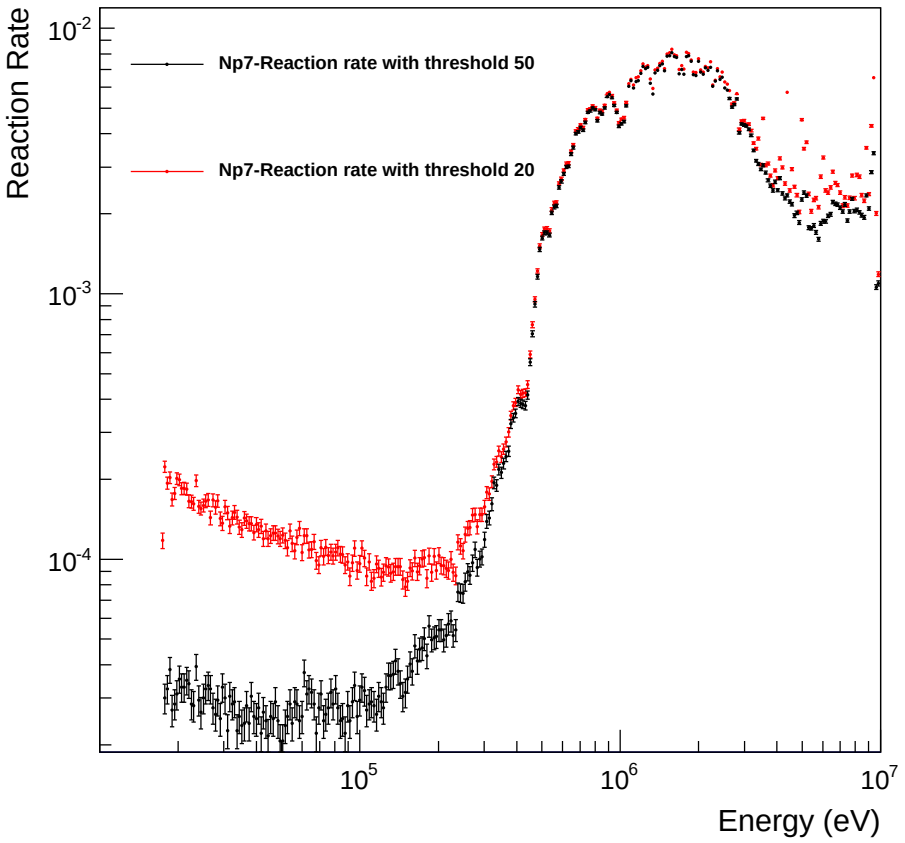

Figure 4.11: The comparison of the obtained reaction rates from the analysis of the Np7 target data, with different thresolds in the pulse shape analysis procedure. The threshold 20 gives unphysical results, meaning thet the code fits small peaks that do not correspond to FFs (probably alpha peaks).

level 50 is chosen many ``peaks'' are considered as FF candidates, which is not the case taking into account the cross section of this isotope and the flux of the n_TOF facility, which decreases rapidly above 2 MeV.

It has to be noted that the change in amplitude is not the only way to check whether the accepted FF candidates fulfil the required criteria. The code does not fit every random spike that is left from not very successful subtractions, but only peaks with a specific shape. If a strange spike with a shape similar to the required one is finally fitted, it will give large fitting parameter errors. As an example, in fig. 4.15, the error of the pt0 fitting parameter is shown for the threshold levels 20, 50, 70 and 80. It is evident that for threshold levels lower than 50 the code starts to fit many peaks with strange shapes (which are of low amplitude - see also fig. 4.10) and this is why the error severely increases. However, if the upper limit of the accepted pt0 error is put at 0.01 then the resulting number of accepted FF peaks is nearly the same, despite the large difference in the threshold levels. So with good control of the fitting parameters and their errors, one can be confident that the pulse shape analysis routine gives reliable results.

From the considerations mentioned above and by checking the raw data, a threshold 70 was chosen for the analysis, for all the targets analyzed. As far as the cross section calculation is concerned, if the same threshold is applied to the target of interest as well as to the corresponding reference target, the systematic uncertainty induced by the choice of the threshold turns out to be negligible.

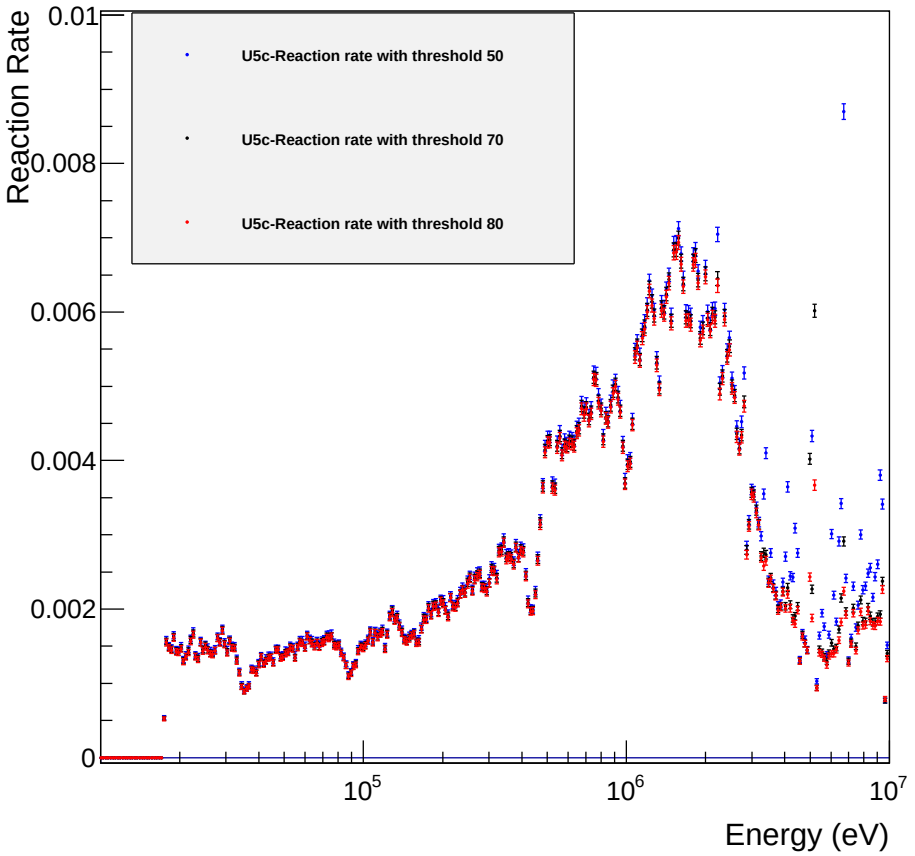

Figure 4.12: The comparison of the reaction rates obtained from the pulse shape analysis with threshold levels 50, 70 and 80 for the U5c target. It is clear that above 2 MeV the pulse shape analysis does not give correct results if threshold 50 is chosen.

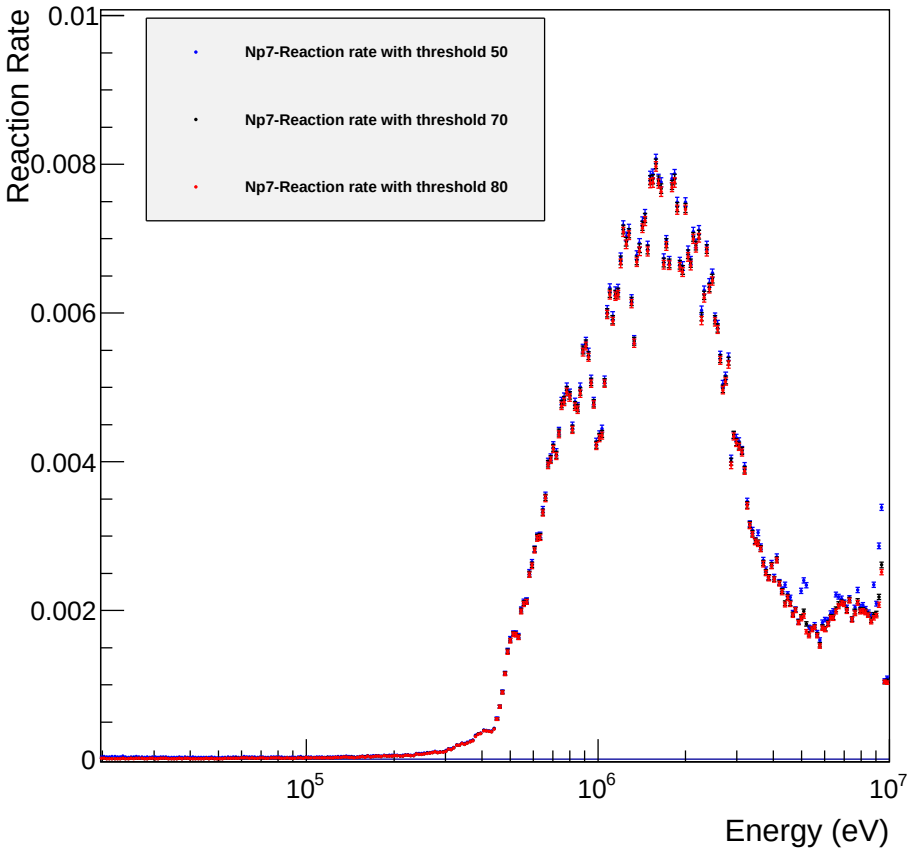

Figure 4.13: The comparison of the reaction rates obtained from the pulse shape analysis with threshold levels 50, 70 and 80 for the Np7 target. The differences between the analysis results with threshold 70 and 80 are small and do not exceed 1%, within the statistical uncertainties. The differences between the analysis results with thresholds 50 and 70 increase with energy and reach 3.5% at $\sim$ 9 MeV.

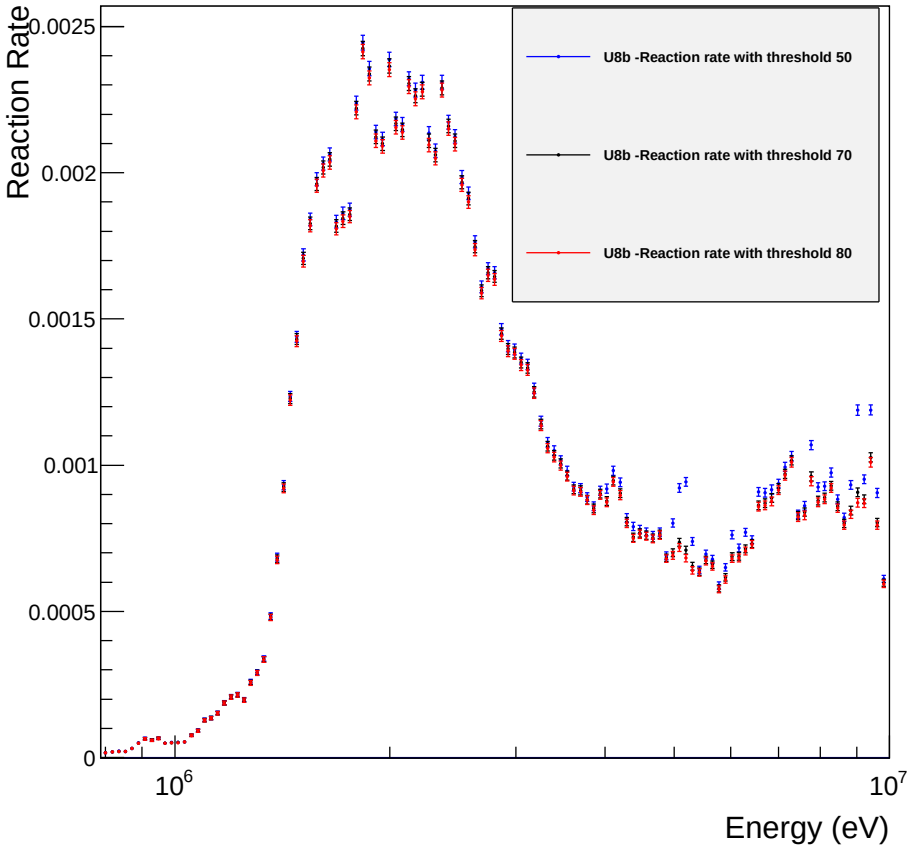

Figure 4.14: The comparison of the reaction rates obtained from the pulse shape analysis with threshold levels 50, 70 and 80 for the U8b target. The differences are small but increase with energy and are less than 2% at $\sim$ 9 MeV (comparing threshold levels 70 and 80).

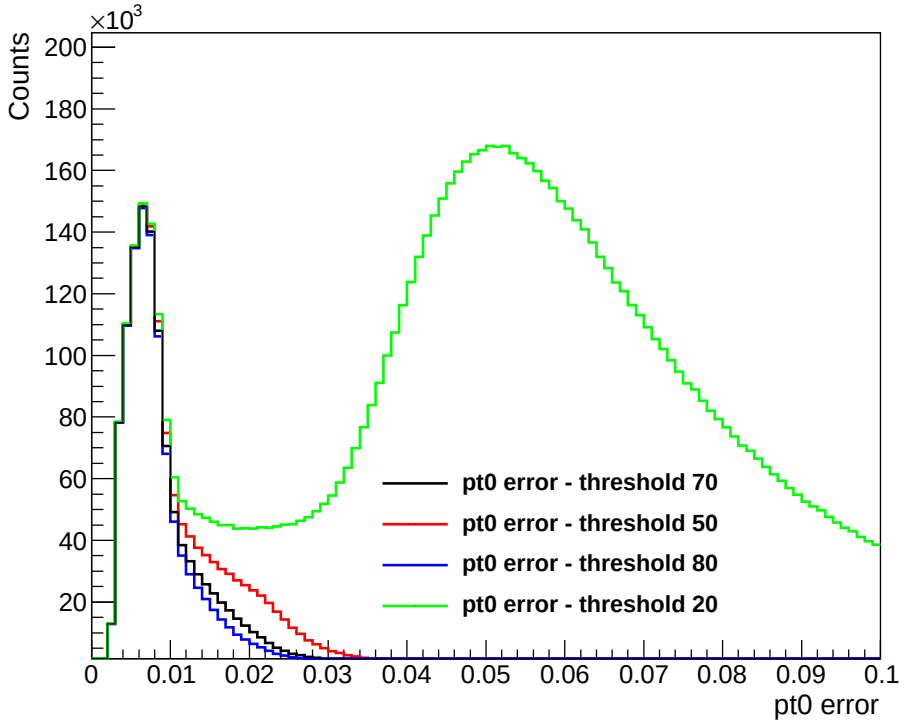

Figure 4.15: The histogram of the pt0 error values occured from the pulse shape analysis of the Np7 data with different thresholds. It is clear that the error is severely increased with a threshold level choice of 20.

4.2.3 Sensitivity on the choice of background for the pulse shape analysis

The choice of the background level determines the point at which the code quits looking for another local maximum and fits the peak(s) found. So it is an important parameter of the pulse shape analysis, especially in the case of non-isolated peaks, as in fig. 4.16, where a fitted quadruple peak in an event of the Np7 target is shown. The background level choice in this case determines the number of peaks that the code fits simultaneously, and thus the success or not of the fitting. A study of the sensitivity of the analysis results on this parameter was thus considered essential, especially for high activity targets as Np7 and U5.

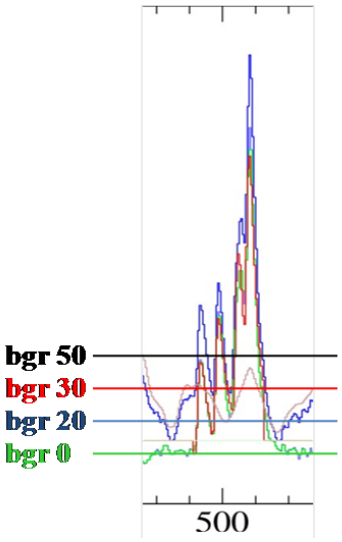

Figure 4.16: Schematic show of the choice of the background level at the fitting of a quadruple peak (event from the Np7 target). Depending on the choice of the background level the code will fit the peaks one by one, or the first two separately and the next two as a doublet etc. This affects the number of successfully fitted peaks with eq. 4.2.

Various background level values were tried. The amplitude distribution of the FF peaks obtained from the pulse shape analysis of the Np7 target for the background levels of 0, 20, 30 and 50 can be found in fig. 4.17. Similar amplitude distributions were obtained for the other six targets analyzed. The differences are mainly found in the low amplitude accepted FF peaks. By checking on an event-by-event basis, it was concluded that the background level of 30 was the most appropriate for the analysis of the targets.

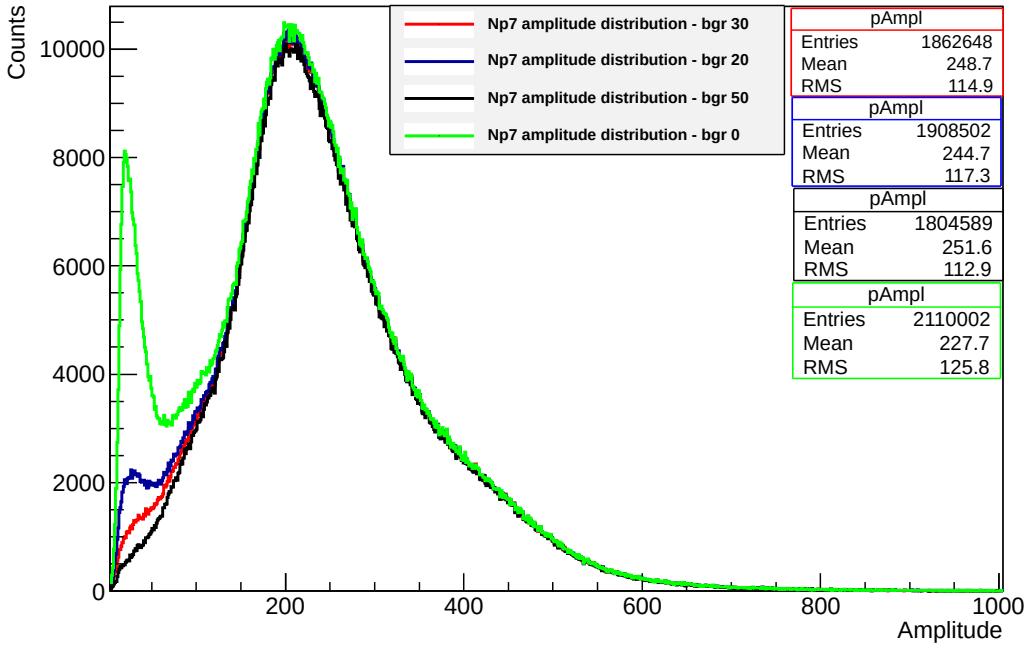

Figure 4.17: The histograms of the FF peak candidate amplitude distributions obtained with different background level choice, from the pulse shape analysis of the Np7 target data.

During the acquisition of the data under analysis, no beam-off or empty target spectra were taken. Consequently, in order to estimate an additional threshold for the exclusion of the residual low amplitude peaks, the amplitude distribution histograms obtained from the analysis of all the targets with background level 0 were used. The threshold was chosen to be at the minimum between the low amplitude peak and the main peak of the FFs (with centroid at ~ 200) - green line in fig. 4.17. The differences in the integrals of the amplitude distribution histograms above the threshold chosen between the analysis with background level 0, 20 and 50 with the analysis with background level 30 do not exceed 5-6% in the worst case (background level 0).

4.3 The selection of the events/FF fitting parameters

After the pulse shape analysis is performed for each target data, the selection of the accepted γ-flash fitting parameters (fA, fY0, ft0, fAmpl - eq. 4.2, 4.4), "average event"fitting parameters (aA, aY0 - eq. 4.1) and FF peak fitting parameters (pA, pY0, pt0, pAmpl - eq. 4.2, 4.4) and their corresponding errors is made with the code *rootres*. The selection of the accepted parameters is made by choosing the lower and upper limit for the parameters and the corresponding errors. A separate selection has been made for each target, by checking the raw data. Some typical histograms of accepted parameters are shown below.

The fY0 accepted values form a gaussian histogram around the value 100, for all the targets analyzed apart from the U5b, for which fY0 values form a gaussian around the value 650, see fig. 4.18. The fY0 errors from the pulse shape analysis did not surpass 0.001 in the worst cases (U5c and U8c).

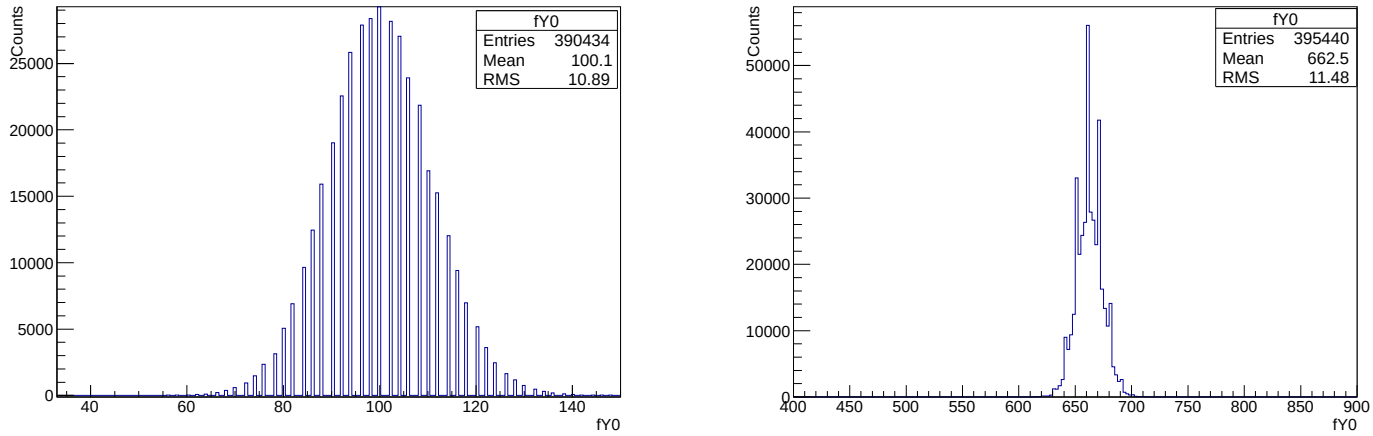

Figure 4.18: Histogram of the accepted fY0 values for the Np7 target (similar for U5, U8a, U8b, U5c, U8c) (left) and the U5b target (right)which was connected to a channel with a much higher gain.

This channel seems to have a much higher gain and for this reason it is the only channel where the raw data do not present saturations at the lower limit of the FADC, as can be seen in fig. 4.19.

The ft0 corresponds to the starting bin of the fitted γ-flash peak and, as expected, the corresponding histogram is separated into two main groups: the EASTC events (starting bin $\sim$ 40) and the TOF events (starting bin $\sim$ 60), see fig. 4.20.

As far as the parameters from the "average event"fitting are concerned, it is desired to have the parameter aA very close to 1 and the parameter aY0 close to 0 (eq. 4.1), which means that a small change was needed in the selected "average event"in order to reproduce the baseline of the event under analysis. Some indicative histograms of the aA parameter are shown in fig. 4.21. The histograms have a gaussian shape with centroid 1 and nearly all the values are within $\pm$10% for the Np7 and U8c target (which is also the case for U5b, U5c, U8a and U8b), with the width of the U8c histogram being slightly smaller. However, the situation is somewhat different for the U5 target: the centroid of the gaussian is slightly shifted to 0.99 and the values are within $\pm$20% from the centroid. The corresponding errors (fig. 4.21) are very small for all the targets and follow the same trend, the biggest errors being the ones from the U5 analysis and the smallest from the U8c analysis.

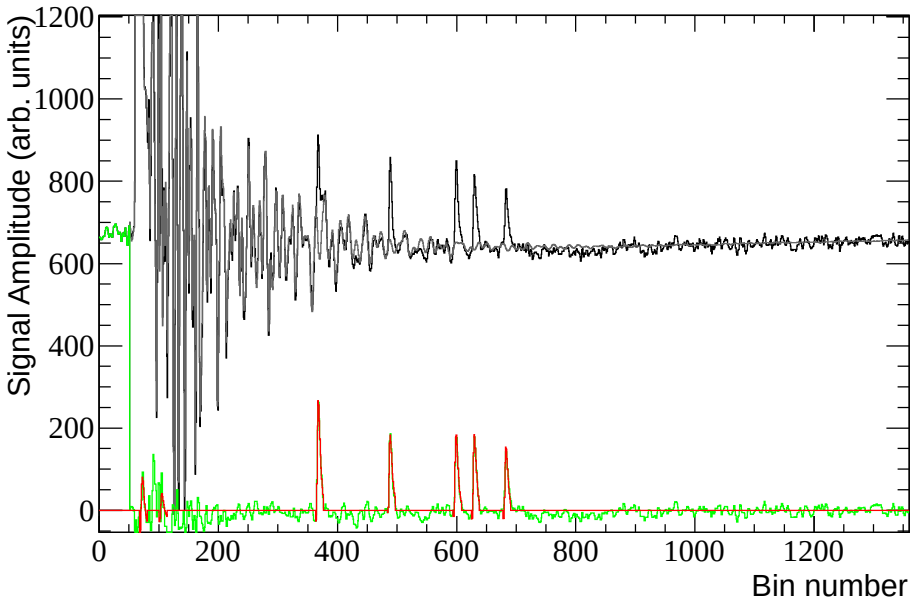

Figure 4.19: Pulse shape analysis example for raw data from the U5b target which was connected to a channel with a much higher gain. The baseline of the event is at an amplitude value of ∼650. No saturations were observed for the raw data of this target in the region above bin 160.

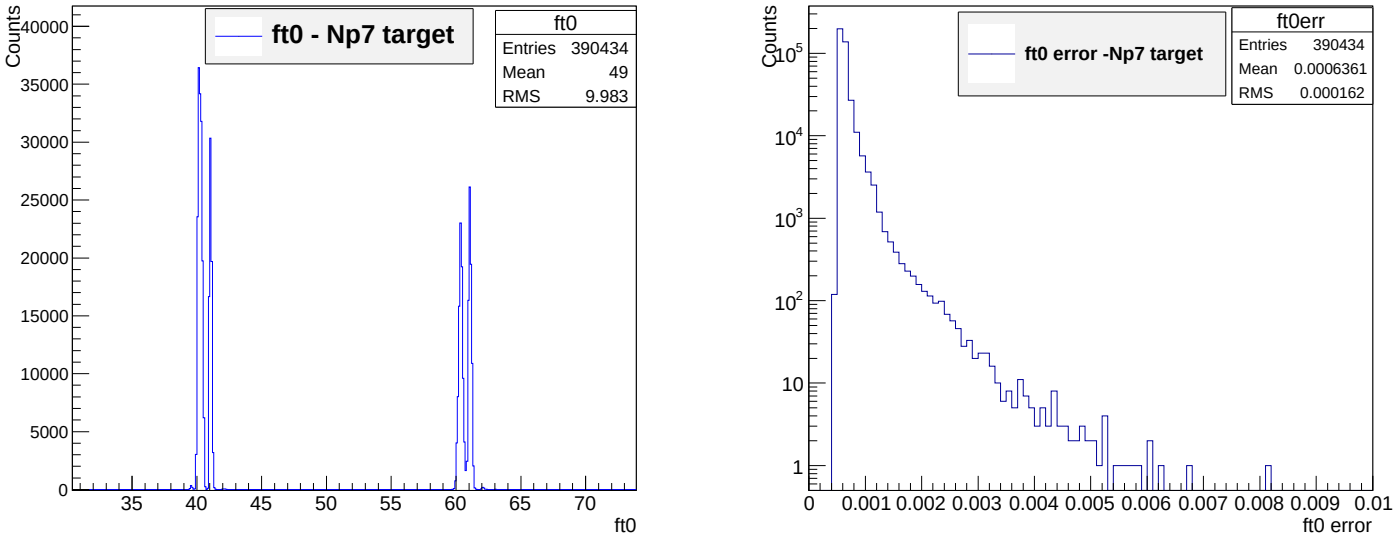

Figure 4.20: The histogram of the accepted ft0 values obtained from the γ-flash fitting of the Np7 target events (left) and the histogram of the corresponding errors (right).

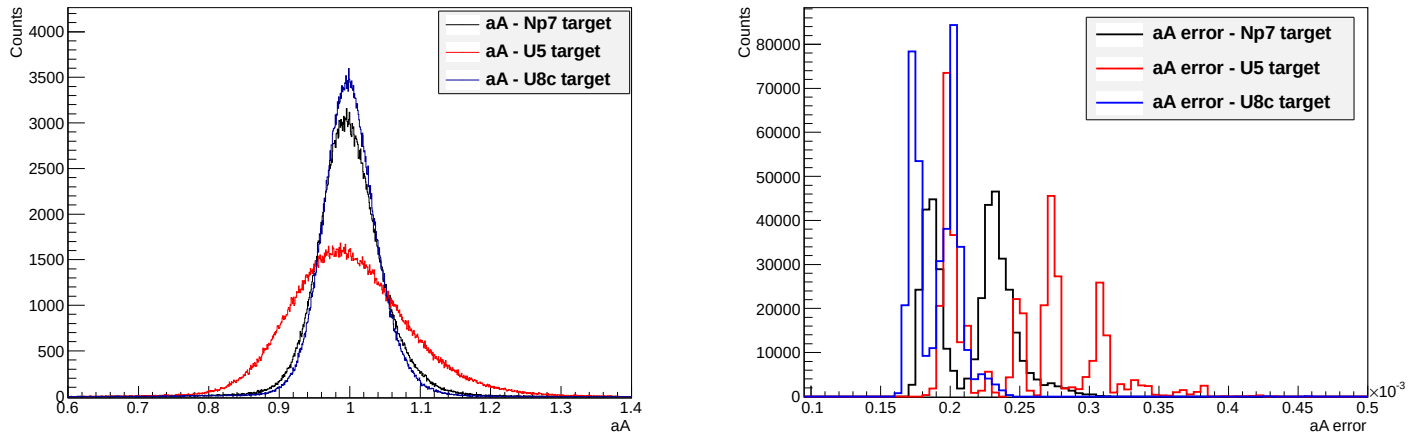

Figure 4.21: The histogram of the accepted aA values obtained from the "average event"fitting from the analysis of the Np7, U5 and U8c target events (left) and the histogram of the corresponding errors (right).

The same situation is reflected in the aY0 histograms (fig. 4.22), where the same targets are shown for comparison.

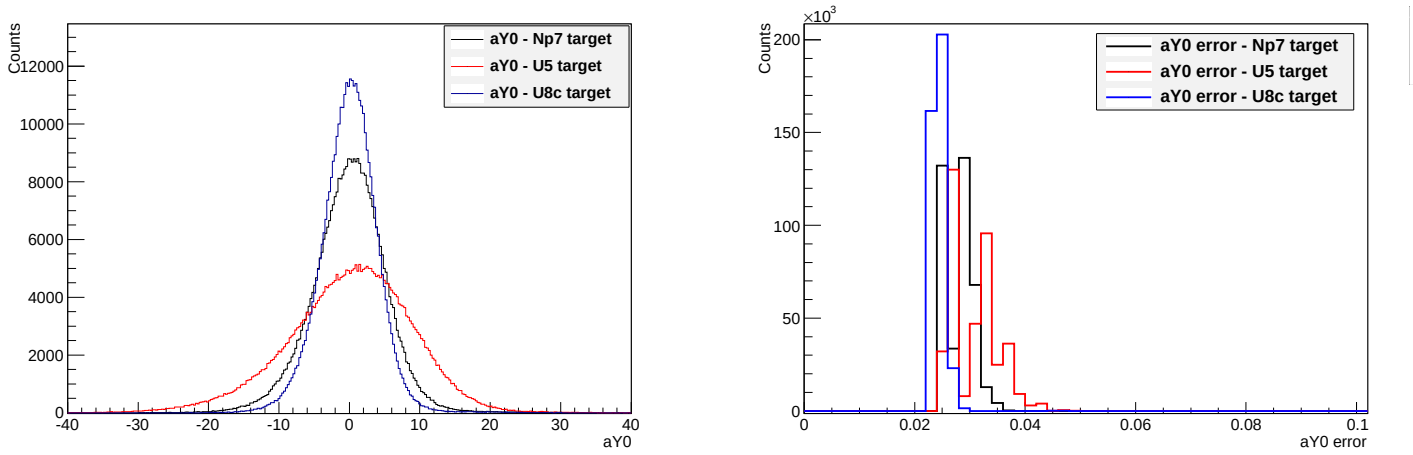

Figure 4.22: The histogram of the accepted aY0 values obtained from the "average event"fitting from the analysis of the Np7, U5 and U8c target events (left) and the histogram of the corresponding errors (right).

From the above indicative comparisons between the "average event"fitting parameters, it can be seen that the higher the FF activity of the target the more difficult it gets to reproduce the baseline of the events. By checking the raw data this effect can be seen also in some of the Np7 events, but it is more intense in U5 events and it can cause the failure of fitting of FF peak candidates and consequently loss of FF peaks. It can be seen in fig. 4.23 that the fitted average event overestimates the baseline of the movie, especially in the bin region 300-700, i.e. for the neutron energy range ∼600 keV - 4 MeV and this is due to the high FF activity of the target in this energy region which prevents the complete smearing out of the FF peaks at the average event. For higher neutron energies however (i.e. down to bin 300), the baseline oscillations are well reproduced because the FF activity drops rapidly as a result of the neutron flux decrease (see fig. 3.2).

Various efforts were made in order to improve the situation, by limiting the accepted aA and aY0 fitting parameters, the bin range of the fitting for the reproduction of the baseline (instead of the whole movie only the first part of the sequence where the problem exists), by changing the initial values of the parameters etc., however no great improvement was made. As a result, some underestimation of the real number of FF peaks is expected from the analysis of this target and it will be discussed in section 4.5.

The histogram of the accepted pY0 values from the analysis of the Np7 target can be found in fig. 4.24 (similar histograms are obtained for the rest of the targets). From this histogram, it can be seen that the majority of the accepted FF peaks are lying on zero background, meaning that the baseline is properly subtracted, many FF peaks however are lying on negative and a few on positive backgrounds meaning that in many cases the fitted average event overestimated the baseline of the movie under analysis (negative pY0) or underestimated it (positive pY0), especially in the early phase of the movies. However, these FF peaks were considered accepted, after checking such cases in the raw data as well as the corresponding fitting parameter errors.

The amplitude distribution of the FF peaks occured with the above described analysis for all the targets are shown in fig. 4.25 and 4.26. In the same figure the amplitude distribution with and without the threshold chosen for cutting away the residual low amplitude FF candidates is shown for comparison. As already discussed in 4.2.3 the threshold was chosen to be the minimum between the low amplitude peak and the main FF peak, from the amplitude distributions obtained from the pulse shape analysis with background 0.

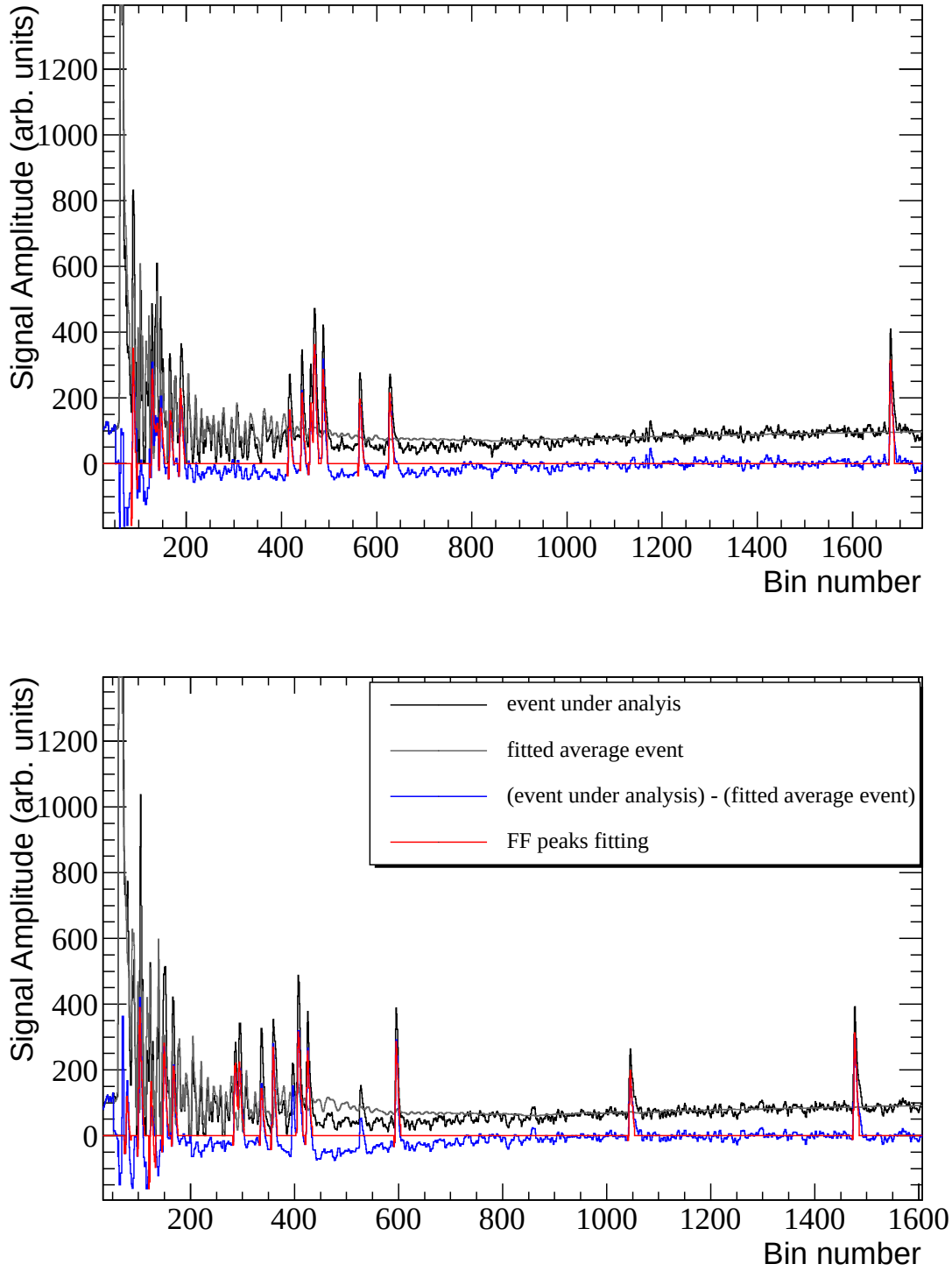

Figure 4.23: Indicative analysis of events obtained from the U5 target where it can be seen that in the bin region 300-700 the fitted average event overestimates the raw data. This effect causes loss of fission fragment peaks in some occasions (lower figure).

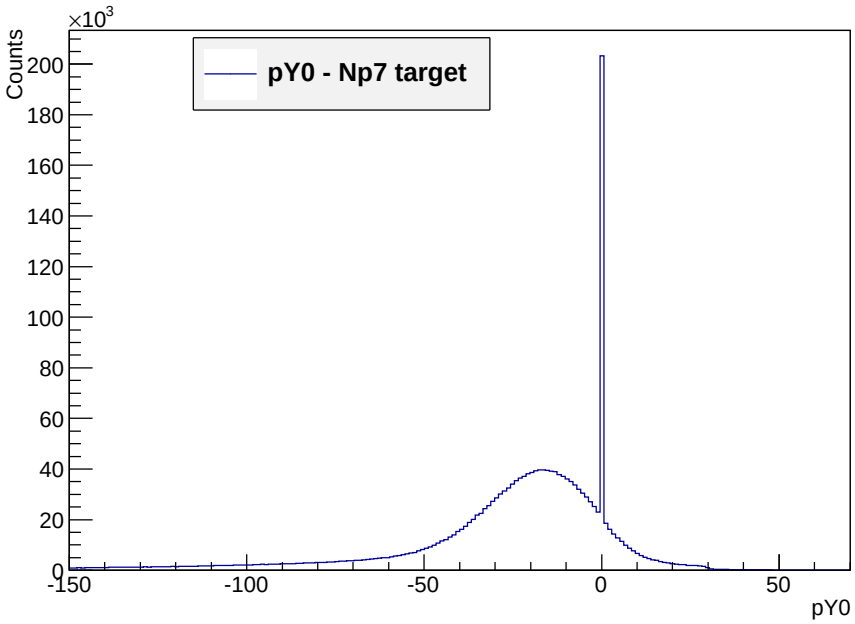

Figure 4.24: The histogram of the pY0 parameter values obtained from the analysis of the raw data of the Np7 target. As expected, most of the peaks have pY0=0, which means that the background has been properly subtracted.

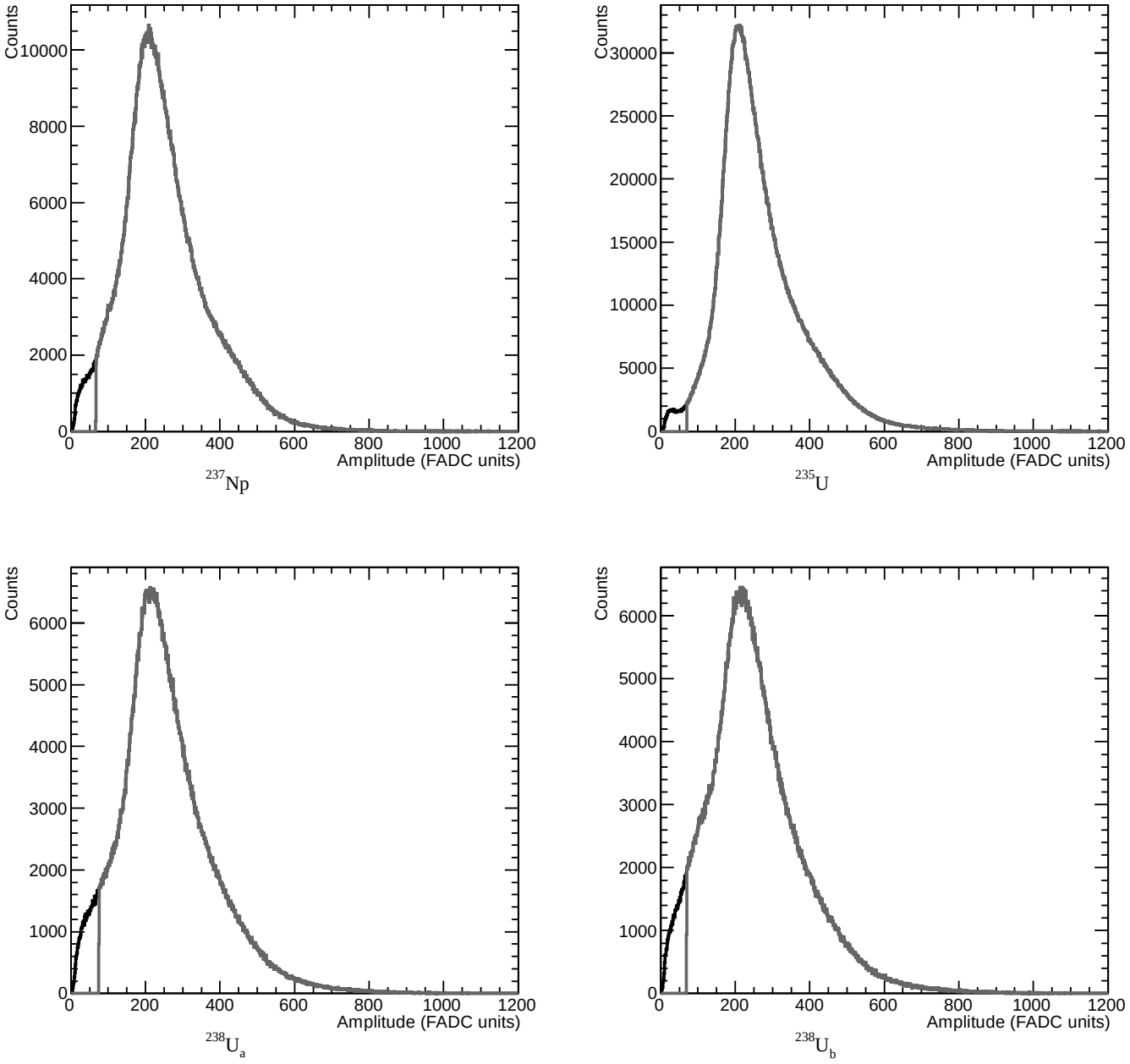

Figure 4.25: The obtained amplitude distribution from the pulse shape analysis of the 8 cm diameter targets (Np7, U5, U8a and U8b). The black curve corresponds to the analysis without additional threshold for the exclusion of low amplitude pulses, and the grey line to the amplitude distribution with the threshold chosen for each target.

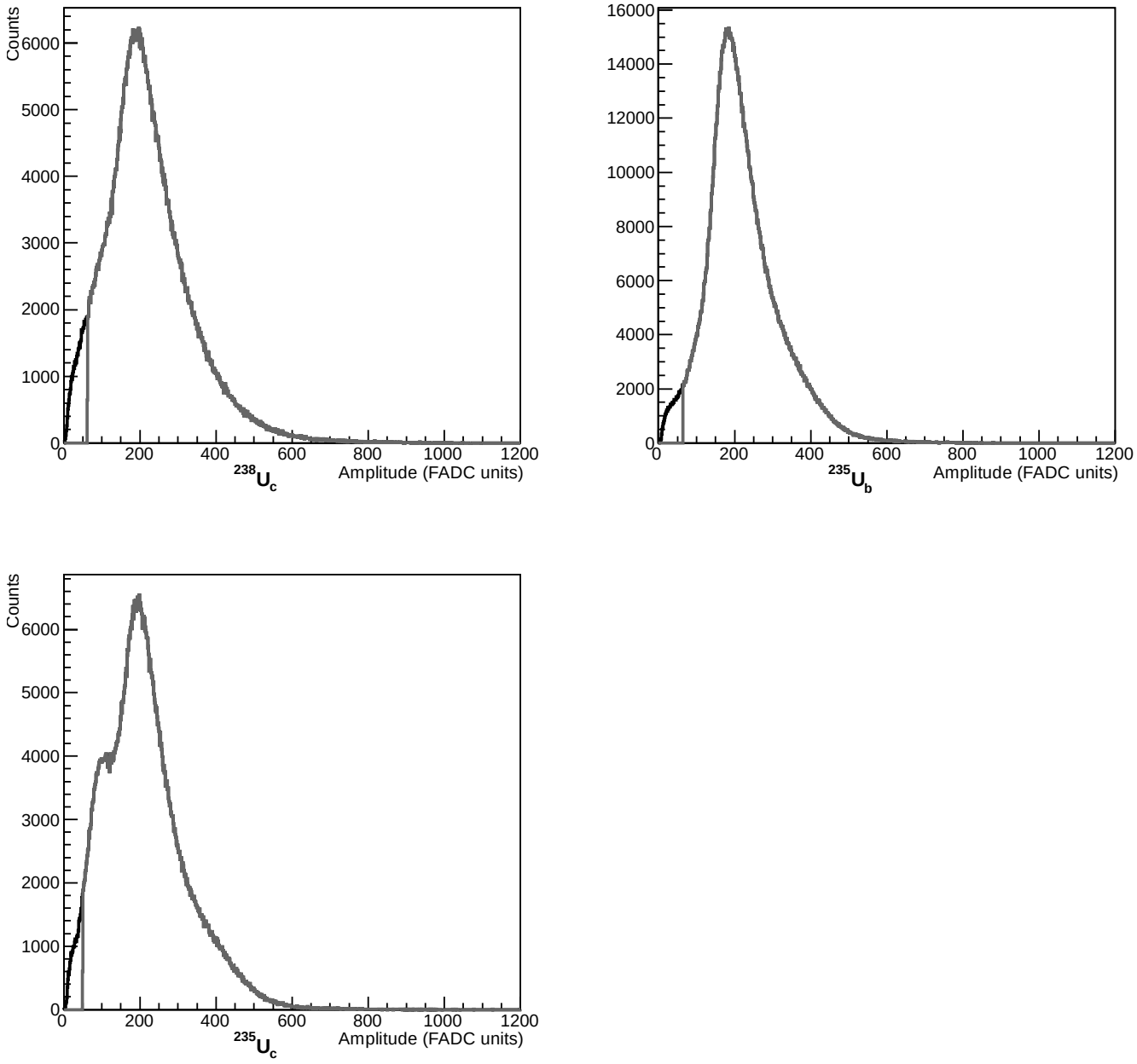

Figure 4.26: The obtained amplitude distribution from the pulse shape analysis of the 5 cm diameter targets (U5, U8a and U8b). The black curve corresponds to the analysis without additional threshold for the exclusion of low amplitude pulses, and the grey line to the amplitude distribution with the threshold chosen for each target.

4.4 Corrections in the cross section calculation

A correction that needs to be applied in the cross section calculation is related to the detection efficiency. As already mentioned in the description of the FIC assembly, the solid angle coverage of the detector is very close to 2π. However, the number of FFs that exits the sample and the histogram of the energy deposition of the FFs in the detector gas is dependent on the sample thickness, so differences in the detection efficiency exist for the different isotopes. Thus, two correction factors need to be estimated: 1) an efficiency correction factor due to the self absorption of the FFs in the samples and 2) a correction factor for the percentage of the FF counts below the threshold chosen during the analysis (see 4.3) which depends on the energy loss of the FFs while exiting the sample.

These correction factors were estimated with Monte Carlo simulations performed with the code FLUKA [62]. In the latest versions of FLUKA (i.e. since version fluka2011.2) the stopping power models have been thoroughly reworked, and are more precise particularly for heavy ions: the Barkas (Z^3), Bloch (Z^4), and Mott corrections have been implemented, and nuclear stopping power is calculated and taken into account.

4.4.1 Description of the simulations

A schematics of the simple geometry implemented in the simulations can be found in fig. 4.27.

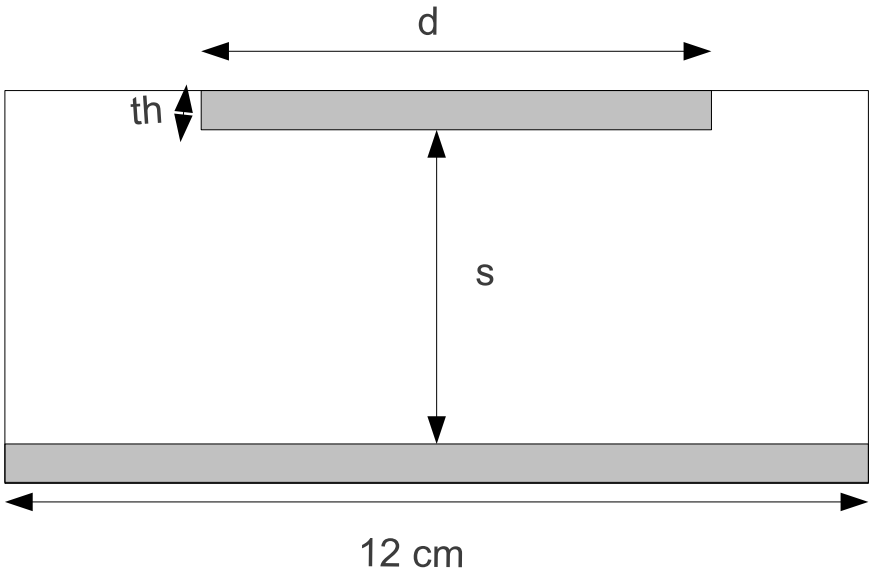

Figure 4.27: Schematics of the geometry implemented in the simulations of the energy deposition of FFs in the gas of the FIC: d is the diameter of the sample (5 or 8 cm), s the thickness of the active volume of the gas (2 cm for FIC0) and th the thickness of the sample. The diameter of the outer electrode of each FIC cell is 12 cm.

The gas was assumed to be Ar(90%)-CF_4(10%) at 720 mbar ($\rho = 1.3 \cdot 10^{-3}$ g/cm^3). The thickness (th) of the samples is known from RBS measurements only for the Np7, U5c and U8c targets, as described in chap. 2. For the rest of the reference targets (U8a, U8b, U5, U5b) only the nominal mass values were reported (table 3.3). For these targets, the thickness was estimated with a multiplication factor on the thickness of the measured targets (either of U5c or U8c, depending on the isotope of the target of interest) that depends on the diameters and the masses of the targets of the measured and the unknown thickness. For this calculation of course, homogeneity is assumed, which was found to be true, as already mentioned in chapter 2. The thicknesses of the targets of

the FIC assembly can be found in the table 4.1. The targets were assumed to be oxides in the most commonly found form (NpO_2, U_3O_8).

Target name	Thickness (μm)
Np7	0.1 ^{meas}
U5	0.53
U8a	0.31
U8b	0.31
U8c	0.62 ^{meas}
U5b	0.45
U5c	0.35 ^{meas}

Table 4.1: Summary of the thicknesses of the samples of the FIC0 detector used in the present work. The thickness values with the superscript ``meas'' are experimentally determined with the RBS technique as described in chap. 2.

The generation of the FFs was performed with an external routine writen in gFortran [63] which provided FLUKA with an ASCII file (with use of the card SOURCE) containing the atomic number Z, the mass number A and the position of the FFs generated, as well as the corresponding direction vector and energy. The mass and charge distributions of the FFs for each isotope, as well as the total kinetic enegy provided to both FFs (heavy and light) after the fission reaction were determined with use of the Adeev's systematics [64], and from [65], a thorough study of the fission mechanism and FF creation for ^{237}Np in the MeV neutron energy range. A heavy fission fragment was selected from a gaussian distribution with mean value μ≈140 and standard deviation σ6.5, while the mass number of the light fragment was calculated by assuming the emission of 1-3 neutrons and an average total kinetic enery of ≈174 MeV was distributed to the fission fragments inversely proportionally to their mass. The atomic number Z of the FFs was sampled from ± 5 around the mean value given in [64]. The mass number and energy distributions of the FFs produced are shown in fig. 4.28.

The total kinetic energy as a function of the heavy FF mass number (i.e. the mass split) for both the FFs and for each one separately can be found in fig. 4.29.

The emission points of the FFs produced by this routine were homogeneously distributed in the volume of the target. Equal numbers of heavy and light FFs ($5 \cdot 10^5$ from each group) were generated and emitted isotropically in an angle of 2π. The energy deposition of the FFs in the detector gas was subsequently scored.

Indicative results for Np (the thinnest target) and U8c (the thickest target) can be found in figs. 4.30 and 4.31.

The thickness of the gap is not adequate to stop the light FFs in the forward direction, while it can nearly stop the heavy FFs as confirmed by SRIM calculations (see appendix A). This is why in figs. 4.30 and 4.31, the light FF histograms present a tail on the left side, while the heavy FF histograms are nearly gaussian. The broadening of the peaks can be attributed to the energy straggling during the interaction of the various ions of different energies in the target and the gas of the detector, and, as expected, is larger in the U8c target histogram. The larger mean energy loss in the U8c target shifts the centroids of the FF peaks to lower energies compared to the peaks of the Np7 histograms, and increases the continuum on the left side of the histogram. Thus, it is clear that even if the same threshold is applied in the analysis of the two targets, a different correction factor due to lost subthreshold FF counts has to be estimated.

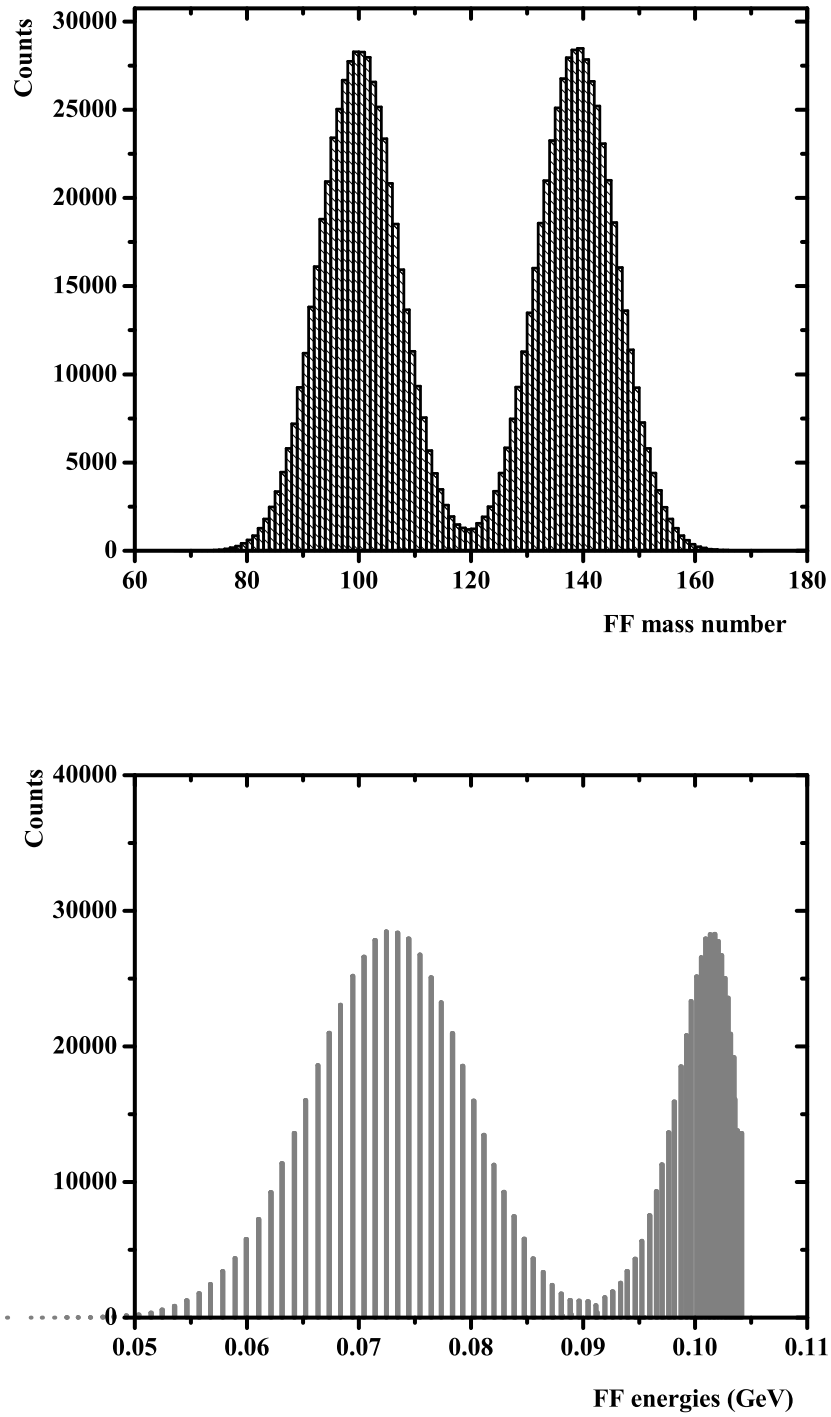

Figure 4.28: Mass and energy distributions of the FFs produced with the routine bazed on systematics [64]. FFs with these characteristics were randomly distributed in the volume of the target for the FLUKA simulations.

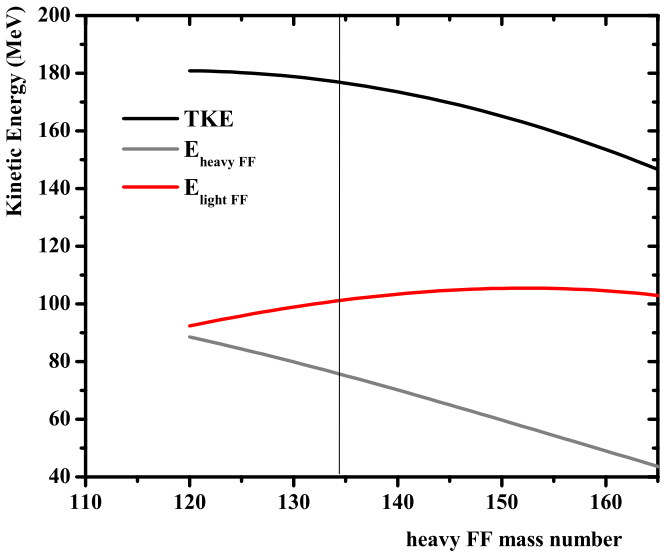

Figure 4.29: The TKE(A) (total kinetic energy as a function of the heavy FF mass number) which is splitted to the FFs inversely proportionally to their mass ($E_{heavyFF}$ and $E_{lightFF}$). The calculations are performed with use of the Adeev systematics. The results are in agreement with the ones found in [65] for ^{237}Np , apart from heavy FF mass numbers lower than 135.

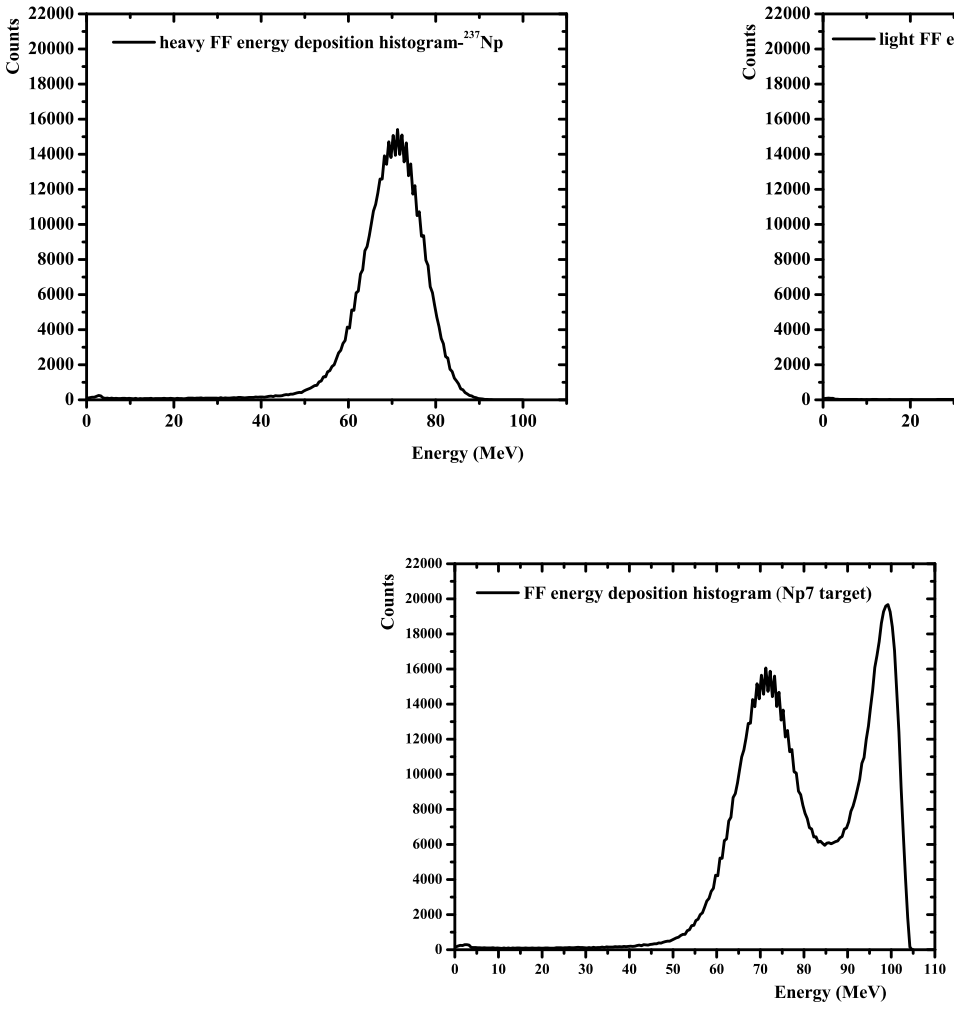

Figure 4.30: The simulated energy deposition histograms obtained for the Np7 target (0.1μm thickness), with a binning of 0.5 MeV. The light and heavy FF histograms are also presented separately in the upper figures.

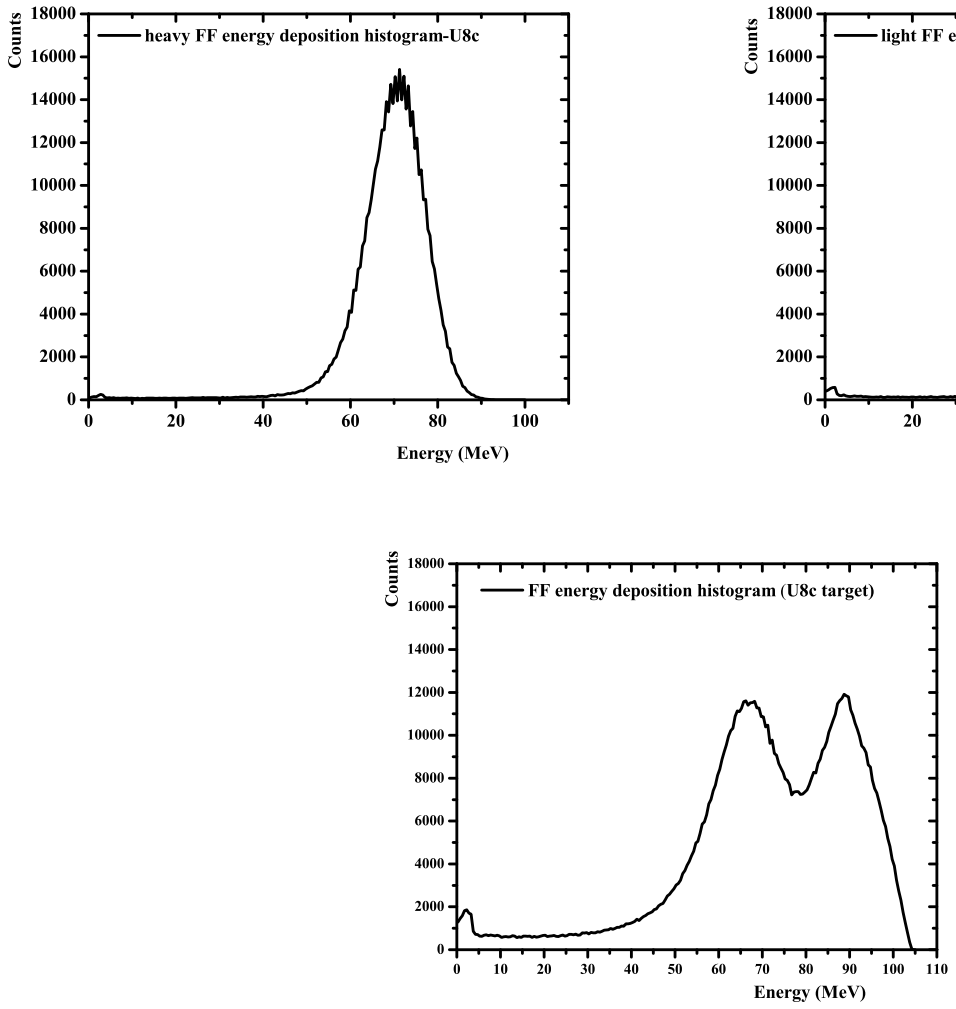

Figure 4.31: The simulated energy deposition histograms obtained for the U8c target (0.6 μm thickness), with a binning of 0.5 MeV. The light and heavy FF histograms are also presented separately in the upper figures.

Target name	efficiency correction factor (%)	uncertainty (statistical) (%)
Np7	99.3	0.1
U5	97.0	0.1
U8a	98.2	0.1
U8b	98.2	0.1
U8c	96.5	0.1
U5b	97.5	0.1
U5c	98.0	0.1

Table 4.2: The efficiency correction factors due to the self absorption of the targets, obtained from the FLUKA simulations.

4.4.2 Estimation of the cross section correction factors from the FLUKA simulations

1) The efficiency correction factor due to the self absorption of the FFs in the samples was also estimated from the FLUKA simulations, by the ratio of the FFs depositing energy in the gas to the total number of FFs generated. The results for all the targets are presented in table 4.2. The loss of FFs in the targets does not exceed 3.5% in the worst case (U8c). Thanks to the high statistics of the simulations, the statistical uncertainty of these values is less than 0.15% for each FF group (light and heavy FFs) and $\sim 0.1\%$ for the sum. A validation of the geometry implemented in the simulations could not be performed, in the absence of beam-off spectra, so the systematic uncertainty of these calculations was estimated about 2-3%, based on the comparison between the simulated and experimental alpha efficiencies at the MicroMegas detector experiment, with similar geometry, as explained in sec. 5.4.

2) In order to estimate the percentage of the FF counts below the threshold chosen during the analysis, based on the simulated energy deposition histograms, the most important parameter is the calibration of the experimental amplitude distributions (fig. 4.25, 4.26). When the calibration is known then the energy corresponding to the bin of the threshold chosen in the analysis can be calculated and then the ratio of the subthreshold FF counts to the total number of FFs depositing energy in the gas is estimated from the simulated histograms (fig. 4.30, 4.31). The major difficulty in the present case is that the amplitude distribution does not present discrete heavy and light FF peaks as predicted by the simulated histograms due to the non-proportionality of the detector and the electronic chain which is based on timing outputs and Flash ADCs, so the channel-to-energy correlation is not easily extracted. An effort has been made to fit the experimental amplitude distributions with two gaussian peaks with the same integral (because a nearly equal number of heavy and light FFs is expected). Furthermore, the second peak (light FF peak) was chosen to be skewed, with a tail on the left side of the peak, going down to lower amplitudes, as predicted by the simulations (figs. 4.30, 4.31). Two spectra analysis programs were used for this fitting, SPECTRW [66] and TV [67], in order to check the sensitivity and estimate the systematic uncertainty of the subthreshold counts correction factor. An example of this analysis for the Np7 target can be found in fig. 4.32.

The reproduction of the experimental amplitude distribution with the two gaussians of equal integrals is quite satisfactory. Assuming a linear relation between the centroid channels of the two gaussians and the centroid energies expected from the simulations, the calibration of the experimental amplitude distributions was performed. From the obtained bin-to-energy relation, the energy corresponding to the threshold bin for each target was obtained and consequently the ratio of the subthreshold FF counts to the total number of FFs scored in the gas. This factor, namely S_{target}, was used as a correction factor in the number of FFs obtained from the pulse shape analysis.

As an additional validation of this procedure an effort has been made to reproduce the experimental amplitude distribution by applying a gaussian response function for the spreading of each bin from the FLUKA simulation histograms. The standard deviation of the response function was assumed to be linearly increasing with the bin

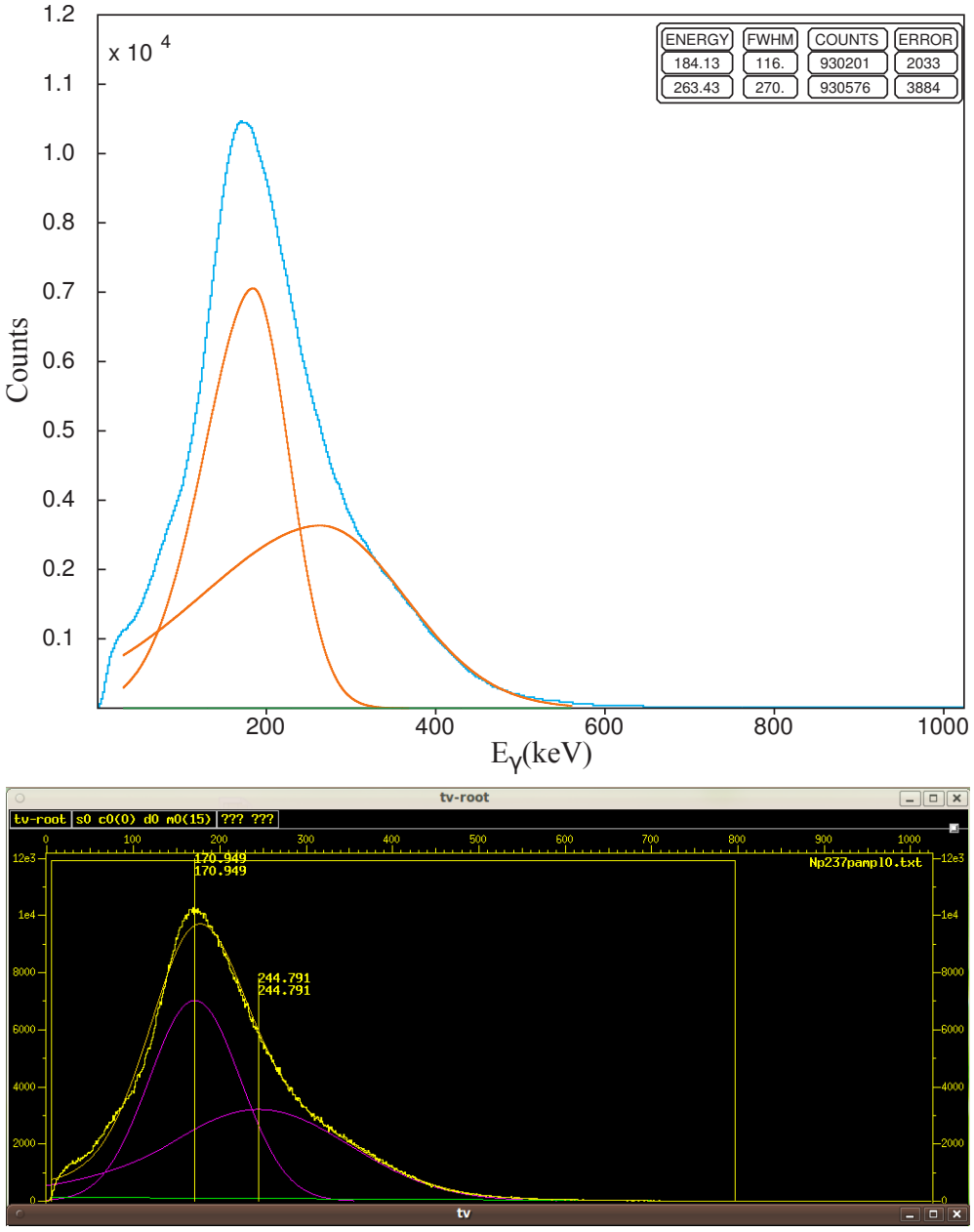

Figure 4.32: An example of the fitting of the Np7 amplitude distribution with two gaussians of equal integral and the second one skewed with the programs SPECTRW (up) and TV (down).

number, with a relation obtained from the subtraction of the simulated FWHM from the experimental one (the FWHM of the two gaussians shown in fig.4.32). The result for the Np7 target can be found in fig. 4.33. The reproduction of the experimental amplitude distribution is satisfactory, taking into account that it was based on the assumption of linear relations for the calibration and the standard deviation of the response function, which is a first order approximation for a detector that is not working in a proportional mode.

The correction factors for the subthreshold FF counts, S_{target}, obtained with the above described procedure can be found in table 4.3. The uncertainties reported in this table are the statistical which are very small due to the high statistics used in the simulations and the systematic uncertainties obtained from the different analyses with the two programs, which changed the energy attributed to the threshold chosen by less than 5 MeV (only the analyses that gave equal integrals for the two FF peaks were considered as acceptable).

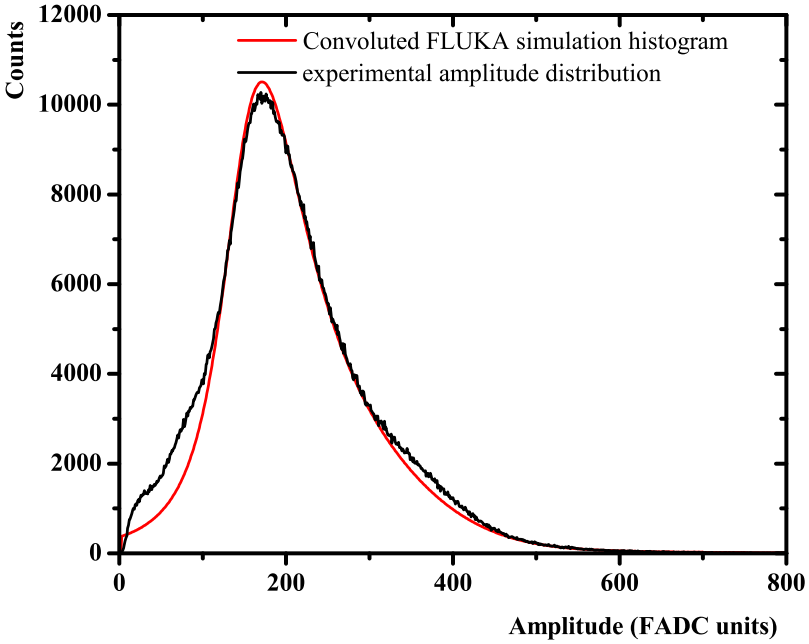

Figure 4.33: The comparison of the convoluted with a gaussian resolution function FLUKA histogram with the experimental amplitude distribution of FF peaks of the ^{237}Np 7 target.

Target name	Energy of threshold (MeV)	Subthreshold counts correction factor (S_{target})	uncertainty
Np7	30.6	1.007	0.00009 (stat)+ 0.002 (syst)
U5	36.3	1.049	0.00023 (stat)+ 0.009 (syst)
U8a	33.3	1.026	0.00016 (stat)+ 0.00003 (syst)
U8b	34.1	1.026	0.00017 (stat)+ 0.003 (syst)
U8c	34.8	1.056	0.0003 (stat)+ 0.010 (syst)
U5b	31.2	1.035	0.00019 (stat)+ 0.005 (syst)
U5c	30.1	1.026	0.00017 (stat)+ 0.001 (syst)

Table 4.3: The subthreshold counts correction factors obtained from the FLUKA simulation histograms. The energy which the threshold bin chosen corresponds to was estimated by calibrating the experimental amplitude distributions as explained in the text. The uncertainties reported are the statistical (stat) and the systematic (syst) obtained from the different analyses.

4.5 Cross section calculation results

The cross section calculation of the neutron induced fission on a target (namely σ_{tar}) with reference to standard fission cross sections (namely σ_{ref}) was performed with use of the formula 4.5:

$$\sigma_{tar} = \frac{C_{tar} \cdot S_{tar} \cdot Nt_{ref} \cdot nEvents_{ref} \cdot eff_{ref}}{C_{ref} \cdot S_{ref} \cdot Nt_{tar} \cdot nEvents_{tar} \cdot eff_{tar}} \sigma_{ref} \tag{4.5}$$

where

1. C_{tar} and C_{ref} are the number of accepted FF peaks above the analysis threshold for the target of interest and the reference target respectively, estimated with the pulse shape analysis procedure explained above (fig. 4.25, 4.26).
2. S_{tar} and S_{ref} are the correction factors for the subthreshold FF peaks, obtained from the FLUKA simulation histograms as explained in 4.4.2 (results in table 4.3).
3. Nt_{tar} and Nt_{ref} are the number of target nuclei for the target of interest and the reference target respectively, obtained from mass measurements with alpha spectroscopy or the nominal mass values from the manufacturer as explained in chapter 3 (see table 3.3).
4. $nEvents_{tar}$ and $nEvents_{ref}$ are the total number of protons impinging on the spallation target for the target of interest and the reference target respectively, and is used for the normalization of the number of accepted FF peaks.
5. eff_{tar} and eff_{ref} are the efficiency correction factors due to the loss of FFs in the target and the reference respectively, and were obtained from FLUKA simulations, as explained in 4.4.2 (results in table 4.2).
6. σ_{ref} is the reference fission cross section. In the present case, the cross section of the ^{235}U(n,f) reaction was used as a reference up to 2 MeV, and of the ^{238}U(n,f) reaction until 10 MeV.

The first attempt was to reproduce the cross section of ^{238}U(n,f) which is considered as a standard, with use of eq. 4.5.

The cross section of the ^{238}U(n,f) reaction taking the U8c as target and the U5c and the U5b as reference, in comparison with the evaluation ENDF/B VII-1 [28] can be found in fig. 4.34. It has to be noted that the ^{238}U(n,f) cross section is considered as a standard, above 1 MeV [69]. The agreement is good, thus partly validating the pulse shape analysis procedure.

However, when the cross section of the ^{238}U(n,f) reaction is calculated taking the U8a or U8b as target and the U5 as reference (8 cm diameter targets), then the data overestimate the evaluations for neutron energies higher than 500 keV, as can be seen in fig. 4.35.

This effect, which varies with energy, is due to the loss of FF peaks from the analysis of the U5 target. As discussed above, this target had a very high FF activity, especially in the bin region 300-700, i.e. the neutron energy range $\sim$600 keV - 4 MeV, so the fitted average event frequently overestimated the raw data, and the loss of FF peaks was noticeable in some cases. By checking on an event-by-event basis, a very rough estimate of this loss was found to be 3-3.5% in this neutron energy region, and it was also found that it varied with the bin number, following the shape of fig. 4.35. This is also reflected in the reaction rate ratio of the U5 target to the U5c target which is of the lowest FF activity. An easy solution to this problem would have been to connect the cells of the detector measuring the induced FF activity from the two sides of the U5 reference target to different FADC modules, thus reducing the activity by $\sim$50%.

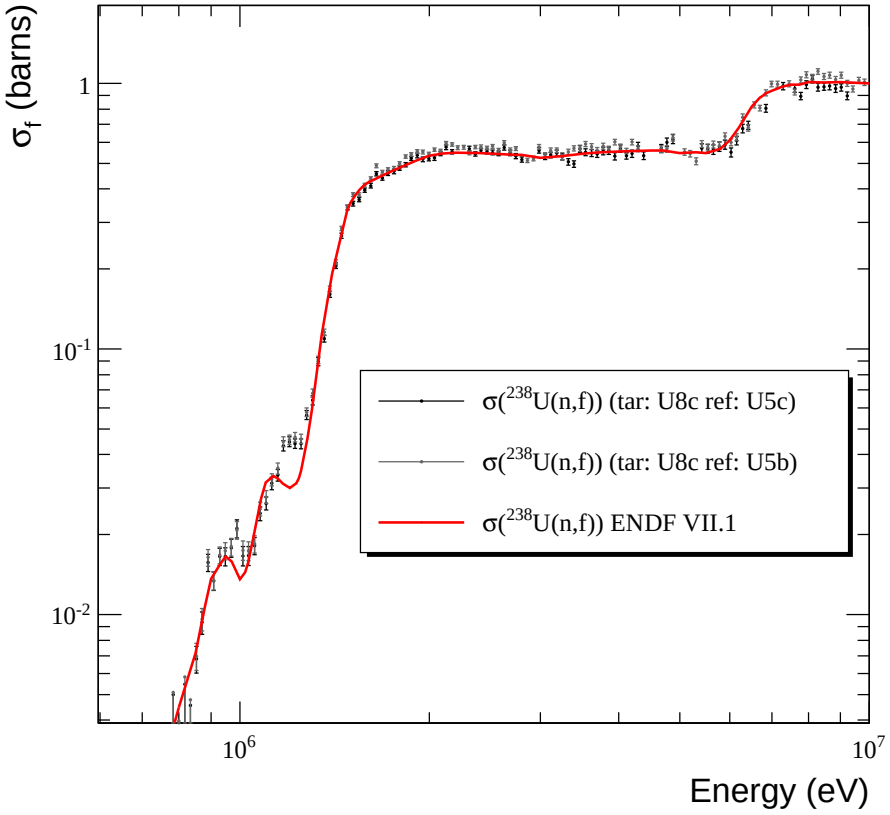

Figure 4.34: The ^{238}U(n,f) cross section calculation with the small diameter targets, i.e. taking the U8c as target and U5c (black points) and U5c (grey points) as reference targets. The ENDF/B-VII.1 is also shown for comparison. The results are shown with 50 bins/decade and the error bars correspond to the statistical uncertainty alone.

The reaction rate ratio is stable for neutron energies lower than 400-500 keV, then decreases with energy up to 2 MeV and then starts increasing again until 5 MeV. The strong oscillations due to the saturations mainly in the raw data of the U5c target preclude the extraction of safe results above that energy. Thus, it was decided not to use the U5 target as reference target for the cross section up to 2 MeV, and the U5b was used instead, because it has a medium FF activity, much closer to Np7 than the U5 and the U5c target, so systematic uncertainties, varying with energy, due to possible losses of FFs will be smeared out. However, a rough estimation of the percentage of lost FF peaks (by checking the raw data analysis event-by-event) gives values less than 1% for both targets. Another reason in favor of the use of the U5b target as reference in the energy region up to 2 MeV is that the raw data of this target do not present saturations in the neutron energy range of interest, as already discussed. The extraction of the cross section relative to a reference reaction assumes that the same flux is impinging on the target of interest and the reference target. Thus, it is not so straightforward to use a target with a different surface as reference. The U5b target has a diameter of 5 cm, while for the Np7 target the corresponding value is 8 cm. Even by assuming central symmetry in the collimation system of the n_TOF tube (table 3.1), Monte Carlo simulations of the beam profile suggest that the neutron fluence decreases at the edges of the big diameter target, while the decrease is lower for the small diameter target. This was roughly checked with use of the Beam Profile Calculator [68] of the n_TOF facility at the position of the Np7 target (the same stands for the other sample positions) and the results for energies 100 keV - 1 MeV and 1 - 10 MeV can be found in fig. 4.37.

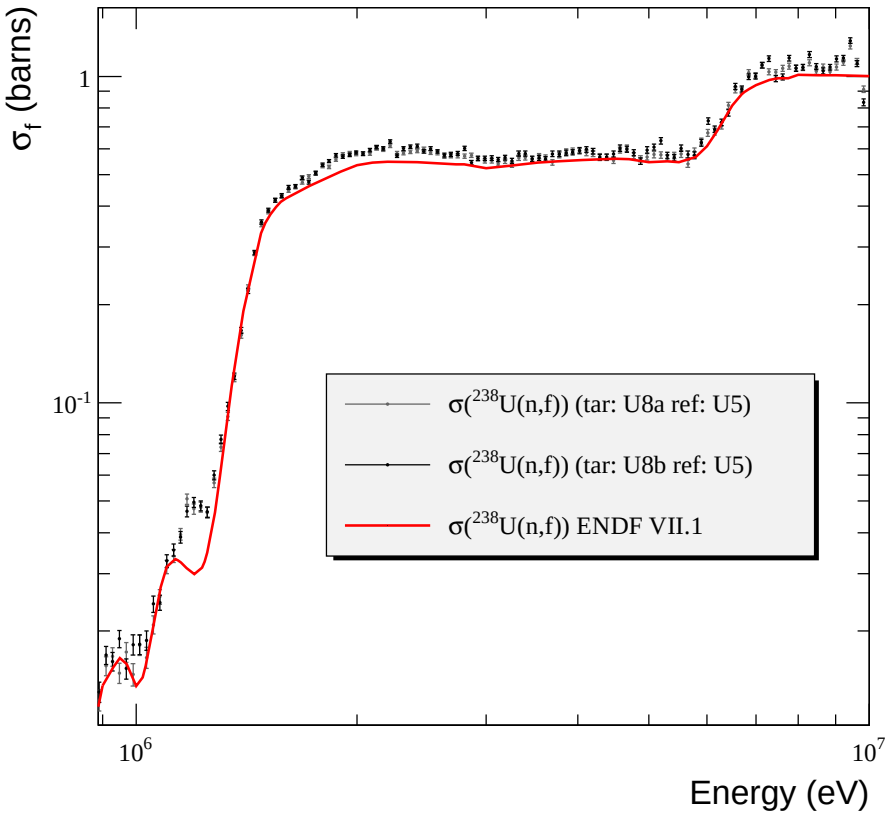

Figure 4.35: The ^{238}U(n,f) cross section calculation with the big diameter targets, i.e. taking the U8a and U8b as target and U5 as reference target. The ENDF/B-VII.1 is also shown for comparison. The results are shown with 50 bins/decade and the error bars correspond to the statistical uncertainty alone.

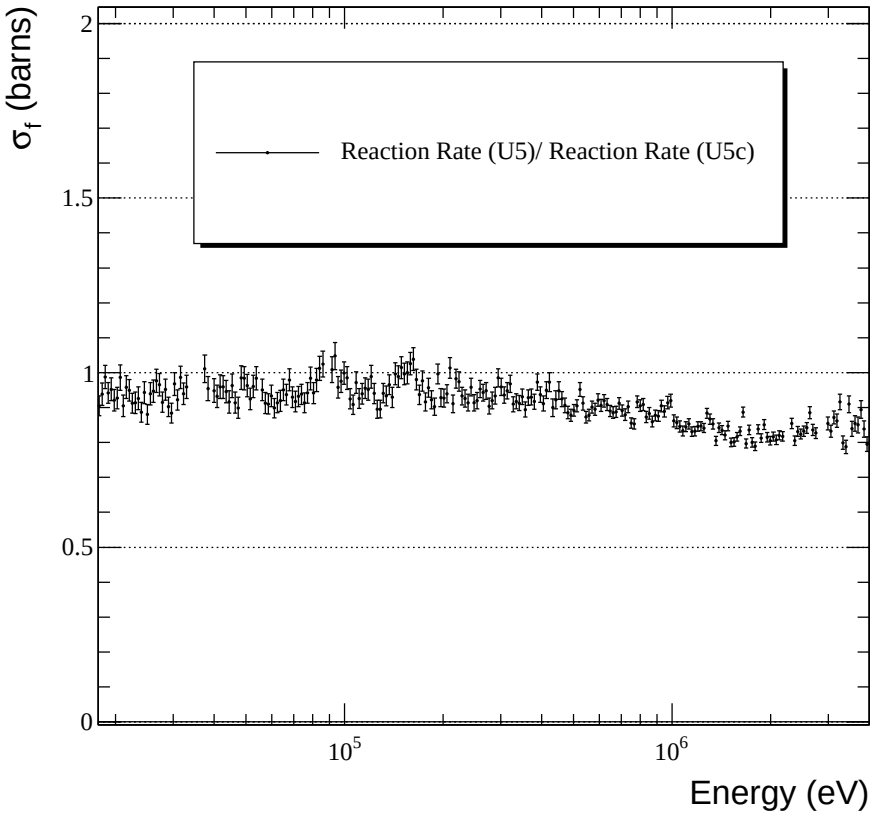

Figure 4.36: The reaction rate of the U5 target to the corresponding value of the U5c target, plotted with 50 bins/decade.

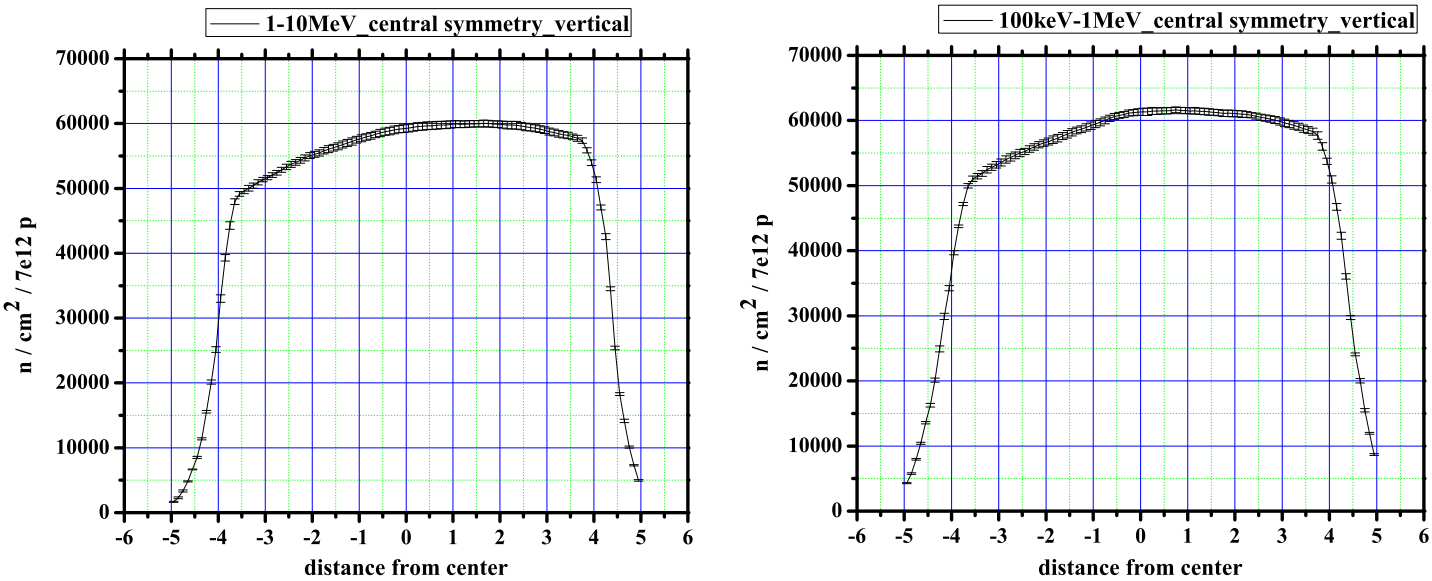

Figure 4.37: Neutron beam profile at the position of the Np7 target (similar results are obtained for the other targets) with the Beam Profile Calculator for the measurements of phase 1 at the n_TOF facility ([68]), with the collimation system in the fission mode, perfectly aligned. The vertical radial profile is shown here but the results are similar for the horizontal one.

Thus the fluence impinging on the surface of the targets (with radii of 2.5 cm and 4 cm) is not stable. The ratio of the integrated simulated fluence to an ideal stable fluence impinging on the surface of the big target (4 cm in radius) is $\sim$ 4% higher than the corresponding value for the small target (2.5 cm radius).

As a result, when eq. 4.5 is used for the cross section calculation and the target is of 4 cm diameter and the reference of 2.5 cm diameter, a multiplication factor needs to be inserted in order to account for this effective neutron fluence differences, namely $S_{effectiveneutronfluence}$. The estimation of $S_{effectiveneutronfluence}$ was based on experimental results using:

1. reaction rate ratios ($\frac{RR_{bigtarget}}{RR_{smalltarget}}$) obtained from targets of the same isotope, with different surfaces, which should be equal to 1. The reaction rate ratios from the U8 samples were used (i.e. $\frac{RR_{U8a}}{RR_{U8c}}$ and $\frac{RR_{U8b}}{RR_{U8c}}$). If the reaction rate ratio is lower than 1 by a value costant with energy, it can be attributed to systematic uncertainties in the masses of U8a or U8b or the effective neutron fluence differences. The reaction rate ratios for U5 samples (i.e. $\frac{RR_{U5}}{RR_{U5c}}$ and $\frac{RR_{U5}}{RR_{U5b}}$) were not used since above 400-500 keV they rapidly decrease with energy as shown in fig. 4.36, due to the loss of FF peaks from the analysis of the U5 target. An example of the reaction rate ratio $\frac{RR_{U8a}}{RR_{U8c}}$ can be found in fig. 4.38. The ratio is clearly lower than 1 by a constant factor which was estimated by fitting the experimental reaction rate ratio with a linear function. Various fittings were tried, for different neutron energy regions, keeping in mind that the slope of the fitting line should be very small (of the order of 10^{-9} - 10^{-10}), as well as the errors of the fitting parameters (offset and slope), and that the neutron energy region up to 2 MeV is of interest for the extraction of the factor $S_{effectiveneutronfluence}$. In figure 4.38 an example of such a fitting is shown.

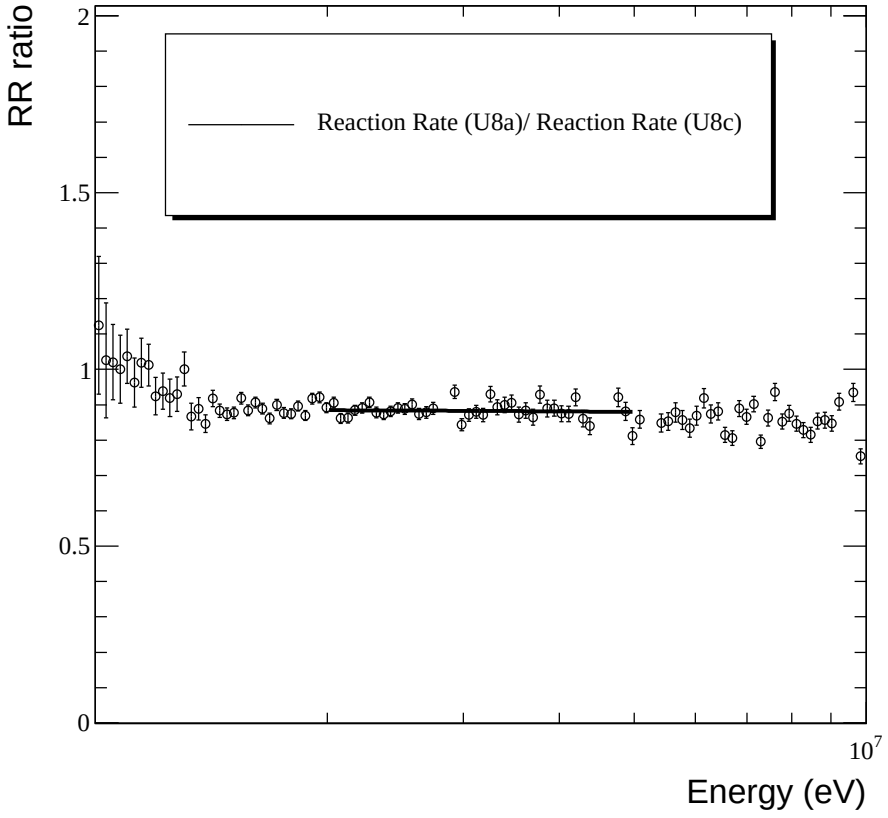

Figure 4.38: The reaction rate of the U8a target (8 cm diameter target) to the corresponding value of the U8c target (5 cm diameter target), plotted with 50 bins/decade.

The average offset value (namely $b_{RRratio}$) obtained from the accepted fittings of the experimental $\frac{RR_{U8a}}{RR_{U8c}}$ and $\frac{RR_{U8b}}{RR_{U8c}}$ was $b_{RRratio}$= 0.90 $\pm$ 0.01 (the uncertainty corresponds to the standard deviation of the various offsets obtained) so $1/b_{RRratio}$=1.11 $\pm$ 0.01.

2. ^{238}U(n,f) cross section ratios ($\frac{\sigma_{^{238}U(n,f)}-ENDF/BVII.1}{\sigma_{^{238}U(n,f)}-measured}$), where $\sigma_{^{238}U(n,f)} - measured$ are cross section values obtained with eq. 4.5, with a big U8 target (U8a and U8b) and a small U5 reference target (U5c, because it is of known mass and of low FF activity). The evaluated $\sigma_{^{238}U(n,f)}$ is considered as a standard above 1 MeV [69] and these ratios should also be equal to 1. An example of the cross section ratio $\frac{\sigma_{^{238}U(n,f)}-ENDF/BVII.1}{\sigma_{^{238}U(n,f)}-measured}$, taking U8b as target and U5c as reference can be found in fig. 4.39. Also in this case, despite the oscillations due to the poor statistics and saturations of the U5c data, it can be concluded that the cross section ratio is higher than 1 by a constant fraction. By fitting the cross section ratios with a linear function with a negligible slope (of the order of 10^{-9} - 10^{-10}) the resulting average offset value for both targets was $b_{CSratio}$=1.10 $\pm$ 0.02 (the uncertainty corresponds to the fitting parameter error, because it was larger than the standard deviation in the present case, due to the spread of the cross section ratio points). An example of such a fitting is shown in fig. 4.39.

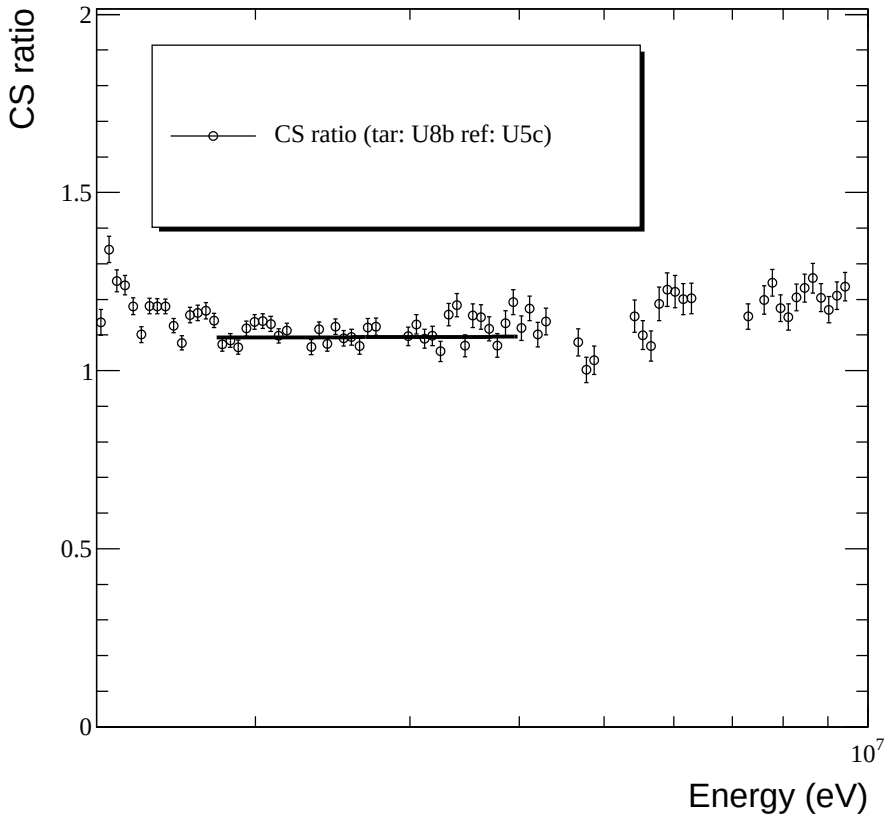

Figure 4.39: The ^{238}U(n,f) cross section ratio $\frac{\sigma_{^{238}U(n,f)}-ENDF/BVII.1}{\sigma_{^{238}U(n,f)}-measured}$, where $\sigma_{^{238}U(n,f)} - measured$ is calculated taking the U8b (8 cm diameter) as a target and the U5c (5 cm diameter) as reference, plotted with 50 bins/decade.

The final value of the effective neutron fluence multiplication factor was the average value from $1/b_{RRratio}$ and $b_{CSratio}$, so $\mathbf{S}_{effectiveneutronfluence}$= **1.10** $\pm$ **0.02**. Due to the fact that it was obtained from ratios of different targets possible systematic uncertainties from the mass values used obtained from the manufacturer were assumed to be smeared out. For the subsequent analysis this correction factor is used when the reaction rate of a big diameter target (Np7, U5, U8a, U8b) is divided by the reaction rate of a small diameter target (U5b, U8c, U5c), but only in the neutron energy range up to 5 MeV in which the reaction rate ratios and cross section ratios were fitted, for other neutron energy regions this correction factor needs to be slightly tuned.

Based on the previous discussion the final cross section values of the ^{237}Np(n,f) reaction were obtained as follows:

- **neutron energy range <400 keV:** The U5 target was used as reference in this neutron energy region, since it has a big mass value and in this energy region the analysis is not problematic (as shown above the loss of pulses starts at neutron energies bigger than 700 keV). However, if the cross section is calculated with U5b or U5c as reference targets (multiplying eq. 4.5 by the $S_{effectiveneutronfluence}$ even if it is a first order approximation because it was calculated for a different energy range), the cross section results agree within their errors, as shown in fig. 4.40.

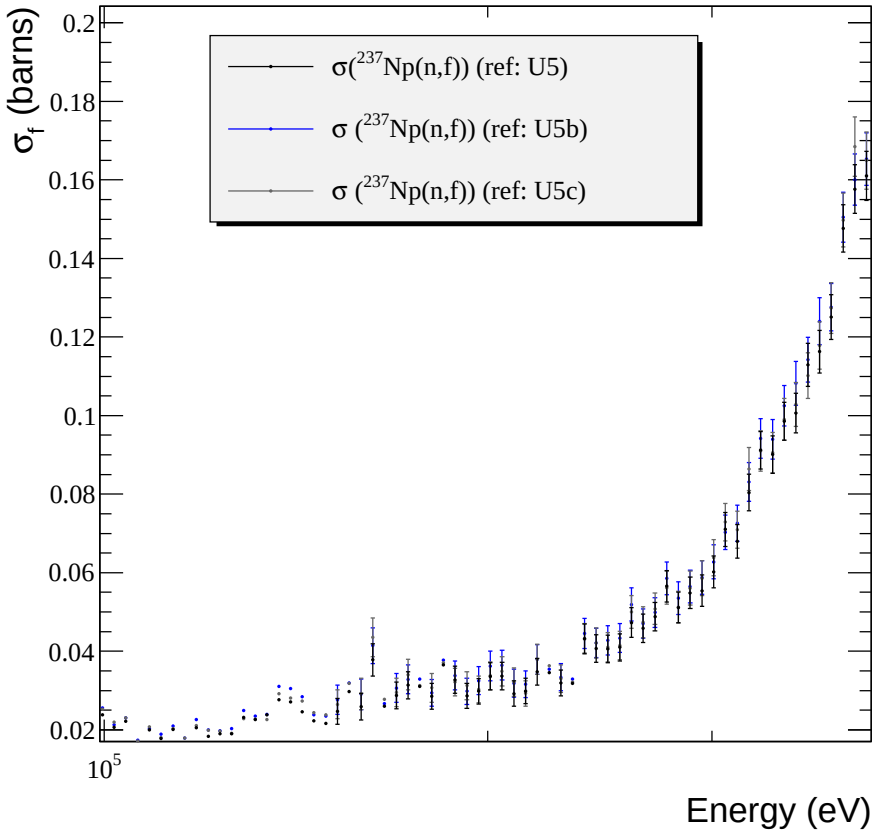

Figure 4.40: The ^{237}Np(n,f) cross section calculation taking the U5 as reference target, shown with 50 bins/decade. The cross section results taking the U5b and U5c are also shown for comparison. The error bars correspond to the statistical uncertainty alone.

- **neutron energy range 400 keV -2 MeV:** The U5b target was used as a reference in this energy region, using eq. 4.5 multiplied by the $S_{effectiveneutronfluence}$.
- **neutron energy range above 2 MeV:** The U8a and U8b targets were used as a reference in this energy region. Two cross section values were calculated and the average value was taken as the final result. The uncertainty attributed to the average cross section values was chosen to be the biggest statistical uncertainty of the two values. As already mentioned, the energy region above 10 MeV could not be recovered due to the saturations of the raw data.

The final cross section values, along with the latest data of Paradela et al., [8] and the latest evaluations ENDF/B-VII.1 [28] and and JEFF 3.2 [30] are shown in fig. 4.41 and for clarity purposes the energy region below 1 MeV is shown in fig. 4.42 and above 1 MeV in fig. 4.43. The few data points at energies of saturations have been removed. The chosen binning is 50 bins/decade, and the uncertainties shown in the figure are the statistical ones. The relative statistical uncertainty for this binning is shown in fig. 4.44 and above 500 keV where fission rapidly increases it does not exceed 3%. The n_TOF data occured from the present work are in agreement with

the latest data of Paradela (2010) and the latest evaluations up to 1 MeV. The cross section presents a local maximum at ∼1 MeV, also seen in the data of Paradela and on the slope of the first chance fission, the shape of which is better reproduced by the JEFF evaluation. Furthermore, despite the statistical uncertainties on the slope of the first chance fission, the data of this work seem to present small humps and plateaus, some of them also seen at the data of Paradela (as for example at ∼810 keV and 890 keV, or the small local maximum at 520 keV). In any case, the cross section is not smoothly increasing at the first chance fission, and this needs to be further investigated in the context of possible structure close to the threshold, which is a common feature for actinide fission (mainly for the even-even and odd-Z actinides). However, above 1 MeV, at the plateau of the first chance fission, the data are systematically lower compared to the latest data of Paradela and the differences between the two datasets reach 7%. The data from the present thesis agree within errors with the latest evaluations ENDF/B-VII.1 and JEFF 3.2.

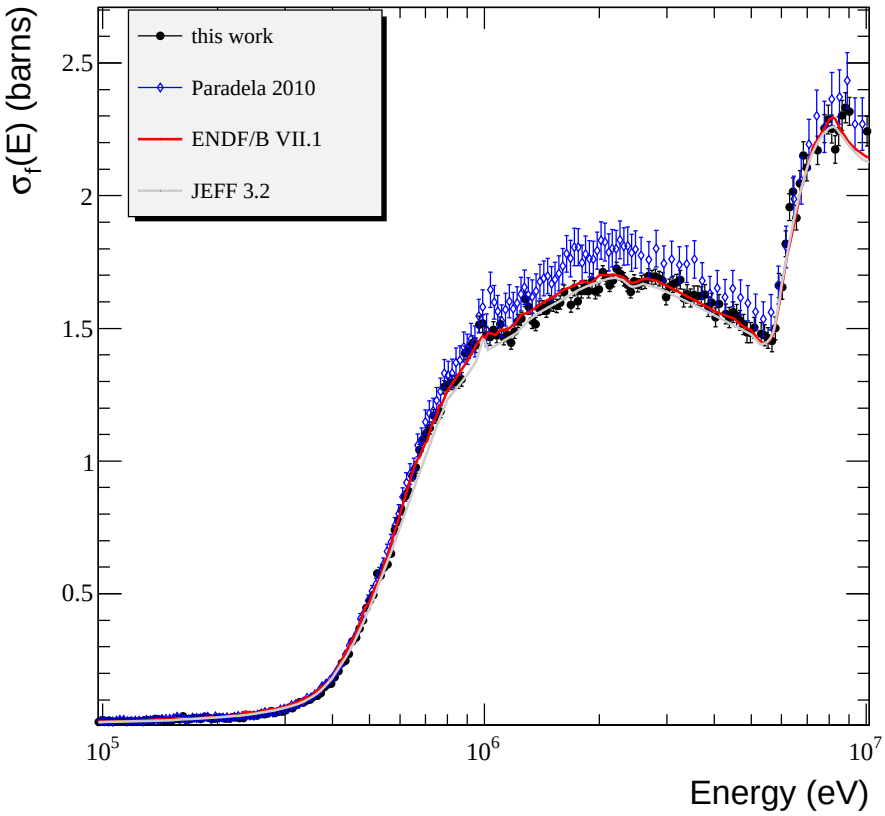

Figure 4.41: The final cross section results obtained with 50 bins/decade in the whole neutron energy range. The statistical uncertainties of the present data are shown. The n_TOF data are compared to the latest evaluations (ENDF/B-VII.1 [28] and JEFF 3.2 [30]), and the latest data [8].

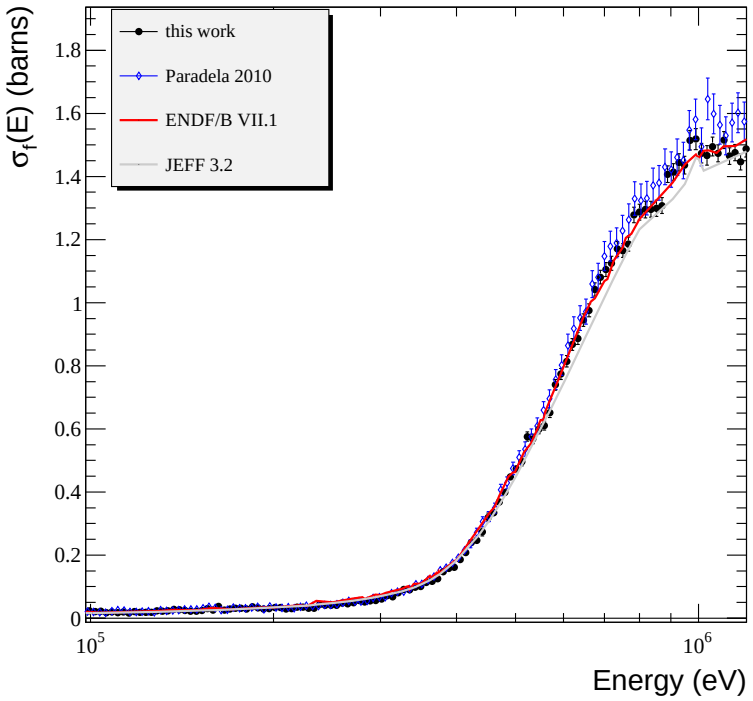

Figure 4.42: The cross section results shown in fig. 4.41 zoomed in the energy region up to 1 MeV, i.e. the threshold of the first chance fission.

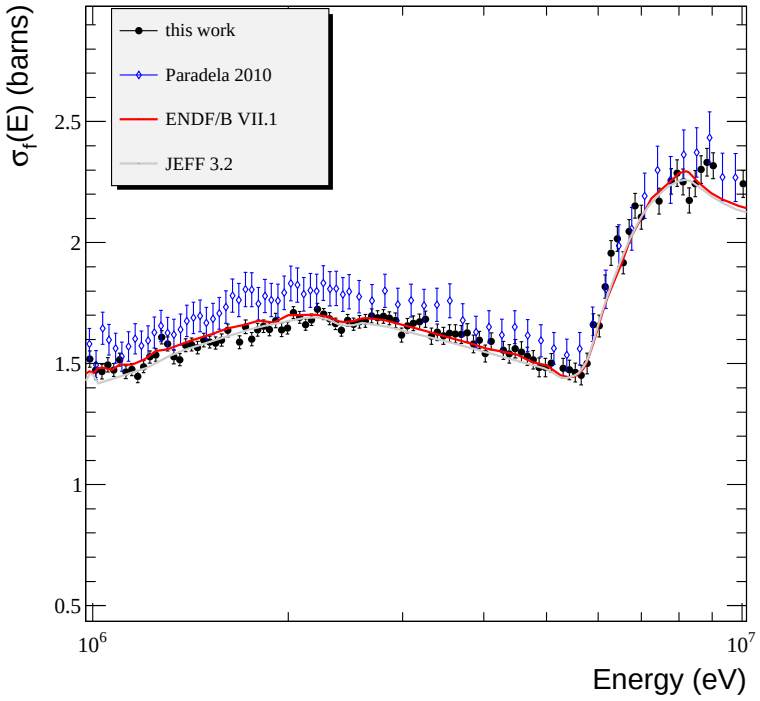

Figure 4.43: The cross section results shown in fig. 4.41 zoomed in the energy region 1-10 MeV, i.e. the threshold of the first chance fission.

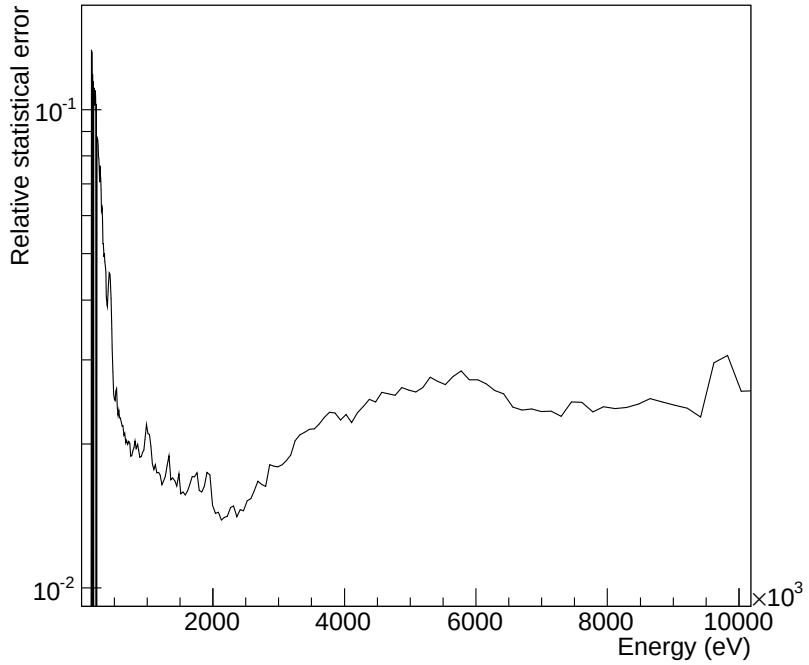

Figure 4.44: Relative statistical uncertainty $\delta\,\sigma\,E/\sigma$ E of the final cross section values. Above the fission threshold it does not exceed 3%.

The data obtained from this work are also shown at different energy regions with previous selected data found at EXFOR [7] for comparison (figs. 4.45, 4.46, 4.47). Up to 1 MeV, the data from the present work agree within errors with the data of Cennini (2004), Scherbakov (2001), Meadows (1983) and Plattard (1975), but not with Jiacoletti (1972). At the first chance fission plateau the present n_TOF data are in good agreement with previous data (mainly with Scherbakov (2010) and Lisowski (1988)), but not with the data of Plattard (1975) and Jiacoletti (1975). Finally, at the second chance fission threshold the present n_TOF data also agree within errors with Lisowski (1988) and Meadows (1983) but seem to be somewhat higher than the data of Scherbakov (2010), although they agree within errors.

Finally, the systematic uncertainties are presented in table 4.4.

Contribution	Uncertainty (%)	Energy range (MeV)
Target mass	1.3-1.7	-
Subthreshold counts correction	$<$0.5	-
Efficiency correction	2	-
$S_{effectiveneutronfluence}$	1.8	0.4-2
$\sigma_{^{235}U(n,f)}$	< 1	0.01-2
$\sigma_{^{238}U(n,f)}$	< 1	2-10

Table 4.4: The systematic uncertainties at the cross section calculation. Their origin is explained in the text. The third column contains the energy range in which these uncertainties contribute to the cross section. When no energy range is reported, the corresponding systematic uncertainty contributes to the whole energy range studied.

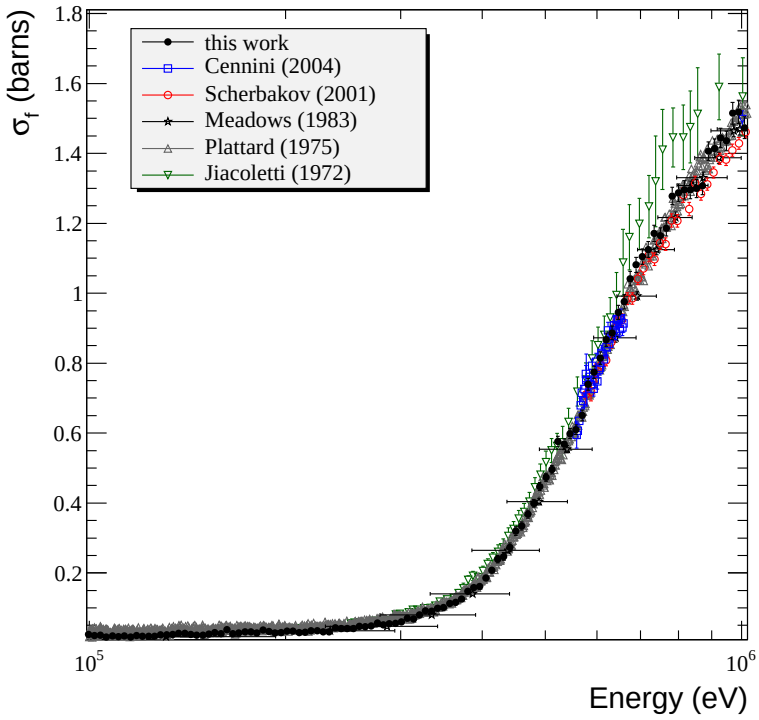

Figure 4.45: The final cross section results obtained from the present analysis compared to selected data from the EXFOR database [7] in the energy range below 1 MeV.

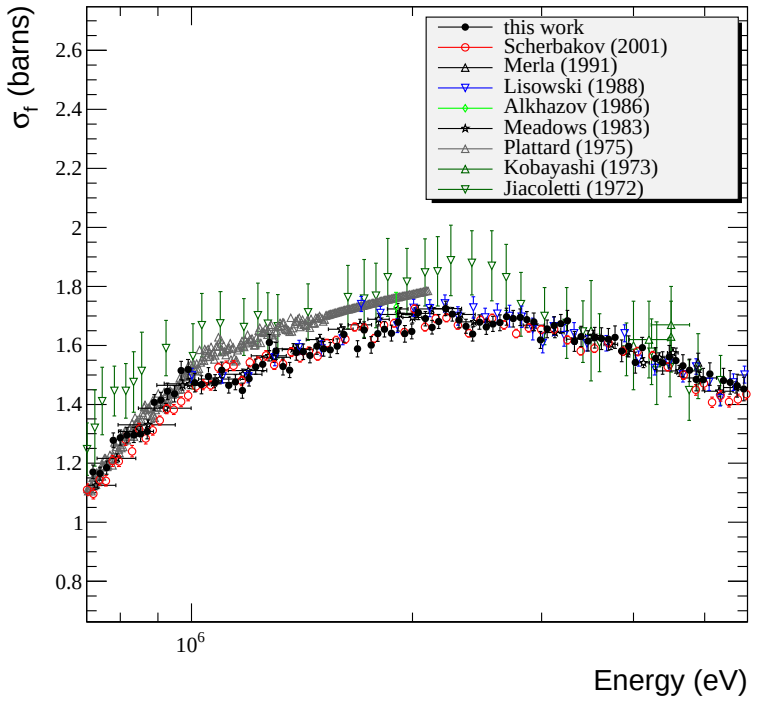

Figure 4.46: The final cross section results obtained from the present analysis compared to selected data from the EXFOR database [7] in the energy range 1-5 MeV.

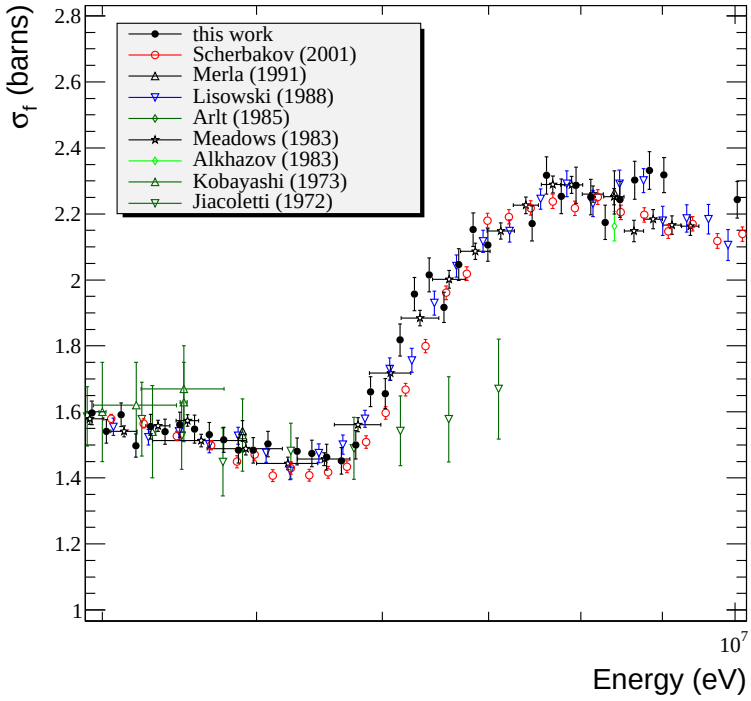

Figure 4.47: The final cross section results obtained from the present analysis compared to selected data from the EXFOR database [7] in the energy range 4-10 MeV.

Chapter 5

The ^{237}Np(n,f) measurement at "Demokritos"with the MicroMegas: Experimental setup

In the context of the present thesis the ^{237}Np(n,f) cross section was also determined with independent measurements using monoenergetic neutron beams at the Institute of Nuclear and Particle Physics of the NCSR "Demokritos". A MicroMegas detector was used, for the first time for the measurement of the fission fragments. This detector was developed at CERN, within the framework of the n_TOF collaboration. Details on the experimental setup, the data analysis and the simulations, as well as the final cross section values are presented in this chapter.

5.1 The neutron production facility at the I.N.P.P., NCSR "Demokritos"

The quasi-monoenergetic neutron beams at the Institute of Nuclear and Particle Physics of the NCSR "Demokritos"are produced via nuclear reactions of ions accelerated with use of a 5.5 MV Van de Graaff Tandem (T11/25, fig. 5.1), impinging on gas or solid targets.

The linear accelerator is divided in two parts: the low energy part (from the ion source to the Van de Graaff generator) and the high energy part (from the Van de Graaff generator to the experimental areas). It has two ion sources and provides various ion beams from hydrogen to oxygen. The ion beams provided are of high purity and very good energy resolution thanks to the combination of three electromagnets, the most important being the so-called "analyser", located after the Van de Graaff generator that diverts the selected ions by 90° and the magnetic field is accurately determined with the Nuclear Magnetic Resonance (NMR) technique. The resulting energy uncertainty for deuterons does not exceed 4 keV. A photo of the accelerator can be found in 5.1.

The selected nuclear reaction depends on the desired energy of the neutron beam. The ^{7}Li(p,n) reaction is used for neutrons in the energy range below 4 MeV, the ^{2}H(d,n) below 7.7 MeV (for strictly monoenergetic beams) and the ^{3}H(d,n) reaction for neutrons with energies up to 20.5 MeV [73].

The measurements in the context of the present thesis were performed with neutron beams produced via the ^{2}H(d,n) reaction [70, 71], in the neutron energy range 4.5-5.3 MeV. A deuterium gas target fitted with 5 μm molybdenum entrance foil and 1 mm Pt beam stop is bombarded with a deuteron beam of the appropriate energy (see fig. 5.2). The total length of the gas cell is 3.7 cm.

The impinging deuteron beam energies varied from 2 to 2.6 MeV, with a step of 0.2 MeV. The mean neutron beam energy is estimated from the ^{2}H(d,n) reaction kinematics, taking the center of the gas cell as the reference point where the reaction took place. The energy rippling of the deuteron beam did not exceed 4 keV, having

Figure 5.1: Photo of the high energy part of the accelerator system at the Institute of Nuclear and Particle Physics of the NCSR “Demokritos”. Two main parts can be seen: the tank where the 5.5 MV Van de Graaff generator is located and the “analyser”magnet.

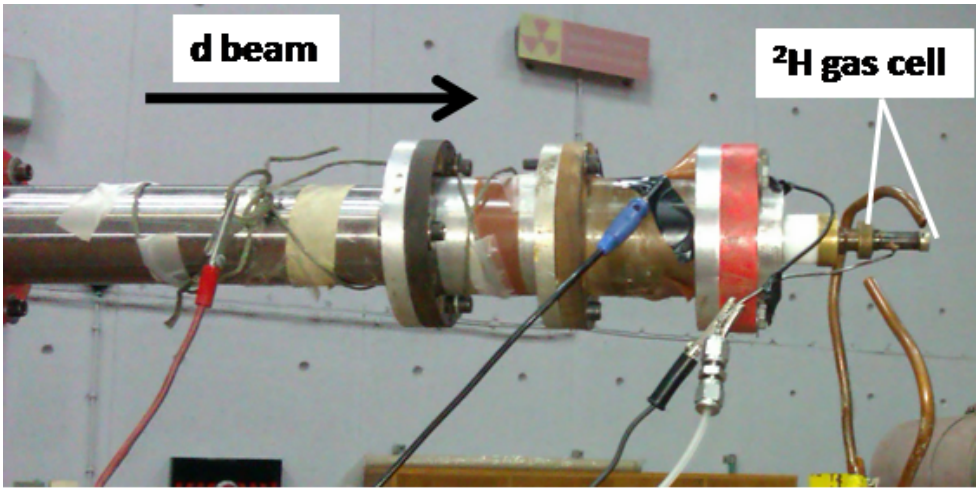

Figure 5.2: Photo of the beam line dedicated to neutron measurements, with the deuterium gas cell mounted at the end. The deuterons pass through the molybdenum entrance foil but they are stopped at the Pt foil.

a negligble effect on the monochromaticity of the produced neutron beam. However, the monochromaticity and the fluence of the neutron beam is affected by several other factors like i) the energy straggling of the deuteron beam from the interaction with the Mo foil and the deuteron atoms in the gas cell, ii) the kinematics of the ^{2}H(d,n) reaction which is not isotropic, iii) deuteron induced reactions in the materials of the collimation system or the gas cell, producing neutrons with energies different than the main beam (the so-called ``parasitic neutrons"), iv) possible scattering of the neutron beam in the surrounding material of the targets. When the cross section measurement of interest corresponds to a non-threshold reaction, or a reaction with a significant cross section value in a wide neutron energy range, like fission, and in the absence of a Time-of-Flight technique, a thorough investigation of the impact of these factors on the monochromaticity and fluence of the neutron beam is essential. This investigation is presented in sec. 6.2.

5.2 Detection setup with the MicroMegas detector

The detector used in the measurements of the present thesis is a low-mass MicroMegas based on the Micro-bulk technology. This detector is part of a new assembly setup at the Tandem accelerator facility of NCSR "Demokritos"in Athens for fission cross section measurements on actinides, using monoenergetic neutron beams, within the context of the n_TOF collaboration.

5.2.1 Description of the MicroMegas detector principle

The MicroMegas detector (Micro-Mesh Gaseous Structure) is a gas detector [72, 74], introduced in 1996, working as a two stage parallel plate avalanche chamber. A typical schematics of this detector, as well as the electric field lines in the gas volume can be found in fig. 5.3. The basic feature of this detector is the separation of the gas-filled region between the cathode and anode electrode in two zones by the so-called "micromesh", a thin electrode with holes. The region between the cathode electrode and the micromesh is called the "drift"region, i.e. the region where the ionization of the gas atoms by the incoming radiation takes place. The electrons created are drifted by the low electric field applied in this region, typically 1 kV/cm, towards the micromesh, and pass through the holes towards the "amplification "region, where due to the high electric field applied (typically 50-60 kV/cm) an avalanche is created from each electron. The avalanche of electrons is created as follows: the primary electron has enough energy to ionize a gas atom, the secondary free electron is accelerated from the high electric field and obtains enough energy to ionize another gas atom and so on, until all the free electrons reach the anode electrode. If n_0 are the primary electrons, the final number of produced electrons n(x) after a path x in the gas is given by the Townsend equation [87]: $n(x) = n_0 \cdot e^{\alpha x}$, where α is the Townsend coefficient (this equation is valid for uniform electric fields). The *gain* of the detector is the ratio n(x)/n_0 and it can not exceed the Raether limit (i.e. 10^8). Typical gain values are 10^3-10^4.

The ability of the field to transfer primary electrons through the holes of the micromesh, i.e. the electron transmission, is called *transparency* and depends on the ratio of the electric field in the amplification region to the electric field in the drift region, namely $\xi = E_{amplification}/E_{drift}$ (the symbol ξ was used in ref. [72]). It has been shown that for low values of ξ the electron transmission is very poor, because most of the electric field lines starting from the drift go straight and reach the micromesh electrode. For large ξ values most of the field lines pass through the holes and reach the anode pad, resulting in high electron transmission that reaches 100%. At the same time, the electric field lines in the amplification region start from the anode pad and reach the mesh electrode and as a result the ions produced in the avalanches are gathered at the micromesh electrode and do not enter the drift region (fig. 5.3, right panel). However, for too high ξ values the electron transparency starts decreasing again, reducing the gain of the detector, because the field lines in the drift region do not curve at the edges of the holes, so the electrons have a higher probability of hitting the mesh electrode than passing through the holes to the ampligication region. Consequently, the MicroMegas detector should be preferably functioning at ξ values where the transparency is maximized.

The spacing between the mesh and the anode electrode is kept small in order to obtain high electric field strength with reasonable applied voltage values and to favor short charge collection times ($\sim$ns). Furthermore, the positive ions are collected in the mesh, so the short collection time allows for fast recovery from space charge effects, and consequently for the use of the detector at high counting rates. The detector can be optimized to measure different kinds of radiation, from X-rays to fission fragments, by changing the distances between the three electrodes, the voltages applied and the gas mixture and pressure. Furthermore, it can be used for the detection of neutrons by choosing the proper conversion reaction (for example ^{235}U(n,f), ^{10}B(n,a) etc.) and with the use of a stripped or pixelized anode pad a position-sensitive detector can be obtained. Good resolution has been reported, for example $\sim$12% for low energy X-rays (5.9 keV - ^{55}Fe) detected with Ar-isobutane mixtures at atmospheric pressure. The resolution gets better as the gas pressure gets higher and it has been shown [75]

that for Ar-isobutane mixtures at 4 bar the 5.5 MeV alpha paticles from the decay of ^{241}Am can be detected with a resolution less than 2%.

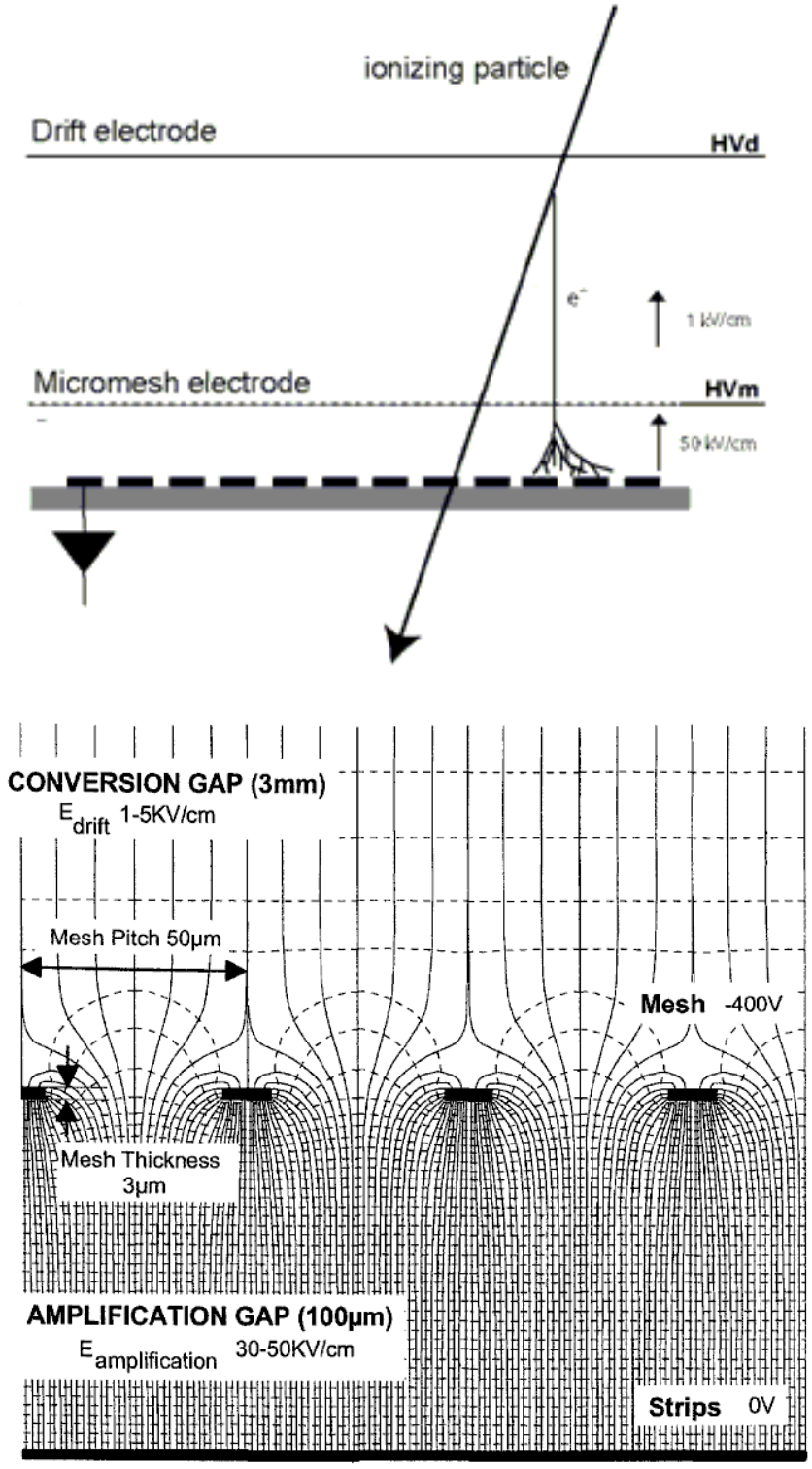

Figure 5.3: Schematics of the Micromegas detector (up) and of the electric field lines in the two regions of the gas volume (down). The field lines in the "drift"region are leading the electrons through the holes of the micromesh to the "amplification"region (taken from [78].

5.2.2 The micro-bulk technology

Detection of radiation in neutron beams requires the use of a low-mass detector in order to reduce neutron scattering and additional γ background from the interaction of the neutrons with the detector material. For this purpose, a state-of-the-art MicroMegas detector based on the Micro-bulk technology [76] was developed at CERN, within the context of the n_TOF collaboration. According to the original version of this method [77], the mesh and pillars are produced via the chemical attack of a coppered kapton film deposited on an anode of a coppered epoxy. In order to minimize the material in the detector, the coppered epoxy anode was replaced by a thin copper layer. Thus, each micro-bulk foil is made of a sandwich of 5 μm thick copper mesh - 50 or 25 μm thick kapton pillars - 5 μm thick copper anode, tended and glued on a Plexiglas ring. The kapton pillars in the micro-bulk are the remaining part of the kapton foil after the chemical attack (fig. 5.4).

Figure 5.4: A schematics of a micro-bulk, taken from [79].

A photo of one of the micro-bulks used for the measurements of this thesis, taken with use of a microscope can be found in fig. 5.5. The holes of the micromesh cover only 13% of the micromesh surface, however, if the detector is working at ξ values where the transparency is maximized, the field lines are curved (fig. 5.3) and drift the electrons through the holes, while the ions produced at the avalanches do not escape the amplification region.

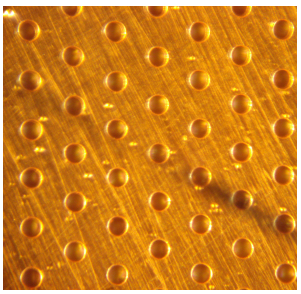

Figure 5.5: Photo of the micromesh from one of the micro-bulks used in the measurements of the present thesis. The photo was obtained with use of a microscope. The diameter of the holes is 40 μm while the distance between two holes is 100 μm.

The major advantages of the micro-bulks are the reduction of the material, the homogeneity of the electric field, good energy resolution and less sensitivity to gas variations and possible disadvantages are higher electronic noise due to the higher capacity, the complexity of the manufacturing process and the fragility.

5.2.3 Characteristics and performance of the MicroMegas detectors used

As already mentioned there are two important features of the MicroMegas detector perfomance that need to be studied before it can be used for cross section measurements: 1) the gain and 2) the transparency curve. As described in [80], these studies were performed by taking spectra from a monoenergetic alpha source (^{210}Po - alpha energy of 5.3 MeV), with the same drift region thicknesses and gas mixture as in the ^{237}Np(n,f) cross section measurements. By keeping the voltage at the micromesh stable and by changing the voltage of the drift electrode it was noticed that the centroid of the Po peak was moving, meaning that the gain of the detector was changing. If the centroid channel is plotted versus the $\xi = E_{amplification}/E_{drift}$, then the transparency curve of the detector can be obtained. By keeping the voltage of the drift electrode stable and by increasing the voltage

of the micromesh electrode, the centroid of the peak was shifting to higher channels of the spectrum, meaning that the gain was increasing. Typical curves obtained by recording the centroid of the alpha peak versus ξ can be found in fig. 5.6.

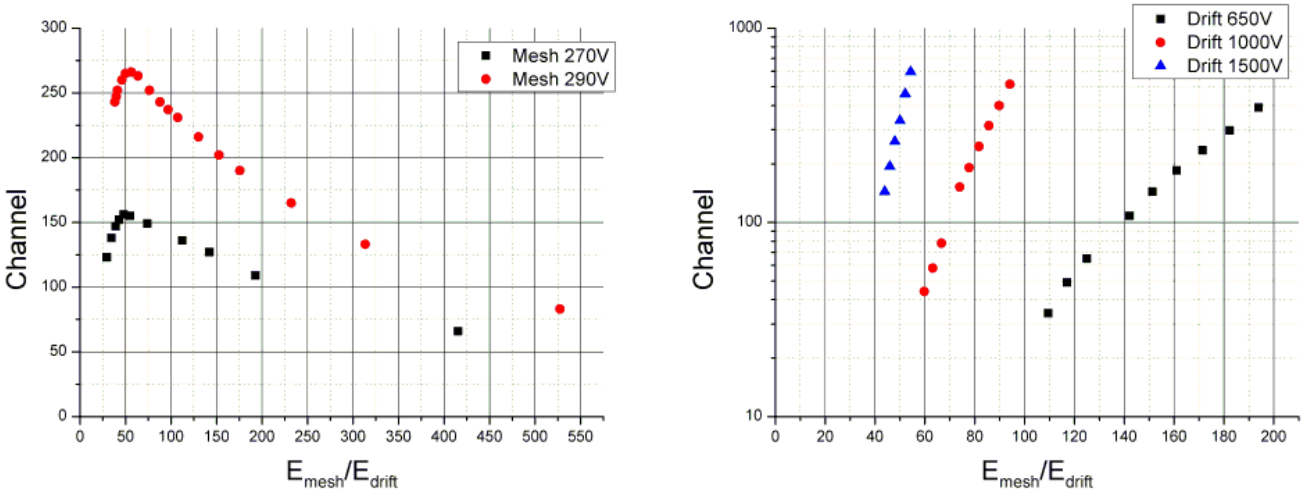

Figure 5.6: The transparency curve (left) and the gain curve (right) obtained from the testing of the micro-bulk DM3. The peak at the transparency is reached when $\xi \sim 55$. The figure is taken from [80].

Characteristic curves as the ones shown in fig. 5.6 were obtained during the tests for each micro-bulk in order to obtain the optimal settings. The testing of the detectors revealed that they are very sensitive to pick-up frequencies and they need to be well shielded. A low pass filter was made and used in order to remove the high frequencies induced by the high voltage supply [80]. Finally, all unused cable terminals in the chamber that housed the detectors were removed in order to reduce the probability of sparks (i.e. sudden discharges) from the drift and micromesh electrodes towards the grounded chamber.

Position	Target	amplification gap (μm)	drift gap (cm)	V_{drift} (V)	V_{mesh} (V)
1	^{238}U (209)-front	25	0.8	-1100	-245
2	^{237}Np (29)	50	1	-1100	-310
3	^{235}U (78)	50	1	-1100	-305
4	^{238}U (210)-back	50	1	-1100	-310

Table 5.1: The targets used for the cross section measurements, the position in the beam, and the information on the corresponding MicroMegas detector for each target measured: the micro-bulk amplification gap, the drift-to-micromesh distance ("drift gap") and the applied voltages at the mesh and drift electrodes.

5.3 Details of the experiment

The ^{237}Np(n,f) reaction cross section was measured with reference to the ^{238}U(n,f) reaction with use of monoenergetic neutron beams in the energy range 4.5-5.3 MeV and the innovative MicroMegas detectors described above. The threshold ^{238}U(n,f) reaction was used as reference, instead of the widely used ^{235}U(n,f) one, because the latter is sensitive to scattered, low-energy neutrons.

Each actinide target along with the micro-bulk chosen formed a MicroMegas detector cell, as shown in fig. 5.7. The target backing served as the drift electrode, the drift region was approximately 1 cm thick, while the amplification region was 25 or 50 μm thick. The gas of the detector was 80% Argon and 20% CO_2.

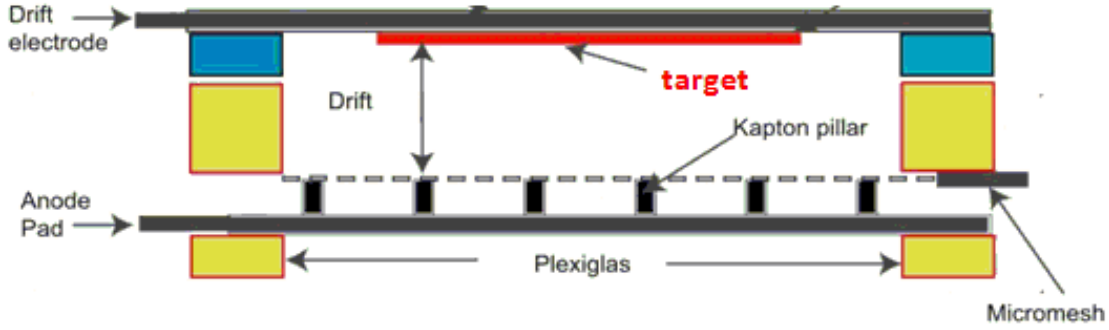

Figure 5.7: Schematic of a MicroMegas detector with the target under analysis used in this work. The target backing served as the drift electrode. The gas of the detector was 80% Argon and 20% CO_2.

The target cells were put in the following order with reference to the beam direction: ^{238}U (209), ^{237}Np (29), ^{235}U (78) and ^{238}U (210). Two ^{238}U reference targets were mounted, in order to have better control of the neutron beam in front of and behind the ^{237}Np 7 target, while the ^{235}U target was put in order to check possible lower energy neutrons. Information on the MicroMegas detector cell for each actinide target can be found in table 5.1. The four actinide targets were characterized as far as their mass and homogeneity are concerned (see chapter 2, tables 2.2, 2.5).

The target and micro-bulk assembly was mounted in an especially made aluminum chamber, with entrance and exit windows made of kapton in order to reduce the interaction of neutrons with the surrounding material as much as possible. A schematic and photos of the setup are shown in fig. 5.8. The detector chamber was filled with the gas mixture (80% Argon - 20% CO_2) at approximately atmospheric pressure and the gas was circulated at a constant flow of 6-8 NL/h.

The deuterium gas target was bombarded with a deuteron beam at energies that varied from 2 to 2.6 MeV with a step of 0.2 MeV, and at currents from 500 nA to 1 μA. During the irradiation the gas cell was constantly cooled with a cold air jet to avoid possible damage of the Mo foil. The deuterium pressure was kept nearly constant at 1300 mbar, while the value of the gas pressure was recorded every 5 minutes in order to check the variation.

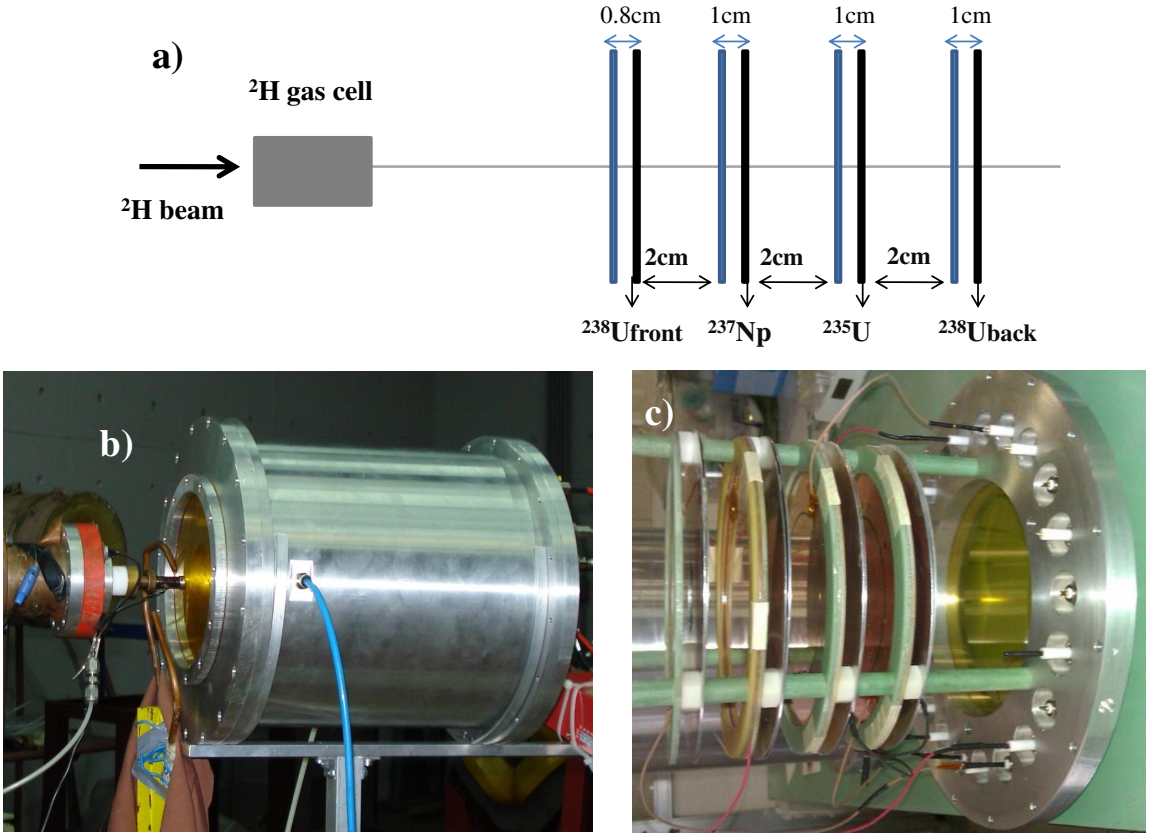

Figure 5.8: a) Schematics of the gas cell and the target assembly in the MicroMegas detector. b) A picture of the detector mounted in the beam line. c) A picture of the target and Micromesh assembly inside the detector.

Using this setup, the achieved flux was about 5×10^{4} n/(cm^{2}·s) in all four runs performed. Each irradiation lasted from 4 to 6 hours, in order to obtain good statistics (uncertainty in counting statistics less than 3 %).

As far as the electronics are concerned, low-gain charge sensitive preamplifiers (C.A.E.N. model A1422), energy amplifiers (C.A.E.N. model N968, shaping time 500 ns) and ADCs (FAST ComTec model 7072) were chosen. This choice was made in an effort to check the energy resolution of the detector, rather than use it as a simple counter and it was rendered possible due to the relatively low neutron flux, resulting in a low counting rate of fission fragments. This choice is not easily achievable with the use of the timing output of fast electronics, usually employed in Time-of-Flight experimental setups, due to the high instantaneous flux. Furthermore, the low gain was needed in order to be able to have the alpha particle signals from the natural activity of the targets as well as the neutron induced FF signals in the same spectrum (i.e. from 1-140 MeV).

During the detector tests it was found that the high alpha activity of the ^{237}Np target caused even triple pile up effects at the spectra, while for the reference target this effect was negligible. After trying various preamplifier-amplifier combinations [80], the best way to severely reduce the pile-up without affecting the energy resolution was found to be the physical reduction of the activity with a mask in front of the ^{237}Np target. Consequently, it was decided to cover each actinide target with a 0.5 mm thick aluminum mask with a hole of 4 cm in diameter. In this way all the targets had similar geometries and the alpha pile-up effect of the ^{237}Np target spectra was severely reduced.

With the above described settings, a typical spectrum from ^{237}Np can be seen in figure 5.9.

The alphas are orders of magnitude higher than the neutron induced FFs but they are well separated. A good discrimination between the heavy and light FF peaks was achieved, due to the proportionality of the detector

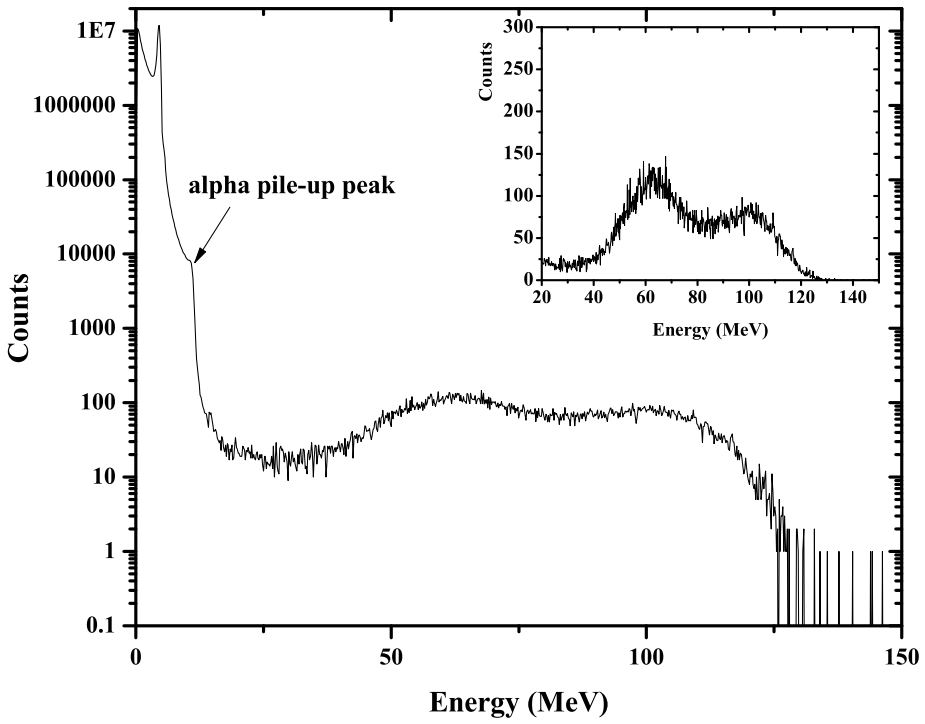

Figure 5.9: A typical spectrum obtained for the ^{237}Np target in logarithmic scale. The high alpha activity is causing pile-up effect, however orders of magnitude lower than the main peak. The inset contains the same spectrum zoomed at the fission fragment pulses, in a linear scale.

and the electronics chosen. Furthermore, the alpha peak presents two maxima (this was already seen from the detector tests), the second one corresponding to the expected alpha energies from the decay of the actinide targets. A threshold was applied in the analysis in order to remove all the alpha particles from the spectrum, estimated from beam-off spectra (chap. 6).

In order to check the performance of the detector as far as the gain and resolution function are concerned, detailed Monte Carlo simulations were performed with the code FLUKA [62] and are discussed in the next section.

5.4 FLUKA simulations and investigation of the MicroMegas detector performance

The geometry of each target-micro-bulk cell (see fig. 5.7) was implemented in the simulations, the thickness of each target was estimated from the RBS measurements considering the NpO_2 and U_3O_8 stoichiometry (see 2.3) and sources of alpha particles were isotropically distributed in the target volume (energies of the emitted alpha particles taken from [33]). The energy deposition of the alphas in the volume of the gas was scored [63]. The histogram of the simulated energy deposition for the ^{237}Np 7 target, as well as the U8 (209) target and the corresponding experimental spectra are shown in figs. 5.10, 5.11.

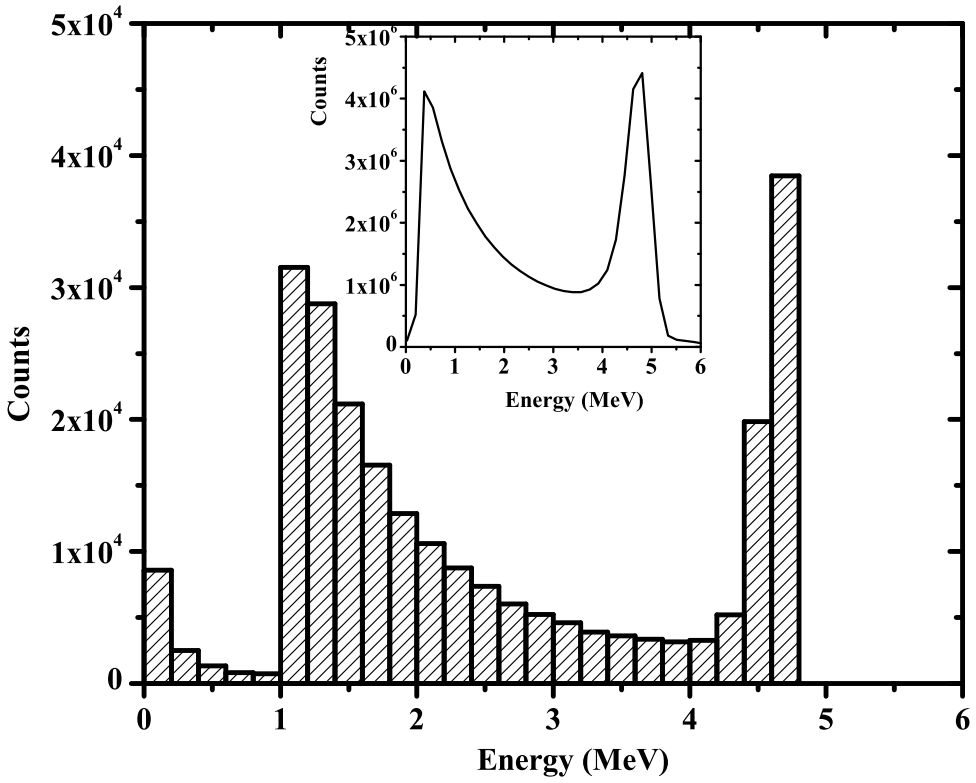

Figure 5.10: The simulated energy deposition of 4.8 MeV alphas in the gas of the detector, emitted isotropically in the ^{237}Np target. The inset contains the corresponding experimental spectrum.

Even in the absence of the correct convoluted detector resolution function, the agreement was satisfactory and the values of the simulated alpha efficiencies agreed with the experimental ones within 2-3 %, as checked with beam-off spectra. The difference in the broadening of the peaks, that appears in both the simulated and the experimental spectra between the two targets is due to the difference in thickness: from the RBS measurements it was found out that the ^{238}U targets (209, 210) are $\sim$6 times thicker than the ^{237}Np targets. Thus, the self absorption of these targets as well as the energy straggling of the ions exiting the target material and in the detector gas are larger. The first peak of alphas corresponds to the energy deposition of alpha particles leaving the target in the forward direction and traversing 0.8 or 1 cm of gas.

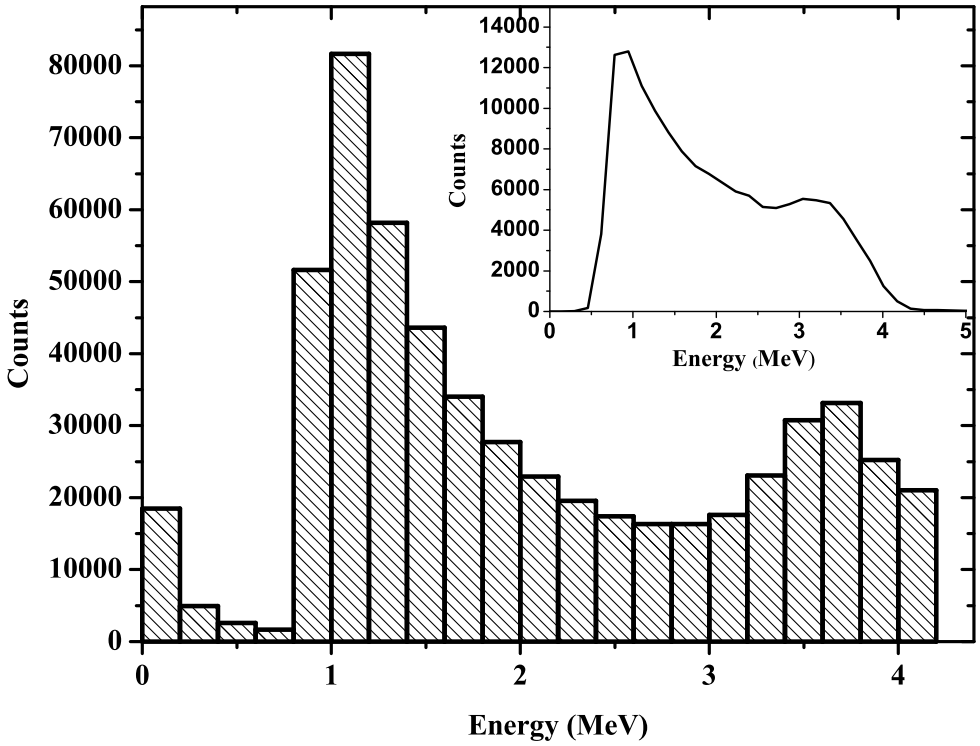

Figure 5.11: The simulated energy deposition of 4.2 MeV alphas in the gas of the detector, emitted isotropically in the ^{238}U target (label 209-front). The inset contains the corresponding experimental spectrum.

After the geometry of the simulations was validated, the FFs were generated with an external routine [63]. Details on this routine and the generation of FFs can be found in 4.4, because the same one has been used for the simulation of the FF energy deposition in the FIC detector. The emission points of the FFs produced by this routine were homogeneously distributed in the volume of the target. Equal number of heavy and light FFs (500000 from each group) was generated and emitted isotropically in an angle of 2π. The energy deposition of the FFs in the detector gas was scored.

The energy deposition histograms obtained for the ^{237}Np target, as well as the ^{238}U (209) target are shown in fig. 5.12 and 5.13.

The difference in the thicknesses of the targets is again reflected in the widths of the peaks.

Based on the FLUKA simulated histograms the calibration of the experimental spectra was made. The first interesting result was that, based on the simulated energy deposition of the alpha peak and the heavy and light fission fragment peaks, the calibration turned out to be linear, with a non-linear term 4 orders of magnitude lower than the linear one (3 points were available for fitting for the reference targets and 4 for the ^{237}Np 7 target, including the pil-up peak). The linear fitting for the channel-to-energy points for the ^{237}Np 7 target spectra can be found in fig. 5.14. This implies that the gain of the detector is practically the same for alphas and fission fragments, despite the large difference in the atomic number and energy of the ions, as well as their production mechanism. The very small non-linear term can be attributed to the recombination of electron-ion pairs which turns out to be slightly more intense along the fission fragment tracks. It has to be noted that the situation might be different if the detectors were not working at the maximum transparency region because the strong field prevents recombinations, or were filled with gas at a higher pressure.

An effort to reproduce the experimental spectrum was made, by applying a response function for the spreading of each bin from the FLUKA simulation histograms, in order to obtain the resolution function of the detector [81]. The gaussian response function given in eq. 5.1 was used,

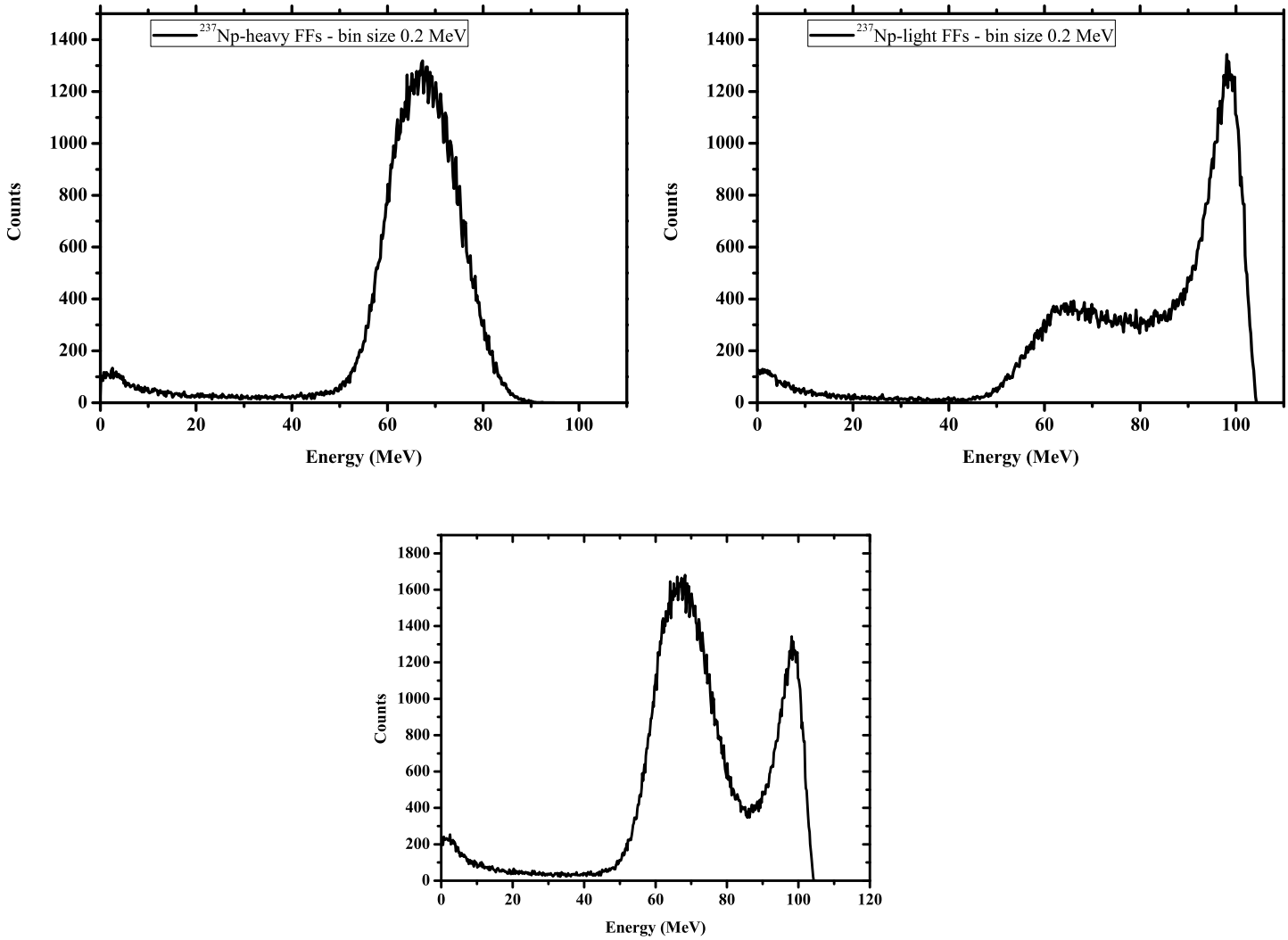

Figure 5.12: The simulated energy deposition histograms obtained for the ^{237}Np 7 target (0.1 μm thickness), with a binning of 0.2 MeV. The light and heavy FF histograms are presented separately in the upper figures.

$$G(H) = \frac{A}{\sigma\sqrt{2\pi}} e^{-\frac{(H-H_0)^2}{2\sigma^2}} \tag{5.1}$$

where G(H) is the number of counts added to channel H due to the spreading of the channel H_0 with a gaussian with a standard deviation σ, while A is a normalization factor. The comparison of the final convoluted spectrum with the experimental one for the ^{237}Np 7 target can be found in fig. 5.15 for the alphas and fig. 5.16 for the FFs. By taking into account that 1) a gaussian response function in such a large energy range is a first order approximation for the behavior of the electronics and 2) the number of counts at the tails of the heavy and light fission fragment peaks of the experimental spectrum are poor, implying that the statistics at these channels do not follow a gaussian distribution, the reproduction of the experimental spectrum is quite satisfactory.

The σ results obtained are shown in Fig. 5.17. These values are the result of the gas multiplication variations for the different isotopes and variations in the response of the electronics and show the expected increasing trend with respect to energy. Nevertheless, the resolution σ/E of the alpha peak seems to be better than the resolution for the fission fragment peaks. Apart from the uncertainties in the Monte Carlo simulation, this could be partially attributed to 1) the different ionization density of the alphas and fission fragments which makes the gas multiplication of the initial ion pairs sensitive to different factors of the detector geometry, 2) possible different transparency properties for alphas and fission fragments and 3) the non-linearities of the electronics in such a wide energy deposition range which can cause a deterioration of the resolution function.

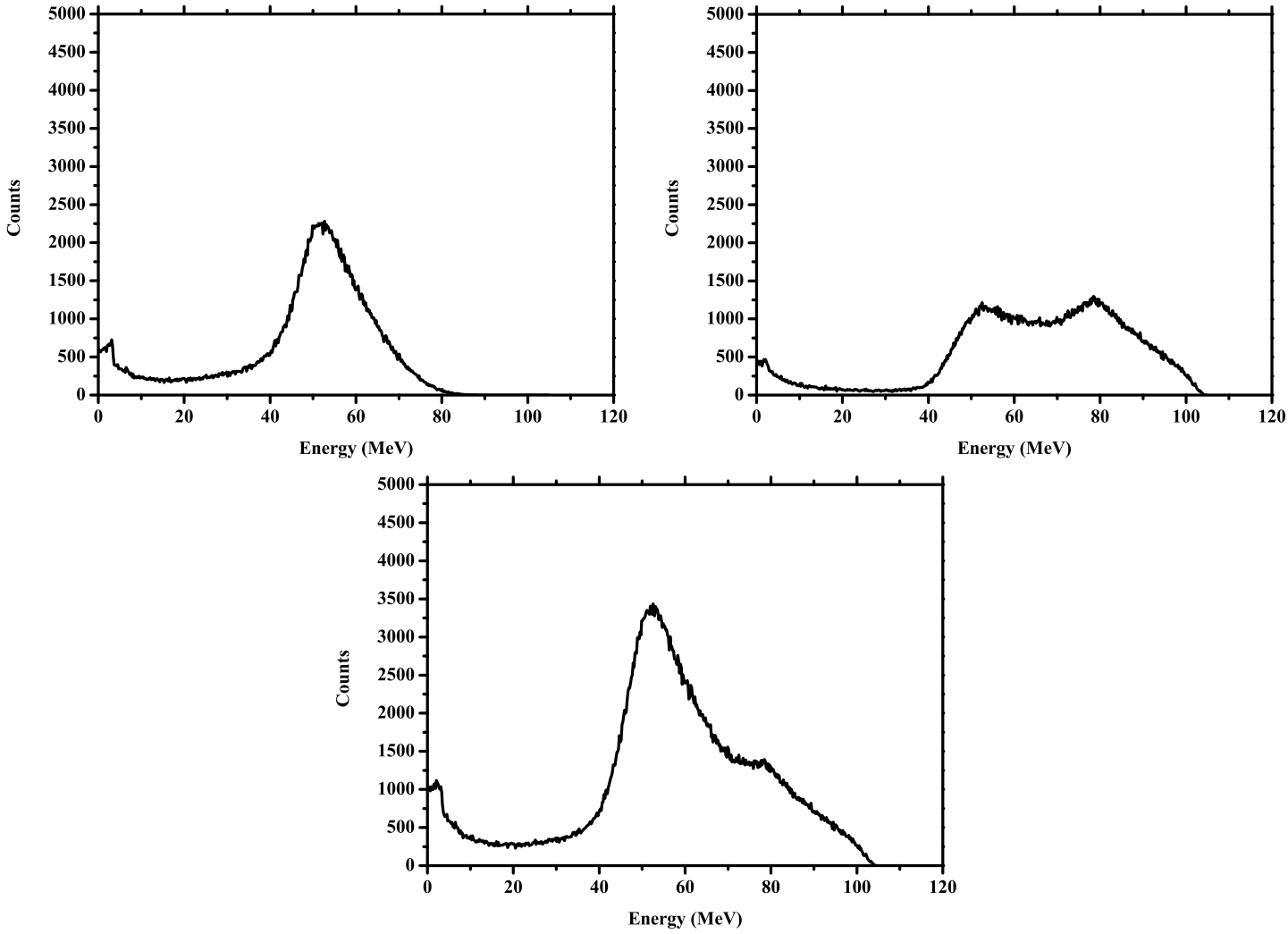

Figure 5.13: The simulated energy deposition histograms obtained for the ^{238}U target (label 209-front / ∼0.6 μm thickness), with a binning of 0.2 MeV. The light and heavy FF histograms are presented separately in the upper figures.

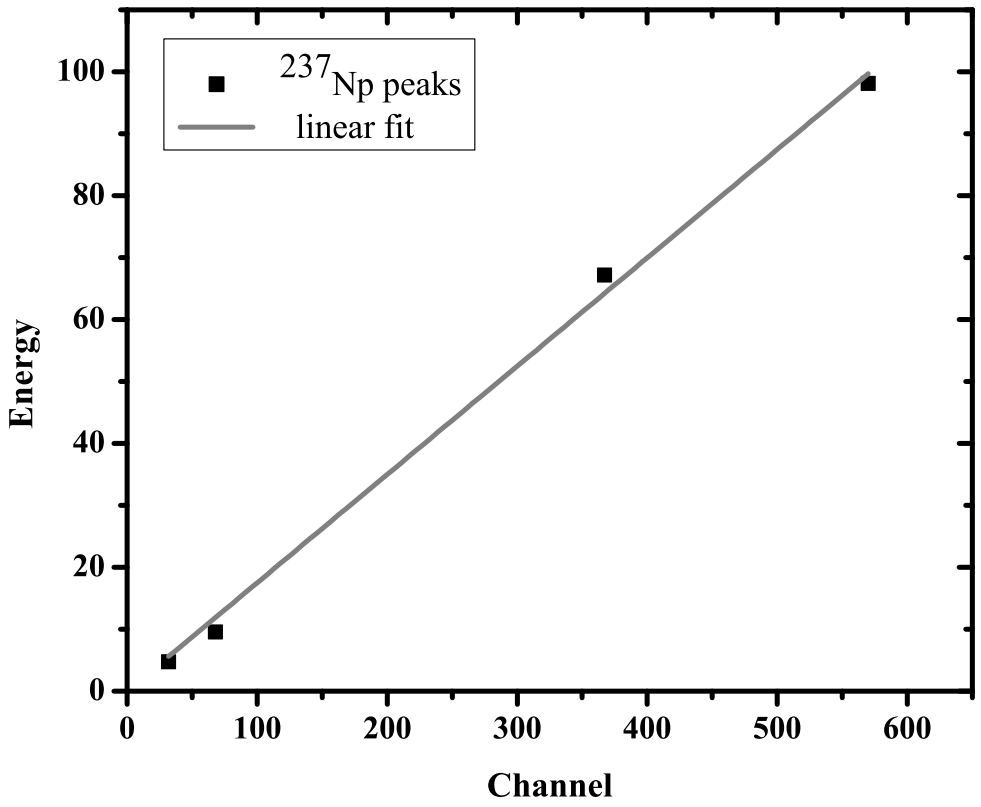

Figure 5.14: The linear calibration occured for the ^{237}Np 7 target spectra, taking into account the alpha peak, the alpha pile-up peak and the heavy and light FF peaks, with the corresponding energies from the FLUKA simulated histograms.

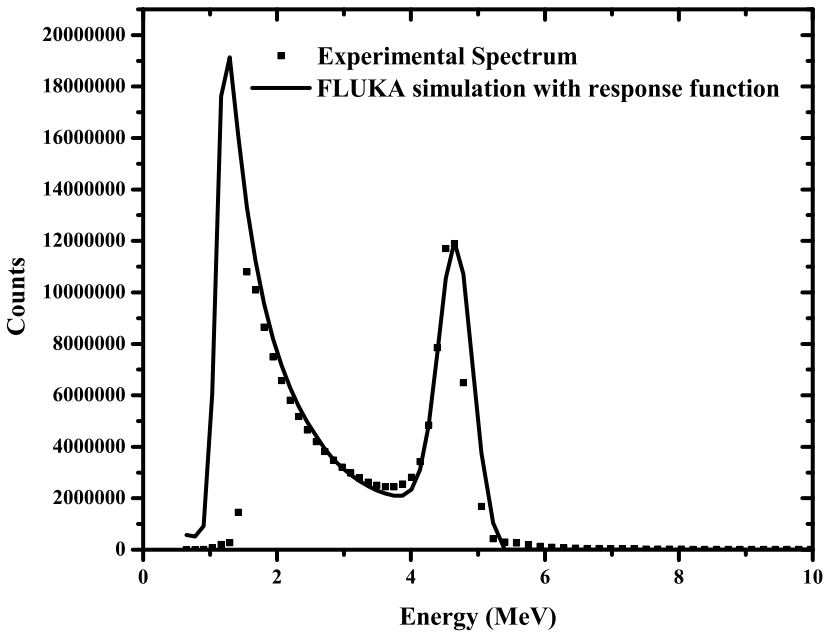

Figure 5.15: The comparison of the convoluted with a gaussian resolution function FLUKA histogram with the experimental one for the alphas. The high alpha activity of ^{237}Np caused pile up of the alpha pulses in the detector, which is not taken into account at the FLUKA simulation. A threshold was applied at the low-energy part of the experimental spectrum.

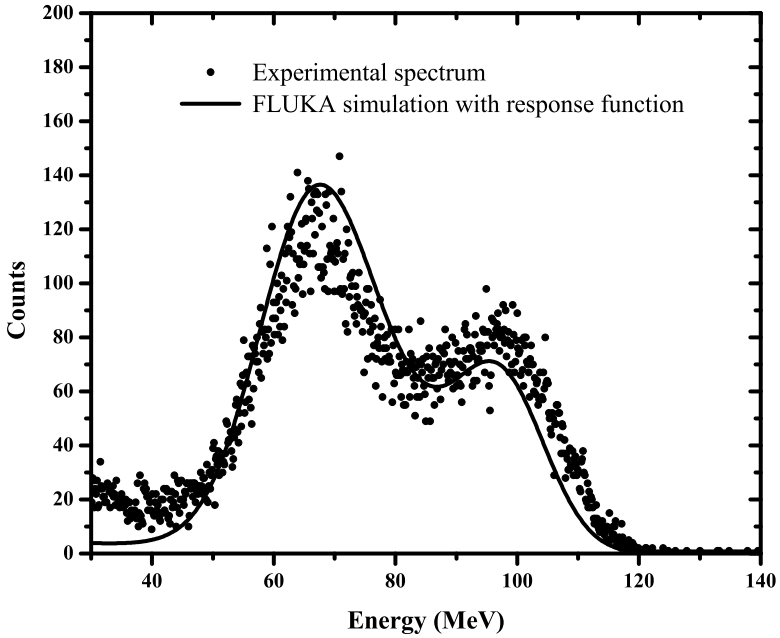

Figure 5.16: The comparison of the convoluted with a gaussian resolution function FLUKA histogram with the experimental one for the FFs of the ^{237}Np 7 target.

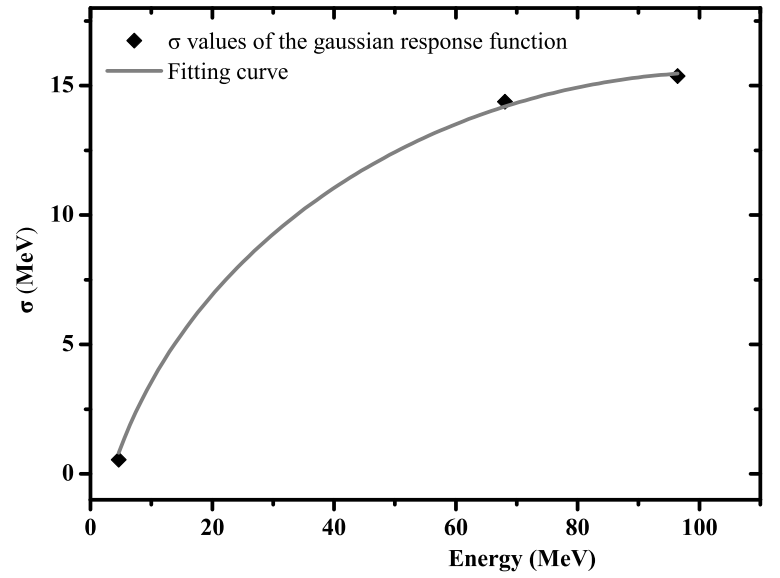

Figure 5.17: The σ values deduced from the convolution of the alpha, heavy and light fission fragment peaks. The fitting curve is of the form $\sigma = A + B\sqrt{E + CE^2}$.

Chapter 6

The ^{237}Np(n,f) measurement at "Demokritos"with the MicroMegas: Data analysis and results

The cross section σ of the ^{237}Np(n,f) reaction for each run was calculated with reference to the ^{238}U targets via the formula 6.1:

$$\sigma(E) = \frac{C_{tar} N t_{ref} \Phi_{ref} \epsilon_{ref}}{C_{ref} N t_{tar} \Phi_{tar} \epsilon_{tar}} \sigma_{^{238}U(n,f)}(E) \tag{6.1}$$

where:

1. C_{tar} and C_{ref} are the total FF yields recorded in the MicroMegas detector for each target (target -^{237}Np and reference-^{238}U) corrected with the dead time correction factor and the subthreshold counts correction factor.
2. Φ_{tar} and Φ_{ref} are the values of the neutron fluence that enters the corresponding target. The Φ_{ref}/Φ_{tar} ratio was determined by detailed Monte Carlo simulations with the code MCNP5 [82].
3. Nt_{tar} and Nt_{ref} are the total number of atoms of the corresponding target, determined from alpha spectroscopy measurements (chapter 2).
4. ϵ_{tar}, ϵ_{ref} the efficiency of the corresponding target cell, estimated from the FLUKA simulations described in 5.4.
5. $\sigma_{^{238}U(n,f)}$ is the cross section of ^{238}U(n,f) which is considered as standard [69] for which, in the energy range used in this work, the evaluations give an uncertainty of 0.8%.

For each run, two cross section values were calculated taking as a reference the ^{238}U (front) and the ^{238}U (back) target, and the weighted average value was taken as the final result.

6.1 Estimation of C_{tar} and C_{ref}

As mentioned in chapter 5 a threshold was applied during the analysis in order to remove all the alpha counts from the natural activity of the targets, chosen from beam-off spectra. The number of FF counts C_{tar} and C_{ref} was the integral of the spectra above the threshold value. Only a small fraction of fission fragments emitted

Target name	Energy of threshold (MeV)	Subthreshold counts correction factor	uncertainty
^{238}U (front)	13.7	1.077	0.0004 (stat)+ 0.003 (syst)
^{237}Np	20.1	1.048	0.0004 (stat)+ 0.0006 (syst)
^{235}U	16.1	1.060	0.0003 (stat)+ 0.002 (syst)
^{238}U (back)	10.1	1.064	0.0003 (stat)+ 0.001 (syst)

Table 6.1: The subthreshold counts correction factors obtained from the FLUKA simulation histograms. The energy which the threshold bin chosen corresponds to was estimated by calibrating the experimental amplitude distributions as explained in the text. The uncertainties reported are the statistical (stat) and the systematic (syst) obtained from the different calibrations.

Incident E_d (MeV)	Average E_d (center of gas cell)(MeV)	Average E_n(0-5^o) (MeV)
2.0	1.39 ± 0.14	4.58 ± 0.14
2.2	1.63 ± 0.13	4.85 ± 0.13
2.4	1.86 ± 0.12	5.09 ± 0.12
2.6	2.08 ± 0.11	5.32 ± 0.11

Table 6.2: The deuteron and neutron energies in the four runs performed.

at large angles exit the sample with very low energies and mix with the alpha background. The subthreshold counts correction factor was estimated from the FLUKA simulation histograms 5.4: the energy corresponding to the threshold channel was found from the calibration of each target spectra and the percentage of the fission fragments below the threshold chosen was estimated from the FLUKA simulation histograms. The subthreshold counts correction factor varied from 5 to 7%. The statistical uncertainty of the simulated subthreshold counts was 0.5-0.9%. A systematic uncertainty is implemented in the energy attributed to the ADC channel chosen as threshold, which is related to the uncertainty in the energy calibration and was estimated to be around 3% in the worst case. Nevertheless, the contribution of this uncertainty to the final cross section values was less than 0.5% in all cases (table 6.1)

The dead time correction factor was 1.5% for the C_{tar} value due to the high radioactivity of the target, while for the reference targets this correction was negligible.

6.2 Neutron beam characteristics

6.2.1 Neutron beam energy

The average energy of the deuterons in the gas cell for each run was calculated with SRIM [40], taking the center of the gas cell as reference point. The values obtained are reported in table 6.2.

The main uncertainty in the neutron energy comes from the energy straggling of the deuteron beam from the interaction with the Mo foil and the deuteron atoms in the gas cell. This uncertainty was estimated by taking into account the energy spread at the beginning and at the end of the gas cell (i.e. the maximum and the minimum values of deuteron energy at which a ^{2}H(d,n) reaction can occur) and was less than 140 keV, even at the lowest energy used in this work. Furthermore, the ^{2}H(d,n) reaction is not isotropic and the kinematics play a less significant role in the width of the final neutron energy distribution. The targets had a different angular acceptance with reference to the center of the beam, depending on their distance from the gas cell. Taking the center of the gas cell as reference point, the angular acceptance of each target with the mask was approximately 7^o for

the $^{238}U_{(front)}$ target, 6^o for ^{237}Np, and less than 5^o for ^{235}U and $^{238}U_{(back)}$. For this angular acceptance, the corresponding effect of the $^{2}H(d,n)$ kinematics in the neutron energy distribution is within 0.4 % for $^{238}U_{(front)}$, 0.3 % for ^{237}Np and within 0.2 % for ^{235}U and $^{238}U_{(back)}$. The final uncertainties reported in table 6.2 correspond to the widths of the neutron energy distributions due to both factors.

6.2.2 Calculation of the neutron fluence - the effect of low-energy neutrons

The neutron fluence was calculated from the ^{238}U reference targets. The neutron fluence ratio $\Phi_{ref}/\Phi_{^{237}Np}$ is a prerequisite for the cross section calculation (eq. 6.1) and this corresponds to a geometrical correction due to the different angular acceptance of each target. However, a simple geometrical correction is not enough in the present work because the neutron beam is produced in a large angular range and interacts with the Al housing of the detector, so the scattering of the main neutron beam at the surrounding material is not negligible and can cause a reduction of the main beam fluence, as well as the emergence of low-energy parasitic neutrons that can induce parasitic fission events. In order to estimate this effect, detailed Monte Carlo simulations using MCNP5 [82] were performed, implementing the gas cell and the MicroMegas assembly, scoring the energy distribution of the average neutron fluence in the volume of the targets (tally F4). Schematics of the simulations can be found in fig. 6.1.

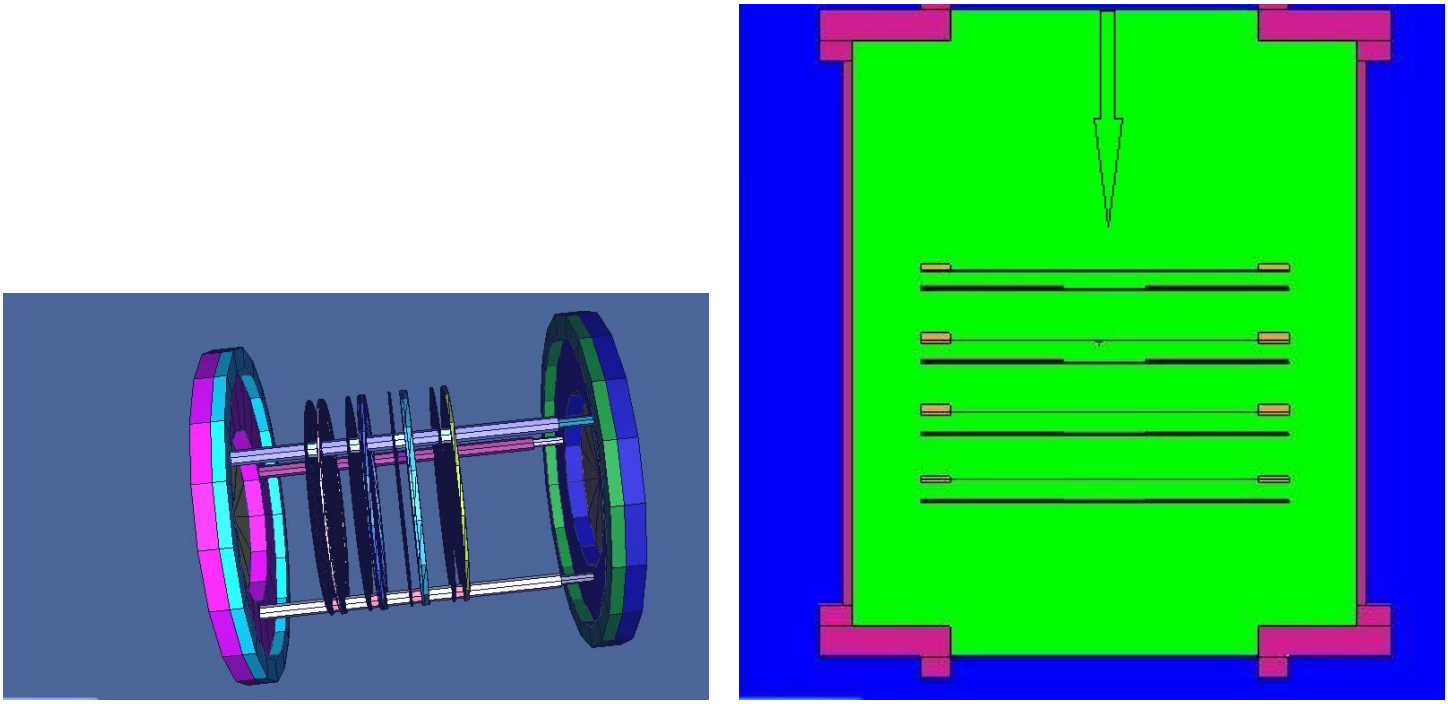

Figure 6.1: Left: A 3D view of the geometry of the Monte Carlo simulations as obtained with the 3D viewer of the MCNP5 program. The inner part of the detector is shown. Right: A 2D view of the target-microbulk assembly. The neutron beam direction is shown with the arrow.

The quality of the simulations was checked by comparing the simulated ratio $\frac{\Phi_{^{238}U_{(back)}} N_{^{238}U_{(back)}}}{\Phi_{^{238}U_{(front)}} N_{^{238}U_{(front)}}}$ to the experimental ratio $\frac{C_{^{238}U_{(back)}}}{C_{^{238}U_{(front)}}}$, and the two values agreed within error.

The $^{238}U(n,f)$ and $^{237}Np(n,f)$ reactions have thresholds that are much lower than the main neutron beam ($\sim$ 1 and 0.7 MeV respectively) so neutrons of lower energies would induce fission events in the targets. For the run of E_d =2 MeV for example, at ^{238}U (front) target approximately 6% of neutrons have energies lower than the main neutron beam (i.e. 4.58 $\pm$ 0.14 MeV) but greater than 1.5 MeV, so they would induce $^{238}U(n,f)$ events in the target with a cross section value within 5% to that of 4.58 MeV. Similarly, the corresponding value for the ^{237}Np

target is 12%, for neutrons with energies greater than 0.7 MeV, although the cross section varies within 13% in this neutron energy interval. Thus it was decided to consider as Φ_{target} the simulated average flux above the (n,f) threshold for both the ^{237}Np and the ^{238}U targets. The systematic uncertainty induced by this integration, due to the assumption of stable (n,f) cross section values above threshold was estimated by taking into account the correlation of the variation of the cross section and the neutron fluence within energy intervals from threshold to the energy of the main neutron beam and was estimated to be around 3%.

The effect of the differential cross sections of the ^{2}H(d,n) reaction on the neutron fluence was also investigated in the simulations. From [83], the neutron flux within 5-10^{o} is approximately 3% less than within 0-5^{o} for the 2.6 MeV incident deuteron beam, while at 2 MeV the corresponding value is less than 2.5%. This has to be taken into account in the flux estimation for the ^{238}U (front) and ^{237}Np targets (^{238}U (back) has an angular acceptance less than 5^{o}). This effect was checked by implementing the angular distribution of the neutrons and scoring the neutron flux in the part of the target included in the mask. The effect at the ratio of the fluxes was less than 1.5%, and the effect at the final cross section values was within error.

It has to be noted that when all the materials of the MicroMegas assembly were removed from the geometry of the simulation the flux of neutrons with energies greater than 1.5 MeV (that induce fission events at ^{238}U) changed within 5-8% which means that the MicroMegas chamber somewhat contributes to the scattering of the neutrons. It is true that the micromeshes of the detector used, due to the little mass achieved with the micro-bulk technique, are considered to cause the minimum possible scattering of the neutron beam [76] but the detector has been optimized for parallel neutron beams as in the n_TOF facility. The neutron beam from the ^{2}H(d,n) reaction is produced in a large angular range, thus the scattering from the Al housing of the detector assembly is unavoidable. Consequently, Monte Carlo simulations were essential for a reliable determination of the neutron fluence.

6.2.3 Investigation of low-energy neutrons from parasitic reactions

In the present case, the deuteron break-up reaction (for $E_d > 4.45$ MeV), which is a major source of parasitic neutrons of lower energy than the main beam, is not a problem since the deuteron energy range used is well below the threshold. Furthermore, possible reactions of the deuteron beam with the Mo isotopes in the gas cell entrance window and produce high energy parasitic neutrons around the main neutron beam region occur for deuteron energies above the Coulomb barrier (Ed $>$ 5 MeV) so they are also excluded in this case. A fresh Pt foil was used before the measurement in order to minimize the presence of implanted deuterons which could undergo ^{2}H(d,n) reactions with different energies than the expected ones (with the center of the gas cell as the reference point). Nevertheless, other (d,n) reactions can occur in impurities at the collimation system and/or the gas cell materials. The existence of such neutrons can be checked by their effect on the ^{235}U fission events, since fission on this actinide has no threshold and its high cross section down to the thermal energies provides high sensitivity for their detection. By calculating the cross section with formula 6.1 taking ^{235}U as the reference target, the ^{237}Np cross section turned out to be about 3 times smaller than the corresponding value with ^{238}U. This means that extra C_{U5} are induced by neutrons with lower energies. This large difference can not be properly explained by the scattered neutrons of the main beam in the MicroMegas assembly, because the MCNP5 simulations showed that, taking into account the neutron flux at different energy intervals from thermal energies to the energy of the main neutron beam correlated to the corresponding ^{235}U(n,f) cross section value, the effect of the scattered neutrons at the ^{235}U(n,f) events would be approximately 25-30%. Thus the extra fission events could only be caused by neutrons from parasitic (d,n) reactions.

In an effort to check the energy range of these parasitic neutrons, additional tests were performed with a HPGe detector, implementing the method suggested in [84] i.e. the ^{74}Ge(n,γ)^{75m}Ge activation reaction by low energy neutrons. This capture reaction produces the 139.68 keV isomeric state in ^{75}Ge ($J^{\pi}=+7/2$) which decays by isomeric transition (99.97%) with a half life of 47.7 s. As reported in [84], the measurement of the ^{75m}Ge activity is a very sensitive detection tool for low thermal neutron fluxes ($\approx$25 n/cm^2). However, it has to be noted that few experimental data exist for the ^{74}Ge(n,γ)^{75m}Ge cross section [85, 86], which state a cross section at thermal neutron energies greater than 100 mb. A HPGe detector of 56% relative efficiency was used, with a Cd shielding around the cylinder of the crystal. The HPGe detector was put right behind the MicroMegas assembly with reference to the beam direction, coaxially to the deuteron beam axis, at approximately 5 cm distance from the exit window of the detector housing (fig. 6.2).

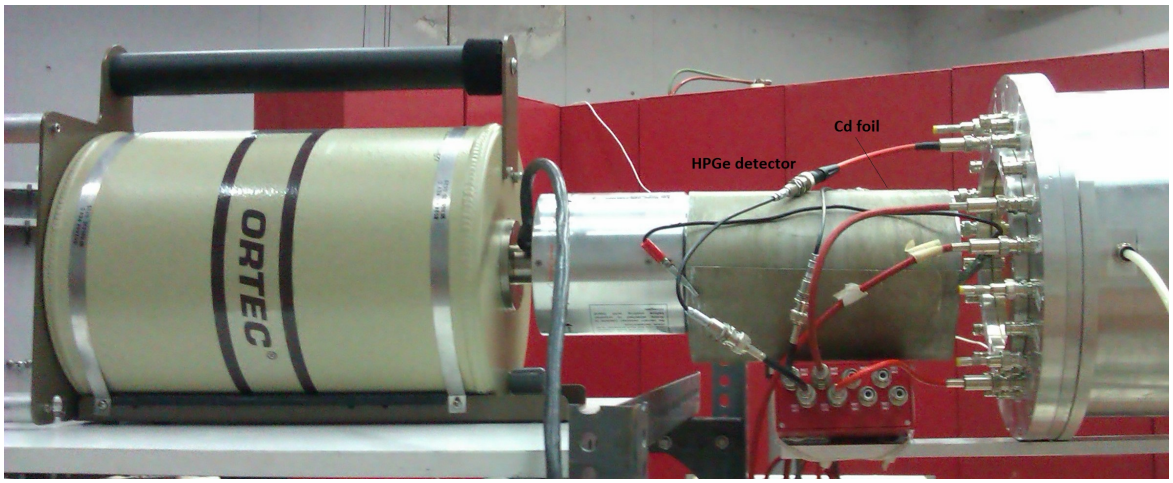

Figure 6.2: A photo of the HPGe detector used for the low-energy neutron investigation, put behind the MicroMegas detector, with reference to the beam direction, coaxially to the deuteron beam axis. The Cd foil surrounding the germanium detector is also shown.

A beam-off spectrum showed mainly gamma ray peaks from the ^{233}Pa isotope, daughter nucleus of ^{237}Np. The deuteron current was less than 100 nA and each irradiation lasted approximately 180 s, in order to obtain saturation activity. Thus the neutron fluence for each run was approximately 10^5 n/cm^2 in order to minimize

E_n	σ (b)	$\delta\sigma$ (b)	$\sigma_{^{238}U(n,f)}$ (b)
4.58 ± 0.14	1.59	0.05	0.546
4.85 ± 0.13	1.50	0.03	0.548
5.09 ± 0.12	1.50	0.03	0.553
5.32 ± 0.11	1.50	0.03	0.558

Table 6.3: The final cross section values-the uncertainties reported are only the statistical ones. The recommended ^{238}U(n,f) cross section values used [69] are also included.

Contribution	Uncertainty (%)
Target mass	1.3-1.7
Subthreshold counts correction	$\prec$0.5
Efficiency correction	2-3
Neutron Fluence	3-4
$\sigma_{^{238}U(n,f)}$	$\prec$ 0.9

Table 6.4: Contribution of the systematic uncertainties of the different factors to the cross section calculation

the risk of neutron damage to the detector. Right after the irradiation, the spectrum of the detector was recorded for two subsequent time intervals of 180 s in order to check the decay of the 139.68 keV gamma ray peak. The incoming deuteron beam energy was changed from 2 MeV to 5 MeV, with steps of 200 keV. The gamma ray peak of interest did not appear below 4.6 MeV (i.e. 7.5 MeV neutron energy) but due to the very high background and the electronic dead time of approximately 20% no accurate quantitative results could be extracted. However, by comparing the spectra from different energies and between the two time intervals, it could be verified that from the energy of 4.6 MeV and above there are some gamma ray events in the 139.68 keV region slightly above the limit of detectability at this region that vanish below a deuteron energy of 4.4 MeV (i.e. 7.23 MeV neutron energy). The energy region used in this work is well below this limit so it can be safely concluded that the contribution of any possible parasitic thermal neutron flux in the obtained cross-section values was negligible. Thus, the main population of parasitic neutrons was of higher energies, but at energy regions well below the ^{237}Np(n,f) threshold, where the cross section ratio $\frac{^{235}U(n,f)}{^{237}Np(n,f)}$ is orders of magnitude larger than the corresponding one at the main beam energy. Such parasitic neutrons could explain the observed difference in the cross section values of the ^{237}Np(n,f) with respect to ^{235}U(n,f) and to ^{238}U(n,f), which presented a ratio of approximately 3. Their origin could be possibly explained by threshold (d,n) reactions with contaminants in the collimators and in the Mo entrance foil, mainly ^{16}O(d,n) (threshold at 1.828 MeV) or ^{12}C(d,n) (threshold at 0.328 MeV). However, their effect on the number of ^{237}Np(n,f) events would be negligible, in the energy range used in his work, and based on calculations, their effect would be evident for incident deuteron energies $\geq$ 3 MeV. A possible solution to this problem, in order to extend the neutron energy range would have been to perform gas-out runs with the same conditions as the gas-in ones, and will be examined in a future work.

6.3 Cross section results

The cross section values obtained with the above analysis along with their statistical uncertainties are reported in table 6.3.

The contribution of the systematic uncertainties to the final cross section values are listed in table 6.4.

The comparison to other data found at EXFOR [7] in the energy range and the ENDF/B-VII.1 [28] and JENDL-4.0 evaluations [29] is presented in fig. 6.3.

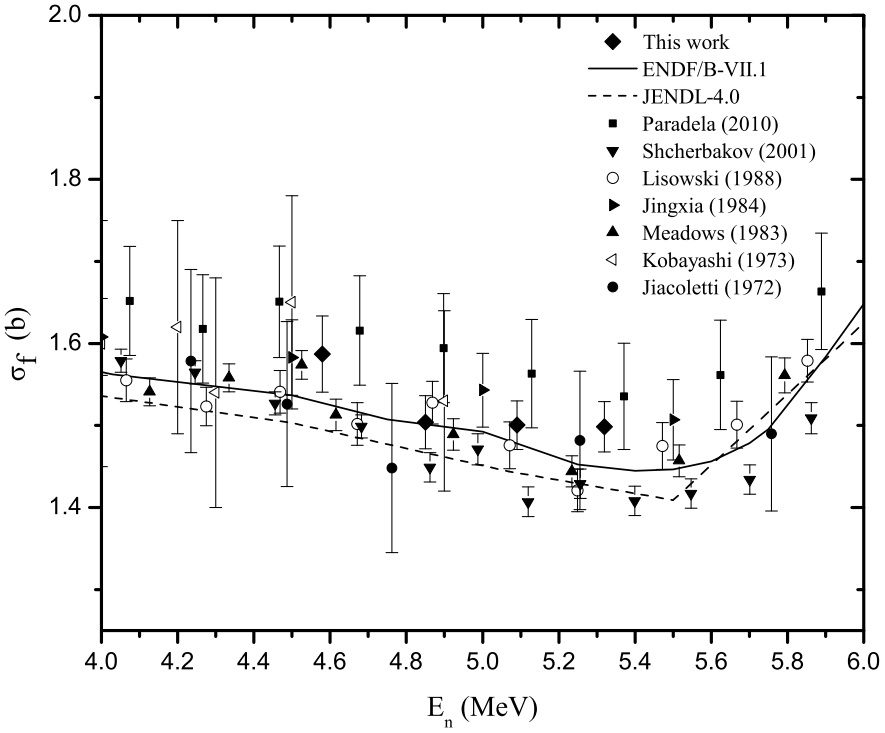

Figure 6.3: The ^{237}Np(n,f) cross section values in comparison with previous measurements and the ENDF/B-VII.1 and JENDL-4.0 evaluations, as well as the results from the analysis of the FIC detector data at the n_TOF facility. The error bars of the present data correspond to the statistical uncertainties.

Firstly it has to be noted that, in this energy range, the four data points obtained from this work agree with the ENDF/B-VII.1 evaluation, within 1 standard deviation is taken into account, and even higher when compared to JENDL-4.0. The present data seem to be in agreement with the newest data of Paradela (2010) [8], although the central cross section values are systematically lower. The data from Shcherbakov (2001) [11] seem to be in agreement with the present data up to 5 MeV, though systematically lower, but above this energy the difference exceeds one standard deviation. The dataset of Lisowski [13] agrees within error with the present data, apart from the cross section value at 5.25 MeV, which is significantly lower. The dataset of Jingxia (1984) [16] is also in agreement with the present data, though after 4.8 MeV the central values are somewhat higher. The data of Meadows (1983) [18] are systematically slightly lower than the present data, but agree within error. Finally, the present data seem to be lower than the older data of Kobayashi (1973) [21] and higher than those of Jiacoletti (1972) [22] although the large errors of these datasets preclude any proper comparison.

Cross section data with only one data point in the energy range used in this work were not included in the figure ([12, 23, 25, 27]), so it has to be noted that the present data seem to be in agreement with Merla (1991) (at 4.9 MeV $\sigma_{^{237}Np(n,f)} = 1.54 \pm 0.03$ b - [12]), a bit higher but within experimental errors than Stein (1968) (at 4.5 MeV $\sigma_{^{237}Np(n,f)} = 1.54 \pm 0.05$ b - [23]) and lower than White (1967) (at 5.4 MeV $\sigma_{^{237}Np(n,f)} = 1.6 \pm 0.1$ b -[25]). Finally, in the dataset of Pankratov (1963) [27] there is one cross section value in the energy range 4.5-5.3 MeV ($\sigma_{^{237}Np(n,f)} = 1.42$ b at 5.2 MeV) which is lower than the value expected from this work.

Datasets with the cross section ratios $\frac{\sigma_{^{237}Np(n,f)}}{\sigma_{^{235}U(n,f)}}$ also exist for the 5 MeV region ([9, 15, 14, 20]). Using the corresponding $\sigma_{^{235}U(n,f)}$ value from [69] to get the $\sigma_{^{237}Np(n,f)}$ in the energy range 4.58-5.32 MeV, it can be said that the present data are i) a bit higher but agree within the experimental errors with Tovesson (2010) [9], ii) in good agreement with Goverdovskii (1985) [15] and Terayama (1986) [14] and iii) higher than Behrens (1982) [20].

All the previous data found in literature use ^{235}U(n,f) as the reference reaction. Two datasets were found relative to ^{238}U(n,f) in the 5 MeV region, of Grundl (1967) [24] and an older work of Schmitt (1959) [26]. According to the first work $\sigma_{^{237}Np(n,f)} = 1.47 \pm 0.07$ b at 4.9 MeV, and a monotonically increasing trend is proposed in the 5 MeV region, which is attributed to the ^{238}U(n,f) cross section values used. The data of the latter work are generally lower than the present data, and show no specific trend since they present large deviations among them. In general, differences from older data can be partially attributed to normalization to evaluated cross section values of the reference reaction that changed.

Finally, the cross section data obtained with the MicroMegas detector agree very well with the n_TOF cross section data obtained with the FIC detector as seen in fig. 6.4.

This is very important because two independent measurements at two different facilities gave similar results, giving confidence about the reliability of the obtained cross section data. Thus, the new detection setup with the MicroMegas detector at the Tandem laboratory of the I.N.P.P. at “Demokritos ”can be used as a complementary system to the wide energy range n_TOF data for the extraction of single energy cross section data. Especially in the case of the ^{237}Np(n,f) cross section this double-check was necessary, in order to reduce the systematic uncertainties related to a single measurement, since the difference of 7% of the latest data of Paradela (2010) from previous datasets and evaluations was relatively small to be resolved by one experiment, but unaccepatably large for the needs of accurate subsequent theoretical investigation or the design ofthe future nuclear reactor technology.

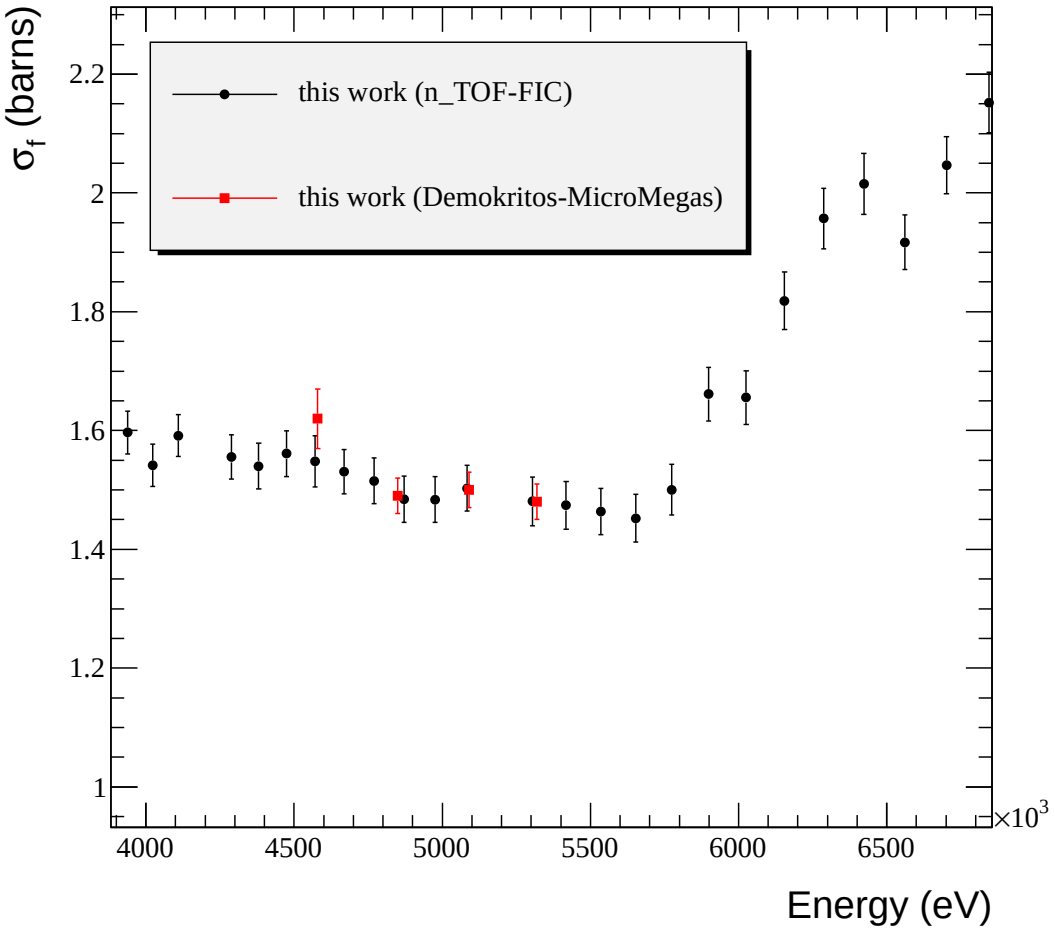

Figure 6.4: The ^{237}Np(n,f) cross section value results from the measurements at ``Demokritos" with the MicroMegas detector, compared to the corresponding values from the analysis of the FIC detector data at the n_TOF facility, performed in the context of the present thesis.

Chapter 7

Theoretical investigation of the ^{237}Np(n,f) cross section

7.1 Characteristics of the nuclear fission

Nuclear fission is a rather complicated process in which a highly-deformed heavy nucleus undergoes a deep rearrangement, breaking into two fragments of comparable masses. The discovery of nuclear fission was made in an effort to produce and study nuclei with increasing atomic numbers by the irradiation of elements by neutrons (started in the 1930s, by Fermi). When natural uranium (99.3% ^{238}U and 0.7% ^{235}U , atomic number 92) was bombarded in order to produce transuranic elements, β^--emission was observed from barium (atomic number 56), instead of elements with larger atomic numbers than uranium. This was confirmed by experiments performed by Hahn and Strassmann (1939 - [89]). This strange behavior in combination with the large energy released by the neutron capture on uranium was explained by Meitner and Frisch in 1939 [90] who were the first to propose that the uranium nuclei following neutron capture are highly unstable and split in two nearly equal parts, or *fission* (term borrowed from biology, used for the cell division). They explained the phenomenon in terms of the splitting of a vibrational liquid drop into two smaller ones. Shortly after, Bohr and Wheeler [91] provided a full theoretical description of the fission mechanism, on the basis of the Liquid Drop Model (LDM). However, the theoretical investigation of the fission process is still ongoing with many new experimental evidence showing that it is a much more complicated procedure than it was initially thought. The first experimental evidence of fission is briefly described in [92]. A simplified desription of the fission mechanism and the fission fragment (FF) characteristics is given below [2, 93, 94].

In the context of the LDM, the concept of the fission barrier is based on the classical description of the nucleus as an electrically charged liquid drop, given in [90, 91]. The nucleus is represented by a spherical drop of incompressible nuclear liquid in which the nucleons interact with a limited number of their nearest neighbours. The analogy of the nuclear behavior to that of a charged liquid drop is reflected by the standard semiempirical formula for the binding energy of nuclear ground states, eq. 7.1:

$$E = E_{vol} + E_{surf} + E_{coul} + E_{sym} + E_{pair} \tag{7.1}$$

where: a) $E_{vol} = -c_1 \cdot A$ is the volume energy, assuming that all the nucleons are of equal importance and attract only the nearest neighbours (A is the mass number of the nucleus). b) E_{surf} is the surface energy term, with opposite sign than the volume term, reflecting that the nucleons at the surface of the drop are only attracted towards the drop, so they contribute less to the binding energy: $E_{surf} = c_2 \cdot A^{2/3}$ (surface tension). c) E_{coul} is the Coulomb energy term from the repulsion of the protons reducing the total binding energy, proportional to Z^2 and inversely proportional to $A^{1/3}$: $E_{coul} = c_3 \cdot Z^2/A^{1/3}$. d) E_{sym} is the symmetry energy term, reflecting

the tendency of nuclei to be symmetric, i.e. have Z=N, especially in lighter nuclei and it given by $E_{sym} = -c_4 \cdot (A-2Z)^2/A$: nuclei with Z=A/2 are favored because this term is vanished and for heavy nuclei this term is severely reduced. e) E_{pair} is the pairing term, of quantal origin, that takes into account the tendency for the same kind of nucleons to couple pairwise to form stable configurations (pairing force): $E_{pair} = \pm\delta = \pm c_5 \cdot A^{-3/4}$, where the +/- sign is used for odd-odd or even-even nuclei, respectively (for odd-A nuclei this term is 0). The factors $c_1 - c_5$ are stable and are obtained from the systematic trend of the resulting binding energy E versus A.

If the initially spherical liquid drop gets deformed, but the nuclear fluid is assumed incompressible (so the volume is constant), then only the E_{surf} and E_{coul} terms of the binding energy will be affected (equation 7.1). The ``stretched" nucleus is represented by an ellipsoid of revolution, and if α is the semimajor axis and *b* the semiminor axis, then the deviation of the ellipsoid from a sphere with radius R is given in terms of a distortion parameter ϵ, which is the eccentricity of the ellipse (eq. 7.2).

$$\begin{aligned} \alpha &= R(1+\epsilon) \\ \beta &= R(1+\epsilon)^{-1/2} \end{aligned} \tag{7.2}$$

This choice of axes is consistent with the incompressibility of the nuclear liquid because the volume of the nucleus $V = (4/3) \cdot \pi\, \alpha\, b^2 = (4/3) \cdot \pi\, R^3$ is the same at the ellipsoidal shape and the sphere. The so-called deformation parameter β is related to the eccentricity parameter ϵ by eq. 7.3.

$$\beta = \epsilon\sqrt{4\pi/5} \tag{7.3}$$

The surface S of the liquid drop increases, and it can be expanded as: $S = 4\pi R^2(1 + \frac{2}{5}\epsilon^2 + ...)$, increasing the surface energy term E_{surf} accordingly. The Coulomb energy term is decreased by a factor $(1 - \frac{1}{5}\epsilon^2 + ...)$, thus the difference ΔE in the binding energies between the spherical nucleus and the ellipsoid of the same volume is given by eq. 7.4:

$$\Delta\, E = E(\epsilon) - E(\epsilon = 0) \tag{7.4}$$

$$= c_2 \cdot A^{2/3}(1 + \frac{2}{5}\epsilon^2 + ...) + c_3 \cdot Z^2/A^{1/3}(1 - \frac{1}{5}\epsilon^2 + ...) - c_2 \cdot A^{2/3} - c_3 \cdot Z^2/A^{1/3} \tag{7.5}$$

$$\approx -\frac{2}{5}E_{surf}(\epsilon = 0) + \frac{1}{5}E_{coul}(\epsilon = 0) \tag{7.6}$$

If the second term is larger than the first, then the $\Delta\, E$ turns out to be positive and thus energy is gained when the liquid drop is stretched, so the nucleus will keep on stretching, gaining more and more energy until it is separated into two parts. Thus a nucleus with $\Delta\, E > 0$ will undergo spontaneous fission, without the need of additional energy. This condition, based on eq. 7.4 gives: $\frac{E_{coul}}{2E_{surf}} > 1$, for this reason the ratio $x = \frac{E_{coul}}{2E_{surf}}$ is called the *fissility parameter*. Numerical calculations for these terms give a typical value $x \approx \frac{1}{50}\frac{Z^2}{A}$. If x>1, fission will occur as already mentioned, and this stands for nuclei with $\frac{Z^2}{A} > 50$, and the larger x value the shorter the half life for the spontaneous fission of the nucleus. If x<1, fission will not occur spontaneously, but as the deformation (ϵ) of the nucleus increases, other terms at the Taylor series start to be more important (for example ϵ^3) so $E(\epsilon)$ increases, reaches a maximum and then decreases. The actinides present x values of 0.7-0.8. A typical set of energy contours in the plane defined by two of the most important parameters in the fission process (the quadrupole and hexadecapole coefficients in a Legendre polynomial of the liquid drop surface) is shown in the upper schematics diagram of fig. 7.1. The energetically most favorable path from the ground state of the nucleus towards fission on this ``potential energy surface" is shown with a broken line and the potential energy corresponding to this path is shown in the lower schematics diagram of fig. 7.1.

The potential energy barrier shown in this figure is the *fission barrier* and corresponds to the difference $E_f = E_{max} - E(\epsilon = 0)$. Transmission through this barrier towards fission can happen with the tunneling effect.

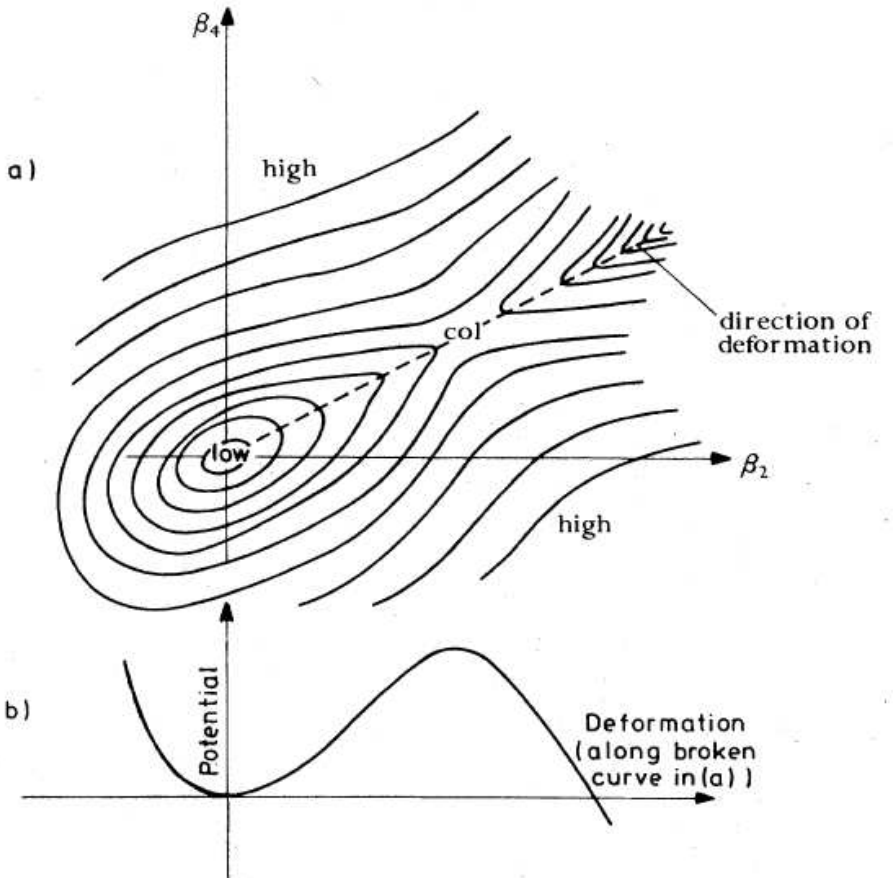

Figure 7.1: a) Schematics diagram of the potential energy surface of a fissionable nucleus as a function of the quadrupole and hexadecapole deformation parameters. The energetically more favorable path to fission is shown with a dotted line and the potential energy barrier is marked with ``col". b) The potential energy along the minimum energy trajectory for increasing elongation. (picture taken from [93]).

Otherwise, energy has to be provided to the nucleus in order to surpass the fission barrier (``induced fission"). If the barrier is assumed to have an inverted harmonic oscillator form, the transmission coefficient of the barrier depends on the barrier height E_f and the frequency of the oscillator ω, and is given by eq. 7.7 [93] (Hill-Wheeler transmission coefficient).

$$T = (1 + exp(2\pi\,(E_f - E)/(\hbar\omega))^{-1} \tag{7.7}$$

7.1.1 The double-humped fission barrier

The first weakness of this picture of the fission barrier was found when a quantitative estimation of the barrier heights was made: the LDM calculations predicted barrier heights that varied from 7.5 to 2.8 MeV in the region from ^{230}Th to ^{253}Cf , while the experimental observation showed that the barriers are nearly the same. This difference was attributed to nucleon shell effects near shell closures, and for this reason Strutinsky proposed [95, 96] the addition of an extra term in the calculation of the ground state binding energy, eq. 7.1, related to the shell effects. With the addition of this extra term, the observed ground-state quadrupole moments, the deviations of magic nuclei energies from the smoothed liquid drop behavior and the fission barrier heights were successfully reproduced. Furthermore, it indicated an oscillation of the energy curve of actinide nuclei with increasing deformation, and thus the simple shape of fig. 7.1 was replaced by a barrier with two minima (``wells"), the so-called *double-humped barrier* (fig. 7.2). The deformation at the second well corresponds to

a spheroidal shape with a ratio of major to minor axis 2:1, giving rise to considerable shell structure and thus great stability for particular nuclei with the appropriate number of protons and neutrons.

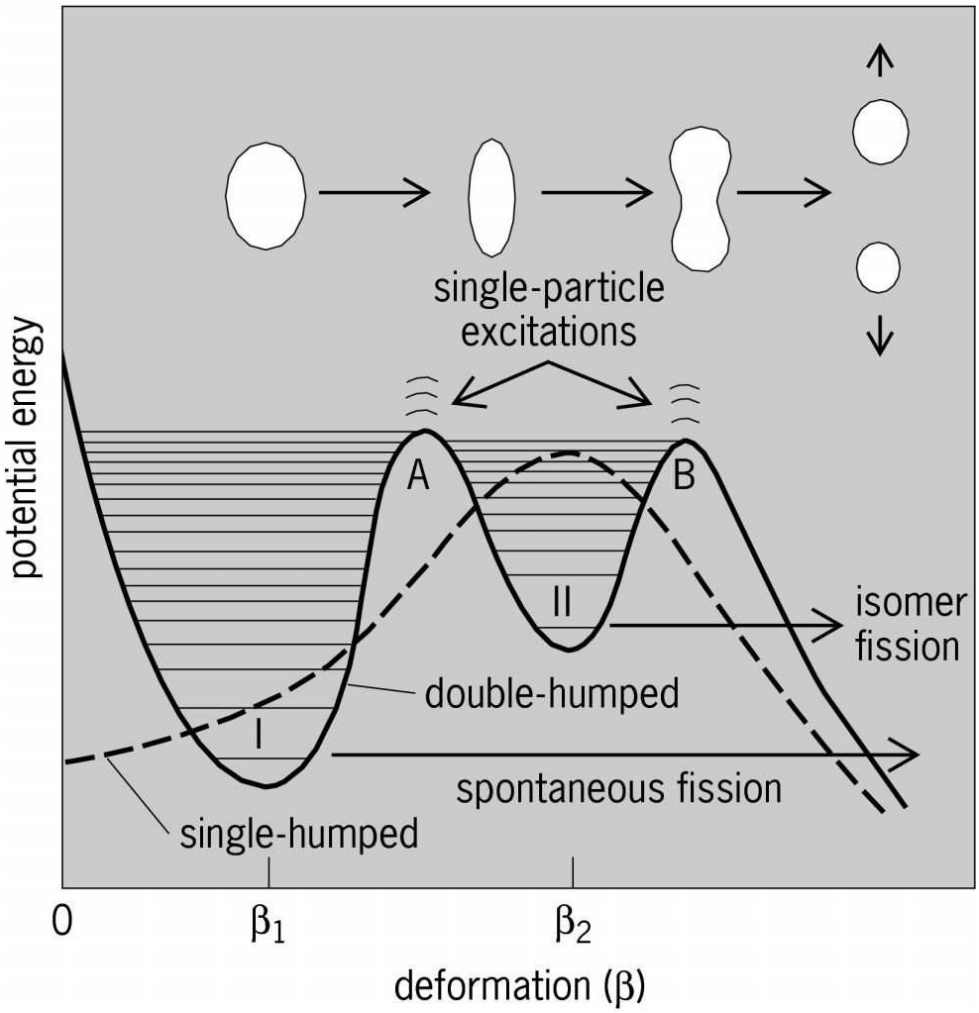

Figure 7.2: Energy of the nucleus as a function of deformation, along the energetically most favorable path to fission. The penetrability of the second hump of the barrier is greater than that of the whole barrier. The nuclear states in the first and the second well are referred to as class I and class II states, while the states on the top of the barriers are the intrinsic or transition states. The dashed line is the energy predicted by the LDM without shell corrections.

The first minimum is containing the ground state and the first excited levels (``class I'' states), while the second one also contains states, mainly of collective nature due to the large deformation of the nucleus at this point (``class II'' states). Furthermore, the states on the top of the barriers are the ``intrinsic'' or ``transition'' states. The experimental observations for which the double-humped barrier provided explanation were a) the existence of spontaneously fissioning isomers with extraordinary stability against γ decay and unusually short half lives for spontaneous fission (the first fissioning isomer was a 14ms state of ^{242}Am [97]) b) the structure in fast neutron-induced fission cross sections with neutrons above 10 keV and c) narrow intermediate structures in slow neutron fission cross section (eV-keV region), especially for even-even (like ^{238}U) and odd-Z nuclei (like ^{237}Np). The spontaneously fissioning isomer of a nucleus is explained as being a vibrational state in the secondary well, and more specifically the lowest state of the class II levels, associated with the highly deformed shape of the nucleus at the secondary well. From these states the nucleus can either decay to the first well or fission. The levels in the second well fission much more easily than levels with the same energy in the first well, because only the second barrier needs to be traversed and are much less dense because they occur from increase in the potential energy due to deformation alone, and not due to excitation of internal degrees of freedom. The resonance structure at the fission cross sections can be explained by the coupling of class I and the more widely spaced class II states. For energies below the first fission barrier height (A) the two groups of levels are well separated. For high

excitation energies above the barrier A, the two types of levels will be coupled. In an intermediate case, there will be a weak coupling between the two types of states through the barrier A. As a general remark, calculations have shown that for the actinides the height of the first barrier is $\sim$6-7 MeV high, the secondary minimum at a prolate deformation and approximately 2-3 MeV shallower than the main well and the second maximum has the same height as the first one for the uranium isotopes, while it decreases as A increases [93]. It has to be noted that the double-humped barrier is not enough to explain some narrow resonances in the threshold region of neutron-induced fission on some light actinides, as ^{230}Th and ^{232}Th, (``thorium anomaly'') and even a triple humped barrier was proposed, initially in [98].

7.1.2 Fission modes - Properties of the fission fragment generation

The nuclear fission is a process dividing the nucleus into two nuclei, the so-called fission fragments (FFs), along with the emittance of neutrons and energy. The fissioning nucleus starts elongating from the initially spherical shape towards the development of two nucleon clusters that form the two nascent FFs with mass M1 and M2 separated by the so-called ``neck'' (fig. 7.3). In case M1=M2 then fission is called mass-symmetric, otherwise it is called mass-asymmetric. The shape dynamics of the fissioning nucleus at the pre-scission phase play an important role in determining the exit channel. The neck rupture can occur at any point leading to different characteristics of FFs and number of emitted neutrons. The Coulomb repulsion between the two fragments at the point of the scission increases the kinetic energy of the FFs.

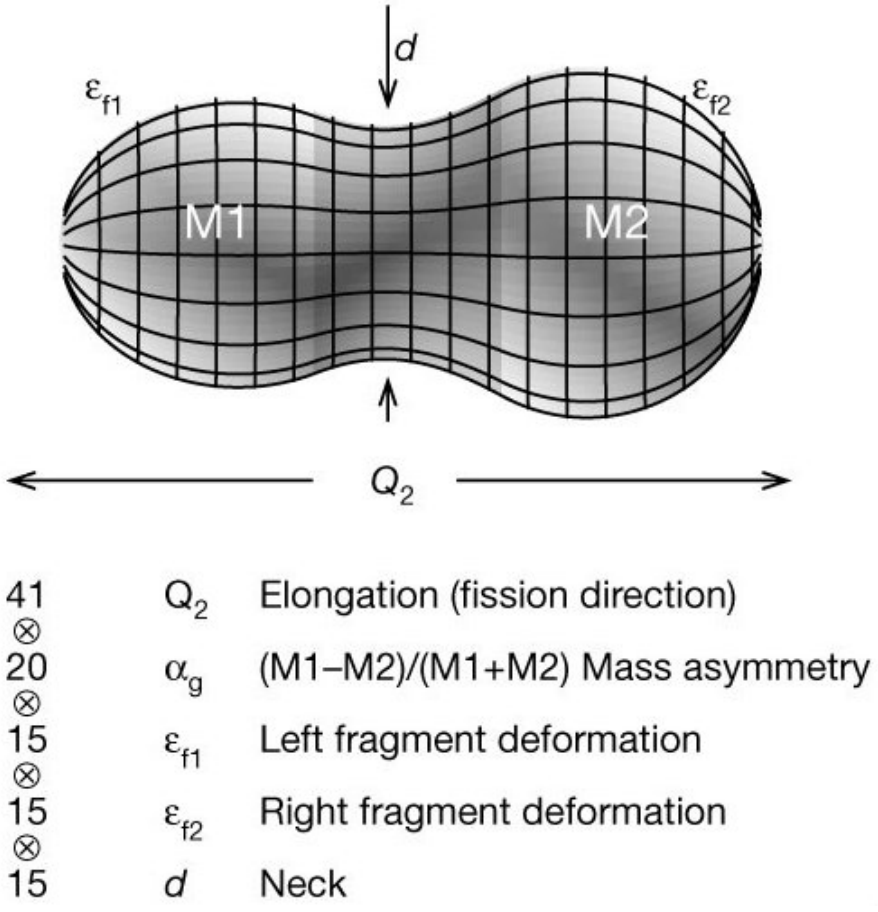

Figure 7.3: Representation of the shape of the elongated nucleus (taken from [99]), at the pre-scission phase.

The mass distribution of the FFs from the fission of actinide nuclei is the asymmetry shown in fig. 7.4. The splitting of the nucleus into two parts of different mass is favored, while the probability of splitting into two equal or nearly equal parts is less probable by a factor of 600. The width of the distribution allows to know the length of the neck since the longer the neck, the larger variety of fragments are produced.

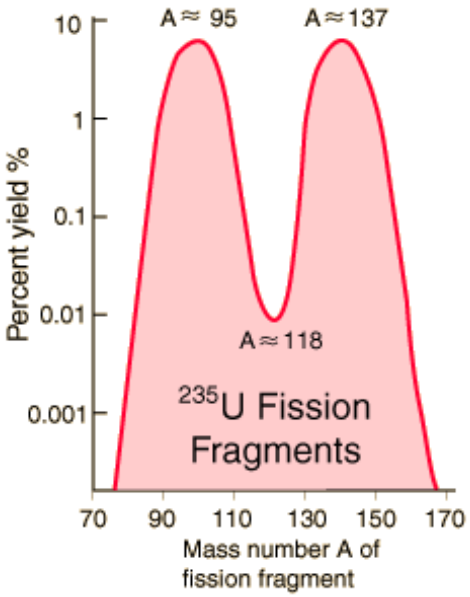

Figure 7.4: Schematic representation of the mass distribution of the FFs from the thermal fission of ^{235}U. The actinide mainly fissions into two FFs of different mass. Similar mass distributions are obtained for spontaneous or low energy fission on other actinides.

For spontaneous or low-energy fission of nuclei near the line of β-stability throughout the actinide region below Fm, nuclei divide into a heavy fragment with a mass close to 140, and a light fragment with mass value that shifts with the total mass of the fissioning nucleus, thus asymmetric fission is the dominant process. This was explained by shell structure effects, and more specifically, it is believed that the spherical shell structure of the doubly magic ^{132}Sn dominates the mass split. For nuclei in the light thorium to astatine region symmetric fission seems to be the dominant mode, although deviations from this trend have been observed, the most striking being the mass asymmetric fission observed for the unstable ^{180}Hg [101], instead of the expected symmetric fission into two ^{90}Zr isotopes (^{90}Zr has a closed neutron shell). Other nuclei, just below the actinide region, close to ^{228}Ra, exhibit both asymmetric and symmetric fission, with different thresholds and different kinetic energies for the fission fragments, and at some excitation energies even a three-peak mass distribution of the FFs has been observed (for ^{227}Ra, see [102]). Such experimental evidence showed that fission is a very complicated process, and a theoretical insight demands a more sophisticated calculation of the potential energy surfaces that guide the nuclear shape evolution from the ground state to the configuration of separated fission fragments, rather than the simple double-humped approximation.

In recent works [99, 100], five-dimensional potential energy landscapes were proposed and explained many of the peculiar characteristics of fission at the different regions of nuclei. The five independent shape parameters used in the potential-energy calculation are shown in fig. 7.3 (elongation, mass asymmetry, left fragment deformation, right fragment deformation, neck). In this way, the potential surface has “valleys”and a system of “saddles”in the space of elongation, as well as “ridges”which are higher than the saddles and inhibit the movement between the valleys. Thus, different paths towards fission are available to the nucleus. Each path is a “fission mode”. The calculated potential energy for ^{234}U can be found in fig. 7.5. The separating ridge is almost as high as the entrance saddle to the symmetric valley, and consequently the symmetric component completely or partially reverts back to the asymmetric valley before scission.

These new calculations have proven that it is not only the mass division that is affected by the shell structure of the fragments, but also the landscape of the potential energy surface determining the fission mode long before the scission point. It has also been shown by other works ([104, 103]) that even the pairing correlations affect the nuclear shape evolution before the nuclear scission point by the exchange of unpaired nucleon between the nascent fission fragments at the last stage of the ``energy sorting'' mechanism which was recently proposed. However, the theoretical investigation is ongoing and even if 80 years since the discovery of fission have passed

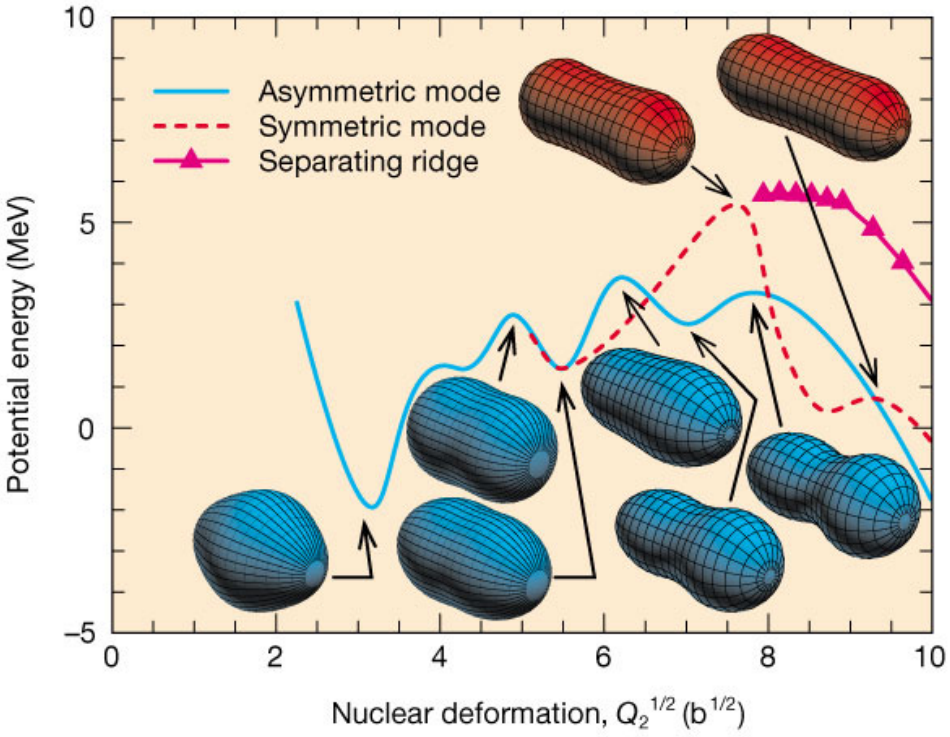

Figure 7.5: Calculated potential energy valleys, saddles and ridges and the corresponding nuclear shapes for ^{234}U, with the five dimensional deformation space, introduced in [99](the picture is taken from [99]). Two fission paths are available for the nucleus the symmetric and the asymmetric path, but the ridge is not high enough to permit both modes to evolve.

many aspects remain unresolved.

As a final remark, each fission event is accompanied by the emission of *prompt neutrons* (within 10^{-16} s) with the number being of statistical nature, weakly changing with the fissioning system and the incoming energy (typically 2-3 neutrons for actinides at low energy neutron induced fission). The large amount of energy (typically 200 MeV for the actinides) appears mainly (about 80%) as FF kinetic energy, while the rest is distributed at the prompt neutrons ($\sim$ 6 MeV), prompt γ rays ($\sim$ 8 MeV), electrons from the β-decay of radioactive FFs ($\sim$20 MeV), secondary γ rays from the FFs ($\sim$7 MeV) etc.

7.2 Neutron induced fission on actinides

In the context of the present thesis neutron induced fission was studied. The reactions studied are ^{237}Np(n,f), ^{238}U(n,f), ^{235}U(n,f), each one with different thresholds. ^{237}Np and ^{235}U are called "fissile"nuclei because they can fission even with a thermal neutron, while ^{238}U (even-even nuclei in general) is called "fissionable"because it can fission only after the capture of a high energy neutron. The evaluated cross sections of the ^{238}U(n,f) and ^{235}U(n,f) reactions are shown in fig. 7.6 for comparison and are discussed below.

The ^{235}U(n,f) reaction has a high cross section value, extending down to thermal neutron energies. In the energy region 1-1000 eV strong resonances appear in the ^{235}U fission cross section due to class II states, which cannot be resolved above a certain energy because of the high density of levels. On the contrary, the ^{238}U(n,f) reaction channel opens above $\sim$1 MeV. However, a narrow intermediate structure also appears in this cross section in the energy region 1-10^5 eV, which is caused by the class II states which fission much more easily than class I states of the same energy. The difference in the threshold of the reaction is due to a different correlation between the

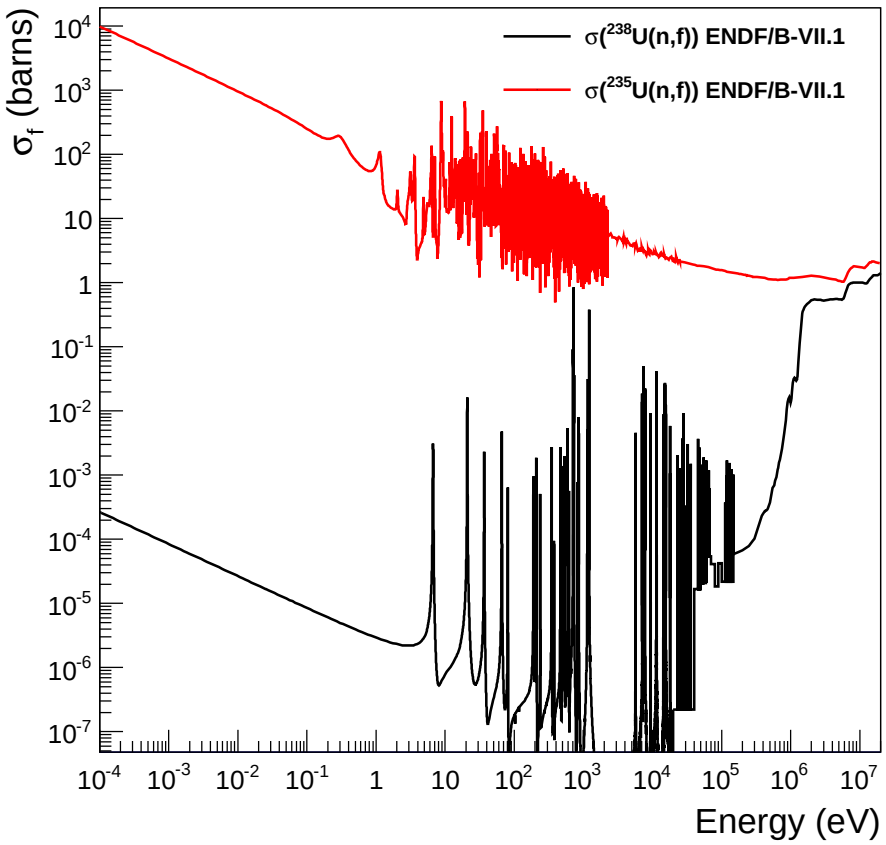

Figure 7.6: The cross sections of the reactions ^{238}U(n,f) and ^{235}U(n,f), taken from ENDF/B-VII.1 evaluation plotted in logarithic scale [28].

neutron separation energy, i.e. the energy increase in the nucleus caused by the absorption of a neutron, and the fission barrier height. As already mentioned, the fission barrier is approximately the same for the actinides, $\sim$ 6-7 MeV while the neutron separation energy depends on the pairing effects of the nucleus. If a neutron with negligible kinetic energy (thermal neutron) is captured by ^{235}U, the excitation energy of the compound nucleus is $\sim$6.5 MeV (fig. 7.7), thus already higher than the fission barrier (6.2 MeV) and fission easily occurs. When a neutron is captured by a ^{238}U nucleus (fig. 7.8), the excitation energy of the compound nucleus is only $\sim$4.8 MeV, thus much lower than the fission barrier which is $\sim$6.6 MeV. As a result, fission can occur for incident neutron energies greater than $\sim$1.8 MeV. This difference can be understood in terms of the pairing energy E_{pair} in the ground state energy calculation (eq. 7.1): the lowering of the ground state energy of the compound nucleus ^{236}U (even-even nucleus) from the pairing of the single neutron with the incoming neutron increases the excitation energy. In the case of ^{238}U (even-even nucleus) the pairing of a neutron and a proton lowers the ground state of this nucleus before the capture of the neutron takes place, and thus the excitation energy of the compound system is decreased.

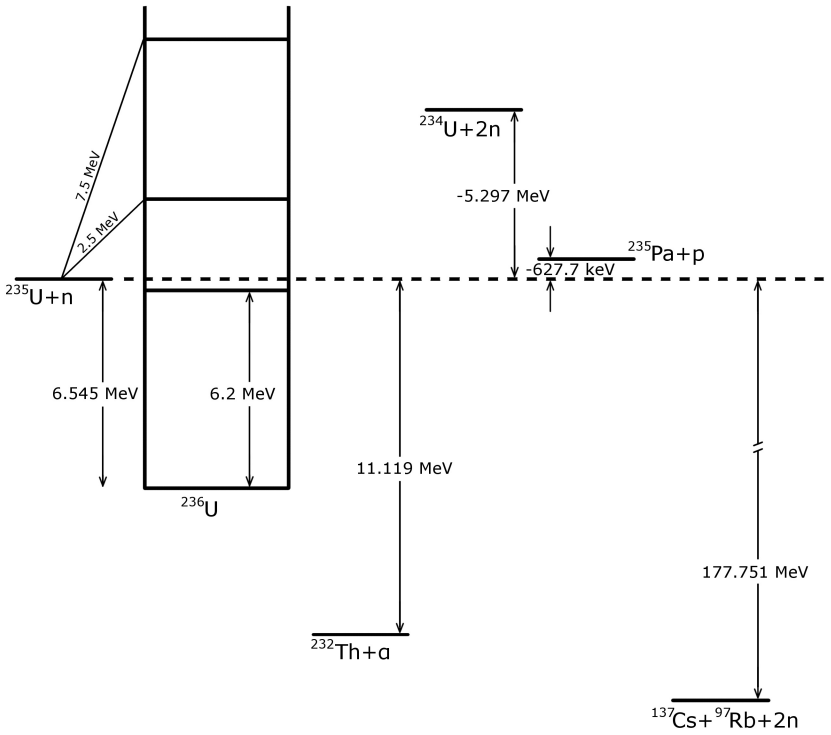

Figure 7.7: Schematics for the reaction scheme of the ^{235}U(n,f) (taken from [80]). Various exit channels like fission, (n,α), (n,p), (n,2n) exit channels are indicatively shown. The fission barrier is 6.2 MeV.

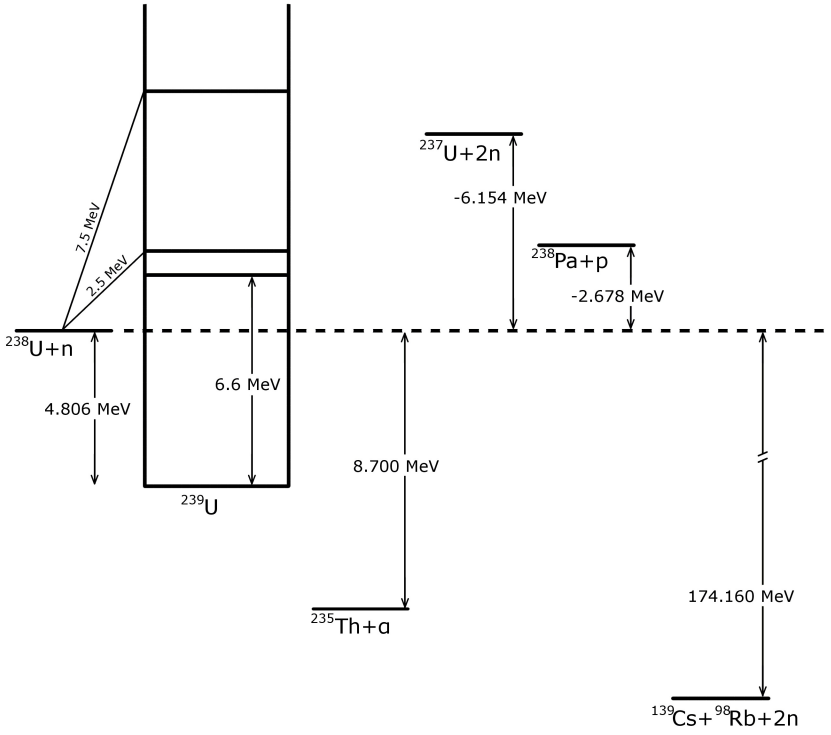

Figure 7.8: Schematics for the reaction scheme of the ^{238}U(n,f) (taken from [80]). It is obvious that the neutron separation energy is lower than the fission threshold (6.6 MeV), so fission cannot occur with thermal neutron energies. Various exit channels like fission, (n,α), (n,p), (n,2n) exit channels are indicatively shown.

The reaction scheme of the ^{237}Np(n,f) can be found in fig. 7.9. Also in this case, the kinetic energy of the neutron needs to be greater than ∼700 keV in order to surpass the fission threshold (6.2 MeV).

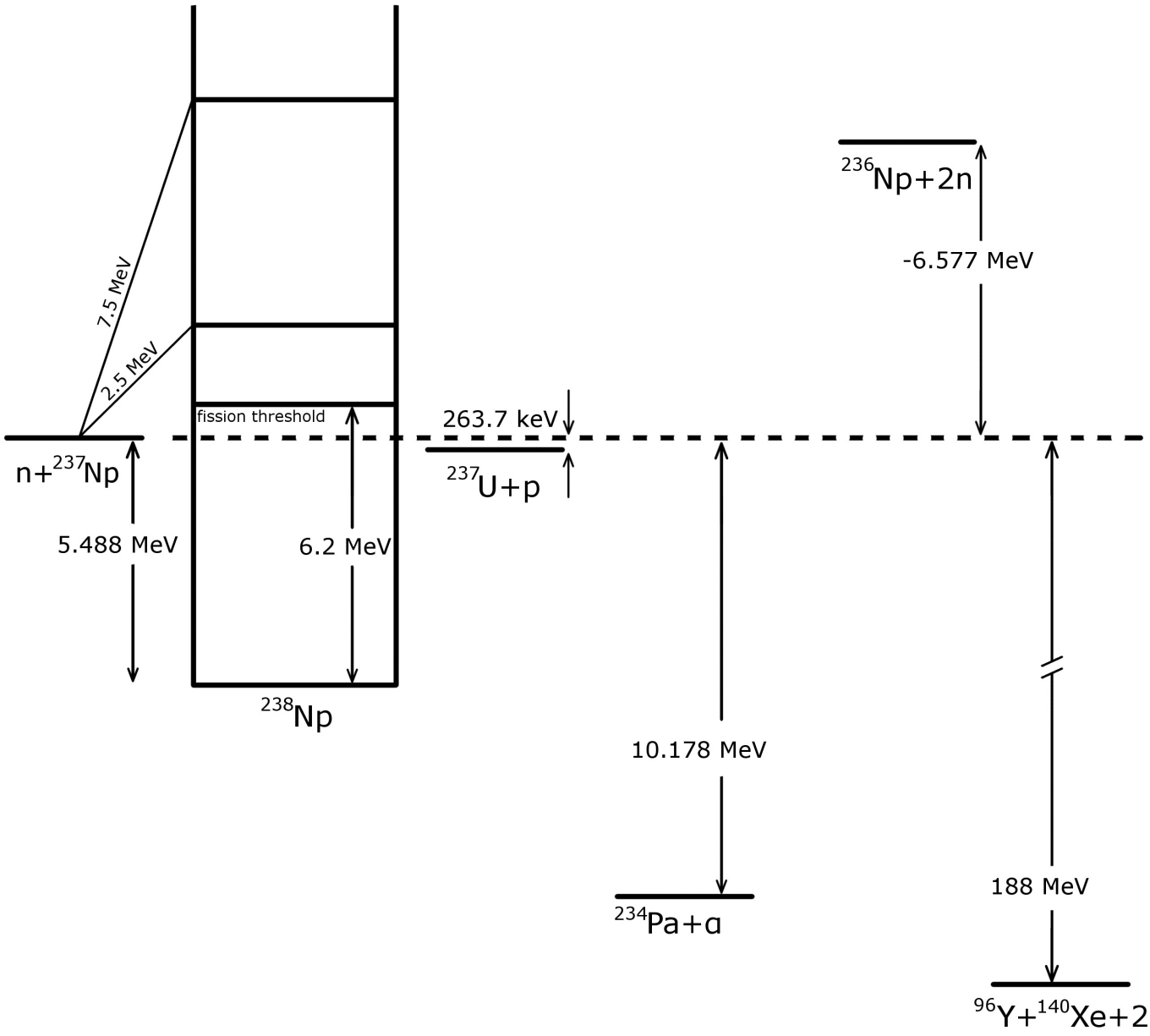

Figure 7.9: Schematics for the reaction scheme of the ^{237}Np(n,f) (taken from [80]). The fission threshold in this case is approximately 700 keV.

As a final remark, above the fission threshold, the actinide fission cross sections have similar behavior (fig. 7.6). As the excitation energy gets higher *multiple chance* fission becomes posible, i.e. fission after the evaporation of a neutron. So when the excitation energy of the compound nucleus exceeds the sum of the fission barrier plus the neutron binding energy the second chance fission (n,nf) occurs (at ∼ 6MeV in fig. 7.6), if it is further increased the third chance fission channel (n,2nf) opens (at ∼ 12MeV in fig. 7.6) etc. and this superposition of the different (n,xnf) channels creates this step-like structure of the fission cross section above the threshold.

7.3 Theoretical investigation of the ^{237}Np(n,f) cross section with EMPIRE

There is no theoretical model based on ab-initio theories able to reproduce cross section data in a large mass number and energy range. Therefore, in order to perform nuclear reaction calculations one needs to use theories with effective potentials and level density models, tuning a set of parameters in order to reproduce the experimental data. In the context of the present thesis, the latest version of the code EMPIRE (version 3.2-Malta) was used for the reproduction of the ^{237}Np(n,f) cross section in the energy range 100 keV-10 MeV.

EMPIRE [105] is a widely used modular system of nuclear reaction codes, comprising various nuclear models and designed for nuclear reaction calculations over a wide energy range and incident particle and target combinations. EMPIRE can be used for theoretical calculations as well as for nuclear data evaluation. The code accounts for the major nuclear reaction models, such as the optical model (for fission as well), coupled channels, DWBA, Multi-Step Direct, Multi-Step Compound, pre-equilibrium exciton model and of course the full Hauser-Feshbach model with γ-cascade including width fluctuations for the compound nucleus decay. The first version of EMPIRE was released in 1980 but, after various modifications, it has been re-written (EMPIRE-2), using different programming concepts in order to make it general-purpose, flexible and fast. The latest version is 3.2-Malta [106], released in 2013, following the 3.1-Rivoli version, released in 2011, with minor changes as far as the fission cross section calculation is concerned. The fission formalism implemented in EMPIRE has been continuously updated by incorporating fundamental features of the fission process and it has been shown that it can successfully reproduce neutron induced cross sections on light actinides [107, 109].

7.3.1 The Hauser-Feshbach formalism in the case of fission

The statistical model calculations were performed with Hauser-Feshbach formalism. In this context, which is based on the Bohr's assumption of independence of the incident and exit channel in a compound nucleus formation, the cross section of a reaction channel (a,b), which is schematically shown in fig. 7.10 is given by equation 7.8, for a certain energy ϵ_a:

$$\sigma_{a,b}(\epsilon_\alpha) = \sum_{J\pi} \sigma_a(\epsilon_a, J\pi) P_\beta(\epsilon_a, J\pi) \tag{7.8}$$

where $\sigma_a(\epsilon_a, J\pi)$ is the cross section of the formation of the compound nucleus in a state of spin-parity Jπ, and $P_\beta(\epsilon_a, J\pi)$ the probability of the compound nucleus to decay with the channel b. If the compound nucleus is excited in a state with energy E_c^* , the decay probability is given in terms of transmission coefficients (eq. 7.9):

$$P_\beta(\epsilon_a, J\pi) = \frac{T_b(E_c^*, J\pi)}{\sum_G T_G(E_G^*, J\pi)} \tag{7.9}$$

where T_b is the transmission coefficient of channel b and the denominator contains the sum of all the other possible exit channels, G, which might be particles emission, photon emission or fission. If the residual nucleus B is left in an excited state E_B^*, which, according to fig. 7.10, is given by $E^*=E_C^*+Q_{C\to b+B}-\epsilon_b$, with a density of states $\rho_B(E_B^*)$, and this stands for all the possible exit channels, then eq. 7.9 becomes:

$$P_\beta^{l\pi} = \frac{T_l(\epsilon_\beta)\rho_B(E_B^*)}{\sum_\gamma T_{\gamma,l}\rho_G(E_G^*)} \tag{7.10}$$

The above discussion stands for spinless particles. In case spin is considered, the probability of the exit channel is a bit more complicated. In addition the cross section of the entrance channel σ_a is calculated by the Optical

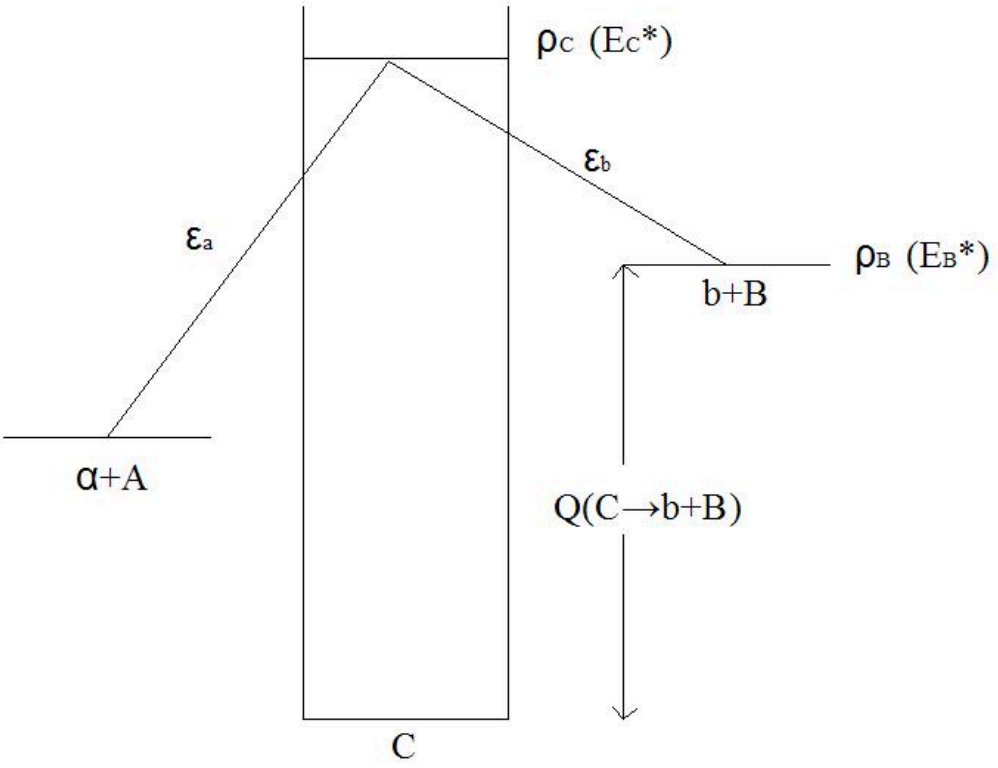

Figure 7.10: Schematic representation of the reaction a + A $\rightarrow$ b+B with the compound nucleus mechanism. Q is the separation energy of the particle b from the compound nucleus C and ρ the density of levels in the corresponding energy.

Model which is based on the analogy of the interaction of the particle beam and the potential of the target nucleus with the scattering of light on a dark sphere, partially reflecting and partially absorbing it [116], [117]. Consequently, by combining eq. 7.8 and 7.10, the sums over the possible spin additions in the entrance and exit channel and the optical model formalism, the final cross section of the reaction channel turns out to be 7.11:

$$\sigma_{\alpha\beta} = \frac{\pi}{k^2} \sum_J \frac{2J+1}{(2s+1)(2S+1)} \frac{\sum_{l,j,l',j'} T_l(\epsilon_\alpha) T_{l'}(\epsilon_\beta) \rho_B(E_B^*, S')}{\sum_{\gamma,l'',j''} T_{\gamma,l''} \rho_G(E_G^*)} \tag{7.11}$$

where the dotted values concern the exit channel. j is the angular momentum of the entrance channel, J of the compound nucleus excitation state, s, S and S' are the spin of the particle a, the target nucleus and the residual nucleus respectively and the selection rules are applied in the sums over j,l (incoming channel) and j',l' (exit channel). The *Hauser-Feshbach denominator* contains all the possible exit channels, allowed by the energy conservation and the selection rules.

If gamma emission is the exit channel, then the transmission coefficients $T_{l'}(\epsilon_\beta)$ are replaced by the *gamma-ray strength functions*. Furthermore, in case the exit channel leaves the residual nucleus in a discrete level, the $\rho_B(E_B^*, S')$ is replaced by δ-functions.

Consequently, for cross section calculations within the Hauser Feshbach formalism it is clear that the level density model, the optical model and the gamma ray strength function model choices play a crucial role. In the Hauser-Feshbach formalism, fission is described as a decay channel of the formed compound nucleus (C). It therefore depends on the transmission coefficients through the fission barriers, and the nuclear level density (NLD) corresponding to the density of levels on top of the fission barrier (transition states). The transmission coefficients are calculated with the optical model for fission. Within this model the incoming flux can be transmitted directly through the barrier or can be absorbed in the isomeric well. The fraction absorbed in the isomeric

well can: a) be re-emitted in the fission channel (indirect prompt fission), b) return back to a class I state or c) undergo γ-decay in the well (schematically shown in fig. 4.4 of the user's manual [106]). So the fission transmission coefficient for a double humped barrier has two components, one for the direct transmission through the barrier (T_d) and one for the indirect transmission (T_i), and is given by eq. 7.12.

$$T_f = T_d + T_i = T_d(1,2) + T_a \frac{T_d(2,2)}{\sum T(2)} \tag{7.12}$$

where $T_d(1,2)$ is the direct transmission coefficient through humps 1 and 2, T_a is the absorption coefficient in the second well, $T_d(h,h)$ is the transmission through hump h (1 or 2 for double-humped) and $\sum T(2)$ is the sum of the transmission coefficients for the competing channels specific to the second well, given by $\sum T(2) = T_d(1,1) + T_d(2,2) + T_g(2)$, where $T_g(2)$ is the gamma decay in the second well and is not yet implemented in EMPIRE.

The transmission coefficients of eq. 7.12 are explained below:

- The transmission coefficient through one barrier $T_d(h,h)$ in the case of a single parabolic barrier is given by the Hill-Wheeler transmission coefficient, eq.7.13 (taken from eq. 7.7):

$$T_d(h,h) = \frac{1}{1 + exp[(2\pi/\hbar\omega_h)(V_h - E_x)]} \tag{7.13}$$

  where E_x is the incoming energy, V_h is the height of the hump h and $\hbar\omega_h$ gives the curvature of the inverted parabola. These two parameters are crucial for the determination of the shape of the barrier and consequently of the probability of transmission.

- The direct transmission coefficient through humps 1 and 2, $T_d(1,2)$ in the presence of absorption is given by eq. 7.14 [119]:

$$T_d(1,2) = \frac{T_d(1,1)T_d(2,2)}{e^{2\delta_2} + 2A^{1/2}cos(2v_2) + A\,e^{-2\delta_2}} \tag{7.14}$$

  where v_2 is the real momentum integral for the hump 2, δ_2 is the contribution from the imaginary potential and $A = [1 - T_d(1,1)][1 - T_d(2,2)]$

- The absorption coefficient for a double humped barrier, T_a stands for the shape transition from the minimum of the first well to the minimum of the second well and is given by eq. 7.15:

$$T_a = T_d(1,2)\left[e^{2\delta_2} - \frac{(1 - T_d(2,2))\,e^{2\delta_2}}{T_d(2,2)}\right] \tag{7.15}$$

Finally, as already mentioned, the total probability of transmission through the barrier depends not only on the transmission coefficients through the fundamental barriers (from the deformation of the ground state), but also on the level densities of the exit channels, thus transmission through all the barriers on top of the fundamental ones characterized by different Jπ numbers have to be taken into account. In this case of fission, the level density of the transition states gets in the play, and the total transmission coefficient is separated in the discrete level part and the continuous level part. The direct transmission occurs only for low sub-barrier excitation energies through discrete transition states, while the continuum contributes at higher energies where the absorption in the well becomes more important. The structure of the transition states is complex and difficult to be predicted accurately, however it is a very important parameter for the prediction of the fission paths and finally the fission cross section.

As a final remark, in order to have a complete theoretical investigation of a reaction cross section, apart from the compound nucleus, the other two possible reaction mechanisms must be taken into account: the direct and preequilibrium emission. The direct mechanism is dominant for larger particle energies, and a small number of

nucleons near the surface of the target nucleus participates in the reaction. Characteristics of the direct reactions is the small reaction time and the strong preference of the outgoing particles in forward directions with respect to the incoming particle direction. For the description of the direct reaction mechanism the proper Optical Model should be chosen. The preequilibrium decay occurs when the ``composite'' nucleus (not yet compound) decays before reaching thermodynamical equilibrium. This process is also assumed to occur with the participation of a limited number of nucleons, leading the nucleus to consecutive stages of increasing complexity, with emission of a nucleon being possible at any of these stages. This reaction mechanism becomes important above 10 MeV[116].

7.3.2 The models chosen for the EMPIRE calculations

For the present calculation of the ^{237}Np(n,f) cross section in the energy range up to 10 MeV performed with EMPIRE 3.2 the decay channels with charged particles were neglected since they are supressed by the Coulomb barrier in this energy range, so the only open channels for the Hauser-Feshbach calculations apart from fission are (n,γ), (n,el), (n,inl), (n,2n). A proper theoretical description of a reaction channel should take into account the constraints imposed by the other reaction channels which are in competition. For this reason, for the present calculations the EMPIRE results were compared to experimental data (when available), not only for the fission channel but also for the (n,tot), (n,γ), (n,el), (n,2n) channels. However, no experimental data were found for the (n,inl) channel which is the main competition channel of the first chance fission in the energy region up to 8 MeV.

In the calculations performed for the present thesis the optical model used for the direct reaction cross sections and neutron transmission coefficients was the RIPL-2408 optical model potential [115]. It is an isospin dependent potential, containing a dispersive term including non-local contribution and covers 1 keV-200 MeV energy range and 31 actinide nuclei [110, 111]. The direct and preequilibrium neutron emission has been tried with the module PCROSS available at EMPIRE which includes the exciton model with nucleon, cluster and gamma emission [113, 114]. Furthermore, the MultiStep Direct (MSD) and MultiStep Compound (MSC) modules of EMPIRE were tried for the inelastic scattering to the neutron continuum. The second combination (MSC+MSD) was finally chosen for the neutron inelastic scattering in the continuum, because it better reproduced the fission cross section above 2 MeV (meaning that the competing channels (n,inl), (n,2n) are better reproduced). The inelastic scattering to discrete collective levels was obtained with the ECIS06 module of EMPIRE.

The level densities in the continuum of the normal states (equilibrium deformation states-class I) were implemented in the calculations using the Enhanced Generalized Superfluid Model (EGSM) [118] available in EMPIRE. According to this model, the level density below a critical energy is strongly influenced by the pairing correlations among the nucleons and the nucleus is in the superfluid phase, while above the critical energy the level density is described by the Fermi Gas Model (FGM). Rotational and vibrational enhancement of the level densities is also taken into account. The difference between the EGSM model (which is now the default level density model in EMPIRE) and GSM lies mainly on the spin distribution in the FG model, since a more accurate treatment of high angular momenta is implemented [106]. The transmission coefficients of gamma-ray emission are expressed in terms of the Weisskopf model and of the Giant Multipole Resonance Model. The gamma ray strength functions were taken into account with the Modified Lorentzian 1 (MLO1) closed formula.

In EMPIRE 3.2 the optical model for fission described above is implemented and was used in the present calculations (FISOPT=1). It describes transmission through multi-humped barriers parametrized analytically by smoothly joined parabolas or defined numerically. It is applicable to multi-chance fission, accounts for the fission mechanisms associated to different degrees of damping of the vibrational states within the minima of the fission path and the coupling among these states, and finally treats multi-modal fission [112]. A double-humped fundamental barrier was assumed for the nuclei involved in the calculations. For the fundamental fission barriers there are a) empirical heights and widths describing the humps of the fission barriers as two decoupled parabolas, available from RIPL-3 (Reference Input Parameter Library [115]) and b) microscopic

Hartree-Fock-Bogolyubov numerical description of the fission path. The first choice was made because it can also offer physical insight concerning the potential behavior of fission for actinides and the sensitivity of the calculations at various parameters. The discrete transition states are provided by recommendations regarding the excitation energies, parity and spin projection along the symmetry axes for each saddle point depending on the odd-even type of the nucleus (experimental data do not exist). The level density model chosen for the description of the transition states continuum was again the EGSM in order to describe the equilibrium and transition states in a coherent way.

As can be seen in fig. 7.11, the (n,tot) channel is very well reproduced with the above mentioned choices of parameters. This basically implies that the optical model chosen is the correct one. The capture channel was also well described, with the MLO1 formalism and the EGSM for the level density (as seen in fig. 7.11, the present calculations are in agreement with the ENDF/B-VII.1 evaluation, while the only existing dataset in the EXFOR database has a reported uncertainty of 30%). However, the energies up to 10^5 correspond to the unresolved resonance region which can only be reproduced with R-matrix calculations, and not with statistical calculations as the ones performed in the context of the present thesis. Finally, the MSC and MSD choice fairly reproduces the low energy tail of the (n,2n) channel cross section (fig. 7.11).

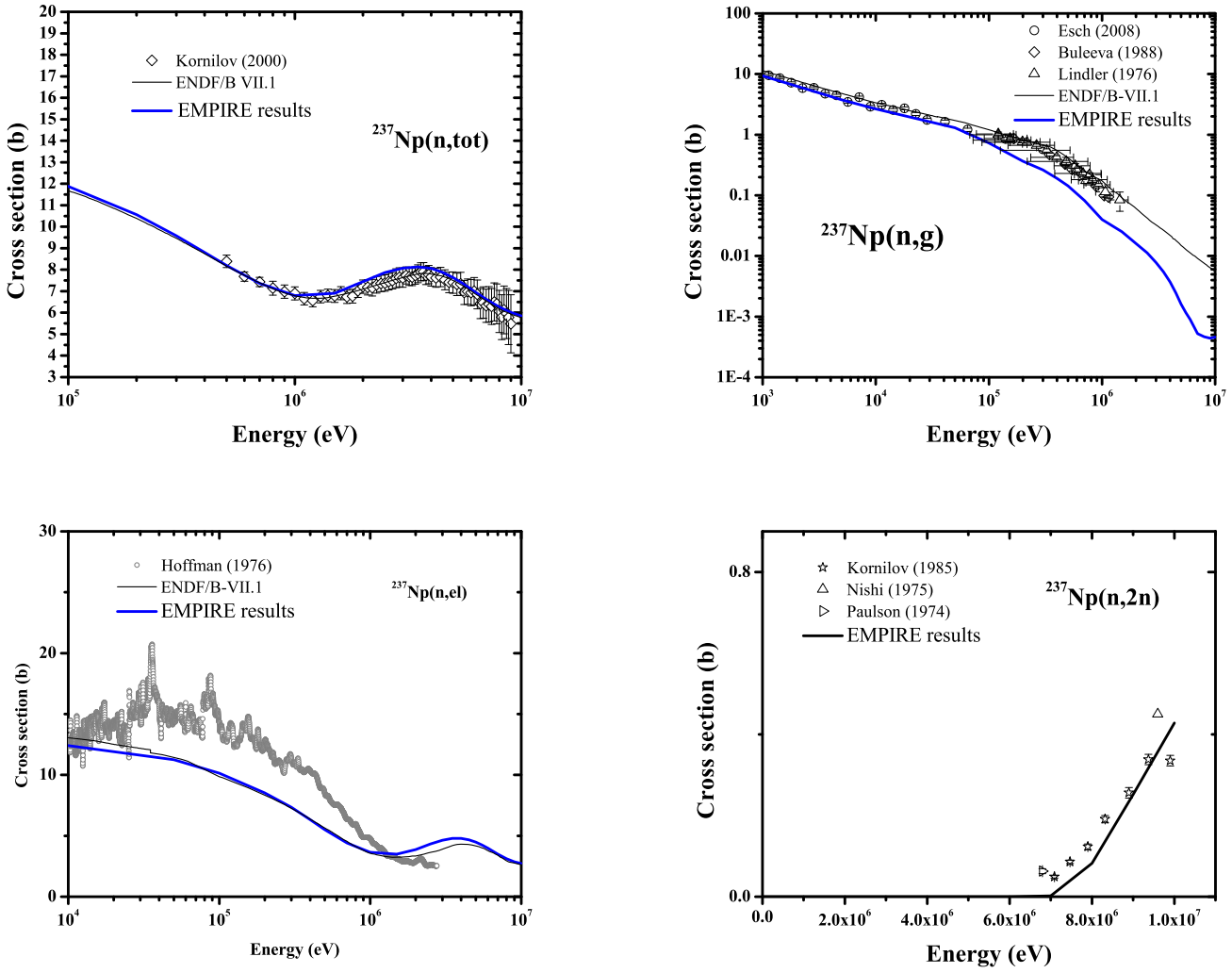

Figure 7.11: Calculated cross section of the reactions ^{237}Np(n,tot) (upper-left), ^{237}Np(n,γ) (upper-right), ^{237}Np(n,el) (lower-left) and ^{237}Np(n,2n) (lower-right), up to 10 MeV. Existing experimental data from the EXFOR database [7] and the ENDF/B-VII.1 evaluated data (red line) are also plotted for comparison. It has to be noted that the error reported at the EXFOR database for the (n,el) data (Hoffman 1976) is 30%, and it is not plotted for clarity purposes.

Once a proper treatment for the competing reactions is chosen and settled, the remaining parameters of the fission channel can be tuned. With the above considerations the results obtained are shown in fig. 7.12, taking the empirical barriers from RIPL-3, as implemented in EMPIRE.

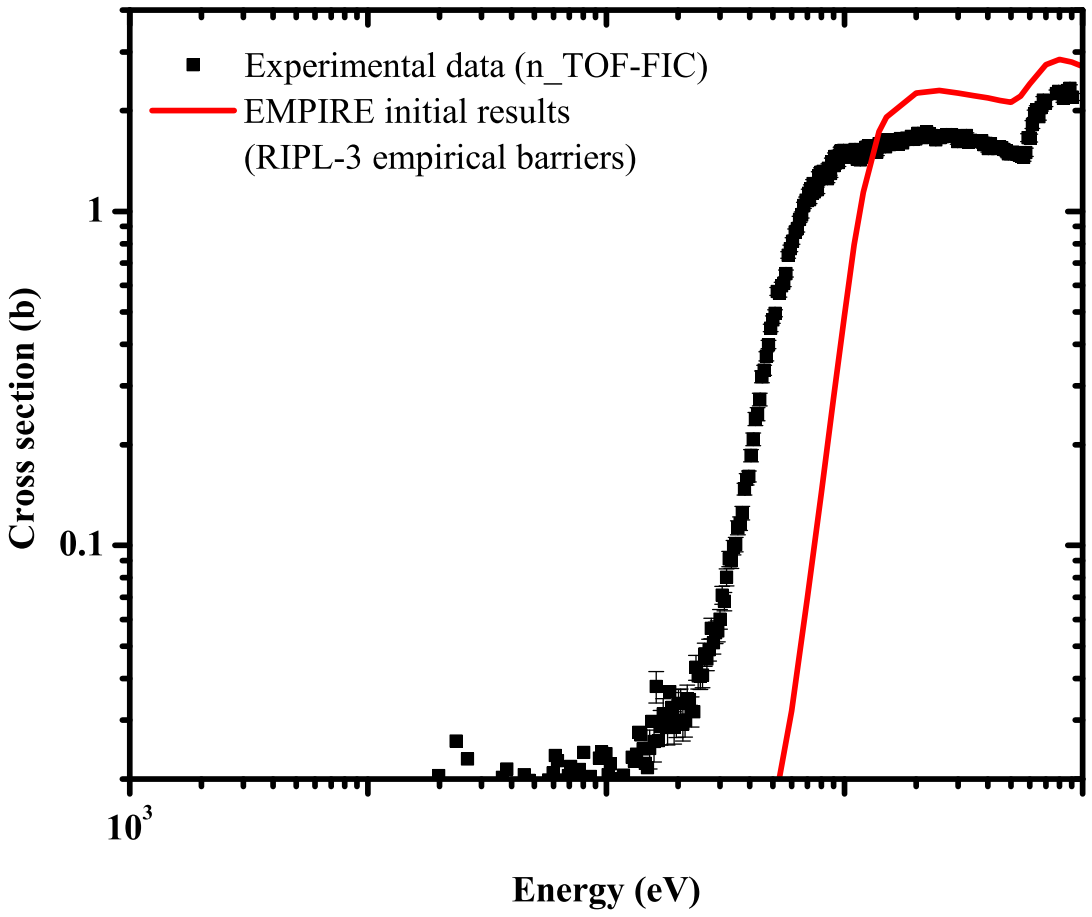

Figure 7.12: The calculated cross section results with the empirical barriers from RIPL-3 (red line) along with the experimental data obtained in the context of the present thesis from n_TOF , in the energy range 1e4-1e7 eV.

The calculated values severely overestimate the fission threshold and above that, the cross section results. Various efforts were made in order to reproduce the data by changing parameters of the fission formalism. As expected, the parameters with the highest impact on the fission cross section are the heights (V_h) and curvatures ($\hbar\omega$) of the fundamental barriers, and the density of the transition states (discrete states and level density at the continuum), as well as the class II states in the well, discrete and continuum (fig. 7.2).

Changes were made in the empirical heights and curvatures ($\hbar\omega$) of both humps for the ^{238}Np and ^{237}Np nuclei provided by RIPL-3, which was easily done from the output file -inp.fis of the code. Furthermore, changes were made in the continuum of the transition states by changing the asymptotic value of the level density parameter of the EGSM, on both saddles of the ^{238}Np nucleus which determines the slope and height of the first chance fission plateau. The asymptotic level density parameter was decreased within 20% in order to decrease the fission cross section mainly above 2 MeV. The changes at the heights and the curvatures ($\hbar\omega$) can be found in table 7.1. It has to be noted that all the above mentioned parameters are correlated and a small change to one of them can be partially cancelled out by changes in other parameters. However, the optimization of the reproduction of the fission cross section was made by tuning parameters for which no experimental data exist, and the changes were kept within physical boundaries.

		First hump		Second hump	
	Isotope	V_1	$\hbar\omega_1$	V_2	$\hbar\omega_1$
RIPL-3	^{238}Np	6.50	0.6	5.75	0.4
	^{237}Np	6.00	1.0	5.4	0.5
modified	^{238}Np	6.05	0.42	5.75	0.4
	^{237}Np	5.80	0.8	5.4	0.5

Table 7.1: Fission barrier heights and widths, initial (RIPL-3) and modified.

The final cross section values calculated with EMPIRE after the above mentioned modifications at the fission channel along with the simultaneous reproduction of the competing reaction channels can be found in fig. 7.13.

The calculated cross section values reproduce quite well the experimental data of the fission cross section as well as the main competing channels in the biggest part of the energy range of interest. In the energy range 1 MeV-2 MeV the fission cross section data are overestimated by 20%. A further decrease of the asymptotic level density parameter at the saddles was not acceptable, because it did not affect much the region below 2 MeV while it decreased the cross section results above, so the slope of the first chance fission plateau did not reproduce the slope of the experimental data. A possible solution would be to adjust the discrete transition states on the first and second saddle of the ^{238}Np barriers, but this needs special care in order to avoid unphysical changes. Furthermore, the interesting maximum of the cross section at 1 MeV as well as the small plateaus on the slope of the first chance fission observed in the experimental data from n_TOF analyzed for the present thesis emerge further theoretical discussion on the possibility of a better description with a triple humped barrier, but these possibilities will be investigated in a future work.

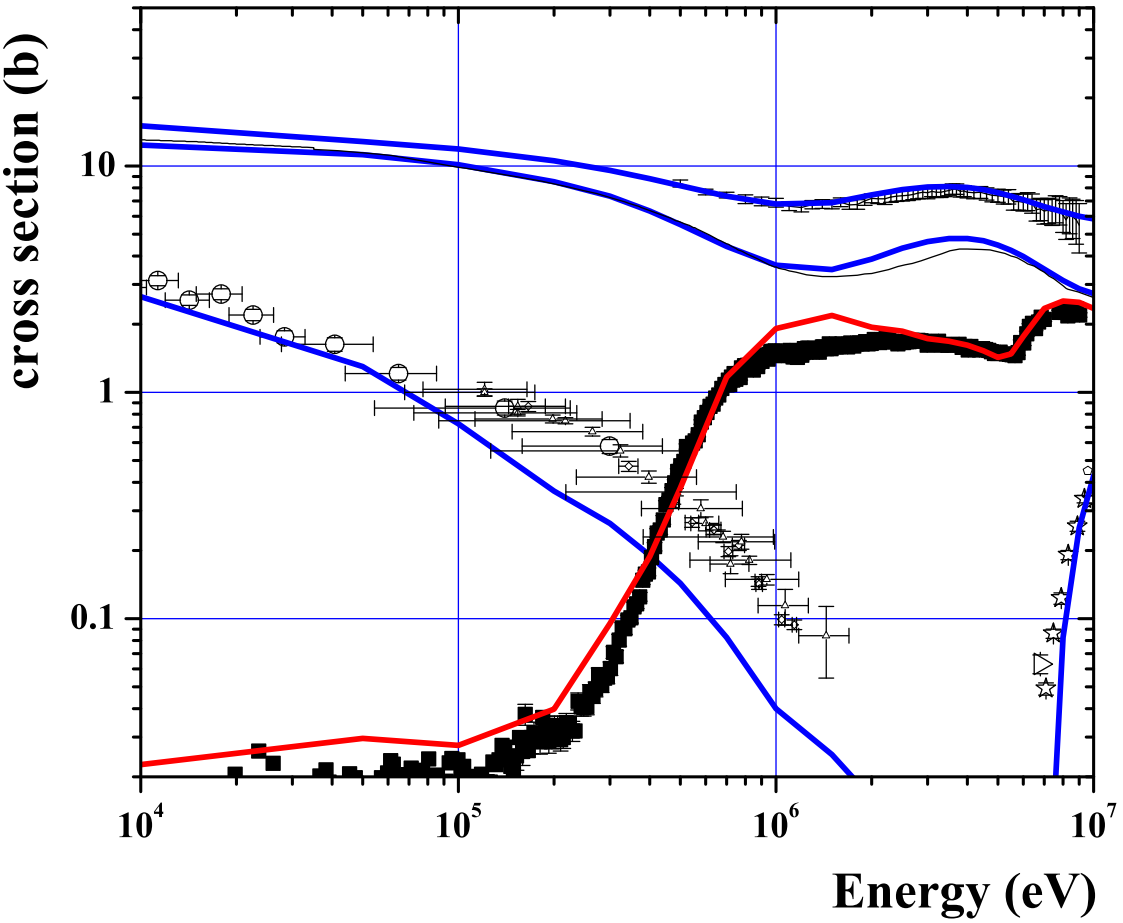

Figure 7.13: The calculated cross section results with the modified parameters of the fission formalism (red line) along with the experimental data obtained in the context of the present thesis, in the energy range 1e4-1e7 eV. Furthermore, the simultaneous reproduction of the competing channels in the same energy range is shown (blue lines: empire calculations, black points: corresponding experimental data).

Chapter 8

Conclusion and future perspectives

8.1 Summary and conclusions

The main purpose of this thesis was the study of neutron induced fission on actinides, and more specifically the ^{237}Np case, within the framework of the n_TOF collaboration, in order to provide high accuracy data for the facilitation of the theoretical investigation of the fission process, which is of the most interesting and still unknown subjects in nuclear physics. Furthermore, such data are needed for the design of the new generation of nuclear reactors and the P&T systems for the nuclear waste (^{237}Np is one of the major components of nuclear waste with a very long lifetime). For this purpose, two independent measurements using different facilities and experimental techniques were performed: 1) The measurement of the ^{237}Np(n,f) cross section at the CERN n_TOF facility with a white neutron beam of high instantaneous flux and of unique energy resolution due to the long neutron flight path, a fast ionization chamber and an event-by-event analysis procedure, bazed on pulse shape analysis techniques and 2) the measurement of the ^{237}Np(n,f) cross section at the Institute of Nuclear and Particle Physics of the NCSR "Demokritos", with monoenergetic neutron beams, relatively low neutron flux and an innovative MicroMegas detector. The cross section results in both measurements were obtained with reference to standard reaction cross section data as the ^{238}U(n,f) and/or the ^{235}U(n,f). The experimental work was completed by the characterization of the actinide targets used as far as the number of target nuclei they contain and the homogeneity of the material on the target surface are concerned, with use of alpha spectroscopy with SSB detectors and the RBS technique respectively. The two experimental setups had different features, advantages and limitations and totally different way of analysis. More specifically:

- The n_TOF facility at CERN, provides a white neutron beam from the spallation of high energy protons impinging on a lead target and combines unique features as high flux, high resolution and low background. It offers the possibility of the simultaneous measurement of cross sections in a wide energy range and extraction of high accuracy data. For the determination of the ^{237}Np(n,f) cross section (n_TOF phase 1 measurement) a Fast Ionisation Chamber was used (FIC0 2003). The ^{235}U targets were used as reference targets below 2 MeV (in total 3 ^{235}U targets were analyzed) and the ^{238}U targets above (in total 3 ^{238}U targets were used). The γ-flash signal, induced by the gamma rays and relativistic particles generated from the spallation process provides a clear starting point for the accurate determination of the neutron time-of-flight and, in combination with the long flight path an excellent neutron energy resolution of $10^{-4} < \delta E < 10^{-2}$ is achieved. However, the large energy deposition from the large γ-flash signal caused oscillations of the signal baseline, even saturating it at some neutron energies, when the baseline was close to the lower FADC limit. The data analyzed presented severe baseline oscillations, especially for neutron energies greater than 10 MeV causing saturations at some neutron energies, i.e. loss of raw data. An analysis procedure on an event-by-event basis, with the successful subtraction of the oscillating baseline and the subsequent pulse shape analysis of the FF peak candidates was followed and the final

number of FF events was extracted by the proper selection of the fitting parameters and their errors. The analysis code used is a very powerful tool for the extraction of accurate cross section results, however, due to the loss of raw data at the energies of saturations, the neutron energy range for which accurate cross section data were extracted was 100 keV- 8 MeV, where the first chance fission is the dominant reaction channel. Nevertheless, in this energy region noticeable discrepancies exist between previous cross section data and evaluations (up to 8%), making the present data of great importance. A limitation of the analysis procedure used was revealed from the present thesis, for high FF activity targets: the combination of high mass value, i.e. large number of target nuclei, along with the high neutron flux and the high fission cross section leads to high FF activity, and this was the case for the U5 reference target at the energy region 700 keV-2 MeV. As explained in chapter 4, the code in this case failed to successfully subtract the baseline of the raw data and this caused loss of FFs peaks, mainly for non-isolated peaks (estimated FF loss less than 4% changing with energy, as expected from the shape of the neutron fluence at the n_TOF facility). In the context of the present thesis, this problem has been solved by using another ^{235}U reference target (U5b target), which had a similar FF activity with ^{237}Np in this energy region, minimizing the systematic uncertainty from such FF peak losses (which is already very low because the Np7 and U5b target are of medium FF activity). An effective neutron fluence multiplication factor due to the different surfaces of the Np7 (8 cm diameter) and U5b (5 cm diameter) targets was accounted for by experimental cross section and reaction rate ratios of reference targets of different surfaces. Above 2 MeV, the U8 targets were used as reference for the cross section calculation. The statistical error of the final obtained cross section data did not exceed 3% while the biggest systematic uncertainty came from the efficiency correction and $\sim$2%.

- The neutron production facility at the I.N.P.P. at the NCSR ``Demokritos" provides monoenergetic or quasi-monoenergetic neutron beams via nuclear reactions of ions accelerated with use of a 5.5 MV Van de Graaff Tandem (T11/25), impinging on gas or solid targets. In the present case the ^{2}H(d,n) reaction was used for the production of monoenergetic neutron beams in the energy range $\sim$4.5-5.5 MeV. The measurement of the ^{237}Np(n,f) cross section was performed in this energy range, relative to the ^{238}U(n,f) cross section which is considered a standard and the ^{235}U(n,f) was used as a sensitive tool for lower energy neutrons. The measurement of the fission fragments from the neutron induced fission on the ^{237}Np and the reference targets (^{238}U and ^{235}U) with an innovative MicroMegas detector assembly, developed at CERN, within the context of the n_TOF collaboration. The detectors were manufactured with the micro-bulk technology, having as main advantages the low mass, the good energy resolution and comparatively low sensitivity to gas variations. The detector setup was tested and optimized for the measurement of the ^{237}Np(n,f) cross section as explained in chap. 5. Thanks to the relatively low neutron flux low-gain charge sensitive preamplifiers, amplifiers and ADC allowed for the fair discrimination of the heavy and light FF peaks, and the alpha particle peaks (from the natural activity of the targets) were also kept in the spectrum. The linearity in the calibration of the experimental spectra with the alpha and FF peaks, despite the large difference in their atomic numbers and energies was an interesting result, observed for the first time for such measurements with a MicroMegas detector. The good energy resolution allowed also for a first estimation of the resolution function of the MicroMegas detector, which is the result of the gas multiplication variations for the different isotopes and the variations in the response of the electronics, and turned out to be increasing with energy. However, the energy resolution (σ/E) seemed to be much better for the alpha particle peaks than for the FF peaks, which can be attributed to factors like the non-linearities of the electronics in such a wide energy range. Due to the limiting statistics of the FF peak tails which precludes the extraction of safe results, this effect will be further studied in a future work. The neutron energy is determined by the accelerated deuteron energy, without a Time-of-Flight Technique, thus a thorough investigation of all sources that would affect the monochromaticity and also the neutron fluence was considered necessary and explained in chap. 6. A contribution of neutrons created from parasitic reactions, of lower energies than the main neutron beam was observed and experimentally investigated. A possible source of these neutrons could be the (d,n) reactions on oxygen and hydrocarbons which are common contaminants in the collimation system and the Mo entrance foil of the ^{2}H gas cell. This was the reason why, from these first fission cross section measurements with the new MicroMegas detector assembly the neutron energy range was not expanded to higher energies. The obtained cross section

results had a statistical uncertainty of ∼3% while the main systematic uncertainty came from the neutron fluence and did not exceed 4%.

The two experiments performed had very different characteristics. On one hand the unique n_TOF facility provides a high instantaneous neutron flux over a wide energy range, allowing for the extraction of high accuracy data with the minimization of the systematic uncertainties. Furthermore, the excellent neutron energy resolution of the facility allowed for the observation of some plateaus and humps in the first chance fission threshold data which provoke further theoretical investigation. On the other hand, the measurement at the I.N.P.P. 'of the NCSR ``Demokritos", due to the monoenergetic neutron beams allowing for a more careful analysis of the different factors affecting the results at different neutron energies, the implementation of a compact, state-of-the-art MicroMegas detector assembly, the detailed characterization of the targets and the thorough investigation of all possible error sources also provides high quality cross section data. Furthermore, the good energy resolution achieved with fast conventional electronics in the obtained experimental spectra allows for the study of certain detector characteristics, something which is not easily achievable with the use of the timing output of fast electronics, usually employed in TOF experimental setups. Despite the large differences in the experimental and analysis procedure the two measurements gave consistent results within their experimental errors, giving confidence that the values reported in the present work allow for safer conclusions and remarks concerning the behavior of the ^{237}Np(n,f) reaction cross section and thus the subsequent theoretical investigation. The cross section results obtained from this work were in good agreement with the latest ENDF evaluation, while at the first chance fission plateau they are systematically lower than the latest data found in literature [8]. Finally, the theoretical investigation of the ^{237}Np(n,f) reaction cross section within the Hauser-Feshbach formalism with the code EMPIRE was performed, in the energy range 100 keV- 10 MeV, by successfully reproducing simultaneously the cross section of the ^{237}Np(n,tot) reaction and the other competing reaction channels ((n,g),(n,el), (n,2n)).

8.2 Future perspectives

- The use of the pulse shape analysis code for the event-by-event analysis of the n_TOF data can be expanded to other fission cross section measurements with the FIC detector. The code deals directly with the raw data (without zero-suppression algorithm), manages to successfully subtract the oscillating baseline which is a major problem at the n_TOF data at the high neutron energy range, after the γ-flash peak, gives the user the possibility to make a selection of the fitted peaks by limiting the accepted fitting parameters and their errors. It has been proven to give very reliable results (by the reproduction of standard cross sections). By proper modifications (for example at the fitting function chosen) the use of this code can be expanded to other detectors and cross section measurements.

- The small plateaus and humps observed at the cross section data from n_TOF in the neutron energy range 500 keV-1 MeV (first chance fission threshold) need to be further investigated, both experimentally and theoretically. The new experimental area of the n_TOF facility (EAR-2) located on top of the spallation target at 90° with respect to the proton beam, with a much shorter flight path (20m) where the flux is expected to be more than 10 times higher than the existing one would be a very good choice for the extraction of high accuracy data up to 1 MeV.

- The new MicroMegas detector assembly has been tested and used in the measurement of the ^{237}Np(n,f) cross section and the use of this system will be expanded to other actinide targets (like ^{236}U, ^{234}U , ^{232}Th which are already at the I.N.P.P. ``Demokritos", or ^{242}Pu which is expected, provided by the n_TOF collaboration) with monoenergetic neutron beams, complementary to the wide energy n_TOF facility. The neutron energy range can also be expanded by other neutron producing reactions like ^{7}Li(p,n), under the condition of monoenergiticity, because no neutron Time-of-Flight exists and fission is a non-threshold reaction. A more sophisticated collimation system and measurement of the incoming ion beam current,

as well as cleaning of the beam line and gas-in and gas-out measurements (in case of the ^{2}H(d,n) neutron production reaction) are foreseen for the next measurements in order to reduce as much as possible the parasitic neutron producing reactions and their effect on the cross section results.

- The resolution function of the MicroMegas detector at the detection of fission fragments will be further investigated, firstly by increasing the statistics at the FF peak tails and secondly by refining the Monte Carlo simulations for the extraction of the FF energy deposition histograms, for example, by using the GEF (GEneral Fission) code [120] for the generation of the FFs.
- The alpha spectroscopy setup with the two SSB detectors is set, tested and can be used for the accurate determination of the mass of alpha emitting actinide targets.
- The theoretical investigation of the ^{237}Np(n,f) reaction with the code EMPIRE is ongoing, and an effort to reproduce the shape of the cross section up to 2 MeV with the small humps and maxima observed from this work will be made in order to understand their origin.

Appendices

Appendix A

Interaction of alpha particles and FF with the detector gas

When ions travel in matter,they gradually loose their initial kinetic energy due to the intaractions mainly with the electrons and also the nuclei [87]. This process is phenomenologically described by the specific energy loss, i.e the energy loss per unit path length (dE/dx). The two componens of the ion energy loss are the electronic energy loss occuring from the interaction with the electrons of the absorber atoms, and the nuclear energy loss occuring from the interaction with the absorber nuclei. The second component becomes more important at the end of the ion track, i.e. when the ion energy is very low, however it is much smaller than the electronic energy loss. A quantity that describes the same effect is the so-called linear stopping power S=-(dE/dx).

For particles in a given charge state the Bethe formula is used for the classical description of S, given by eq. A.1.

$$-\frac{dE}{dx} = \frac{4\pi e^4 z^2}{m_0 v^2} NB \tag{A.1}$$

where

$$B = Z\left[ln\frac{2m_0v^2}{I} - ln\left(1-\frac{v^2}{c^2}\right) - \frac{v^2}{c^2}\right]$$

In the above expressions, v and ze are the velocity and charge of the primary ion, N and Z the number density and atomic number of the absorber atoms, m_0 the electron rest mass and e the electron charge. The parameter I represents the average excitation and ionization potential of the absorber (experimentally determined). Eq. A.1 refers to the electronic eenrgy loss alone and is generally valid for different types of charged particles, given that their velocity remains large compared to the velocities of the atomic electrons of the absorber medium. From this equation it is obvious that the stopping power for particles with low initial charge state as alphas or protons increases as the ion velocity gets lower, but at very low ion velocities electron pickup becomes significant, so z in eq.A.1 is reduced and thus S is rapidly decreased.

Another useful quantity is the range, i.e. the mean distance covered by the ion in the medium, projected to the propagation axis. The range is stochastic by nature with fluctuations given by the longitudinal and the lateral straggling, which are parallel and perpendicular to the propagation axis, respectively.

The fission fragments are peculiar ions in several ways. Most of them are unstable isotopes and rapidly decay (usually by β decays) to stable isotopes. Furthermore, their initial charge state is large and unknown, because they start out stripped of many electrons. Thus the specific energy loss is much higher than other ions, but thanks to the very high initial energy, they manage to have a typical range which is approximately half of a 5 MeV

alpha particle. An important feature of the FF track in matter is that the initial large effective charge continuously decreases after the interactions in the medium. Consequently, the specific energy loss of the FFs decreases as they slow down in the medium, a behavior opposite to that of lighter particles. The pickup of electrons begins immediately at the start of the FF track, so the factor z at the numerator of eq. A.1 continuously drops, resulting in a decrease in the stopping power (-dE/dx) which is large enough to overcome the increase caused by the decrease in the velocity v.

SRIM [40] is a widely used code for the calculation of the dE/dx, the range and the longitudinal and the lateral straggling values as a function of the ion energy, the atomic number and mass, the medium composition and density. It is based on accurate experimental data extended using unified theoretical concepts. For the reasons explained in the previous paragraph, SRIM is not designed to deal with fission fragments. Nevertheless, by comparing experimental values of dE/dx and ranges of FF emitted from spontaneous fission sources such as ^{252}Cf with the calculated ones by SRIM [88], it has been shown that the calculated dE/dx are generally lower by no more than 23 % and thus the calculated ranges overestimated. Taking into account the complexity of the FF generation and the lack of accurate data concerning FF atomic numbers and masses, as well as the initial energy , parameters that strongly affect the SRIM calculations, the agreement is considered acceptable. So, in order to illustrate the different behavior between the alphas coming from the natural activity of the actinide targets and the FFs from the neutron induced fission, while they interact with the detector gas, the SRIM code was used. Calculations were performed for alpha particles, and two FF from the ^{237}Np neutron induced fission, ^{99}Mo and ^{132}Te, representatives of the light and heavy group of FFs respectively. The light FFs have a distribution of energies with centroid kinetic energy of $\sim$100MeV, while the heavy FFs a centroid of $\sim$70 MeV. The absorber medium is the gas of the FIC detector (Ar(90%)-CF_4(10%)) at 720 mbar, but similar results occur for the gas of the MicroMegas detector. The resulting specific energy loss from SRIM tabulated results for these ions can be found in fig. A.1. In these figures the specific energy loss with respect to the ion energy is plotted. Firstly, it can be seen that the nuclear energy loss is orders of magnitude lower than the electronic energy loss for the alpha particle. Even at very low alpha energies, ($\prec$ 0.5 MeV at the plot (a) of the fig. A.1) i.e. at the end of the range, where electron pickup starts, the electronic energy loss rapidly decreases and the nuclear energy loss increases, the difference between the two components is large. The total energy loss (plot (a') of the fig. A.1) generally increases while the ion loses energy, i.e. gets deeper into the matter, until the end of the range where it rapidly decreases as explained above. The situation is somewhat different for the FFs. An important result is that the specific energy loss is quite similar for the light (^{99}Mo) and the heavy (^{132}Te) FF. The nuclear energy loss is now more important, and at very low ion energies (below $\sim$5 MeV) it becomes higher than the electronic energy loss. Finally the specific energy loss decreases as the ion loses energy, contrary to the alpha particle behavior.

- **Alpha and FF range in the FIC detector gas [Ar(90%)-CF_4(10%)) at 720 mbar, 2 cm thick (calculations with SRIM)]:** The range of the alpha particles of 5 MeV is $\sim$ 49 mm. Consequently the alpha particles are not stopped in the forward direction (0deg in 2 cm of gas thickness) and they exit the gas with a mean kinetic energy of 3.5 MeV. The range of the light FFs (^{99}Mo-100 MeV) is $\sim$ 32 mm so the ones emitted in the forward direction are not stopped in the gas and exit with an average energy of 16 MeV. For the heavy FFs (^{132}Te-70 MeV) the range is $\sim$19 mm with a longitudinal straggling of 0.8 mm, so even at the forward direction most of the FFs will be stopped in the gas, while the few ones exiting the gas have an average energy of 8 MeV. Of course at larger angles the distance covered in the gas and the sample is larger thus above a critical angle of emission, also the alphas and the light FFs leave all their energy on the gas. Assuming that they are emitted from the surface of the target this critical angle is approximately 65 $^\circ$ for the alpha particles of 5 MeV and 50 $^\circ$ for the ^{99}Mo isotopes of 100 MeV.

- **Alpha and FF range in the MicroMegas detector gas [Ar(80%)-CO_2(20%) at 1 atm, 1 cm thick (calculations with SRIM):** The range of alpha particles of 5 MeV in the MicroMegas detector gas is approximately 37.5 mm, thus those emitted at 0 $^\circ$ leave only a small part of their energy in their gas (they exit with an average energy of $\sim$ 4 MeV). The range of ^{99}Mo isotopes of 100 MeV is approximately 25

mm and the corresponding value for ^{132}Te at 70 MeV is 20 mm. The critical angles above which the ions are stopped in the gas are $\sim$75 $^\circ$ (alphas-5MeV), $\sim$65 $^\circ$ (^{99}Mo-100MeV) and $\sim$60 $^\circ$ (^{132}Te-70MeV).

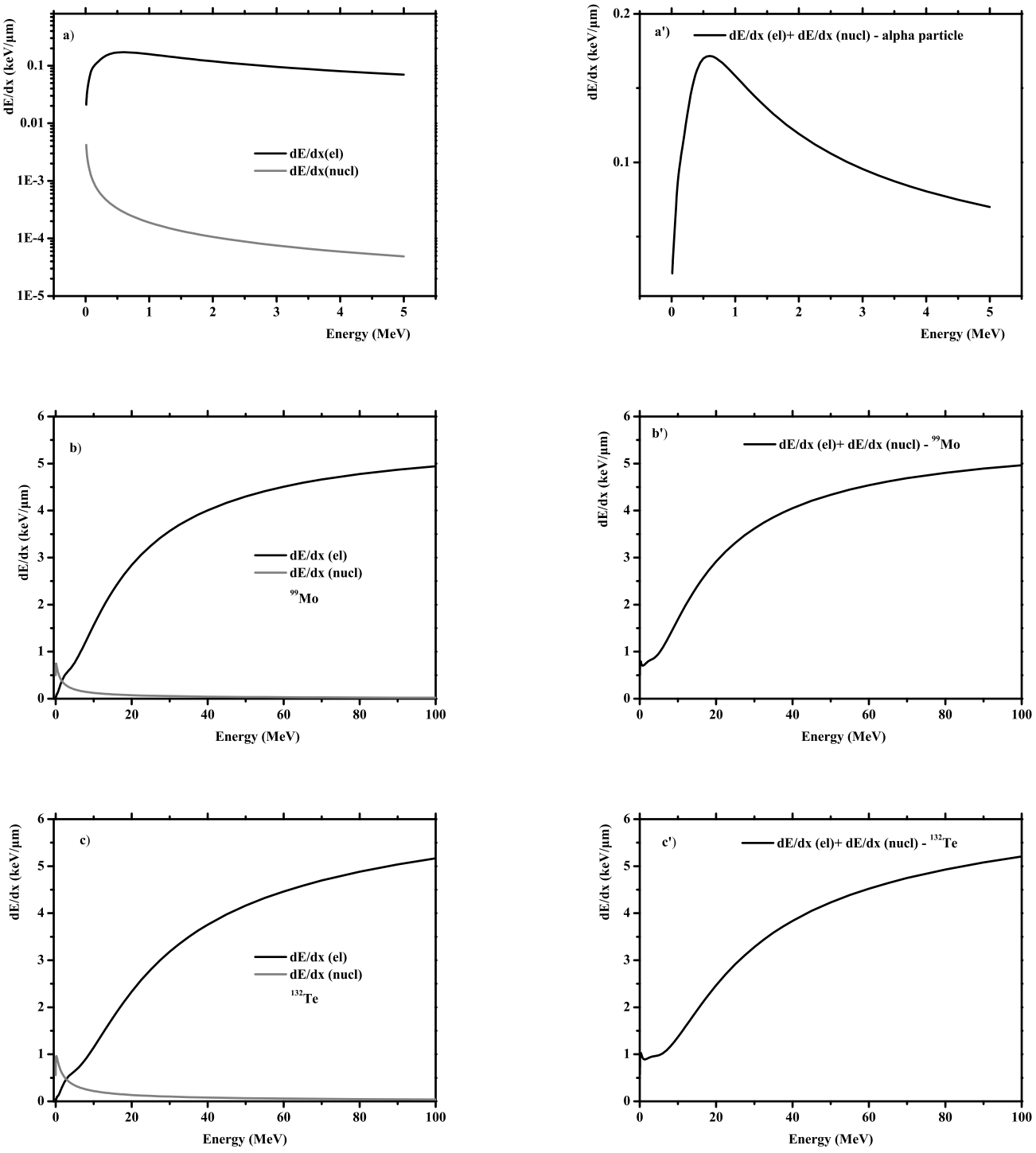

Figure A.1: The calculated values of the specific energy loss for alphas (a and a') and the FFs ^{99}Mo (b and b') and ^{132}Te (c and c'), with respect to the ion energy. The calculations are performed with the SRIM [40] code, for the FIC detector gas. At the left hand figures the specific energy loss due to electron and nuclear interactions are shown separately while at the right hand figures they are added and the total dE/dx is shown for the three ions.

Bibliography

[1] ``Key World Energy Statistics", International Energy Agency, 2013 (available at: www.iaea.org).

[2] ``Introductory Nuclear Physics", K. S. Krane, John Wiley & Sons.

[3] J. R. Lamarsh, A. J. Baratta, Introduction to Nuclear Engineering (Prentice Hall, 2001, Third Edition).

[4] A Technological Roadmap for Generation VI Nuclear Energy Systems, Technical Roadmap Report, September 2002.

[5] Accelerator-driven Systems (ADS) and Fast Reactors (FR) in Advanced Nuclear Fuel Cycles, A Comparative Study, Nuclear Energy Agency, Organisation for Economic Co-operation and Development (2003).

[6] A European Roadmap for Developing Accelerator Driven Systems (ADS) for Nuclear Waste Incineration, The European Technical Working Group on ADS, April 2001.

[7] http://www.nndc.bnl.gov/exfor.

[8] C. Paradela, et al, the n_TOF collaboration, Phys. Rev C **82** 034601 (2010).

[9] F. Tovesson, T. S. Hill, Phys. Rev. C **75**, 034610 (2007).

[10] P. Cennini, E. Chiaveri, A. Ferrari, A. Mengoni, C. Rubbia, A. Vlachoudis et al., Int. Sem. on Interactions of Neutrons with Nuclei, No.12, p.456 (2004), Russia.

[11] O. Shcherbakov, A. Donets, A. Evdokimov, A. Fomichev, T. Fukahori, A. Hasegawa, A. Laptev, V. Maslov, G. Petrov, S. Soloviev, Y. Tuboltsev, A. Vorobyev, J. Nucl. Sci. Tech. Suppl. **2**, (2002) 230-233.

[12] K. Merla, P. Hausch, C. Herbach, G. Musiol, G. Pausch, U. Todt, L. Drapchinskiy, V. Kalinin, V. Shpakov, *Proceedings of the International Conference on Nuclear Data for Science and Technology, Juelich, Germany* (1991), edited by R. Haight, M. Chadwick, T. Kawano P. Talou (American Institute of Physics, College Park, MD, 2005) 510.

[13] P. Lisowski, J. Ullman, S. Balestrini, A. Carlson, O. Wasson, N. Hill, *Conference on Nuclear Data for Science and Technology*, Mito 1988, edited by S. Igarasi (Japan Atomic Energy Research Institute, 1988) 97.

[14] H. Terayama, Y. Karino, F. Manabe, M. Yanagawa, K. Kanda, and N. Hirakawa, Technical Report **47**, Internal Tohoku University Reports (1986).

[15] A. A. Goverdovskii, A. K. Gordyushin, B. D. Kuzminov, V. F. Mitrofanov, A. I. Sergachev, S. M. Solovev, G. M. Stepchenkova, Sov. At. Energy **58**, (1985) 137.

[16] W. Jingxia, R.Chaofan, S. Zhongfa, L. Jingwen, Y. Zongyuan, D. Xinlu, Chin. J. Nucl. Phys. **6**, 369 (1984).

[17] K. R. Zasadny, H. M. Agrawal, M. Mahdavi, G. F. Knoll, Transactions of the American Nuclear Society, Vol.47, p.425 (1984), USA.

[18] J. W. Meadows, Nucl. Sci. Eng. **85**, (1983) 271.

[19] M. Varnagy, S. Juhasz, J. Csikai, Nuclear Instrum.and Methods in Physics Res., Vol.196, p.465 (1982), Netherlands

[20] J. Behrens, J. Browne, J. Walden, Nucl. Sci. Eng. **80** (1983) 271.

[21] K. Kobayashi, I. Kimura, H. Gotoh, H. Yagi, Technical Report **6**, Kyoto University, Research Reactor Institute (1973).

[22] R. Jiacoletti, W. Brown, H. Olson, Nucl. Sci. Eng **48** (1972) 412.

[23] W. E. Stein, R. K. Smith, H. L. Smith, Technical Report **9205**, Los Alamos Scientific Laboratory (1968).

[24] J. Grundl, Nucl. Science and Engineering, **30** (1967) 30.

[25] P. H. White and G. P. Warner, J. Nucl. Energy **21** (1967).

[26] H. W. Schmitt and R. B. Murray, Phys. Rev. **116** (1959) 1575.

[27] V. M. Pankratov et al, Atom. En. **9** (1960) 399.

[28] M. B. Chadwick et al, Nuclear Data Sheets **112** (2011) 2887-2996.

[29] K. Shibata, O. Iwamoto, T. Nakagawa, N. Iwamoto, A. Ichihara, S. Kunieda, S. Chiba, K. Furutaka, N. Otuka, T. Ohsawa, T. Murata, H. Matsunobu, A. Zukeran, S. Kamada, and J. Katakura: "JENDL-4.0: A New Library for Nuclear Science and Engineering," J. Nucl. Sci. Technol. 48(1), 1-30 (2011).

[30] JEFF-3.2, Evaluated Data Library (neutron data), OECD Nuclear Energy Agency, 2014.

[31] CENDL-3.1, Chinese Evaluated Neutron Data Library, 2009.

[32] ROSFOND-2010, Neutron Library, Obninsk, Russia, 2010.

[33] National Nuclear Data Center, Brookhaven National Laboratory, www.nndc.bnl.gov.

[34] R. B. Gardner, K. Verghese, H. M. Lee, Nucl. Instrum. Methods **176**, (1980) 615-617.

[35] Eckert & Ziegler Reference & Calibration Sources, Product Information.

[36] MCNPX, Version 2.5.0, LA-CP-05-0369 (Los Alamos National Laboratory, April 2005).

[37] D. Sokaras, E. Bistekos, L. Georgiou, J. Salomon, M. Bogovac, E. A.-Siotis, V. Paschalis, I. Aslani, S. Karabagia, A. Lagoyannis, S. Harissopulos, V. Kantarelou, A.-G. Karydas, Nucl. Instr. Meth. B **269** (2011) 519-527.

[38] *'Backscattering Spectrometry'*, W-K.Chu, J.W. Mayer, M-A. Nicolet, Academic Press, New York (1977).

[39] M. Mayer in: J. L. Duggan, I. L. Morgan (Eds.), Proceedings of the 15th CAARI, AIP Conference Proceedings, **475** (1999) 541.

[40] J. F. Ziegler, J. P. Biersack, U. Littmark, *The stopping and range of ions in solids* (Pergamon Press, New York 1985).

[41] www.cern.ch.

[42] C. Rubbia, et al., A high resolution spallation driven facility at the CERN-PS to measure neutron cross-sections in the Interval from 1 eV to 250 MeV, CERN/LHC/98-02 (EET).

[43] M. Giovannozzi et al.,``The proton beams for the time-of-flight neutron facility at the CERN-PS", CERN-PS/2000-009(AE).

[44] Y. Kadi, J. P. Revol. Design of Accelerator-Driven System for the Destruction of Nuclear Waste. Accelerator-Driven Systems for Energy Production and Waste Incineration: Physics, Design and Related Nuclear Data (2002).

[45] ``CERN n_TOF Facility: Performance Report", CERN/INTC-O-011,INTC-2002-037,CERN-SL-2002-053 ECT, 2002.

[46] C. Borcea et al., Nucl. Instr. and Meth. A, 513, (2003) 524–537.

[47] C. Borcea et al., ``The Neutron Time of Flight Facility at CERN", Journal of Nuclear Science and Technology, Supplement 2, (Aug. 2002) 653-656.

[48] C. Borcea et al., ``Results from the Commissioning of the n_TOF Spallation Neutron Source at CERN, CERN-SL-2002-051.

[49] Fr. Belloni, PhD thesis, ``Neutron induced fission cross section measurements aimed at nuclear technology development", Università degli studi di Trieste, 2009.

[50] M. Calviani, ``Measurement of fission cross-section of actinides at n_TOF for advanced nuclear reactors", Università degli studi di Padova, 2009.

[51] D. Karadimos, ``Experimental determination of neutron induced fission cross section of ^{234}U and ^{232}Th", University of Ioannina, 2007 (in greek).

[52] A. Abànades et. al., Nucl. Instr. Methods A, 577-730, 2002.

[53] G. Lorusso et al., the n_TOF collaboration, Nucl. Instr. Methods in Phys. Res. A 532 (2004) 622-630.

[54] M. Calviani et al., the n_TOF collaboration, Nucl. Instr. Methods A 594 (2008) 220-227.

[55] http: // www.kayelaby.npl.co.uk / atomic _ and _ nuclear _ physics / 4_4 /4 _4 _ 2.html.

[56] H.G. Hughes, et al., Mathematical and Computation Topical Meeting, American Nuclear Society, Madrid Spain, September (1999) 27.

[57] U. Abbondanno et al., the n_TOF collaboration, Nucl. Instr. Methods in Phys. Res. A 538 (2005) 692–702.

[58] D. Karadimos et al., the n_TOF collaboration, Nucl. Instr. Methods in Phys. Res. B 268 (2010) 2556–2562.

[59] D. Karadimos, R. Vlastou, K. Ioannidis, P. Demetriou, M. Diakaki et al., the n_TOF collaboration, ``Neutron induced fission cross section of ^{234}U at the CERN n_TOF facility", Phys. Rev. C (accepted).

[60] F. James, MINUIT: Function Minimization and Error Analysis Reference Manual (Version 94.1), Program Library D506, CERN, Geneva, 1998.

[61] R. Brun and F. Rademakers, ROOT - An Object Oriented Data Analysis Framework, Proceedings AIHENP'96 Workshop, Lausanne, Sep. 1996, Nucl. Inst. Meth. in Phys. Res. A 389 (1997) 81-86.

[62] ``FLUKA: a multi-particle transport code", A. Ferrari, P.R. Sala, A. Fasso, and J. Ranft, CERN-2005-10 (2005), INFN/TC_05/11, SLAC-R-773.

[63] L. Skordis, MSc thesis, National Technical University of Athens, Athens, 2012 (in greek).

[64] G. D. Adeev et al., *A method of calculation of mass and energy distributions of fission residuals in reactions induced by intermediate energy particles*, Preprint INR RAS 861/93, 1993.

[65] F.-J. Hambsch, F. Vives, P. Siegler, S. Oberstedt, Nuclear Physics A **679** (2000) 3-24.

[66] *Program SPECTRW*, K. Kalfas, private communication.

[67] *Program Tv*, J. Theuerkauf,S. Esser, S. Krink, M. Luig, N. Nicolay, O. Stuch, H Wolters, Institute of Nuclear Physics, University of Cologne.

[68] Beam Profile Calculator, V. Vlachoudis, available at http://pceet076.cern.ch.

[69] http://www-nds.iaea.org/standards.

[70] G. Vourvopoulos, T. Paradellis, A. Asthenopoulos, Nucl. Instrum. Methods A **220** (1984) 23-25.

[71] R. Vlastou, M. Kokkoris, M. Diakaki, Ch. Constantinou, C. A. Kalfas, A. Kotrotsou, A. Lagoyannis, M. Lambrou, V. Loizou, E. Mara, V. Paneta, G. Provatas, A. Tsinganis, Nucl. Instrum. Methods B **269** (2011) 3266-3270.

[72] Y. Giomataris, Ph. Rebourgeard, J. P. Robert and G. Charpak, Nucl. Instrum. Methods A **376**, (1996) 29-35.

[73] "Neutron sources for Basic Physics and Applications", OECD/NEA Report, Neutron Physics and Nuclear Data in Science and Technology, Vol. 2, Pergamon Press.

[74] Radiation Detection and Measurement, G. F. Knoll, Fourth Edition, John Wiley & Sons.

[75] T. Dafni, E. Ferrer-Ribas, I. Giomataris, Ph. Gorodetzky, F. Iguaz, I. G. Irastorza, P. Salin, A. Thomas, Nucl. Instr. and Meth. in Phys. Res. A 608 (2009) 259–266.

[76] S. Andriamonje et al. (The n_TOF Collaboration), Journal of the Korean Physical Society **59**, No 2, (August 2011) 1597-1600.

[77] I. Giomataris and R. De Oliveira, Method for fabricating an amplification gap of an avalanche particle detector (Patent CEA-CERN, Application Number 09 290 825.0, 2009).

[78] Y. Giomataris, ``Development and prospects of the new gaseous detector "micromegas" ", Nucl. Instr. and Meth. in Phys. Res. A 419 (1998) 239–250.

[79] S. Andriamonje, D. Attie, E. Berthoumieux, M. Calviani, P. Colas, T. Dafni, G. Fanourakis, E. Ferrer-Ribas, J. Galan, T. Geralis, A. Giganon, I. Giomataris, A. Gris, C. G. Sanchez, F. Gunsing, F. J. Iguaz, I. Irastorza, R. D. Oliveira, T. Papaevangelou, J. Ruz, I. Savvidis, A. Teixera, and A. Tomas, ``Development and performance of microbulk micromegas detectors,'' Journal of Instrumentation, vol. 5, P02001 (2010).

[80] "Study and characterization of MicroMegas detectors for the measurement of the cross section of the reaction ^{237}Np(n,f)", Alexandros-Andreas Kyrtsos, Undergraduate thesis, National Technical University of Athens, Athens, 2013 (in greek).

[81] M. Diakaki, M. Kokkoris, A. Kyrtsos, N. G. Nicolis, E. Skordis, R. Vlastou, S. Andriamonje, E. Berthoumieux, and A. Lagoyannis, Nucl. Data Sheets, in press.

[82] F. B. Brown, R. F. Barrett, T. E. Booth, J. S. Bull, L. J. Cox, R. A. Forster, T. J. Goorley, R. D. Mosteller, S. E. Post, R. E. Prael, E. C. Selcow, A. Sood, and J. Sweezy, Trans. Am. Nucl. Soc. **87**, (2002) 273.

[83] H. Liskien, A. Paulsen, Nuclear Data Tables **11**, (1973) 569-619.

[84] S. Kumar, G. L. N. Reddy, P. Rao, R. Verma, J. V. Ramana, S. Vikramkumar, V. S. Raju, Nucl. Instrum. Methods B, **274** (2012) 154-161.

[85] J. E. Naya, P. Jean, J. Bockholt, P. von Ballmoos, G. Vedrenne, J. Matteson, Nucl. Instrum. Methods A **368** (1996) 832-846.

[86] G. Meierhofer, P. Grabmayr, J. Jochum, P. Kudejova, L. Canella, J. Jolie, Phys. Rev. C **81**, 027603 (2010).

[87] Radiation Detection and Measurement, G. F. Knoll, Third Edition, John Wiley & Sons.

[88] P. Filliatre, C.Jammes, B.Geslot, Nucl. Instr. Methods in Phys. Res. A 618 (2010) 294–297.

[89] O. Hahn, F. Strassmann. Naturwissenschaften, 26:755, 1938.

[90] L. Meitner, O. R. Frisch. Nature, 143:239, 1939.

[91] N. Bohr and J. A. Wheeler. Phys. Rev., 56:426, 1939.

[92] G. Herrmann. Nucl. Phys. A, 502:141, 1989.

[93] ``The double-humped fission barrier", S. Bjornholm, J. E. Lynn, Review of Modern Physics, Vol. 52, No 4, October 1980.

[94] ``Nuclear Physics", K.N. Mukhin, MacDonald Technical and Scientific, London.

[95] V. M. Strutinsky, Nucl. Phys. A, 95:420, 1967.

[96] V. M. Strutinsky, Nucl. Phys. A, 122:1, 1968.

[97] S. M. Polikanov, V. A. Druin, V. A. Karnauchov, V. L. Mikheev, A. A. Pleve, N. K. Skobelev, V. G. Subotin, G. M. Ter-Akapian, V. A. Fomichev, Zh. Eksp. Teor. Fiz. 42, 1016 (1962).

[98] P. M*ö*ller and J. R. Nix. In Proceedings of the Third IAEA Symposium on the Physics and Chemistry of fission, Rochester, New York, 1973, page 103, 1974. INDC(NDS)-245.

[99] P. M*ö*ller, D. G. Madland, A. J. Sierk, and A. Iwamoto. Nature, 409:785, 2001.

[100] P. M*ö*ller, A. J. Sierk, T. Ichikawa, et al. Phys. Rev. C, 79:064304, 2009.

[101] A. N. Andreyev, J. Elseviers, M. Huyse, P. Van Duppen, et al., Phys. Rev. Let. 105, 252502 (2010).

[102] E. Konecny, H. J. Specht, J. Weber, Proc. Third IAEA Symp. Phys. Chem. Fission Vol. II, 3-18 (International Atomic Energy Agency, Vienna, 1974).

[103] Schmidt, K. -H., Jurado, B. Phys. Rev. Lett. 104, 212501 (2010).

[104] K. H. Schmidt, B. Jurado, Phys. Procedia 47 (2013) 88-95.

[105] ``EMPIRE: Nuclear reaction model code system for data evaluation", M. Herman, R. Capote, B. V. Carlson, B. Oblozinsky, M. Sin, A. Trkov, H. Wienke and V. Zerkin, Nucl. Data Sheets 108 (2007) 2655-2715.

[106] EMPIRE-3.2 Malta, M. Herman, et al., INDC(NDS)-0603, BNL-101378-2013.

[107] M. Sin, R. Capote, S. Goriely, S. Hilaire, A. J. Koning, International Conference on Nuclear Data for Science and Technology 2007, DOI:10.1051/nddata:07370.

[108] M. Sin, P. Oblozinsky, M. Herman, R. Capote, Journal of the Korean Physical Society, Vol. 59, Np. 2, August 2011, pp. 1015-1018.

[109] M. Sin, P. Oblozinsky, M. Herman, R. Capote, Journal of the Korean Physical Society, Vol. 59, No.2, August 2011, pp. 1015-1018.

[110] R. Capote, M. Herman et al., Nucl. Data Sheets 110, 3107 (2009).

[111] R. Capote, S. Chiba, E. Soukhovitskii, J. M. Quesada, E. Bauge, J. Nucl. Sci. Technol. 45, 333 (2008).

[112] M. Sin, R. Capote, Phys. Rev. C 77, 054601 (2008).

[113] J.J. Griffin, Phys. Rev. Lett. 17, 478 (1966).

[114] C. K. Cline M. Blann, Nucl. Phys. A 172, 225 (1971).

[115] Reference Input Parameter Library (RIPL-3), R. Capote, M. Herman, P. Oblozinsky, P.G. Young, S. Goriely, T. Belgya, A.V. Ignatyuk, A.J. Koning, S. Hilaire, V.A. Plujko, M. Avrigeanu, O. Bersillon, M.B. Chadwick, T. Fukahori, Zhigang Ge, Yinlu Han, S. Kailas, J. Kopecky, V.M. Maslov, G. Reffo, M. Sin, E.Sh. Soukhovitskii and P. Talou, Nuclear Data Sheets - Volume 110, Issue 12, December 2009, Pages 3107-3214.

[116] A. J. Cole, Statistical Models for Nuclear Decay, Fundamental and Applied Nuclear Physics Series (2000).

[117] S. Fernbach, R. Serber, T. B, Taylor, Phys. Rev. 75, 1352 (1949).

[118] A. D. Arrigo et al., J . Phys. G20, 305 (1994).

[119] B. S. Bhandari, Phys. Rev. C 19, 1820 (1979).

[120] GEF (GEneral Fission) model, available at: www.khs-erzhausen.de/GEF.html.